UNIVERSITY OF Southampton

EPSRC Centre for Doctoral Training esa in Energy Storage and its Applications

Image-Based Modelling of Transport Processes in Real Battery Electrodes and Other Electrochemical Devices: The Development of OpenImpala

by

James Le Houx

ORCiD: 0000-0002-1576-0673

June, 2022

A thesis for the degree of

Doctor of Philosophy

Energy Technology Research Group

Faculty of Engineering and Physical Sciences

University of Southampton

Primary Supervisor: Dr Denis Kramer

Secondary Supervisor: Dr Richard Wills

EPSRC Engineering and Physical Sciences Research Council

Abstract

Image-Based Modelling of Transport Processes in Real Battery Electrodes and Other Electrochemical Devices: The Development of OpenImpala

by James Le Houx

In recent years, x-ray tomography has emerged as a powerful analytical tool in the study of batteries and the processes occurring within. A region of specific interest is the porous electrode and, in particular, the heterogeneous geometry of the porous structure.

This thesis introduces the reader to different imaging and physics-based modelling methods used to study the lithium-ion battery. It's found that none of the image-based models presented in the literature scale well with an increasing number of computational cores. This results in representative elementary volumes being used to approximate the heterogeneity of the porous electrode structure.

There is a gap in the literature for the development of a highly parallelisable code that can solve physics equations across large datasets typical of modern tomography. The work presented in this thesis sets out to develop such a code in order to aid understanding of the physical processes within the battery.

This thesis also examines the use of x-ray computed tomography to analyse different electrochemical devices, including titanium dioxide electrodes for an aluminium-ion battery, lithium titanate electrodes for a supercapacitor, and lithium iron phosphate electrodes for a lithium-ion battery.

Acknowledgments

Firstly thank you to my supervisor, Prof. Denis Kramer, for all the coffees, the discussions and your time. Your patience and guidance has made academia a wonderful place to be, and you are one of the main reasons I've enjoyed the process so much. Thank you.

Thank you also to Dr. Richard Wills, for helping me take those first steps into research, and for your guidance in finishing a thesis. To Prof. Andrew Cruden, for giving me the opportunity to get into academia and always supporting me through all my degrees, your advice has been invaluable.

Thank you to all the CDT. To Sharon and Tracey, for fostering such a sense of community. To Harriet for always keeping me on my toes in the office. To Tom, George and Alex for showing me how to finish. To Andreas for showing me that there's life outside University. To Nick for all the laughs and schemes. But most of all to Ewan, for being such a great friend. It's been an absolute honour being by your side and I can't thank you enough for all the support you've given me. And I couldn't not mention Chef China.

Thank you to Dr. Rachel McKerracher and Dr. Dan Wright, for guiding me around the chemistry lab and how to make batteries. To Dr. Richard Boardman for all your support in running X-ray CT experiments. To Dr. Weiqun Zhang and Dr. Ann Almgren, for their support in getting AMReX running. To Dr. Ryan Pepper, for teaching me MPI and OpenMP. To Dr. Tom Tranter, for your support in running PoreSpy. And to Dr. Sam Cooper, for leading the way in image-based modelling.

Thank you to Jon Marsh and Prof. Suleiman Sharkh, for teaching me to always feel comfortable asking questions. To Dr. Ed Richardson, Dr. David Toal and Dr. Thomas Blumensath, for giving me the opportunity to teach. To Dr. Mohamed Torbati for your guidance in consulting. And to Dr. Sharif Ahmed, for taking a chance on me, and not letting me forget about my thesis.

To all my friends and family for putting up with me talking about batteries for four

years. To my mum and Steve, my sister and Neil, my brother and Louise, and all the Niblings, thank you for all the support you've all given me, you all kept me going. And thank you to Nick and all the Arthur Road crew for being with me through all the ups and downs.

And lastly to Dr. Robert Bird, Birdy. Thank you for stepping up when I needed you most, you're a true friend.

James Le Houx

Declaration of Authorship

I declare that this thesis and the work presented in it is my own and has been generated by me as the result of my own original research.

I confirm that:

1. This work was done wholly or mainly while in candidature for a research degree at this University;

2. Where any part of this thesis has previously been submitted for a degree or any other qualification at this University or any other institution, this has been clearly stated;

3. Where I have consulted the published work of others, this is always clearly attributed;

4. Where I have quoted from the work of others, the source is always given. With the exception of such quotations, this thesis is entirely my own work;

5. I have acknowledged all main sources of help;

6. Where the thesis is based on work done by myself jointly with others, I have made clear exactly what was done by others and what I have contributed myself;

7. Parts of this work have been published as:

    - Le Houx, James, Markus Osenberg, Matthias Neumann, Joachim R. Binder, Volker Schmidt, Ingo Manke, Thomas Carraro, and Denis Kramer. "Effect of Tomography Resolution on Calculation of Microstructural Properties for Lithium Ion Porous Electrodes." ECS Transactions 97, no. 7 (2020): 255.
    - Le Houx, James and Denis Kramer. "OpenImpala: OPEN source IMage based PArallisable Linear Algebra solver." SoftwareX 15 (2021): 100729.
    - Ojha, Manoranjan, James Le Houx, Radha Mukkabla, Denis Kramer, Richard George Andrew Wills, and Melepurath Deepa. "Lithium titanate/pyrenecarboxylic acid decorated carbon nanotubes hybrid-Alginate gel supercapacitor." Electrochimica Acta 309 (2019): 253-263.

- Le Houx, James, and Denis Kramer. "Physics based modelling of porous lithium ion battery electrodes—A review." Energy Reports 6 (2020): 1-9.
- Le Houx, James, and Denis Kramer. "X-ray tomography for lithium ion battery electrode characterisation—A review." Energy Reports 7 (2021): 9-14.
- Wang, Andrew, Simon O'Kane, Ferran Brosa Planella, James Le Houx, Kieran O'Regan, Maxim Zyskin, Jacqueline Sophie Edge et al. "Review of parameterisation and a novel database (LiionDB) for continuum Li-ion battery models." Progress in Energy (2022).
- Fraser, Ewan, James Le Houx, Luis Fernando Arenas, Kahanda Koralage Ranga Dinesh and Richard Wills. "The soluble lead flow battery: Image-based modelling of porous carbon electrodes." Journal of Energy Storage 52 (2022): 104791.
- Dataset supporting the thesis 'Image-Based Modelling of Transport Processes in Real Battery Electrodes and Other Electrochemical Devices: The Development of OpenImpala' DOI: 10.5258/SOTON/D2267.

Signed:..... Date:.....

List of Figures

List of Tables

Contents

Nomenclature

Abbreviations

2D	Two Dimensional
3D	Three Dimensional
AFM	Atomic Force Microscopy
AMR	Adaptive Mesh Refinement
AMReX	Adaptive Mesh Refinement Exascale Computing Framework
API	Application Programmer Interface
CBD	Carbon Binder Domain
CDT	Centre for Doctoral Training
CFD	Computational Fluid Dynamics
CNS	Compressible Navier Stokes
CNT	Carbon Nanotubes
CPU	Central Processing Unit
CT	Computed Tomography
DFN	Doyle-Fuller-Newman
DSPSM	Direct-Shortest Path Searching Method
EV	Electric Vehicle
FBP	Filtered Back Projection

FDM	Finite Difference Method
FEA	Finite Element Analysis
FEM	Finite Element Method
FIB	Focused Ion Beam
FIB-SEM	Focused Ion Beam Scanning Electron Microscopy
FMM	Fast Marching Method
FVM	Finite Volume Method
GMRES	Generalised Minimal Residual
HPC	High Performance Computing
IPCC	The Intergovernmental Panel on Climate Change
LBM	Lattice Boltzman Method
LCO	Lithium Cobalt Oxide
LFP	Lithium Iron Phosphate
Li-ion	Lithium Ion
LMO	Lithium Manganese Oxide
LTO	Lithium Titanate Oxide
MPI	Message Passing Interface
MRI	Magnetic Resonance Imaging
NMC	Lithium Nickel Manganese Cobalt Oxides
NMR	Nuclear Magnetic Resonance Spectroscopy
OpenImpala	Open Source Image Based Parallelisable Linear Algebra Solver
OpenMP	Open Multi-Processing
P2D	Newman's Pseudo-2D Model

PCA	1-Pyrenecarboxylic Acid
PCM	Pore Centroid Method
PDE	Partial Differential Equation
PET	Porous Electrode Theory
PNM	Pore Network Modelling
ppi	Pores per Inch
PSF	Point Spread Function
PTCR	Positive Temperature Coefficient of Resistivity
RAM	Random Access Memory
REV	Representative Elementary Volume
RVC	Reticulated Vitreous Carbon
RWM	Random Walk Method
SEI	Solid Electrolyte Interphase
SEM	Scanning Electron Microscopy
SSPSM	Skeleton Shortest Path Search Method
TEM	Transmission Electron Microscopy
TWS	Trainable Weka Segmentation
XCT	X-ray Computed Tomography
XRD	X-ray Diffraction
XRM	X-ray Microscopy
XuM	X-ray Ultramicroscopy

Symbols

α	Bruggeman Exponent

δ	Proportionality Constant
η	Dynamic Viscosity
λ	Thermal Conductivity
μ	Linear Attenuation Coefficient
Ω	Domain
ρ	Density
σ	Electrical Conductivity
τ	Tortuosity of Porous Domain
ε	Porosity
φ	Concentration of Diffusing Species
ξ	Particle Sphericity
A	Cross-Sectional Area
B	Layer Thickness
Bo	Computational Box Size
C	Concentration
D	Diffusivity
d	Diffusion Coefficient
E	Parallel Efficiency
f	Formation Resistivity Factor
g	Point Spread Function Value
H	Hydraulic Pressure
I	Beam Intensity

K	Hydraulic Conductivity
L	Length
M	Mass per Unit Area
P	Number of Computing Cores
p	Grain Shape Empirical Constant
Q	Conducting Region
q	Porous Media Empirical Constant
r	Point Spread Function Parameter
s	Ray Path
T	Temperature
t	Time
x	Integer Voxel Coordinates
Z	Integers
$\mathbf{F}$	Force
$\mathbf{J}$	Steady-State Flux of Transport Matter
$\mathbf{n}$	Unit Normal
$\mathbf{U}$	Velocity

Subscripts

0	Total Domain
$1D$	One Dimensional
act	Active Material
AP	Active Particle Domain

B	Carbon-Doped Binder Domain
$coat$	Electrode Coating
$crystal$	Crystal Phase
cv	Control Volume
d	Diffusion
$drive$	Driving
E	Electrolyte Domain
e	Electrical
eff	Effective
g	Geometrical
H	Hydraulic
h	Effective Path
i	Voxel Coordinate
m	Momentum
p	Parallel
seq	Sequential Algorithm
t	Temperature
x	X Direction
y	Y Direction
z	Z Direction

Chapter 1

Introduction to Lithium-Ion Battery Modelling

This introductory chapter starts by explicitly stating the claims of novelty contained within this thesis, shown in Section 1.1 and then giving details of each of the publications associated with this work, shown in Section 1.2. Next, a wider introduction to the literature around lithium-ion (Li-ion) batteries is presented, with specific interest shown in the motivation behind their importance, the cause and effects of thermal runaway and the influence of electrode architecture, all detailed in Section 1.3.

Section 1.4 introduces the reader to the concept of tortuosity [1] and its importance to transport mechanics in porous media, such as Li-ion battery electrodes. Different methods of obtaining tortuosity are introduced, comparing experimental methods, theoretical models and finally image-based simulation. With the concept of image-based simulation introduced, next a wider review of using computed X-ray tomography to characterise Li-ion electrodes is performed in Section 1.5. Specific attention is given to the different length scales of imaging and the different experimental techniques employed to identify different characteristics. Finally, a review of physics-based battery models is presented in Section 1.6. This section compares different image-based modelling techniques and states the current difficult and most important challenges remaining in this field.

[1] Tortuosity is the measure of the geometric complexity of a porous medium.

1.1 Claims for Novelty

The author makes the following claims of novelty for work contained within this thesis:

Novel contribution	Associated publication
1. Development of an open-source parallelisable image-based simulation software, used by multiple university research groups and the UK's national synchrotron, the Diamond Light Source, in Sections 3.1-3.4, pp. 67 - 93	Le Houx, James and Denis Kramer. "OpenImpala: OPEN source IMage based PArallisable Linear Algebra solver." SoftwareX 15 (2021): 100729, DOI:10.1016/j.softx.2021.100729.
2. Development and implementation of an efficient box sizing algorithm to improve OpenImpala's computation time, in Section 3.3.3.1, pp. 85 - 88	Publicly available at: https://github.com/kramergroup/openImpala
3. Computed tomography and structural analysis of a lithium titanate/pyrenecarboxylic acid decorated supercapacitor electrode, improving morphological understanding of this novel material, in Section 4.2, pp. 101 - 104	Ojha, Manoranjan, et al. "Lithium titanate/pyrenecarboxylic acid decorated carbon nanotubes hybrid-Alginate gel supercapacitor." Electrochimica Acta 309 (2019): 253-263, DOI:10.1016/j.electacta.2019.03.211.
4. Study of the effect of tomography resolution on parameter calculation in a lithium iron phosphate electrode, improving understanding of experimental setup for lithium-ion electrode characterisation, in Section 4.3.1-4.3.2, pp. 104 - 115	Le Houx, James, et al. "Effect of Tomography Resolution on Calculation of Microstructural Properties for Lithium Ion Porous Electrodes." ECS Transactions 97.7 (2020): 255, DOI:10.1149/09707.0255ecst.
5. Study of the effect of lead deposition on reticulated vitreous carbon electrodes for a soluble lead flow battery, highlighting the importance of electrode design for the soluble lead flow battery, in Section 4.3.3, pp. 115 - 120	Fraser, Ewan, et al. "The soluble lead flow battery: Image-based modelling of porous carbon electrodes" submitted to Carbon.

Table 1.1: Novel contributions contained within this thesis.

1.2 Publications

A number of publications have resulted from the work contained in this thesis. They are listed here, with the section of the thesis they correspond to. Each section that derives from published work starts with the details of the associated publication for clarity.

1.2.1 Journal papers

- Le Houx, James, Markus Osenberg, Matthias Neumann, Joachim R. Binder, Volker Schmidt, Ingo Manke, Thomas Carraro, and Denis Kramer. "Effect of Tomography Resolution on Calculation of Microstructural Properties for Lithium Ion Porous Electrodes." ECS Transactions 97, no. 7 (2020): 255, DOI:10.1149/09707.-0255ecst. Section 3.3 and Section 4.5.1.

- Le Houx, James and Denis Kramer. "OpenImpala: OPEN source IMage based PArallisable Linear Algebra solver." SoftwareX 15 (2021): 100729, DOI:10.1016/j.-softx.2021.100729. Section 4.1-4.4.

- Ojha, Manoranjan, James Le Houx, Radha Mukkabla, Denis Kramer, Richard George Andrew Wills, and Melepurath Deepa. "Lithium titanate/pyrenecarboxylic acid decorated carbon nanotubes hybrid-Alginate gel supercapacitor." Electrochimica Acta 309 (2019): 253-263, DOI:10.1016/j.electacta.2019.03.211. Specifically, the author carried out the computed tomography, postprocessing and structural analysis of a lithium titanate/pyrenecarboxylic acid decorated supercapacitor electrode, as shown in Section 3.2.

- Wang, Andrew, Simon O'Kane, Ferran Brosa Planella, James Le Houx, Kieran O'Regan, Maxim Zyskin, Jacqueline Sophie Edge et al. "Review of parameterisation and a novel database (LiionDB) for continuum Li-ion battery models." Progress in Energy (2022), DOI:10.1088/2516-1083/ac692c. Section 2.3.

- Fraser, Ewan, James Le Houx, Luis Fernando Arenas, Kahanda Koralage Ranga Dinesh and Richard Wills. "The soluble lead flow battery: Image-based modelling of porous carbon electrodes." Journal of Energy Storage 52 (2022): 104791, DOI:10.1016/j.est.2022.104791. Section 4.5.2.

1.2.2 Conference papers

- Le Houx, James, and Denis Kramer. "Physics based modelling of porous lithium ion battery electrodes—A review." Energy Reports 6 (2020): 1-9, DOI:10.1016/j.egyr.2020.02.021. Section 1.4.

- Le Houx, James, and Denis Kramer. "X-ray tomography for lithium ion battery electrode characterisation—A review." Energy Reports 7 (2021): 9-14, DOI:10.1016/j.egyr.2021.02.063. Section 1.3.

1.2.3 Data

- The data contained within this thesis can be accessed through "Dataset supporting the thesis 'Image-Based Modelling of Transport Processes in Real Battery Electrodes and Other Electrochemical Devices: The Development of OpenImpala'", DOI: 10.5258/SOTON/D2267.

1.3 Li-ion Batteries

Lithium-ion (Li-ion) batteries are currently the most established energy dense cell for electrochemical energy storage [1], and their development is paramount to the path to net zero. Li-ion batteries have a key role to play in society over the coming decades; a time during which combustion engine sales will be banned across large parts of the world [2], and electric vehicle (EV) uptake significantly expanded. Batteries integrated into power grids to support increasing proportions of renewable electricity generation and remote communities depending on micro-grid systems.

1.3.1 Popularity of Li-ion Batteries

Climate change concerns, government policy and consumer action have led to increased deployments of renewable energy technology, such as solar and wind, across the globe [3], exemplified by the recent 2021 Intergovernmental Panel on Climate Change (IPCC) report [4] and UK government 'ten point plan' [5]. These energy sources have

the potential to significantly reduce current demands on fossil fuels, and reduce greenhouse gas emissions for the electrical sector [4]. However, the inconsistency and unpredictability of these energy sources results in variable outputs, leading to uncertainty regarding the electrical grid's reliability. Energy storage technology provides a way of decoupling energy generation from demand [6] and has therefore been described as 'an essential component of future energy systems' [7].

The current transportation network is predominantly based on utilising hydrocarbons as an energy carrier, due to their comparably high energy density and ease of distribution [8]. In order to effectively reduce the reliance on hydrocarbons, and therefore reduce humanity's environmental impact, alternative energy carriers are required that would, ideally, compete with hydrocarbons [6]. Both electrification of the transportation network and the move to a sustainable hydrogen economy [9] have been considered viable solutions to this problem. However, they both require dedicated onboard vehicle energy storage solutions.

Li-ion batteries have emerged as the favoured onboard vehicle energy store due to their comparatively high power and energy densities [10]; they are also used extensively within the consumer electronics industry for this reason [11]. Most recently Li-ion batteries are being installed in large stationary applications in order to support the higher penetration of renewables onto the grid. Examples of this include the majority of the National Grid 200 MW enhanced frequency response tender [12] as well as the 100 MW Tesla installation at Hornsdale wind farm in South Australia, which consists of over 25 million 21700 cylindrical cells [13].

1.3.2 Thermal Runaway

With this significant demand in the production of Li-ion batteries, a number of safety concerns have been found, with the most catastrophic failure being a cascading thermal runaway. Thermal runaway is an exothermic chain reaction where the individual battery cells self-heat; this eventually leads to spontaneous combustion of the chemical components. This combustion typically causes a large quantity of gas to be formed,

which needs to be subsequently vented to reduce the explosion risk to the surrounding areas. It is also important to include a failure point within the battery design to accommodate the associated pressure rise, as this helps to mitigate the risk of an unknown failure point causing a pressurised explosion [14].

This exothermic reaction typically begins in a single cell, causing a large output of thermal energy. If this energy is not absorbed or moved away from the battery pack, the energy will be absorbed by adjacent cells, with the potential of causing a thermal runaway in these cells. This reaction could then propagate throughout the battery pack causing significant safety concerns. Thermal runaway can be triggered by events such as internal/external short-circuiting, over-(dis)charging or overheating.

An explosion or fire scenario is most severe for large battery packs required for transport and stationary applications, with the potential for destruction of property or an immediate threat to life, where the heat generated by one failed cell can lead to a thermal cascade throughout the battery pack. Safety concerns have adverse implications for manufacturing output, system complexity, volume and cost, legislation, and public perception/adoption of Li-ion batteries. As recently as January 2016, the United Nations backed banning Li-ion battery shipments on passenger planes as a consequence of high-profile battery fires in the aviation sector. An example of which is the whole fleet of 787 Dreamliners being grounded due to installation issues causing two battery failures [15]. Some 30 % of Li-ion batteries were shipped by air globally [16]. Li-ion batteries are considered hazardous goods and are subject to tight transport regulations in several countries, including the US, Canada, and the EU [15].

The automotive industry has also seen several high-profile electric car fires [17]. Hence, the Tesla Model S contains safety features such as an extensive cooling system, sophisticated battery management software, and a thick aluminium plate to protect against mechanical abuse. Reliability and safety are the highest consumer priorities after the cost of electric cars [18].

Amongst the failure mechanisms that can lead to thermal runaway, internal shorts

are the hardest to mitigate. Between August 14, 2006, and October 24, 2006, 9.6 million laptop batteries were recalled due to potential fire hazard from metal impurities potentially causing an internal short [19]. Consequently, rigorous and costly cleanroom standards are maintained by manufacturers, partly to mitigate internal shorts.

The number of electric vehicles on the road is still too low to conduct reliable statistical studies of incidents and accidents. It has, however, become clear that safety measures external to the battery cell are inadequate to prevent all incidents.

1.3.2.1 Positive-Temperature Coefficient of Resistivity Materials

Thermal runaway can occur due to exposure to excessive temperatures, external or internal shorts due to cell defects or mechanical abuse, and electrical abuse such as excessive charge/discharge rates. It can result in the venting of toxic and highly flammable gases and release a significant amount of heat, potentially leading to rapid combustion and severe damage to the battery, surrounding equipment and/or people.

One approach to address this problem is to functionalise passive materials [2] within the electrode to retain the complete choice of active materials [3]; whilst improving lifetime and safety without compromising on energy density, rate capability or cost [20]. Figure 1.1 shows a scanning electron microscopy (SEM) image of a typical positive Li-ion electrode. The active material (A) is embedded within a conductivity additive (B).

Positive-Temperature Coefficient of Resistivity (PTCR) and thermo-responsive polymer additives are currently being developed at the University of Southampton in order to prevent excessive temperature rises due to uncontrolled or abusive electrochemical charge/discharges, hot spots, and other thermal runaway causes. As the local electrode temperature passes a threshold value, the new electrodes would become non-conducting, suppressing all electrochemical reactions and preventing further temperature rises. These smart additives are employed in battery electrodes as coatings on the active materials or as a replacement of the conductivity additive, which is typically

[2] The electrode materials not involved in the electrochemical reaction.
[3] The electrode materials involved in the electrochemical reaction.

carbon black. A suitable morphology of the composite electrodes is consequently essential to interrupt electron pathways [21].

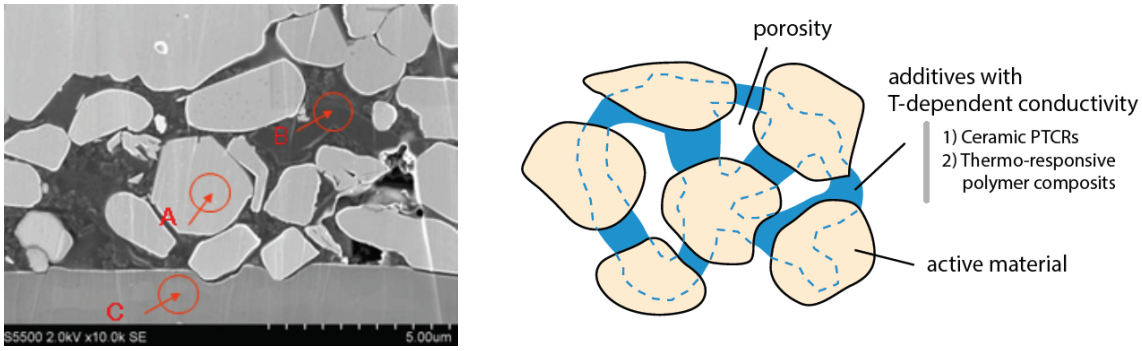

Figure 1.1: Left: SEM of a positive lithium cobalt oxide (LCO) electrode; A: active material; B: conductive additive; C: current collector. Right: concept sketch showing functionalisation of the electrically conducting additives directly within the electrode [21].

1.3.3 Electrode Architecture

The electrode architecture plays a crucial role in the performance of Li-ion batteries [22, 23]. The internal microstructure of the Li-ion battery electrode influences the performance by dictating the interfacial surface area, Li-ion diffusion path, and active material connectivity [24, 25]. These are particularly relevant in applications where the demands of energy and power densities are high [26].

The operating temperature directly controls the electrochemical performance of the Li-ion chemistry, charge acceptance, power and energy capability and cycle life [27]. The exposure of the cell to high temperature is directly linked to fast ageing and accelerated capacity fade [28]. This capacity fade has been studied by Ramadass et al. [29], who cycled a 1.8 Ah Sony 18650 Li-ion cell at elevated temperatures of 45-55°C. After 800 cycles, it was found that the test cells had lost between 31% and 36% of their initial capacity at 25°C. Whereas when the cells were cycled at 50°C, they lost more than 60% of their initial capacity after only 600 cycles. Maintaining an optimised and continuously regulated temperature profile for the battery pack is therefore directly linked to improving the cycle life. This requires an efficient thermal management system that minimises the temperature gradient between adjacent cells within the modules [30].

1.3.3.1 Degradation Mechanisms

In order to better understand how temperature change affects Li-ion batteries, it is necessary to look at the degradation mechanisms of the battery. A Li-ion battery is composed of two electrodes, the anode and the cathode, which are separated by a polymer membrane. In order to conduct ions between the electrodes, an electrolyte is used, which can be liquid, solid or polymeric. The interactions at the electrolyte/electrode interface account for the largest percentage of thermal degradation, but the mechanisms vary depending on which electrode surface it is.

At the anode, during the first discharge of the Li-ion cell, a certain amount of the electrolyte decomposes, causing an irreversible loss of lithium ions, reducing available capacity [31]. However, this decomposition of the electrolyte forms a protective solid-electrolyte interphase (SEI) layer on the electrode surface, this layer is permeable to lithium ions but prevents further electrolyte decomposition. The structure, composition and morphology of the SEI layer are critical parameters of the performance of the battery and the modification of any of these parameters can affect battery performance, capacity and life. Higher temperatures favour both SEI formation and growth causing morphological and compositional changes, this negatively affects the porosity of the SEI layer and eventually leads to increased cell impedance and lithium-ion loss, resulting in power and capacity fade [32].

Li-ion cathodes are composite structures containing a lithiated metal oxide active material, conductive additives to increase overall electrical conductivity, and binders coated together on an aluminium current collector. Elevated temperatures can cause increased decomposition reactions of the inactive components such as the binder, enhance oxidation of the conductive additives and increase corrosion of the current collector from the electrolyte [33]. Depending on the composition of both the active material and electrolyte, increased temperatures can increase decomposition and allow structural changes that can cause effects such as islanding, where parts of the active material are separated from connection due to decomposed material [14].

A combination of these degradation pathways results in an overall loss of capac-

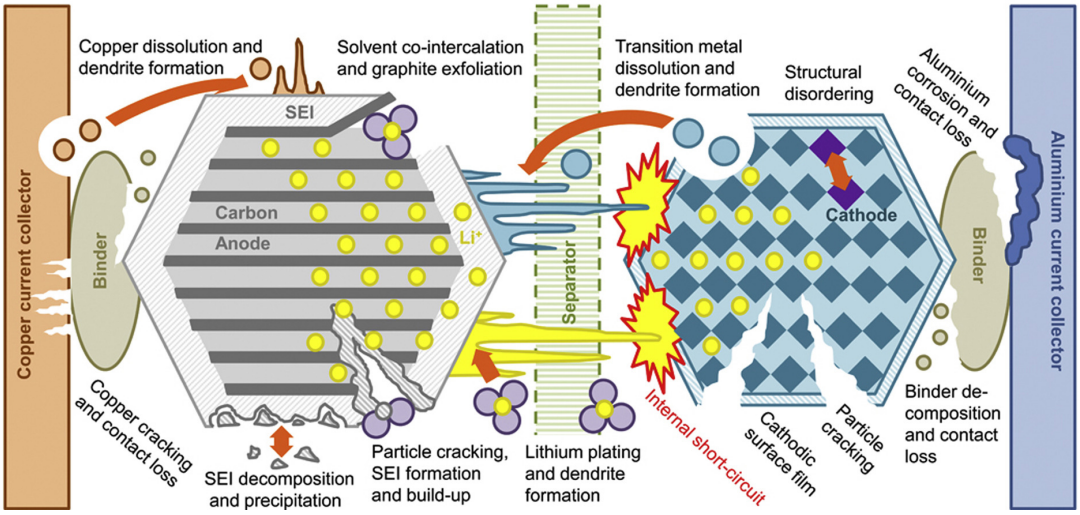

Figure 1.2: Summary of the degradation pathways in lithium-ion batteries, reproduced under the creative commons licence from [34].

ity and power fade, an overview of these different mechanisms can be seen in Figure 1.2. Thus, it can be seen that thermal degradation mechanisms are complex and very material dependent. Understanding the active material microstructure and how it performs during charge/discharge can, therefore, lead to the development of safer battery systems.

1.3.4 Geometric Parameterisation

This section is a modified version of the authors contribution to "Review of parameterisation and a novel database (LiionDB) for continuum Li-ion battery models", published in "Progress in Energy 4(3) 2022" by "Wang, Andrew, Simon O'Kane, Ferran Brosa Planella, James Le Houx, Kieran O'Regan, Maxim Zyskin, Jacqueline Edge, Charles Monroe, Sam Cooper, David Howey, Emma Kendrick and Jamie Foster".

The Doyle-Fuller-Newman (DFN) LiB model, based on Newman and Tobias' porous electrode theory (PET) and concentrated-solution theory, is broadly acknowledged to be a useful model for describing the behaviour of a single Li-ion cell (an anode/cathode pair) and it is simulation at these relatively small scales that underpins those at the larger scales, where anode/cathode pairs are grouped into pouch and cylindrical cells and then into modules and packs. The DFN or Newman model was first proposed in the seminal works [35–37] and used to make predictions which exhibit quantita-

tive agreement with a wide variety of experimental measurements, see, e.g. [38]. The mathematical model itself is relatively complex and contains upwards of 20 scalar parameters and around five scalar functions [39]. It is difficult to parameterise the model as many of the requisite quantities are difficult or impossible to measure directly and instead are inferred indirectly. Moreover, there can be significant device-to-device variability, even in cells that are prepared in the same way.

Typically, the two electrodes are produced by coating a slurry (consisting of active material particles, conductive additive and binder, in a solvent) onto a metal foil (i.e. the current collector), drying to remove the solvent and then calendaring (i.e. applying compression). The calendaring pressure is key to the process as it impacts not only the thickness of the resulting electrodes, but also their porosity and morphology. The geometry of the electrode mesostructure that results from the processing (in combination with the inherent morphology of the active particles used) determines the effectiveness of the various transport and kinetic processes occurring in the electrodes. The porous structure of polymer separators will also affect the effective transport properties of the permeated electrolyte.

To minimise repetition in the following subsections, it should be stated that although volume fractions, particle sizes, surface areas, and tortuosity factors are all typically reported as single averaged values for each component (i.e. anode, separator and cathode); they can, in fact, all be varied as a function of depth through any component. In addition, all of the parameters reported in this section may in reality vary with state-of-charge, temperature and even state-of-health of the cell, although this is usually ignored.

Each of the parameters listed in this section are geometric in nature and could be obtained through image-based analysis, demonstrating how image-based simulation fits into the wider landscape of multi-scale battery modelling.

1.3.4.1 Layer Thickness (B)

Although perhaps the easiest parameter to understand, the layer thickness of components within the cell is not always straightforward to measure. Particularly in the case of the separator, which is usually made of a compressible porous polymer and so might have a different thickness when wound or stacked into an assembled cell than if measured *ex-situ*. Another consideration is that volume expansion occurs in some active materials during lithiation [40] and therefore it may be that the layer thicknesses are not fixed during operation. These considerations are typically disregarded and single values are used, measured either separately (prior to assembly) or following teardown [41].

1.3.4.2 Volume Fraction (ε)

The two electrodes usually contain four distinct phases: active material particles, a conductive additive, a polymeric binder, and the pore phase.

The conductive additive (often carbon black) is present to increase the electronic conductivity of the solid phase. The conductive additive particles are generally much smaller than those of the active material, improving the surface area coverage and thus percolation. Furthermore, since the conductive additive is typically well mixed with a polymeric binder and hard to distinguish using most imaging techniques, these two phases are usually treated as a single-phase referred to as the Carbon-Binder-Domain (CBD).

In general, Li-ion battery manufacturers aim to maximise the energy density of cells by using a very sparse CBD. Many models, including the original DFN models, then assume active material particles are entirely surrounded by the electrolyte domain as the CBD is negligible [36, 37, 42]. The electrolyte volume fraction can be defined as:

$$\epsilon = 1 - \epsilon_{act} = 1 - \frac{M_{coat}}{B\rho_{crystal}} \tag{1.1}$$

where ϵ is the volume fraction of electrolyte, or porosity, ϵ_{act} is the active material volume fraction, M_{coat} is the electrode coating mass per unit area, B is the electrode thick-

ness, and $\rho_{crystal}$ is the crystal density of the active material. If the exact slurry composition is known, the ratio between actual and theoretical electrode density will also provide volume fraction information [42].

The active material volume fractions, in combination with the layer thicknesses, are needed to determine the theoretical areal capacity of the cell. They are also used to calculate the maximum Li concentration in active materials, as well as for anode-cathode stoichiometric balancing.

The porosity (i.e. the electrolyte volume fraction) is critical for the rate performance of the cell as it impacts the macroscopic transport of ions in the electrolyte phase permeating all three components. Further elaboration on the impact of porosity on pore transport, and the methods used to represent this, is provided in Section 1.4.

1.4 Tortuosity

Porous and permeable structures, both natural and artificial, often comprise of heterogeneous microstructures such that the internal flow paths for fluid permeation, molecular diffusion, electrical conduction and heat transfer are tortuous and meandering [43, 44]. Microstructural properties such as porosity [45], specific surface area [46], pore size distribution [47], constrictivity [48] and tortuosity [49] play important roles in characterising the morphology of porous structures. Tortuosity is used to explicitly describe the complexity of internal flow paths as well as quantify the transport properties of the porous structure [50].

The porous electrodes used in Li-ion batteries are one such example of where tortuosity plays an important role; however, this field has been studied extensively in sister fields such as geoscience [51], chemical catalysts [52], acoustics [53], water treatment [54], bone tissue engineering [55] and additive manufacturing [56]. Despite this broad influence on diverse fields, tortuosity is not consistently defined by geologists, engineers, chemists and biologists; and different types of tortuosity can even be used in-

terchangeably in the same literature. In order to mitigate against this, the following subsections describe different methods of obtaining tortuosity, compare their results and describe some of the common issues facing these methods.

1.4.1 Experimental Measurement

In order to model the permeability of porous structures, tortuosity was first introduced in [57], based on a capillary tube experiment and then further improved in [58]. Tortuosity was initially used as a parameter to describe the effect of pore structure on fluid flow in porous media [59, 60]. The solid phase of the porous structure causes the flow path to deviate from a straight line; tortuosity adjusts the length scale of the pore channel to approximate the effective flow path [44]. As well as fluid permeation, tortuosity has also been applied to other transport processes in porous structures such as molecular diffusion, electrical conduction and heat transfer.

Two experimental approaches are generally used to measure the tortuosity of porous structures, with each generally giving discrete results. The first method is based on the electrical conductivity experiment; the porous test sample is saturated with an electrolyte, and the tortuosity calculated using the effective conductivity of the sample [61–63]. The second method measures the diffusion coefficient of a nonreactive species diffusing through the porous structure sample, and the tortuosity is calculated using the measured diffusivity, such as mercury porosimetry [59, 64, 65]. The diffusion process in porous structures is much slower than the electrical conductivity measurements, and the experiment is sensitive to the selected chemical species and temperature. The measured tortuosity values from these two experiments are generally different, and, therefore, different tortuosities are defined depending on the physical process [66].

1.4.2 Theoretical Models

There have been a large number of different theoretical models proposed to estimate the tortuosity of a porous structure, most of them expressing tortuosity as functions of porosity. Of these, the Bruggeman correlation [67] is one of the most commonly used, expressed as an exponential equation, given by:

$$\tau = \epsilon^{1-\alpha} \tag{1.2}$$

where τ is the tortuosity, ϵ is the porosity, and α is the Bruggeman exponent, usually assumed to be 1.5. The Bruggeman relation is also formally consistent with Archie's law [68]: $f = \epsilon^{-\alpha}$, where the formation resistivity factor f, is defined such that $\tau = f\epsilon$. Another popular model was presented in [69] by Comiti and Renaud, which defines tortuosity as a logarithmic function of porosity:

$$\tau = 1 - p\ln\epsilon \tag{1.3}$$

where p is an empirical constant related to grain shape. Iversen and Jorgensen proposed a model in [70], where the linear relationship between porosity and tortuosity is defined as:

$$\tau = 1 + q(1-\epsilon) \tag{1.4}$$

where q is an empirical constant depending on the type of porous media. Du Plessis and Masliyah [71] formulated an analytical model from an idealised granular pore structure, without involving any undetermined parameters, expressed as:

$$\tau = \frac{\epsilon}{1-(1-\epsilon^{2/3})}. \tag{1.5}$$

Lanfrey et al. [72] derived another representative theoretical model from a fixed bed of randomly packed identical particles, given by:

$$\tau = 1.23\frac{(1-\epsilon)^{4/3}}{\xi^2\epsilon} \tag{1.6}$$

where ξ is the shape factor (sphericity) of a particle, $\xi = 1$ for a sphere and $\xi < 1$ for non-spherical particles.

These five formulations are the most prevalently used tortuosity estimations in literature, and further discussion of these models can be found in [73] and [44]. Most of them contain empirical or uncertain coefficients, such as α, p, q and ξ, and accurate determination of them is difficult. Moreover, these parameters can vary significantly,

causing substantial errors in tortuosity estimation [73, 74]. More sophisticated formulae and additional parameters have been proposed to improve prediction accuracy; however, they are only typically suitable for a narrow range of microstructures [75, 76]. In [73], it has been found that tortuosity-porosity models differ greatly and may not be used interchangeably. Furthermore, most theoretical models assume porous structures to be homogeneous and isotropic, whereas, in practice, many are highly heterogeneous anisotropic structures.

Shape, size, orientation and spatial distribution of grains and pores all affect the tortuosity of porous media. Porous structures typically consist of a large number of geometrically irregular pore bodies, some connected, some isolated and some acting as a dead end to flow paths. These complications make it highly challenging to develop an explicit mathematical model that can accurately predict the tortuosity for general porous media [44].

1.4.3 Image-Based Simulation

Modern imaging techniques are capable of providing high-resolution visualisation and characterisation of 2D and 3D porous microstructures [77]. These techniques include X-ray computed tomography [78], focused ion beam and scanning electron microscopy (FIB-SEM) [79], scanning electron microscopy (SEM) [80], transmission electron microscopy (TEM) [81], atomic force microscopy (AFM) [82] and magnetic resonance imaging (MRI) [83]. Although these techniques use different imaging mechanisms, the image data acquired are comparable at similar resolutions. These image datasets can then be used for further analyses of geometrical characterisation and physical simulation to obtain physical properties such as tortuosity.

1.4.3.1 Geometrical Tortuosity

The increasing availability of digital image datasets has increased interest in understanding how these complex microstructures affect macroscopic transport properties. One way to derive tortuosity is through geometric image analysis, where the tortuosity is defined as the ratio of the effective flow-path length to the straight-line distance in the macroscopic flow direction [50]. The transport flow inside the porous microstruc-

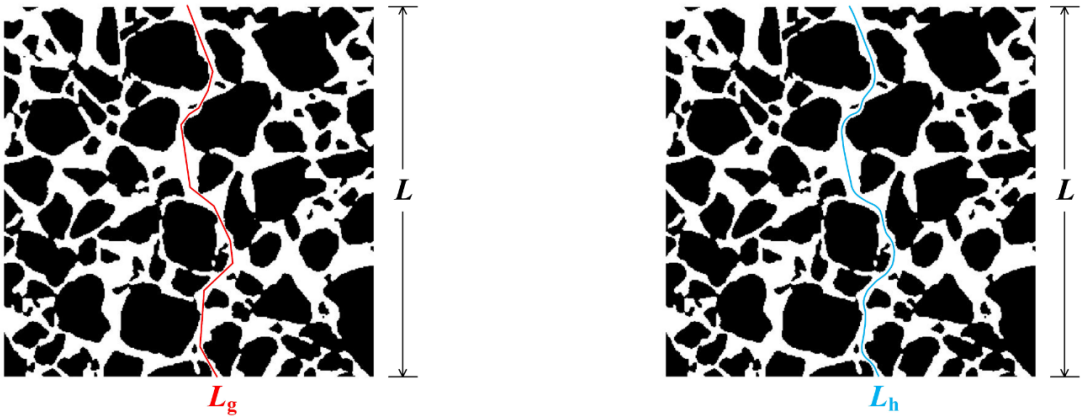

(a) (b)

Figure 1.3: A 2D digital microstructure of distance L displaying (a) the shortest pore-channel (geodesic) length L_g and (b) the effective flow-path length L_h, reproduced with permission from Elsevier [44].

ture is shaped by the pore network, so the shortest pore channel L_g is usually adopted as the effective flow path L_h to compute the geometrical tortuosity τ_g [84], as seen in Figure 1.3, given by:

$$\tau_g = \frac{L_g}{L}. \tag{1.7}$$

where the shortest pore-channel line, L_g, is more zigzagged compared to the effective flow-path length, L_h, which is smoother.

Geometrical tortuosity is considered a microstructural characteristic as it is purely determined by the morphological features of the porous structure [50]. Various algorithms have been developed to search for the shortest pore channels that can be equivalent to the effective flow paths, including the direct-shortest path searching method (DSPSM), the skeleton shortest-path search method (SSPSM), the fast marching method (FMM) and the pore centroid method (PCM). Further detail around the most popular image-based geometrical tortuosity calculation methods is given in Table 1.2.

Geometrical tortuosity often fails to accurately predict transport properties of porous structures such as permeability, effective diffusivity and conductivity. It should be noted that geometrical tortuosity is a microstructural characteristic, independent from specific transport processes in the porous structures. Furthermore, although bottle-

Analysis Method	Porous Medium	Dimension	Reference
DSPSM (Dijkstra's algorithm)	Porous rocks, nanocomposites, fuel cell electrodes	3D	[85–90]
DSPSM (wavefront propagation algorithm)	Structures of sodium chloride compacts	2D	[91]
DSPSM (A-star algorithm)	Structures of sintered compacts	2D	[92]
SSPSM (Dijkstra's algorithm)	Porous rocks, fuel cell electrodes, alumina, paper	3D	[93–97]
FMM	Porous rocks, fuel cell electrodes, infiltrated aluminium, cellular materials, energy storage materials	3D	[98–102]
PCM	Porous rocks, soil, fuel cell electrodes	3D	[103–106]
Path tracking method	Artificial models	3D	[107]

Table 1.2: Popular image analysis methods to calculate geometrical tortuosity [44].

necks and constrictions of pore channels can significantly affect the transport behaviours [48], geometrical tortuosity only considers the longitudinal distance of potential flow paths and neglects the variation of flow in the cross-section of pore channels.

1.4.3.2 Physical Tortuosity

Conversely to geometrical tortuosity, it is possible to approximate the underlying physics of the tortuosity steady-state problem through high-resolution numerical simulations as a complementary comparison to laboratory data; so that tortuosities can be calculated from physical simulations of fluid permeation, electrical conduction, molecular diffusion and heat transfer in porous media [74, 108, 109]. These physical tortuosities are calculated through pore-scale simulations based on transport processes, and methods include the lattice Boltzmann method (LBM), finite element method (FEM), finite volume method (FVM), finite difference method (FDM), the random walk method (RWM) and others. A summary of different diffusion-based physical tortuosities is given in Table 1.3.

Fluid permeation, electrical conduction, molecular diffusion, heat transfer and momentum exchange are all examples of transport phenomena that are studied in porous structures. Two principles of steady-state govern these transport phenomena: 1) the

Discretisation Method	Porous Medium	Reference
FEM (Finite Element Method)	Fuel cells and battery electrodes	[101, 110, 111]
FVM (Finite Volume Method)	Porous rocks and battery electrodes	[112, 113]
FDM (Finite Difference Method)	Porous rocks, fuel cells and battery electrodes	[75, 96, 109, 114, 115]
LBM (Lattice Boltzmann Method)	Soils, fuel cells and battery electrodes	[62, 116, 117]
RWM (Random Walk Method)	Porous rocks, fuel cells, battery electrodes, concretes and bead packs	[116, 118–121]

Table 1.3: Numerical simulation methods for the calculation of physical diffusion-based tortuosities [44].

Transport Phenomena (Transport Matter)	Driving Force	Constitutive Relation	Phenomenological Property	Definitive Law
Fluid permeation (Volume)	Hydraulic gradient ∇H (pressure gradient)	$J_H = -K\nabla H$	Hydraulic conductivity K	Darcy's Law
Molecular diffusion (mass)	Concentration gradient ∇C	$J_d = -d\nabla C$	Diffusion coefficient d	Fick's Law
Electric conduction (charge)	Voltage gradient ∇V	$J_e = -\sigma\nabla V$	Electrical conductivity σ	Ohm's Law
Heat transfer (energy)	Temperature gradient ∇T	$J_t = -\lambda\nabla T$	Thermal conductivity λ	Fourier's Law
Newtonian viscous flow (momentum)	Velocity gradient ∇U	$J_m = -\eta\nabla U$	Dynamic viscosity η	Newton's Law of viscosity

Table 1.4: Analogy of various transport phenomena in porous structures [44].

conservation law, where the quantity of transport matter (mass, charge, energy, momentum etc.) are conserved; 2) the constitutive relation, which describes how the transport matter responds to stimuli.

For these different transport phenomena, and assuming the density of the transport matter is constant, the continuity equation is expressed as [122]:

$$\nabla \cdot \mathbf{J} = 0 \tag{1.8}$$

where $\mathbf{J}$ is the steady-state flux of the transport matter. As seen in Table 1.4, the constructive relations of each of these transport phenomena are almost identically de-

scribed. Each of their transport processes is governed by similar definitive laws: Fick's, Ohm's, Fourier's, Newton's and Darcy's. The general expression of these is:

$$\mathbf{J} = -\delta \nabla F_{drive} \tag{1.9}$$

where **J**, the steady-state flux of transport matter, is proportional to the applied driving force, F_{drive} and δ, the proportionality constant, is the phenomenological coefficient corresponding to the transport property: intrinsic permeability, diffusion coefficient, electrical conductivity, thermal conductance or dynamic viscosity.

The analogy of these different transport phenomena means the development of a suitable modular image-based modelling framework could solve each, or all, of these different transport processes.

1.5 Review of X-ray Tomography Characterisation of Li-ion Electrodes

This section is a modified version of the authors contribution to "X-Ray Tomography for Lithium Ion Battery Electrode Characterisation – A Review", published in "Energy Reports 7(2): 9-14 (2021)" by "James Le Houx and Denis Kramer".

In the past decade, X-ray tomography has emerged as a powerful analytical tool in the study of Li-ion batteries, as shown in Figure 1.4. The broader availability of lab-based X-ray computed tomography (CT) scanners, the multi-length scale 3D imaging capabilities and the non-destructive nature of the technique have all led to the increase in popularity. X-ray tomography can be used to image the whole battery but, in particular, the porous electrode is a region of interest due to its direct link to the performance of the battery. Although there already exists an excellent review and introduction of the use of X-ray tomography in the study of Li-ion batteries [123], the field is rapidly developing. This chapter aims to update the reader on the development of the field and to aid in understanding the outstanding challenges.

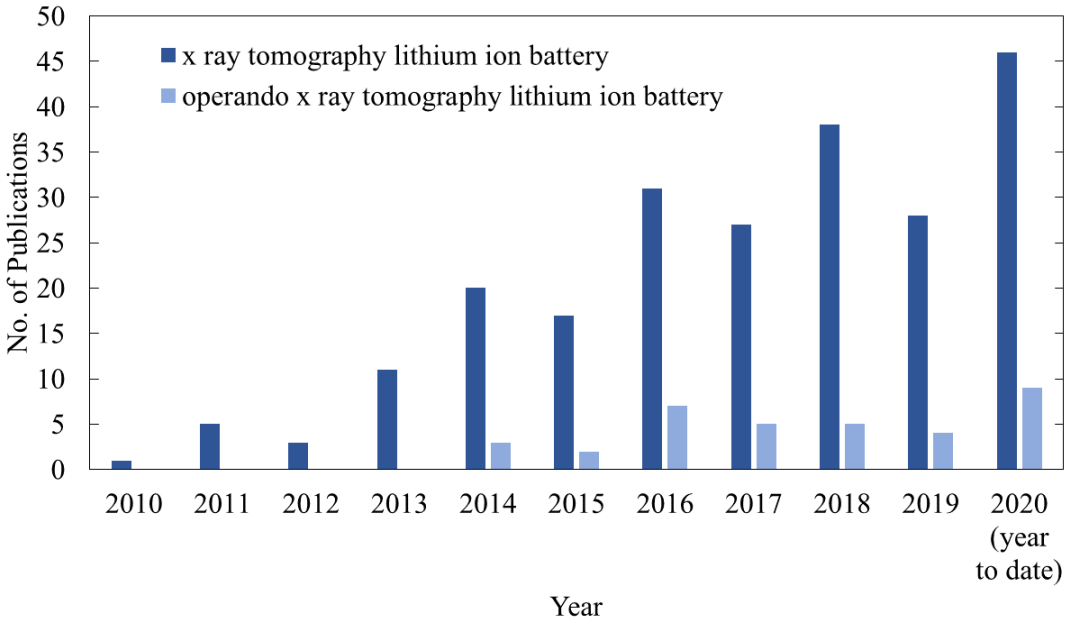

Figure 1.4: The number of publications per year searchable from Web of Science. Key term searches "x ray tomography lithium ion battery" and "operando x ray tomography lithium ion battery". Data collected 20/09/20.

1.5.1 Why X-ray Tomography?

In the past decade, CT scanners have significantly improved in terms of image resolution, imaging speed and target radiation dose, and many examples of their use in electrochemical imaging can be found [105, 124, 125]. Both focused ion beam-scanning electron microscopy (FIB-SEM) and micro-CT [4] have been shown to be suitable for capturing fine structures of porous components, many examples can be found in fuel cell research [117, 126, 127]. FIB-SEM combines the imaging capabilities of SEM with the milling and cross-sectioning abilities of FIB. This enables serial-sectioning [5] of a target sample, producing high-resolution 3D reconstructions. X-ray tomography can be a non-destructive imaging technique, as opposed to FIB-SEM which mills the target sample away [88], meaning in-situ experiments are possible, as discussed in Section 1.5.2.1.

Generally, CT scanners either use X-ray tubes or synchrotron radiation as the X-ray source. Synchrotron radiation has a higher brilliance, resulting in superior achievable spatial resolution and signal to noise ratio, but facilities are limited and have higher

[4] Micro-CT is X-ray computed tomography with a resolution at the micron scale.
[5] A series of sections cut in sequence.

operational costs [128]. Lab-based systems have a lower X-ray flux but are being used increasingly due to their cost efficiency and improved performance. The most common lab-based micro-CT is the standard cone-beam, where geometrical magnification is possible by positioning the sample between the X-ray and the detector [129]. This method can be combined with the addition of finer focusing optics, allowing for a sub-micron resolution. State of the art CT systems can achieve resolutions of 50 nm, meaning sufficient microstructural detail can be captured. Additionally, a study performed by Shearing et al. [105] on a commercial manganese-based Li-ion battery cathode, shows that a pixel size in the order of 100 nm provides consistent measurements for porosity and tortuosity calculations. This hypothesis of the effect of tomography resolution on the calculation of microstructural properties is further explored in [130], and Section 4.3.

Recent advances in X-ray computed tomography (XCT) have made nano-scale 3D microstructure imaging a reality. Nano-XCT allows the user to capture the 3D structure of porous electrodes non-destructively by reconstructing a stack of 2D images into a 3D image. It is also possible to use computationally generated geometry as a representation of the physical microstructure [131, 132]; however, imaging the electrode directly ensures the microstructure is representative without *a priori* knowledge.

Imaging of Li-ion battery electrodes allows the user to characterise the 3D microstructure, particle distribution and perform pore-scale morphological and transport property analysis [133–135], described in Section 1.5. More recently, however, the reconstructed 3D microstructure is used as a domain to simulate multi-physics phenomena occurring inside the cell, such as discharge/charge performance [136] and thermal behaviour [137], as explored in Section 1.6. Work is ongoing to develop open-source software tools to facilitate research groups using image-based modelling methods, as outlined in Chapter 3.

1.5.1.1 Macroscopic Level

At the macroscopic level, X-ray tomography can be used to measure design tolerances and defects in Li-ion batteries. The packing density of cells within an assembly, align-

ment of assembled cells, manufacturing defects such as tab adhesion and electrode thicknesses are all explored at this level [138]. In the quest for improved pack energy density, X-ray tomography has an important role to play in visualising and verifying the final assembly. X-ray tomography is an important tool in the characterisation and visualisation of macroscopic structural degradation, such as delamination, gas formation, ageing or islanding [139]. Additionally, cell level tomography provides an important tool in understanding the mechanisms of a catastrophic failure such as thermal runaway, especially when combined with operando techniques as discussed in Section 1.5.2.1.

1.5.1.2 Microstructural Level

At the microstructural level, X-ray tomography can play an important role in the quantitative analysis of Li-ion electrode structure. Tomography allows for spatially resolved studies of inhomogeneity of particle packing [6] and electrode structure, and the extraction of geometrical parameters. The two electrodes usually contain four distinct phases: active material particles, a conductive additive, a polymeric binder and the pore phase. X-ray tomography can be used to calculate the volume fraction of the pore and solid phases, important parameters in determining the theoretical areal capacity as well as the rate performance of the cell, due to the pore phases impact on the macroscopic transport of ions. Furthermore, tortuosity, which plays an important role in ionic transport is of particular interest. Recent work has introduced the concept of electrode tortuosity factor which captures the transport process relevant to porous electrodes, an important tool in the optimisation of electrode design [140].

The first example of a characterization of the 3D microstructure of a porous Li-ion electrode is performed in [124]. X-ray tomography is used to reconstruct a 43 x 348 x 478 µm sample volume with voxel dimensions of 480 nm. This volume is then subsequently divided into different sub-volumes to determine microstructural parameters as a function of sub-division size, known as Representative Elementary Volume (REV). It is found that porosity and tortuosity require the total sample volume.

[6] The packing density of structural electrode particles.

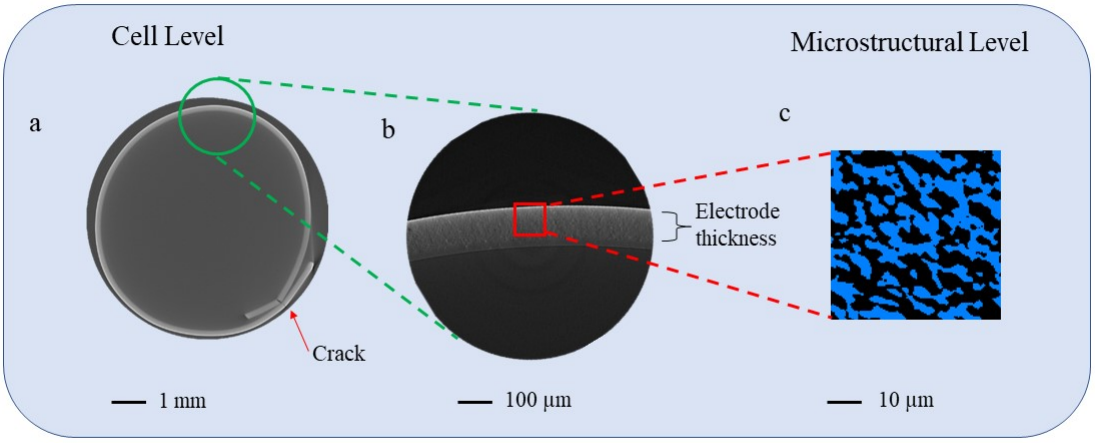

Figure 1.5: Diagram to show the different length scales used in X-ray tomography of a lithium iron phosphate electrode (a) detailing cell level, (b) an intermediary level and (c) a two-phase segmentation at the microstructural level, blue showing the porous phase and black detailing the solid phase [130].

Predicting cell degradation using macro-homogeneous porous electrode models is a challenge as there seem to be many unrelated degradation mechanisms. 3D microstructure analysis allows these degradation pathways to be measured. Tomographic techniques have allowed unprecedented access to fuel cell microstructural information through both computerised X-ray tomography and focused ion beam tomography (FIB); however, they have not been used extensively in the analysis of battery electrodes. FIB has a short stopping range of ions in graphite, meaning the sample volume that can be reconstructed is limited; therefore, X-ray CT is the preferred method [124].

Shearing et al. [124] use a Gatan X-ray ultramicroscope (XuM) system to acquire projected X-ray images at 1-degree rotation increments over 190 degrees of a graphite anode from a commericial 18650 cell. The total acquisition time is 4.2 hours. Tortuosity is calculated from the sample sizes through the geometrical definition provided by Shen in [141]. Higher porosity allows easier Li-ion diffusion through the electrolyte and therefore results in a higher power, but also means less active material per unit volume, reducing energy capacity. The volume-specific surface area is found to have a minimum REV of 90 x 121 x 124 voxels. Tortuosity and porosity are found to have a minimum REV of at least 90 x 726 x 996 voxels (the bulk volume). Mosaic plots show the

extent of inhomogeneity and that tortuosity, volume-specific surface area, and porosity do not scale together. The Bruggeman correlation does not hold for any of these findings [124].

Shearing et al. [105] investigate the microstructural properties of a commercially manufactured lithium manganese oxide cell. X-ray diffraction (XRD), X-ray microscopy (XRM) and electron microscopy are all used to characterise the cathode which has been removed from the cell. Li-ion intercalation leads to volume changes of 10% in graphite electrodes and 400% in Si-based electrodes. Being able to analyse this expansion during charge/discharge cycles in more detail would allow a greater understanding of the intercalation process. SEM, transmission electron microscopy (TEM) and nuclear magnetic resonance spectroscopy (NMR) have all been used extensively in electrode analysis. However, they only analyse 2D samples meaning 3D volumetric properties are missed.

Diffusion has traditionally been measured experimentally through the use of a diffusion cell [142]. However, with advances in Computational Fluid Dynamics (CFD), Finite Element Analysis (FEA), and more advanced imaging techniques, further investigations can be carried out. This multi-length scale method is required due to the wide range of scales of reactions, SEI growth at the nm level and failure by short-circuiting at the pack level [105].

In [105], Shearing et al. use three different X-ray resolutions: 597 nm voxel size, 65 nm voxel size and 15 nm voxel size. The two larger resolutions are found to have an excellent agreement in both solid/pore fractions and tortuosity. The slight increase in porosity is believed to be due to the increased resolution revealing smaller pore geometries. These two larger systems find pore connectivity of near to 100%, suggesting that the electrolyte phase is very well percolated. However, the most noticeable difference between these two resolutions is the volume-specific surface area which is more than twice as large due to the increased resolution [105].

For bulk porosity and tortuosity measurements, these lower resolutions can be tol-

erated with minor loss to data quality whilst also increasing analysis volumes, leading to statistical advantages. Surface calculations are, however, very sensitive to length scale. The finest resolution X-ray has a large discrepancy in porosity. This is as the sample is so small that the entire volume is within a single particle. The porosity of this image, therefore, represents internal defects in the solid structure. No connection between these internal pores and the bulk pores is witnessed, meaning there is no penetration of electrolyte into the solid structure, so 4.5% of the volume is chemically inactive [105].

These samples are then imported into commercial CFD software, Star CCM+, in order to calculate tortuosity based on Fick's and Fourier's Laws using adaptive polyhedral volume meshes. It is found that tortuosity varies in all directions, which is in agreement with studies of fuel cells [105].

1.5.2 X-ray Tomography Techniques

This section explores different techniques that have been or could be used in X-ray tomography to study Li-ion batteries. It explains different experimental setups that are specific to imaging Li-ion batteries, as well as exploring some of the more cutting-edge techniques being used. These techniques can be used to inform materials design, improve image quality or generally improve understanding of the electrode microstructure.

1.5.2.1 Ex Situ, In Situ, Operando

Li-ion batteries have reaction mechanisms operating over different time and length scales. In order to better understand these processes, different experimental techniques have been developed for X-ray tomography, namely: ex-situ, in-situ and operando [143].

Ex-situ tomography takes place on specimens that have been removed from the Li-ion battery. Either the material is imaged before the battery has been assembled [144] or the battery is cycled to a specified age and potential, and then the electrode material is extracted, such as the examples in Section 1.5.1.2. Removing material from

an already cycled battery needs to be performed in a glovebox or dry room to prevent spontaneous reactions with moisture in the air [123]. When the battery is cycled to a specified state of charge the system is in a metastable state, which, by the time of the tomography, will have relaxed to a new state whilst side reactions continue. Additionally, the removal of material generally results in the destruction of the battery, it is, therefore, difficult to obtain multiple reproducible sample results at different ages or potentials. Furthermore, the mechanical stability of extracted samples can be compromised leading to the pulverisation of electrode particles, so samples are often strengthened using epoxy or silicone infiltrations [25]. In order to avoid these problems, in-situ experiments were developed.

In-situ experiments are systems where the battery can be electrochemically cycled in place, but not operated during the tomographic imaging. They are advantageous for carrying out experiments at the same point in space but with different electrode ageing or potential, allowing for more direct comparison. One common experiment is to image a pristine electrode and then again after a number of cycles with a particular charge/discharge profile. In-situ experiments generally require the development of specific experimental cells in order to improve image quality [145–147]. The steel casing typically found around Li-ion batteries is a stronger attenuator of X-rays compared to the electrode material, reducing the intensity according to the Beer-Lambert Law, as shown in Equation 2.1. At the cell level, this is compensated by using higher beam energies, however, at the microstructural level, these higher beam energies reduce the contrast in the electrode material, reducing image quality. There is, therefore, a compromise between image quality and accurate battery performance due to the change in apparatus. Generally, in order to fully characterise the Li-ion battery electrode, both techniques are required.

Finally, during operando imaging, the Li-ion battery is operated during the X-ray tomographic imaging. Operando experiments require suitably fast acquisition times to capture the dynamics of the experiment, which generally means the use of a Synchrotron beamline [134, 148]. The operando technique means dynamic events such as thermal runaway can be captured to understand key degradation mechanisms, such as

delamination from gas production, pulverisation of the electrode layer and structural separation of islands from the electrode bulk, mechanisms that occur over a number of seconds [149–152].

1.5.2.2 Multimodal Imaging

Multimodal imaging is the practice of combining two different tomography imaging techniques. The combination of two differing but complementary techniques allows for a greater microstructural understanding of the Li-ion battery.

As an example, one challenge in the imaging of battery structures lies in the heterogeneity of the materials, which include active materials, conductive additives and binder, and the pore space of the battery. There is currently no single technique that can accurately capture each of these phases in sufficient detail [153]. One way to circumnavigate these challenges is to combine two different tomographic imaging techniques, first, ptychographic X-ray computer tomography is used to provide high resolution dataset of microstructures [154] and second, transmission X-ray tomographic microscopy, used to provide the contrast needed to distinguish between different material compositions. Further detail on ptychography as an imaging technique can be found in [155]. These two scans are then combined using image registration protocols, allowing for new types of structural analysis and physical simulation [156].

Another multimodal imaging technique is the combination of X-ray and neutron based CT imaging [157]. The absorption of X-ray photons by their interactions with the electron clouds within materials determines the contrast seen in X-ray imaging. The degree of X-ray absorption tends to increase with the atomic number of the element. Low atomic number elements, such as lithium, therefore, tend to display weak interactions and low contrast. Conversely, neutron imaging operates using the same principles as X-ray imaging, but the neutrons interact with the atom's nucleus. Meaning that the technique can show high sensitivity for some lighter elements, such as hydrogen, carbon, and lithium, where the nuclei are more closely packed [158], more detail on neutron-based imaging can be found in [159]. X-ray CT is therefore used to

identify features beyond the resolution capability of neutron CT, whereas neutron CT is used to track the spatial dynamics of light materials such as: lithium metal, lithium ions, lithium salt and the hydrogen in the electrolyte [160].

1.5.2.3 Materials Design

A recent development in the field is the emergence of using X-ray tomography to inform materials design [161]. X-ray tomography is used to capture 3D microstructural electrode data which is superimposed with the carbon binder domain (CBD) [7] to obtain a 3-phase dataset [8], by means of a multi-modal imaging technique, dual-scan superimposition. Morphological operations are then applied to the 3D microstructural data to create a virtual graded-microstructure electrode, which is then used as the computational domain for a physical model. Comparing the results of the two datasets allows fast virtual microstructures to be created and compared, and ultimately inform materials design, closing the loop between experimentation and computation.

1.5.2.4 Results Informed Imaging

Synchrotron light sources worldwide can achieve sub-second dynamic 3D acquisition times [162]. These short acquisition times enable the possibility for operando measurements, as quickly evolving systems can now be studied in detail. Furthermore, with the combination of an efficient real-time reconstruction, segmentation and on-the-fly simulation, real-time adjustments can be made to the imaging experiments whilst the processes are still running. Dynamic feedback control means areas of interest during dynamic events can be imaged in greater detail, for example, delamination areas, gas formation or islanding events. It also results in the reduction of imaging errors as any artefacts can resolved during the operation of the experiment.

[7] The CBD is the passive material that binds the electrode together and is electrically conductive.
[8] The three phases consist of active material, electrolyte and the CBD.

1.6 Review of Physics-Based Li-ion Battery Modelling Methods

This section is a modified version of the authors contribution to "Physics based modelling of porous lithium ion battery electrodes—A review." published in "Energy Reports 6 (2020): 1-9" by "James Le Houx and Denis Kramer".

Mathematical models have been used to simulate the physical and electrochemical processes occurring inside batteries in order to aid understanding and design [163]. A variety of length scales can be modelled, ranging from the atomistic (density functional theory) to pack level. Larger length scale models generally use empirical methods in order to predict the operation of the battery. However, empirical models have domain-specific strengths [9] that limit utility outside the envisioned application. Physical models, models based on fundamental physical and chemical equations [164], provide a way of understanding the processes occurring within the battery but generally require a greater amount of computing power compared to empirical models. A region of specific interest is the porous electrode, where lithium de/intercalation is governed. However, the complex geometry of the porous structure has resulted in practical difficulties in developing a suitable model [165].

1.6.1 Doyle-Fuller-Newman Model

Doyle and Newman developed one of the most popular Li-ion battery models (commonly referred to as the Newman model) based on the porous electrode and concentrated solution theory [35, 36]. This model used work from 1975 by Newman and Tiedemann, who developed the macroscopic porous electrode theory for battery applications [164, 166]. Newman's pseudo-2D (P2D) model assumes that the porous electrode is made of equally sized, isotropic, homogeneous spherical particles [35]. This homogeneous description of electrode microstructure results in smooth, uniform intercalation/de-intercalation of lithium inside the electrode and has proven to be successful in characterising discharge/charge behaviours, particularly at low to moderate rates [167].

[9] That you cannot use parameter values which are outside the range used to derive the models.

The P2D model has been shown to fail to predict phenomena related to the inhomogeneous morphology of the electrode microstructure, such as drop in charge/discharge performance at high rates [168]. The Bruggeman equation, as seen in Equation 1.2, correlates tortuosity factors of porous media with their porosity and are commonly used in modelling Li-ion transport through a flooded porous electrode. This correlation is based closely on previous work by Lorentz [169] and Lorenz [170] and has found usage in fields such as optics, electromagnetics and electrochemical research.

The Bruggeman equation is found to only be valid in situations where the insulating phase is present in a low volume fraction and represented by random, isotropic spheres. It cannot account for directional differences which arise from non-spherical particle packing. Applying this correlation to heterogeneous structures (e.g. battery electrodes) is invalid [76], and more complex approaches are required to sufficiently characterise the transport properties of the material and its resulting tortuosity factor [171]. This situation is further explained in [99] and [101], where it is stated that path length analysis can only be used to quantify tortuosity factor in simple capillary type geometries; it cannot be used reliably in more complex pore networks [172]. Therefore, there is a need for a model that utilises real microstructure as a basis for the mathematical model.

The tortuosity factor, τ, is defined for computation within this thesis as:

$$\tau = \epsilon \frac{D}{D_{eff}} \tag{1.10}$$

where ϵ is the volume fraction of the conducting phase, D is the intrinsic diffusivity of the conducting phase, and D_{eff} is the effective diffusivity through the porous volume where the second phase is insulating [109, 173].

1.6.2 Image-Based Modelling

Image-based simulation is the process by which physics-based calculations are performed on image datasets. These images capture the different materials and particles composing the porous electrode as well as the voids between which are filled by the electrolyte. Including this real geometry in the numerical computation improves understanding of how electrode morphology impacts performance. However, this does not mean it is always the best model to use as it poses two main challenges. First, these models can be computationally expensive meaning it is not always practically viable depending on the computational resource available. Furthermore, a representative microscale geometry of the battery needs to be obtained (e.g. from tomography imaging). The different techniques used to perform image-based modelling are discussed in this sub-section.

1.6.2.1 Homogenisation

Richardson et al. [174] developed a way to determine effective transport coefficients of composite materials through a mathematical homogenisation approach. A similar homogenisation approach has also used in [175–177]. Effective transport properties are defined such that an equivalent homogeneous material would carry the same flux as the original composite material using the same imposed boundary conditions. Namely, the effective transport coefficients represent a method to replace a complex heterogeneous structure with a simple homogeneous material that has the same macroscale properties, as seen in Figure 1.6.

Richardson et al. [174] consider three distinct phases within a Li-ion battery cathode: the electrolyte Ω_E, the active particles Ω_{AP} and the carbon-doped binder Ω_B. It also states that recent studies have incorporated the concept of tortuosity factor in order to be able to understand the transport properties of electrodes, as can be seen in Figure 1.8. However, it goes on to state that calculating tortuosity factor is not possible directly even if the entire microstructure is known, and it can only be found by first calculating the effective transport properties of the microstructure and then performing a reverse calculation.

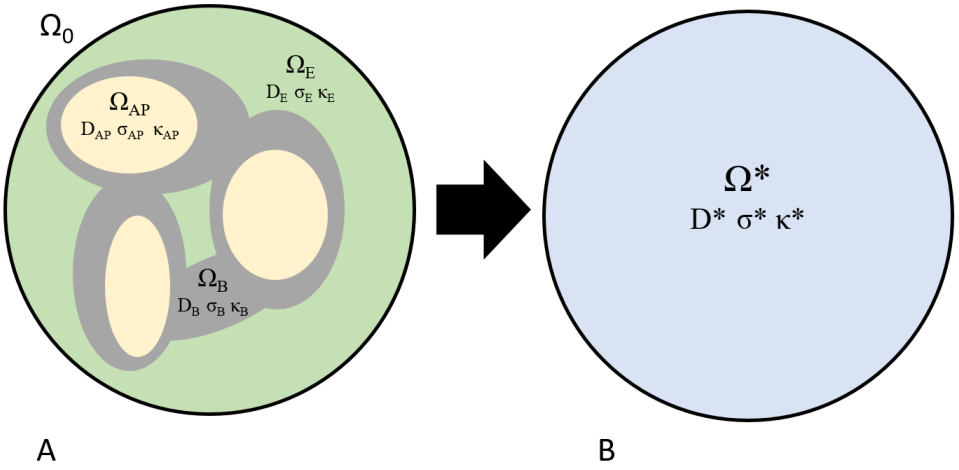

Figure 1.6: (A) A heterogeneous periodic microstructure, Ω_0, featuring three distinct phases with associated transport coefficients represented by the subdomains Ω_{AP}, active particle (yellow) Ω_E, electrolyte (green) and Ω_B, binder (grey) where the geometry can consist of any combination and structure of the three phases. (B) The homogenised equivalent domain, with transport properties of the three phases represented as effective coefficients [165].

Indeed this is the method discussed by Cooper et al. in [109] where steady-state diffusive flow is calculated across the heterogeneous structure in order to calculate the diffusivity coefficient, which is then used to calculate the tortuosity factor. Gully et al. [177] state that if the original objective is to calculate the effective transport properties, then this leads to a circular argument. The tortuosity factor is a convenient way to characterise the flow path resistance, but ultimately it is the effective transport coefficients that define the equations.

Homogenisation is achieved by using analytic continuation methods [178] that deal with geometrical information separately from material properties in order to calculate effective transport properties. This method also gives rigorous maxima and minima bounds which allow comparison of how a given microstructure performs in comparison to a geometrically optimal configuration. A number of assumptions are made in order to use this method, namely:

- Ω_0 is periodic in all three directions.
- Ω_0 is a union of three subdomains Ω_1, Ω_2 and Ω_3 corresponding to three distinct phases, i.e. $\Omega_0 = \Omega_1 \cup \Omega_2 \cup \Omega_3$.

- Each of the phases Ω_j, $j = 1,2,3$, is isotropic.
- Each phase is characterised by non-zero conductivity coefficients σ_j, $j = 1,2,3$ [174].

Focused ion beam-scanning electron microscopy (FIB-SEM) is used to capture microstructural electrode data, and this is then post-processed in order to achieve three-phase segmented datasets that can be used to solve the homogenisation tensor. The final datasets are downsampled to reduce the processing power required to solve the resulting computational problem and consist of a 51 x 51 x 51 set of voxels.

It is found in [174] that the homogenised microstructures yield different effective transport coefficients to the constant value predicted by the Bruggeman equation, Equation 1.2. It is also found in [174] that post-processing filters applied to microstructural dataset do not change the transport coefficients significantly. Lastly, it is found that for the specific sample chosen, the diffusion coefficients vary by a standard deviation of 6% depending on the direction of flow chosen. The downsampling performed to reduce the computational load is considered the main inaccuracy of the proposed approach, and the authors suggest building a software tool that can make use of parallelisation to solve the problem on a suitably large supercomputer [177].

1.6.2.2 Pore Network Modelling

Pore network modelling is a method to simulate transport inside porous materials [179]. As opposed to solving nth-order partial differential equations, the heterogeneous porous electrode is approximated as a network of pipes. The network consists of varying size and connectivity pores and throats that are chosen to match the known physical structure, obtained either by imaging techniques [180] or computer-generated structures [181]. The transport physics is solved using a 1D finite differences scheme. This scheme allows the relationship between structure and flow properties to be characterised [182].

OpenPNM is an open-source [183] software package developed in Python for pore network simulations. Unlike traditionally used continuum models, OpenPNM does

not require constitutive relationships for multiphase transport properties, such as effective diffusivity, meaning transport properties can be predicted as a function of the porous structure. Moreover, by treating the porous medium as a volume-averaged continuum, the pore-scale phenomena remain unresolved, as only the average amount of the conducting phase is known in each computational node. One of the most effective uses of this model is to simulate transport phenomena through the porous electrode. This allows choke points within the 3D space to be recognised and, through experimental iteration, could be used to tailor electrode design to improve power capabilities.

1.6.2.3 Finite Difference Methods

TauFactor is an open-source MatLab application for efficiently calculating the tortuosity factor, volume fraction, surface area and triple phase boundary density from image-based microstructural data. This tool provides a computational platform for medium-sized, three dimensional datasets (10^8 voxels) [109].

TauFactor utilises a ghost cell approach [184] in order to determine the Dirichlet boundary conditions for edge nodes. It also employs an over-relaxation iterative Jacobi method [185] in order to improve computational time. Furthermore, the voxel volume array is checkerboarded to decompose it into vectorised subdomains for the conducting phase, as seen in Figure 1.7. A direct solution method utilising matrix inversion takes over 2 hours to solve a 10^6 voxel volume, whilst the TauFactor method solves an equivalent volume in less than 30 s [109]. However, the application is not easily parallelisable and can only be run on shared memory machines, and this means that with an increasing number of voxels, calculations begin to take hours and days to solve.

The software takes an input file where the domain has been thresholded into solid and fluid phases in a per voxel basis. From this, it calculates the tortuosity factor, as well as a more detailed report: percolation fraction, a graph of volume fraction variation, and a map of total flux through each voxel can all be generated. The flux map, in the case of current flow, could help in understanding local degradation mecha-

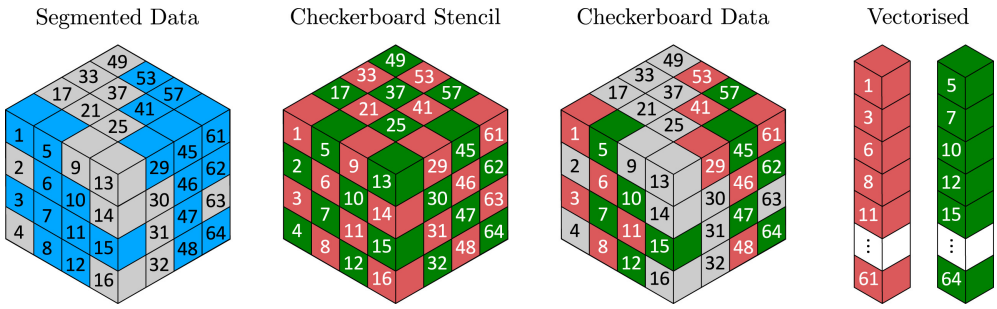

Figure 1.7: Schematic representation of converting 3D geometric data (where the blue voxels represent the conducting phase) into checkerboard adjusted vectors, reproduced under the creative commons licence from [109].

nisms through overheating. This calculation is performed directly on the thresholded domain, as opposed to re-meshing the microstructure as is usual for FEM-based approaches [147]. Four different REV analyses can also be implemented in order to directly determine what volume needs to be further worked on [109].

As the model uses an assumption of perfect tomography, where voxels containing >0.5 of a phase are modelled as a voxel entirely of that phase, true surface area and triple phase boundary densities are subject to significant error. Correction factors can be applied, but it is key to be aware of this limitation.

Figure 1.8 is a graph of eight different tortuosity factor calculation methods, and it shows that there is substantial variation across the various methods. A significant result from this graph is that the Bruggeman correlation, as given in Equation 1.2, is shown to consistently underestimate the value of tortuosity. TauFactor provides a way of standardising the calculation of tortuosity factor by working from the original steady-state diffusive flow definition [109].

1.6.2.4 Finite Element Methods

Kashkooli et al. [111] developed a multi-scale platform in order to model Li-ion battery electrodes based on actual microstructure morphology. This multi-scale platform consists of the microscale level where the morphology of the electrode is modelled and the macroscale level where discharge/charge is simulated. The microscale domain is a REV of the total reconstructed electrode; the macroscale is a one-dimensional

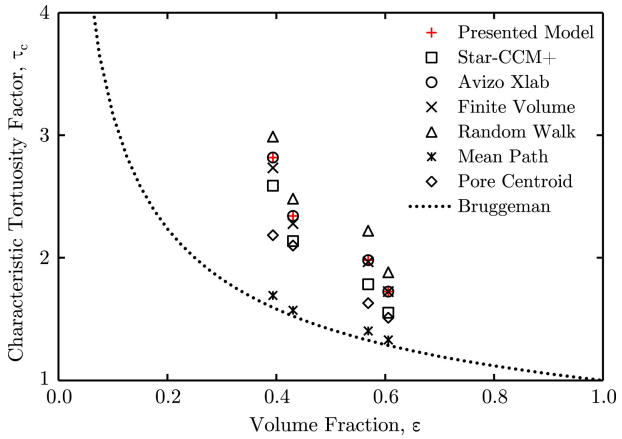

Figure 1.8: Comparison of characteristic tortuosity factors calculated using eight different methods, the presented model corresponds to Taufactor, reproduced under the creative commons licence from [109, 147].

sandwich model of Li foil | separator | cathode to simulate a half-cell reaction. These two scales are coupled in real-time, meaning the calculated intercalation flux from the macroscale is used as a boundary condition for the microscale [111].

In the macroscale, governing equations of mass and charge transfer are developed for each component of the 1D cell structure, including lithium iron phosphate (LFP) porous cathode, porous and ion-permeable membrane separator, Li foil counter electrode, and the electrolyte. The strong form statement of the problem is used to simulate the transport of lithium ions inside the electrolyte is the concentrated solution theory. The Li-ion intercalation is estimated from the Butler-Volmer equation. In the microscale, conservation of mass is governed by Fick's mass transfer equation [111].

This model utilised a finite element type simulation by taking a REV of the electrode, in this case, 750 nm x 750 nm x 750 nm. The calculations were then performed using COMSOL commercial software. This model was found to perform more accurately than homogeneous models (e.g. Newman Pseudo 2D); however, it does not consider bulk heterogeneities due to its use of REV. This method requires re-meshing the electrode dataset into polyhedral elements to be used in the FEA simulation; however, it does not require downsampling as was used by the homogenisation method.

Yan et al. [136] simulated the discharge behaviour of $LiCoO_2$ (LCO) based on nano-

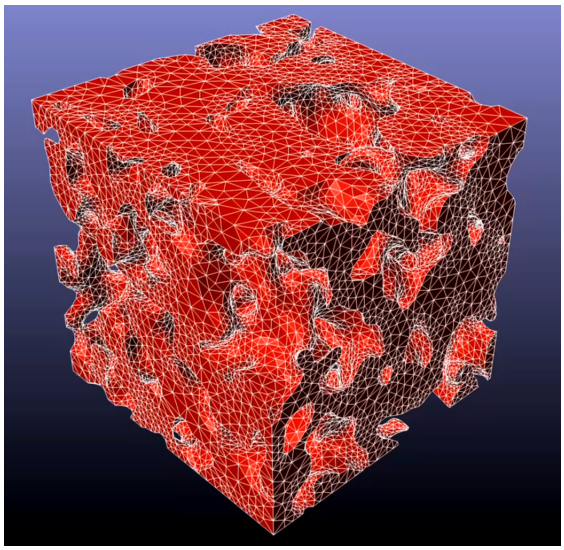

Figure 1.9: A finite element mesh of a 750 nm x 750 nm x 750 nm LFP electrode, reproduced under permission from Elsevier from [111].

XCT data. They developed an in-house model using C++ to build a microstructure based on 2D scanned images. These image-based simulations show that the electrolyte concentration distribution, current density, overpotential and intercalation reaction rate are significantly different from the results calculated using the P2D model. Furthermore, the microstructural inhomogeneity is found to be a significant factor in the performance loss, noticeably at high discharge rates. Yan et al. [137] then extended this model to simulate the heat generation during galvanostatic discharge in LCO microstructure. Their results show that the simulation based on reconstructed microstructure predicts more heat generation than the P2D model at high discharge rates. The simulation based on the reconstructed microstructure includes the heterogeneity of the structure, distributing the physical and electrochemical properties throughout the electrode. The authors attributed the higher predicted heat generation to this wider electrochemical properties distribution.

Similar methods can be used to compute other properties within the electrode. Lim et al. [135] modelled diffusion-induced stress inside LCO particles which were reconstructed using XCT. Stress-strain relations with a Li-ion concentration term and a diffusion equation with hydrostatic stress effect were used in order to simulate these effects. Their results demonstrated that the highest von Mises and Tresca stresses in reconstructed particles are several times greater than those obtained from a simple

spherical or ellipsoid particle with the same volume. Furthermore, that the intercalation stresses of the particles are dependent on their geometric characteristics.

batts3D is a set of python-based software libraries written to model the electrochemical response of heterogeneous rechargeable porous electrodes in three dimensions based on the discrete element method. Vijayaraghavan et al. [186] used batts3D to extend the widely used Bruggeman relation to incorporate the effects of mesoscale tortuosity. This method could then be used to combine a mixture of two porous particle systems of differing length scales into a single macroscopic tortuosity expression that agreed with experimental results. Chung et al. [187] studied the electrochemical and chemo-mechanical response of $LiMn_2O_4$ (LMO) cathodes based on the XCT method. Both reconstructed images and computationally generated data were simulated using batts3D. These computational experiments show that microstructural particle size polydispersity is a significant factor in the local chemical and electrical behaviour of a porous electrode.

1.6.3 Suggestions and Challenges

A summary of the models reviewed can be seen in Table 1.5. Recent years have seen the introduction of imaged electrode datasets that introduce heterogeneity to the model domains, increasing accuracy [111, 183]. However, considering the models presented, there are still a number of open issues that should be addressed in future studies [165].

Across the image-driven simulations, a variety of imaging techniques and standards are employed. XCT and FIB-SEM both operate at varying resolutions, but both obtain 3D image data. Whilst SEM and TEM both produce 2D image data. Whilst, [105] started to investigate the effect of image resolution on the results of the simulation, a more rigorous study is required to fully characterise the effects. Imaging the same electrode sample at a number of resolutions, at the same point in space and with the same overall dimensions, would allow a direct comparison of the effect of resolution on structural properties key to solving transport equations, such as tortuosity and porosity.

Name	Open Source	Description and Methodology
Chung et al. 2014 [187]	batts3D	Particle packing based on CT imaging is used to model the electrode in Batts3D
Cooper et al. 2016 [109]	TauFactor	Matlab based finite differences scheme used to calculate tortuosity directly from 3D image data
Doyle et al. 1993 [35]	N/A	Pseudo-two-dimensional model using a combination of porous electrode theory and the concentrated solution theory
Ebner et al. 2014 [188]	BruggemanEstimator	Wolfram Mathematica based tool that fits ellipsoids to 2D image data to estimate the Bruggeman exponent
Gostick et al. 2016 [183]	OpenPNM	Pore network model used to calculate transport properties from 3D image data
Gully et al. 2014 [177]	N/A	A three-phase homogenisation method is used on 3D image data
Kashkooli et al. 2016 [111]	N/A	COMSOL based multi-scale model based on 3D image data, utilises a REV to reduce computation time
Landstorfer et al. 2013 [175]	N/A	A mathematical model for the homogenisation of porous insertion electrodes based on non-equilibrium thermodynamics
Lim et al. 2012 [135]	N/A	COMSOL based model to examine effects of diffusion induced stresses in the electrodes
Richardson et al. 2012 [174]	N/A	A mathematical model for the homogenisation of a two-phase porous electrode is presented
Shearing et al. 2012 [105]	N/A	Star CCM+ model used to calculate tortuosity from 3D image data
Vijayaraghavan et al. 2012 [186]	batts3D	An analytical framework to extend the Bruggeman relation to incorporate the effects of mesoscale tortuosity
Yan et al. 2012 [136]	N/A	C++ code used to populate domain with particles based on 2D image data, then used to simulate galvanostatic discharge
Yan et al. 2013 [137]	N/A	Extends the previous model to include heat generation

Table 1.5: Main features of the physics-based porous electrode models reviewed.

One of the key themes from these models is the limitation of computational power. REVs, downsampling, particle approximations and pore network modelling are all used to try to reduce the computational resource required. Each of these comes with an associated limitation. When creating REVs, computations can be performed on volumes that are too small to be representative, potentially losing statistical relevance to the bulk and macrostructural information in the process. Macroscale heterogeneity, manufacturing defects [189] and asymmetric structures [190, 191] could all be missed by using this method. Correlation of REV size against transport properties has been performed, but this is material, sample and property dependant; therefore, further investigation is required in this field. Downsampling and particle approximations reduce the particles' microscale interactions and change the contact surface area between the phases. Finally, pore network modelling simplifies the interactions by replacing the image with a network of regular pores and throats. This method's accuracy depends on the corresponding pore network's quality compared to the original porous microstructure [192]. Being able to fully model the physical interactions at the imaging method's resolution requires a significant computing resource. However, a suitably parallelisable code explicitly written for high-performance computing environments would al-

low such calculations to be performed efficiently, revealing further scientific insight into the properties and performance of such structures [165].

Implementing one of the models discussed can take a substantial amount of time. One of the steps that is commonly carried out in these studies is the re-meshing of the image data. FEA studies require the cube-shaped voxels to be re-meshed into polyhedral shapes, pore network modelling requires the network to be created from the image data, and homogenisation requires the image data to be coarsened. Each of these steps requires human oversight and is hard to automate, and could lead to other approximation errors whilst re-meshing the dataset. However, as shown by [109], it is possible to carry out calculations directly on the imaged dataset. By solving the physical equations directly on the voxels, a step is removed from the simulation process, improving both the speed and accuracy of the modelling process [165].

1.7 Summary

Section 1.3 has highlighted the importance of Li-ion batteries to the automotive, consumer electronics and energy industries. It also has stated that thermal runaway continues to be a significant safety concern, and current prevention methods have not entirely eliminated this effect. The University of Southampton is exploring using PTCR materials in order to provide a thermal response at the runaway temperature, shutting down the battery. However, in order to understand the effects of these PTCR materials on the normal operation of the battery, physical modelling is required.

The electrode architecture plays a crucial role in the performance of Li-ion batteries. The internal microstructure of the Li-ion battery electrode influences the performance by dictating the interfacial surface area, Li-ion diffusion path, and active material connectivity. These are particularly relevant in applications where the demands of energy and power densities are high. Furthermore, a combination of degradation pathways results in an overall loss of capacity and power fade. Thus, it can be seen that thermal degradation mechanisms are complex and very material dependent.

Section 1.4 introduces the role of tortuosity in the characterisation of porous structure morphology, like Li-ion electrodes. Two experimental methods, five theoretical methods and various image-based methods are introduced.

The diffusion process in porous structures is much slower than the electrical conductivity measurements, and the experiment is sensitive to the selected chemical species and temperature. The measured tortuosity values from these two experiments are generally different, and, therefore, different tortuosities are defined depending on the physical process. It has been found that the theoretical models differ greatly and may not be used interchangeably. Furthermore, most theoretical models assume porous structures to be isotropic, whereas, in practice, many are highly heterogeneous anisotropic structures.

Geometrical tortuosity often fails to accurately predict transport properties of porous structures such as permeability, effective diffusivity and conductivity. It should be noted that geometrical tortuosity is a microstructural characteristic, independent from specific transport processes in the porous structures. Furthermore, although bottlenecks and constrictions of pore channels can greatly affect the transport behaviours [48], geometrical tortuosity only considers the longitudinal distance of potential flow paths and neglects the variation of flow in the cross-section of pore channels.

Tortuosities can be calculated from physical simulations of fluid permeation, electrical conduction, molecular diffusion and heat transfer in porous media. The analogy of these different transport phenomena means the development of a suitable modular image-based modelling framework could solve each, or all, of these different transport processes.

Section 1.5 has reviewed the open literature in X-ray tomography of lithium-ion battery electrodes. The past decade has seen significant improvements with regards to improved feature resolution and faster image acquisition. The availability of lab-based tomography systems, with ever improving performance, has made X-ray tomography more accessible to researchers for routine analysis. X-ray tomography is routinely used

for both cell characterisation, to investigate electrode thickness, packing density and macroscopic structural defects, and microstructural characterisation, to obtain electrode parameters such as particle size, volume fraction and tortuosity.

Different techniques have been employed across the field to elucidate different properties from the battery. In particular, in-situ operando experiments have become more popular in recent years, leading to better understanding of dynamic events such as thermal runaway. Some of the more recent studies have made use of multimodal imaging techniques to combine advantages of different imaging methodologies. Further work is expected in this area, improving our understanding of multi-phase porous electrodes. Furthermore, there has been the first instance of tomography informed materials design which is expected to be an increasingly used technique in the quest for improved electrode design. Finally, looking at the X-ray tomography field in general, there has been a push towards real time results informed imaging. This is expected to cross over to the field of lithium-ion batteries and is expected provide an important method in the understanding of dynamic events.

Section 1.6 reviewed the open literature in physics-based Li-ion porous electrode modelling. Physical based models, coupled with experimental validation, have helped reveal a greater scientific understanding of the processes inside the battery. The porous electrode is of specific interest as it is where lithium de/intercalation occurs. However, the complex geometry of the porous structure has resulted in practical difficulties, due to the size of datasets involved, in developing a suitable model. The models developed to approach this problem have been presented in this section.

It is found that there has been a general trend to improve the accuracy of physical-based models by including the heterogeneity of the porous electrode structure. This is in contrast to the traditional method of assuming the electrode to be a homogeneous structure through using the Bruggeman equation, Equation 1.2. Both image obtained and computationally generated datasets have been used to include this complexity in the model domain.

Considering the models that have been presented, there are still a number of open questions that remain to be solved: 1) to fully characterize the effects that image resolution has on transport properties, such as porosity and tortuosity; 2) to develop an easily parallelisable code explicitly written for high-performance computing, allowing larger image datasets to be solved; 3) to remove the re-meshing step from the simulation process, improving the speed and accuracy of the whole modelling workflow.

The Newman pseudo 2D model has been used extensively within the field of battery modelling, where the porous electrode is assumed to be made of equally sized, isotropic, homogeneous spherical particles. This model provides a good approximation of the operation of the battery. However, this model fails to predict phenomena related to the inhomogeneous structure of the electrode microstructure. The Bruggeman relation is used to correlate the porosity of the material to its tortuosity and then used to calculate effective diffusion. This relationship has been shown to be invalid for porous battery electrodes.

Homogenisation models take image-based, micro-structural data from electrodes and determine effective transport coefficients for these heterogeneous structures. This method allows complex heterogeneous structures to be replaced with simple homogeneous materials that have the same macroscale properties. However, it is shown that the mathematical method used significantly reduces either the volume of electrode studied or the resolution used. This is due to the large computational load required to solve these equations.

Image-based models have been developed that solve continuum equations on REVs. However, these models are based on commercial finite element schemes, which make them harder to parallelise across distributed memory computing systems. This reduces the volume that can be analysed, meaning bulk heterogeneities are not taken into account. TauFactor makes use of a finite difference scheme to solve the diffusion equation across microstructural data. This programme solves an equivalent volume in 30 s in comparison to direct matrix inversion, which takes over two hours. However,

Taufactor is not easily parallelisable and can only solve a single physics diffusion problem on the electrodes.

It is found that tortuosity and porosity analysis of image data required the whole sample volume, using an REV provided inaccurate results. The Bruggeman correlation was also shown to be incorrect for these results. It was also hypothesised that improved resolution revealed smaller pore geometries within the porous electrode, reducing tortuosity due to the improved interconnectivity.

None of the models presented in the literature scale well with an increasing number of computational cores. This results in REVs being used to approximate the heterogeneity of the porous electrode structure. There is a gap in the literature for the development of a highly parallelisable code that can solve the multi-physics equations across large datasets. The work presented in this thesis sets out to develop such a code in order to aid understanding of the physical processes within the battery. The code will be released as open-source software, and, with sufficient performance, is envisioned to be used by academic imaging research centres.

1.7.1 Aims and Objectives

The overall aims of this thesis are as follows:

- To develop an image-based, parallelisable, single-physics, modular computational framework capable of modelling aspects of Li-ion batteries, Chapter 3
- To use an imaging method to capture 3D microstructural data of Li-ion battery composite electrodes for use in image-based simulation, Chapter 4

In order to achieve these overarching aims, a number of individual objectives need to be accomplished:

- Establish the most suitable imaging method to capture electrode microstructure, Chapter 2

- Explore post-processing techniques that improve image quality and perform a segmentation of the microstructure datasets, and establish a standard process that can be applied in future, Chapter 2
- Develop a microstructure-based, single-physics, parallel, partial differential equation (PDE) solver, Chapter 3
- Compare the single-physics solver's results to other battery models, Chapter 3
- Use the selected imaging method to obtain microstructure datasets of a variety of electrodes Chapter 4
- Use the single physics solver to improve understanding of image-based microstructural datasets 4
- Summarise findings, Chapter 5

Chapter 2

Methodology

This Chapter presents an overview of the methods used throughout the thesis. Section 2.1 introduces a variety of imaging techniques which underpin the definition of the domain for computational analysis, generating a data set configured for a large range of length scales necessary for accurate modelling. Due to required accuracy of the domain and the accuracy of the solve, Section 2.2 introduces the computational methods used in the development of the software, including the finite-differences based modelling framework which is found to be highly applicable due to the ease of parallelisation. Finally, the findings are summarised in Section 2.3.

2.1 Imaging Methods

In order to capture the 3D microstructure of a Li-ion electrode, an imaging method needs to be chosen; this section will discuss the options available. Scanning electron microscopy and transmission electron microscopy are introduced in Section 2.1.1. Focused ion beam scanning electron microscopy in Section 2.1.2. Finally, a broader introduction is given to X-ray computed tomography in Section 2.1.3, and the specific experimental setup for the work carried out in this thesis in Section 2.1.4.

2.1.1 Scanning Electron Microscopy and Transmission Electron Microscopy

Scanning electron microscopy (SEM) and transmission electron microscopy (TEM) have both been widely used in electrode analysis [193–196]. The main components of the devices used in each method are the same. They both use an electron source and a series of electromagnetic and electrostatic lenses to control the beam and electron apertures.

SEMs scan a beam of electrons across the target in a raster-like pattern and then detect the scattered electrons and can achieve a resolution of ~0.5 nm. However, the scattered electrons mean that SEMs cannot capture 3-dimensional data sets as they do not penetrate the target [193] and are therefore unsuitable for this purpose.

TEMs transmit electrons through the sample before being detected, offering a way of capturing the internal detail such as crystal structure and morphology. Additionally, TEMs can achieve much smaller resolutions by an order of magnitude, with some reports of 50 pm. However, when considering the thickness of a standard Li-ion electrode, ~50 µm, TEM cannot penetrate deep enough to capture all the microstructure [197], therefore, it is also unsuitable.

2.1.2 Focused Ion Beam Scanning Electron Microscopy

A focused ion beam (FIB) instrument typically is made up of a stage, detector, vacuum system, a liquid metal ion source, gas inlets and an operating computer [198]. A focused ion beam is made using the liquid metal ion source, which is sputtered onto the target sample to facilitate the high resolution removal of material.

A focused ion beam scanning electron microscope (FIB-SEM) device combines the serial sectioning cabability of a FIB, with the 2D imaging capability of an SEM. This inherently means the method is destructive, as to image the next layer of material, the previous must be removed. However, it does allow for 3D imaging of microstructures,

as a stack of 2D images is produced which can be reconstructed into a 3D volume. Additionally, the achievable resolution is good, with reports of 10 nm per pixel [88]. Finally, FIB-SEM measurements require the use of a vacuum for the correct operation of the ion beam, which compromises the capability of in-situ experimental conditions.

2.1.3 X-ray Computed Tomography

X-ray computed tomography (CT) is a radiographic experimental technique used to image volumetric detail in three dimensions. The relatively good, in comparison to FIB-SEM stopping distance, penetration of X-rays permits the nondestructive imaging of the internal structure of materials [199]. This is the method that is used to image electrodes throughout this thesis.

2.1.3.1 Principle of X-ray Computed Tomography

X-rays have been used extensively in a number of different research fields. This type of radiation can penetrate materials to varying degrees and is mathematically formulated by Beer's Law. Where the transmitted intensity, I, of a monochromatic X-ray passing an object is given by:

$$I = I_0 e^{-\int \mu(s) ds} \tag{2.1}$$

where I_0 is the incident beam intensity, and $\mu(s)$ is the local linear attenuation coefficient along the ray path s [200]. This property has lead X-rays to be used extensively in the field of medical science, among other disciplines. However, the major drawback of this technique is the loss of information in one dimension. Radiographs project a three-dimensional object onto a two-dimensional detector plane, losing depth information [129]. In order to overcome this, a technique was developed in the 1970s called *Computerised transverse axial tomography* (CAT or CT). Images are acquired from different directions and then reconstructed into a 3D volume by computer algorithms, typically by a back projection algorithm [201]. From Equation 2.1, the integrated linear attenuation coefficient can be derived at each point of a radiograph:

$$\int \mu(s) ds = -ln\left(\frac{I}{I_0}\right). \tag{2.2}$$

By applying a rotational movement of the sample relative to the X-ray source and detector, a number of different projection images are made. Appropriate reconstruction algorithms [202] are then used to calculate the local value of μ for each point within the scanned volume. This value of μ is dependent on the material density ρ and the mass attenuation coefficient μ/ρ.

CT's main advantage is that it allows the nondestructive capturing of quantitive densitometric (density and geometric) images of thin cross sections through an object. The resultant image is a cross-sectional quantitave map of the linear X-ray attenuation coefficient, μ. An important property is that the attentuation values are related to the material densities of the sample. In the case where no *a priori* material information is available, it is not possible to use CT densities to identify unknown materials, as an infinite spectrum of compounds could yield the same result. Instead, in this instance, CT could still be used to analyse the morphology of the structure and any structural irregularities [199].

In a CT image, the different values of μ are represented as shades of grey. The accuracy of the resultant image depends on a number of performance factors, primarily of which is the spatial resolution. The spatial resolution is the quantifiable parameter of a CT system that refers to the size of features that can be reasonably resolved, specifically meaning the smallest separation at which two points can be distinguished as separate entities [203]. It is a result of the physical design and arrangement of the CT system, the sampling scheme used and the computational power available, as the amount of data produced can become cumbersome to handle in a reasonable time. Reducing the pixel, or voxel, size can improve the spatial resolution until the limits of the CT system are reached, beyond this point smaller pixels do not improve spatial resolution and instead can introduce artifacts into the image [199].

2.1.3.2 Image Artifacts

An image artifact is a part of the image data that does not represent the physical structure of the test sample. There are a wide range of possible image artifacts associated with CT imaging, as detailed in Chapter 7 of [201]. For brevity, a short introduction to

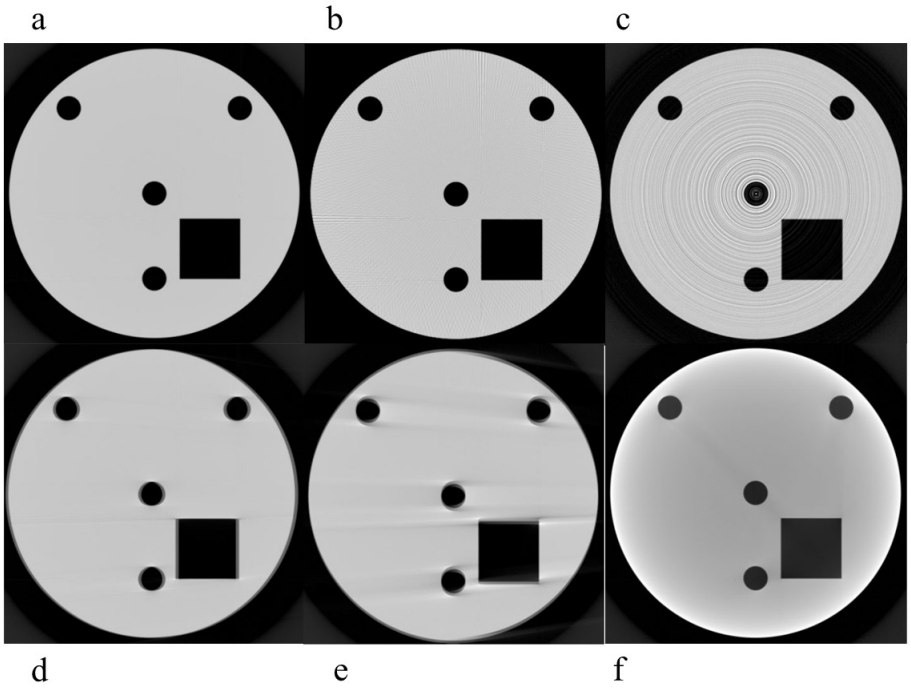

Figure 2.1: CT scans of a test phantom comparing different artifacts: (a) perfect reconstruction, (b) edge streaks, (c) ring artifacts, (d) variable spacing double edges, (e) double edges and streaking, and (f) beam hardening, reproduced with permission from Taylor and Francis from [205].

some of the more common artifacts is given in this section, including radiation scatter, statistical noise, edge streaks, beam hardening and ring artifacts. From these it can be seen that a successful CT experiment requires the careful balancing of different experimental parameters. An overview of what different artifacts look like on the resulting image is shown in Figure 2.1.

Radiation scatter occurs when the incident X-ray photon interacts the matter and is scattered. There are different types including elastic Rayleigh and inelastic Compton scattering, and the amount of these types of scatter vary depending on the X-ray energy and wavelength [204]. As the beam energy increases, so does the presence of Compton scattering, making it harder to distinguish the true signal from the scatter, reducing quality of the image. Additionally, scattered radiation can be picked up by different detectors for systems employing multiple detector elements, further reducing signal quality [199].

The physical interactions used to make CT images exhibits intrinsic statistical noise.

This noise comes from two sources: the finite number of photons measured and the method of instrumentation and processing used. For CT images, statistical noise is seen as random variation imposed on object, this can lead to difficulties in determining mean gray values and distinguishing small features from surrounding material [206]. Statistical noise is unavoidable, but can be reduced by increasing the desired signal. This is achievable experimentally by increasing scan times, the energy of the X-ray source or the size of the source and detector. Increasing the size of the source and detector will, however, reduce the spatial resolution, meaning a balance must be struck between spatial resolution and statistical noise [199].

Another source of inaccuracy is the finite width of the X-ray beam. The width of the beam strip is generally small enough that no major artifacts are generated, except for some minor loss of spatial information. This, however, is not true when there are sharp changes in signal level, i.e. in areas of high-contrast edges. These errors manifest themselves as edge streaks, as seen in Figure 2.1b and e [207]. They can be reduced by decreasing the effective size of the focal spot or detector aperture, but this leads to reduced count rates, increasing noise or scan time [199].

Beam hardening is a phenomenom occuring in polychromatic sources, where lower-energy photons are preferentially absorbed, leading to a flux with a progressively higher radiation energy as it penetrates a sample. Beam hardening leads to problems with calculating the correct values of μ, as the effective energy is changing throughout the ray path [201]. This effect can be reduced by applying suitable beam filtration to remove the lesser-penetrating parts of the spectra [199]. This effect can be seen in Figure 2.1 f.

2.1.3.3 Characterising the Accuracy of CT Imagery

Over the past 20 years, there has been a proliferation of CT based research groups [208–210]. The performance and variety of equipment have also increased as well as volumetric image processing methods [211]. CT data and analysis results are generally verified within a given research group; however, the reader of a publication has no quantitative basis for comparing results. Additionally, the validity of a given analysis and the possible effects on the measurements extracts from the dataset is not known;

this is especially true in image-based modelling. Indeed within this thesis, different image processing methods are shown: binarised thresholding with anisotropic diffusion filters, watershed thresholding and a trainable WEKA machine-learning scheme. It is standard practice within the field to quote the voxel scale; however, this information is not sufficient to evaluate the fidelity of features that are of a similar size to the CT data voxels [211].

Standardised CT system calibration methods exist that provide a way to quantify spatial and density resolution [212], and these are used to establish uniform performance benchmarks. However, there exist a number of drawbacks meaning they cannot be used routinely in regular analytical practice. They require the use of a phantom and are calibrated to perform a suite of specialised calculations against that phantom. A phantom is an object of known dimensions that can be used to characterise the blurring caused by the CT process. The performance of a system at a specific resolution may not be the same when scanning a sample due to variance in size and material composition compared to the phantom.

Figure 2.2 is an illustration of the effect CT resolution can have on the segmentation of the dataset. Figure 2.2 left is a CT image of trabecular bone from a human heel, imaged in [213]. To be able to see the location of the trabeculae within the heel and to be able to completely characterise the load-bearing properties of the bone, the whole heel was imaged. However, this resolution then had an impact on the ability to quantify the bone structure. In Figure 2.2 centre, a magnified image is shown where the bone has a variable brightness; this was not caused by variations in bone density but instead by bone thickness. If the bone is segmented using a standard greyscale thresholding algorithm (a similar algorithm to what was performed to produce Figure 4.3), then, as shown in Figure 2.2 right, some bone structures are omitted (shown by 'x' marks) while some holes are filled (shown by '+' marks). In short, a set of segmenting criteria applied uniformly across the dataset has resulted in too little material being selected in some regions and too much in others.

These two situations occur because the apparent bone thickness is a function not

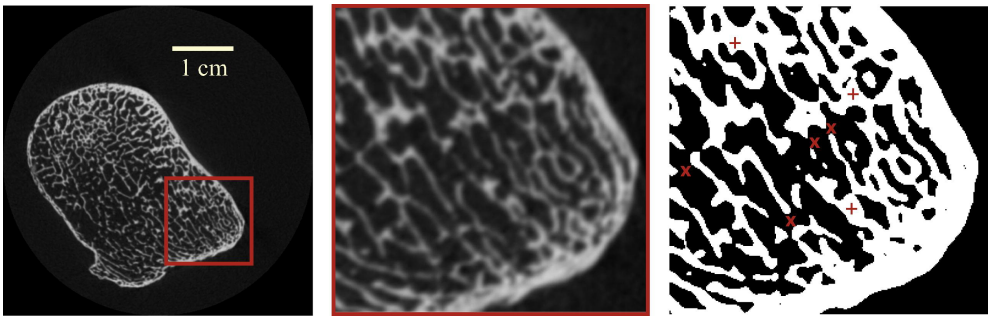

Figure 2.2: CT scans of a human heel bone, showing the effect of finite data resolution on attempts to segment bone and void, reproduced with permission from Elsevier from [211].

only of the material itself, but also of the blurring introduced by the CT scanning process. It is possible to describe the blurring introduced by the CT process as a point-spread function (PSF) that combines with underlying material via a convolution operation to achieve the final image data [214]. Blurring has the effect of a voxel CT greyscale number not only being a function of the volume subtended by that voxel but also from surrounding voxels as well [215]. Therefore walls that are thin compared to the PSF appear dimmer than typical solid as they are averaged with the adjacent void, while cracks appear narrow due to averaging with the surrounding solid. Ketcham et al. [214] introduced a methodology to analyse and use the PSF to improve the accuracy of fracture measurement, using principles from Johns et al. [216] and Van Geet and Swennen [217], but including the idea of using an explicit deconvolution operation to use the information obtained from characterising the PSF. The PSF can be specified as a smoothing-window function in the discrete voxel domain [214]:

$$g_i = exp\left[\frac{-8(x_i - r_c)^2}{(r_{PSF.v})^2}\right] \tag{2.3}$$

where g_i is the PSF value at voxel coordinate i, $r_{PSF.v}$ is the PSF parameter in voxel edge lengths in the x-y plane, r_c is the smallest integer greater than or equal to r, and x_i are integer voxel coordinates from 0 to $2r_c$, defining the size of the convolution kernel. This definition corresponds to a Gaussian function to approximately four standard deviations, ensuring smoothness. The kernel is normalised to sum to 1 to allow comparison.

The factor 8 is used to give $r_{PSF.v}$ an intuitive value, 96% of the signal from a point will lie within a region of that voxel diameter. For example, looking at a sharp crossing

between two materials, an $r_{PSF.v}$ of 5 indicates that the majority of the transition occurs over five voxels. Measured values have been shown to range from between 3 and 10 [211]; the lower the value, the sharper the imagery. This gives a quantifiable value that can be used to compare the validity of CT scans: decreasing the voxel dimensions may only increase the inaccuracies due to blurriness; however, by using this value, it is possible to quantify the accuracy of the image. A number of open-source plugins have been created to calculate PSF from deconvolution [218, 219].

2.1.3.4 Representative Elementary Volume (REV) Size and Resolution

A REV is the smallest volume over which a computation or measurement can be made that is representative of the whole volume [220]. In periodic materials, this is trivial as a periodic unit cell can be used; however, in highly heterogeneous materials, an REV must be defined. The choice of REV size and resolution (voxel size) is critical in computations and measurements involving digital microstructures. Generally, to serve as good statistical representations for the specific digital microstructure, sufficiently large REV volumes are required. Furthermore, to provide accurate pore space geometry close to reality, the microstructure must be at a sufficiently high resolution.

It is challenging in practice to deal with 3D REV samples with super-high resolutions as they can contain billions of voxels. Therefore, in practice, the raw digital microstructure data is often rescaled to a lower resolution, reducing the computational cost [221]. The choice of REV sample is often then a compromise between accuracy requirement and computational complexity.

2.1.3.5 Micro-CT

In recent years, CT scanners have significantly improved in terms of image quality, imaging speed and deposited radiation dose [211]. These developments have resulted in higher-resolution X-ray CT, commonly referred to as micro-CT. This method can be performed using X-ray tubes, gamma-ray sources or synchrotron radiation as the X-ray source. Gamma-ray sources have a low brilliance, meaning they are rarely used in micro-CT. Synchrotron source radiation has a higher brilliance compared to lab-based source, resulting in superior achievable spatial resolution and signal to noise ratio, but

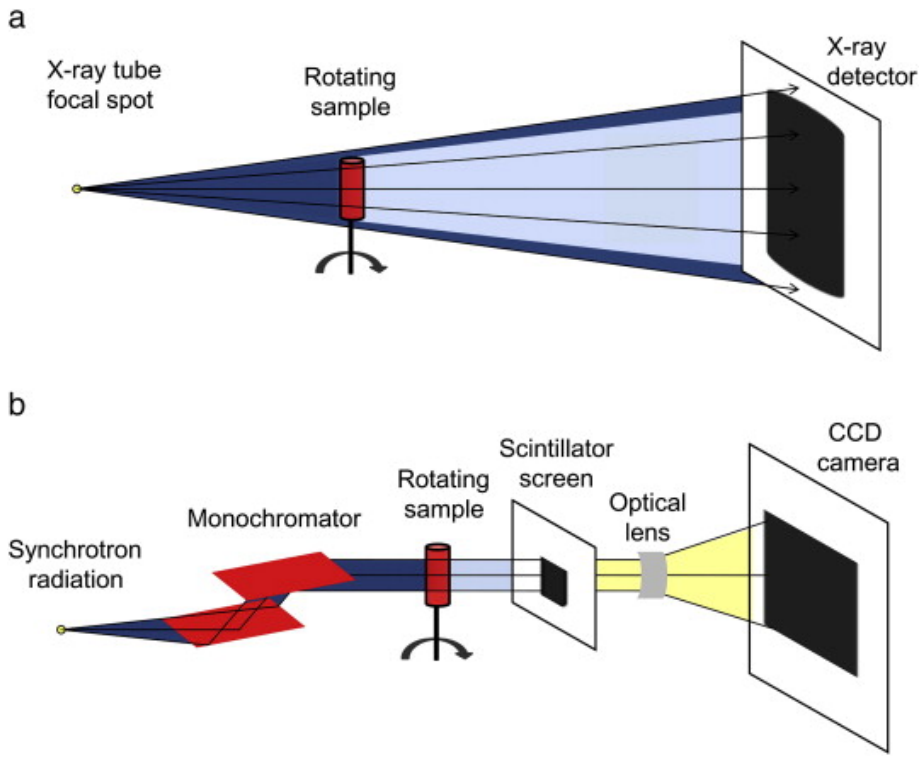

Figure 2.3: (a) Schematic diagram of a typical lab-based micro-CT with a conical X-ray beam allowing for geometric magnification. (b) Schematic diagram of a typical synchrotron-based micro-CT setup, reproduced with permission from Elsevier from [129].

the number of facilities is limited and the operational cost high. Lab-based systems have a lower X-ray flux but are used more often due to their cost-efficiency [129].

The most common lab-based micro-CT is the standard cone beam, where geometrical magnification is possible by positioning the sample between the X-ray and the detector, Figure 2.3 (a). However, the highest achievable resolution is predominately limited by the focal spot size of the X-ray source. A smaller focal spot size generally requires a reduced X-ray flux, increasing the time taken to resolve the scan. On the other hand, synchrotron sources have an almost parallel beam, making geometric magnification impossible without X-ray optics, Figure 2.3 (b). Thus, there is a trade-off between a very thin scintillator (detector), which increases the obtained resolution, or improving the detection efficiency by using a thicker scintillator.

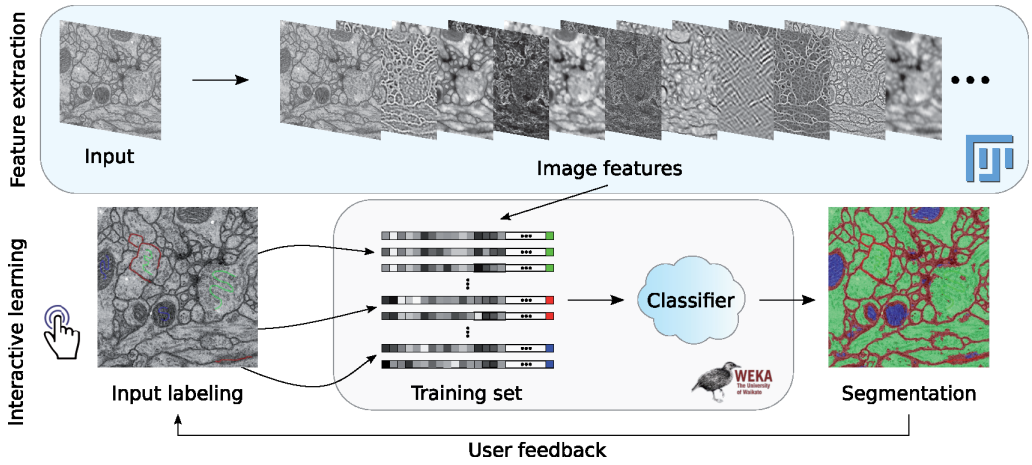

Figure 2.4: TWS example workflow for pixel classification. Image features are extracted from an input image using ImageJ. Next, a set of pixel samples is defined and represented as feature vectors, and a WEKA learning scheme is trained on those samples and finally applied to classify the remaining image data, reproduced with permission from Oxford University Press from [222].

2.1.3.6 Machine Learning Segmentation

Segmentation is the classification of a x-ray reconstruction into its consitituent materials. These classifications can be simply based on the greyscale value, or include further detail such as feature size and shape. Machine-learning algorithms have found extensive use within the post-processing community as they allow an algorithm to be 'trained' on a single tomographic slice through user input and then applied to the entire volume. Using this method, it is possible to not only differentiate materials by greyscale value but also by other characteristics such as shape and location. Machine-learning based methods can lead to more accurate segmentation but are generally more computationally expensive. As these segmented image datasets are used as computational domains for physical models, accuracy is key. Therefore, a machine-learning algorithm could be used to improve results, namely, Trainable Weka Segmentation (TWS). TWS is an open-source plugin used within a popular image processing program, ImageJ [222]. By selecting image features within the electrode microstructure - such as binder, active material and pockets of porosity - it is possible to train the algorithm to segment the entire image. An overview of the workflow for TWS can be seen in Figure 2.4 [222].

After the dataset is loaded into the plugin, image features are extracted using stan-

dard filters available within ImageJ. Features can be categorised as *edge detectors*, which try to find the boundary of objects within the image (e.g. Laplacian filters, difference of Gaussians and Hessian matrix eigenvalues); *texture filters*, which extract texture information from the dataset (e.g. minimum, maximum, variance, median filters); *noise reduction filters*, similar to the ones used to clean the dataset to produce Figure 4.3 (e.g. anisotropic diffusion, gaussian blur and bilateral filters); and *membrane detectors*, which find membrane-like structures of a given size and thickness. After the initial features have been extracted, a set of pixel samples is defined from the dataset through user input and represented as feature vectors; these samples are then used to train a WEKA machine learning scheme. This machine learning scheme is then applied across the whole dataset to classify the remaining image data. It is then possible to refine the solution by changing the pixel samples used to train the WEKA scheme until a suitable solution is found [222].

2.1.4 Imaging Experimental Setup

At the University of Southampton is the μ-VIS X-ray imaging centre, a suite of seven CT scanners and post-processing computers. A variety of CT scanners are available, such as the 225 kVp Nikon HMX, which can achieve a spot size of down to one micron using a transmission anode, and the customised 450/225 kVp Hutch that can achieve a spatial resolution of 3 microns at low energies; however, the Zeiss 160 kVp Versa 510 was chosen as it can achieve a pixel size down to 70 nm, attaining sub-micron spatial resolution. This sub-micron resolution is suitable for identifying features and particles in the microstructure of some electrodes. However, it should be noted that some feature sizes are smaller than this still but would require the use of beam-line synchrotron or highly specialised scanners such as the Zeiss Ultra.

The Zeiss Versa was chosen to acquire data for the experiments contained in this thesis, due to its widespread accessibility, availability and suitable spatial resolution. The scanner utilises a two-stage magnification, fitted with X0.4, X4, X20 and X40 magnification lenses mounted on a barrel mount and the geometric magnification of the X-ray imaging. The Versa can vary beam energies between 30-160 kVp and has a 2048

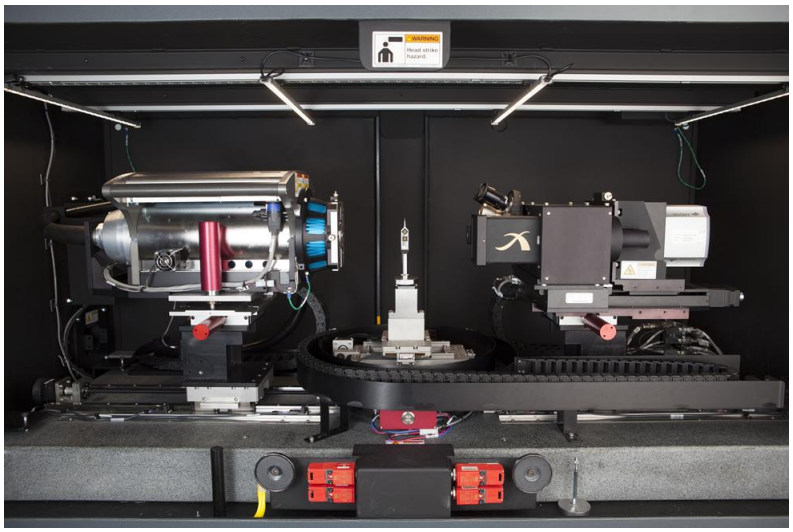

Figure 2.5: Picture showing the internals of the Zeiss Versa 510 [223].

x 2048 pixel detector. A picture of the Versa can be seen in Figure 2.5.

2.2 Computational Methods

In parallel with the work carried out on imaging the electrodes, work was also undertaken to start developing the mathematical model. Section 2.2.1 details the computational facilities that were used to carry out the computations contained in this thesis. Section 2.2.2 introduces different discretisation methods that could be used to solve this problem. Due to size of the domains being produced by X-ray CT, and the accuracy of the solve, it is important to choose an appropriate programming framework that is easily parallelisable, as discussed in Section 2.2.3. Lastly different computational methods are introduced, with parallelisation routines discussed in Section 2.2.4 and containerisation in Section 2.2.5.

2.2.1 Computational Facilities

Different computational facilities were used to complete the simulation work contained within this thesis, including Iridis4 and Iridis5 supercomputing clusters, and a local desktop machine. The local machine consists of an Intel Core i7-6700 3.40GHz quad-core with an 8MB cache and 16GB of DDR4 memory. Iridis4, consists of 750 com-

puter nodes, each with dual 2.6 GHz Intel octa-core Sandybridge processors and 64 GB of memory. Iridis5, is made up of 464 compute nodes with dual 2.0 GHz Intel Skylake processors, giving 40 CPUs and 192 GB of DDR4 memory per node. The clock speed of these processors is slower than both Iridis4 and the desktop machine; however, the large memory available per node means large datasets can be loaded entirely, improving computation times, as memory transfers to node are a costly aspect of multi-node parallel processing.

2.2.2 Discretisation

The finite element method (FEM) is used to solve boundary valued problems by integrating the strong form equation, the partial differential equation (PDE) describing the underlying physics at the material point, over elements, that can be triangular, polyhedral or a variety of other shapes [224]. Within the element the solution is approximate by the span of polynomial functions with unknown coefficients; the coefficients are the known to be solved for. Higher fidelity solutions are found by increasing the number of elements, which reduces the element's volume over which the polynomial function approximates exist. The rate of convergence of the error with element size for smooth, and non-smooth, problems is determined through a priori residual error estimator analysis [225].

The finite differences method (FDM) is a differential scheme, where the Taylor series expansion is used to approximate the PDE over a finite length using a linear or quadratic polynomial. The method finds the first order and second-order differentials in terms of the difference between discrete point values. FDM methods are usually run in regular, discretised cube meshes. Meaning they are less computationally intensive to implement during the meshing stage but can bring about an approximation of the error due to the differences method [226].

2.2.3 Finite Difference Modelling Framework

Various commercial and open-source programming frameworks are available to assist researchers in the solution of partial differential equations. In order to aid with choice,

first, the desired attributes need to be listed. The framework should be:

- Highly parallelisable. The code needs to be able to deal with a domain that could consist of up to 10^{11} voxels and must be able to solve across multiple physical fields and across the time period of a charge-discharge cycle.
- Computationally efficient. This can be achieved through adaptive mesh regimes that focus on regions of interest, both spatially and temporally.
- Minimal optimisation overhead. By focussing the model on image-based modelling, the FDM scheme can be readily deployed to a range of different CT imaging fields, improving flexibility .
- Open-source. The model should be able to be distributed open-source in order to allow for further development and for collaborators to work with the code.

Having highlighted these features, two primary candidates were chosen that satisfied these criteria: Chombo and AMReX. Chombo is an established software framework (last release 2009) that provides the capability to implement finite difference-based methods in the solution of partial differential equations on block-structured adaptively refined rectangular grids [227]. It also supports calculations of complex geometries using the embedded boundary method [228]. Chombo has been used extensively within the research community and has a wide area of applications, including compressible Navier-Stokes solutions [229], modelling the dynamics of land ice sheets [230] and simulation of carbon sequestration through porous media [231].

AMReX also uses block-structured adaptive mesh and is developed by the same researchers as Chombo. However, AMReX is being developed as part of the Department of Energy's exascale computing project; this refers to a computing system that is capable of 10^{18} floating-point operations per second [232]. Through using more computationally efficient adaptive mesh regimes, implementing a hybrid OpenMP/MPI parallel approach and by developing the framework from the ground up, AMReX-based solvers have been shown to reach a solution up to 200 times faster than Chombo using the same number of processors [233]. However, the development of AMReX began in 2017, meaning it is a much younger software and has not achieved full functionality

yet; monthly updates are currently being released regularly. An example of this is the embedded boundary technique for incorporating complex geometries, which has not been fully developed yet.

In deciding between the two software frameworks, the choice is between an established framework with a history of successful publications or a developmental, faster software that will be future-proofed for exascale computation. The decision was made to use AMReX. Due to the large number of voxels, any computational speed-up is very valuable. Additionally, as AMReX is currently under significant development, it gives a number of opportunities to collaborate with the authors and help to develop this open-source tool.

2.2.3.1 Adaptive Meshing

An extremely powerful and essential development for multiscale simulations of high fidelity in the field of computational methods is adaptive mesh refinement (AMR). In numerical analysis, AMR is a method of adapting the mesh of a solution to focus on regions of sensitivity, and this mesh can be adapted both spatially and temporally, the combination of which is especially powerful. Usually, numerical solutions are calculated on pre-determined grids in the Cartesian plane, whereas this method allows the mesh to fit to regions of interest in complex domains [234]. AMR has been applied to FDM problems in order to reduce the error produced by adapting the mesh to regions of interest whilst still retaining a significant computational advantage over FEM methods.

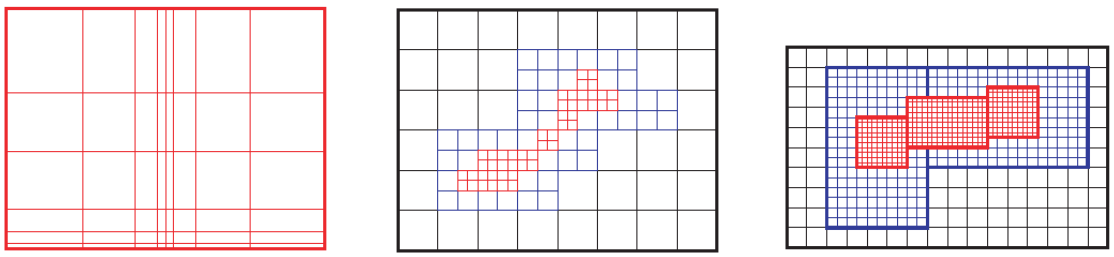

Figure 2.6: Diagrams to show adaptive mesh for distortion (left), point-wise (centre) and block-structured (right) [235].

A number of different mesh refinement methods are possible, as seen in Figure 2.6.

On the left, mesh distortion is demonstrated, where the mesh is simultaneously coarsened and refined in order to retain the same number of overall cells but realigned to a region of interest, this is known as r-adaptive mesh adaptivity where the total number of nodes does not change [236]. This is useful in a number of fields; however, in the case of a complex battery electrode, it would be very computationally intensive to continually distort the mesh. In the centre, point-wise (tree-based) meshing is demonstrated, individual cells are refined in order to focus on regions of interest, this is a type of h-adaptivity where the polynomial degrees remain the same but the number of nodes may change [237]. This provides a good method to refine the mesh, but the mesh is often left with 'hanging cells' where multiple cells border a single cell; this presents additional challenges in parallelising the code. Finally, on the right, block-structured meshing is shown, where patches of refinement are applied to regions of interest sequentially depending on the refinement required, another h-adaptive method. This is a quick method to implement whilst also allowing for a reduction in error through the refined mesh, the use of block refinement means the frequency of hanging nodes is reduced compared to point-wise. For a complex structure such as battery electrodes, block-structured meshing has been shown to be a computationally efficient method [238].

In block-structured AMR, there is a hierarchy of logically rectangular grids. The computational domain on each AMR level is decomposed into a union of rectangular domains. Figure 2.6 right shows an example of three-levelled AMR. The coarsest level is level 0, and the bold lines indicate grid boundaries. There are two intermediate resolution grids (blue) at level 1, and the cells are a factor of two finer than the black cells, whilst the three finest grids (red) are a factor of four finer than the level 0 cells. There is no direct parent-child connection meaning it is much easier to parallelise, as these different regions correspond to different nodes, it is also possible to make spatial parallelisations of the same grid size [238].

2.2.4 Parallel Computing

Within parallel computing, there are two main protocols for parallelising a program. First, the message passing interface (MPI) is "a message-passing application programmer interface (API), together with protocol and semantic specifications for how its features must behave in any implementation" [239]. MPI remains the dominant model in high-performance computing due to its ability to operate over distributed memory systems (where there is no shared RAM). This means that on supercomputer clusters, a program can be distributed to a number of threads and use the MPI communication protocol to allow the threads to communicate [240].

Second, Open Multi-Processing (OpenMP) is an API that supports multi-platform shared-memory multi-processing. OpenMP is a collection of library routines, compiler directives, and environmental variables that can be applied to pre-existing portions of C, C++ and Fortran code in order to parallelise them. OpenMP is considered to be easier to implement on pre-existing code but can only run on shared memory (shared RAM) systems. This means OpenMP cannot be used over an entire supercomputer cluster and only on an individual node [241].

2.2.5 Containerisation

Containerisation is the process of packing up software with all of its dependencies and libraries in a single lightweight container, so that it can be deployed consistently on multiple environments [242], which has been widely popularised by Docker [243]. High-performance computing (HPC) systems are typically used to perform large-scale engineering simulations, but they are multi-user environments. It can be challenging to install new software as it may raise security concerns or alter the environments of existing users. Moreover, if HPC systems do provide the correct software, the installed version will be different across different systems and the build will not allow for user customisation. Containerisation allows for greater control over specific libraries and dependencies, and can improve portability of software. As opposed to running the whole operating system for each application, as seen in a virtual machine, containers share the machine's operating system kernel meaning they are inherently smaller. Singularity has emerged as a popular container tool specifically designed for use on HPC

systems, and will be used to deploy the software produced in this thesis [244].

2.3 Summary

This Chapter has presented an overview of the experimental methodologies used throughout this thesis. Scanning electron microscopy and transmission electron microscopy have both been used extensively in the field of electrode image analysis, however, they cannot capture 3D microstructural information so are unsuitable. FIB-SEM can achieve impressive resolution capabilities, however, the use of the focused ion beam means the imaging method is destructive. X-ray CT is a radiographic experimental technique used to image volumetric detail in three dimensions. The relatively good penetration of X-rays permits the nondestructive imaging of the internal structure of materials. The Zeiss Versa 510 was chosen for the imaging experiments due to its widespread accessibility, availability and suitable spatial resolution. The scanner utilises a two-stage magnification, fitted with X0.4, X4, X20 and X40 magnification lenses mounted on a barrel mount and the geometric magnification of the X-ray imaging.

An image artifact is a part of the image data that does not represent the physical structure of the test sample. There are a wide range of possible image artifacts associated with CT imaging, such as: radiation scatter, statistical noise, edge streaks and beam hardening. Reducing/removing each of these artefacts requires the careful balancing of experimental parameters in order to improve image quality. An REV is the smallest volume over which a computation or measurement can be made that is representative of the whole volume. It is challenging in practice to deal with 3D REV samples with super-high resolutions as they can contain billions of voxels. Therefore, in practice, the raw digital microstructure data is often rescaled to a lower resolution, reducing the computational cost. The choice of REV sample is often then a compromise between accuracy requirement and computational complexity.

The FEM is used to solve boundary valued problems by integrating the strong form equation, the PDE describing the underlying physics at the material point, over elements, that can be triangular, polyhedral or a variety of other shapes. The FDM is a

differential scheme that is an approximation of a Taylor series expansion. FDM methods are usually run in regular, discretised cube meshes. Meaning they are less computationally intensive to implement during the meshing stage but can bring about an approximation of the error due to the differences method. AMReX is block-structured adaptive mesh software framework, developed as part of the Department of Energy's exascale computing project; this refers to a computing system that is capable of 10^{18} floating-point operations per second. Through using more computationally efficient adaptive mesh regimes, implementing a hybrid OpenMP/MPI parallel approach and by developing the framework from the ground up, AMReX-based solvers have been shown to reach a solution up to 200 times faster than Chombo using the same number of processors.

Different computational facilities were used to complete the simulation work contained within this thesis, including a local desktop machine, and Iridis4 and Iridis5 supercomputing clusters. Within parallel computing, there are two main protocols for parallelising a program. MPI remains the dominant model in high-performance computing due to its ability to operate over distributed memory systems (where there is no shared RAM). OpenMP is a collection of library routines, compiler directives, and environmental variables that can be applied to pre-existing portions of C, C++ and Fortran code in order to parallelise them on shared memory systems. Containerisation is the process of packing up software with all of its dependencies and libraries in a single lightweight container, so that it can be deployed consistently on multiple environments.

The methodologies presented during this chapter detail the justification for techniques used in Chapters 3 and 4. Specifically, the use of X-ray CT for imaging electrodes, the use of the FDM programming framework, AMReX, and its subsequent containerisation and parallelisation.

Chapter 3

OpenImpala - OPEN source IMage based PArallelisable Linear Algebra solver

This chapter is a modified version of the authors contribution to "OpenImpala: OPEN source IMage based PArallisable Linear Algebra solver", published in "SoftwareX 15(2021): 100729" by "James Le Houx and Denis Kramer".

Recent advances in X-ray microtomography (micro-CT) have made the characterisation technique widely available across both industry and academia [125]. Three-dimensional material microstructures can now be used to calculate effective homogenised material properties [174, 177] or be used directly as the computational domain to solve relevant physical equations [105, 111]. These processes are known as image-based modelling [165].

A common challenge from image-based modelling is the size of 3D tomography datasets, which can be of the order of several billion voxels [245]. In order to address this: representative elementary volumes (REV) [111], downsampling [177], particle approximations [136] and pore network modelling [183] are all used to try to reduce the computational resource required. Each of these comes with an associated limitation. REVs reduce the size of the microstructure being modelled, potentially losing microstructural information in the process. Macroscale heterogeneity, manufacturing

defects [189] and asymmetric structures [190, 191] could all be missed by using this method. Correlation of REV size against transport properties has been performed, but this is material, sample and property[1] dependant; therefore, further investigation is required in this field. Downsampling and particle approximations reduce the particles'[2] microscale interactions and change the contact surface area between the phases[3]. Finally, pore network modelling simplifies the interactions by replacing the image with a network of regular pores and throats. This method's accuracy depends on the corresponding pore network's quality compared to the original porous microstructure [192]. Being able to fully model the physical interactions at the imaging method's resolution requires a significant computing resource. However, a suitably parallelisable code explicitly written for high-performance computing environments would allow such calculations to be performed efficiently, revealing further scientific insight into the properties and performance of such structures [165].

Implementing an image-based model can take a significant amount of time. One of the commonly carried out steps is the re-meshing of image data. FEA studies usually include a re-meshing step to translate from the cube-shaped voxels to more flexible polyhedral shapes, pore network modelling requires the network to be created from the image data, and the homogenisation method requires the image data to be coarsened. Each of these steps requires human oversight and is hard to automate, and could lead to other approximation errors whilst re-meshing the dataset. However, as shown by [109], it is possible to carry out calculations directly on the segmented voxel dataset. A step is removed from the simulation process by solving the physical equations directly on the voxels. This removal of meshing reduces user input, meaning the process can be more easily automated and has been shown to improve simulation speed in some cases [246].

With these factors in consideration, the OPEN source IMage-based PArallelisable Linear Algebra (OpenImpala) software has been developed during this PhD for larger-scale image-based dataset modelling. The version contained in this thesis can be pub-

[1] Property here meaning what quantity is being calculated, i.e. diffusion, conduction, permeability.
[2] Particle in this context refers to the primary and secondary particles that make up the microstructure of the electrode, where secondary particles are agglomerations of the smaller, true primary particles.
[3] The three phases of the electrode, active particle, CBD and electrolyte.

licly accessed at: https://github.com/kramergroup/openImpala/releases/tag/v1.0.0, and this current version calculates the steady-state diffusive equation through the microstructure directly on the as-imaged cubic voxel dataset, which can be used to calculate the microstructure's tortuosity factor.

This chapter presents an overview of the OpenImpala (version 1.0.0) software. Section 3.1 provides an introduction to the initial development of the software. Section 3.2 explores the software architecture and description, giving an overview of the functionality. Section 3.3 gives a comprehensive overview of the performance of the code on different computing architectures. Section 3.4 details the validation of the software. Section 3.2.2.1 shows an illustrative example of how the software might be used, in this case calculating the tortuosity factor of a lithium-ion battery electrode, before Section 3.5 concludes the chapter.

3.1 Development of Single-Physics Model

In order to achieve the overall aim of developing a modular single-physics modelling framework of the Li-ion battery, a physics field must be chosen. The diffusion equation offered the best opportunity as this model could then also be used to calculate the tortuosity factor of the electrode. As discussed in Section 1.4, the tortuosity factor is a critical parameter in determining the performance of the Li-ion battery. The tortuosity factor is defined in Equation 1.10.

The two phases, in this case, are the insulating phase, the solid matrix of active material and binder, and the conducting phase, the porosity network allowing bulk diffusion to occur. The solid matrix is considered to be completely insulating in this case, as the diffusion caused through bulk transfer is orders of magnitude larger than the ionic solid-state diffusion occurring; however, in the future development of this model, this solid-state diffusivity will be taken into account. However, in this general form, the flow could represent a number of physical fields; electrical current, heat transfer and mass transport can all be used interchangeably. From this general formulation, it can be seen that if $\tau = 1$, then the flow paths are direct through the porous media and are

non-restricting, and if $\tau \geq 1$, then the flow is being augmented by the geometry.

The diffusion within the microscale is governed by Fick's first law, where the diffusive flux is related to the concentration of the conducting media under the assumption of steady-state [247]. Steady-state conditions are used in order to calculate the tortuosity of the microstructure. Through a fully conducting control volume, the equation is written:

$$\mathbf{J}_{cv} = -A_{cv} D \frac{\Delta \varphi}{L_{cv}} \tag{3.1}$$

where J is the steady state flux, D is the diffusivity of the ionic conducting phase, φ is the local concentration of the diffusing species, and A_{cv} and L_{cv} are the cross-sectional area and length of the control volume, respectively. The flow through a porous network is therefore defined as:

$$\mathbf{J}_{p} = -A_{cv} D \frac{\epsilon}{\tau} \frac{\Delta \varphi}{L_{cv}}. \tag{3.2}$$

By taking a ratio of these two expressions and rearranging, a definition is obtained that is equivalent to Equation 1.10, the tortuosity factor. With these governing equations defined, boundary conditions now need to be stated; the flow through the porous medium, Ω, is modelled to:

$$\begin{cases} \nabla^2 \varphi = 0, & \text{in} \quad \Omega, \\ \varphi = 1, & \text{on} \quad T, \\ \nabla \varphi \cdot \mathbf{n} = 0, & \text{on} \quad I, \\ \varphi = -1, & \text{on} \quad B \end{cases} \tag{3.3}$$

where φ is the local concentration of the diffusing species, Ω is the conductive region of the porous medium, $\mathbf{n}$ is the outward pointing unit normal to $\partial\Omega$ and T, B and I are the top, bottom and interfacial faces respectively. The range of -1 to 1 is used to make efficient use of the floating point precision. Figure 3.1 a displays these boundary conditions on a 2D example.

Fixed value (Dirichlet) conditions are imposed at two parallel boundaries, T and B, in order to represent steady-state conditions where $Q = (0, L_x) \times (0, L_y) \times (0, L_z)$ is a cuboid in $\mathbb{R}^3$. $\Omega \subseteq Q$ is the conducting region of the porous structure inside Q. The other subsets listed; T, B and I; are two-dimensional subsets of Q (Top, Bottom and Interfacial), described in 3D space such that $\partial\Omega = T \cup I \cup B$ and $\partial\Omega\,|_{z=L_z} = B$, $\partial\Omega\,|_{z=0} = T$ and $\partial\Omega\,|_{0<z<=L_z} = I$ [109]. $\mathbf{n}$ is the outward pointing unit normal to $\partial\Omega$.

3.1.1 Initialising the Problem

With the problem stated in Equation 3.3, these boundary conditions can be mapped onto a computational domain within AMReX. The solution can be reached by solving the system of linear equations that describe the concentration in each voxel, only in terms of the concentration of its face adjacent neighbours. This is a finite differences type problem. In order to implement these boundary conditions within AMReX, a Fortran routine is needed in order to populate the ghost cells at the boundaries. The ghost cell technique is used to prepare the code to run on distributed memory compute architectures. `AMReX_FILCC_3D.F90` is an F90 routine that is a generic fill function for cell centred data. Using this routine, it is possible to populate cells with values based on boundary condition flags. First, however, both Dirichlet and Neumann boundary condition routines need to be specified.

The Fortran routine, `AMReX_FILCC_3D.F90`, was rewritten to specify both high and low Dirichlet flags: the high Dirichlet flag specifies that the cells are populated with a value of 1, whilst the low Dirichlet flag specifies the cells are populated with -1. The Neumann flag is specified to ensure that the normal derivative of the solution with respect to space is equal to 0. In reality, this means that there is no flux across this boundary. With these three conditions, it is possible to populate the ghost cells surrounding the computational domain with a choice of Neumann zero flux, low Dirichlet or high Dirichlet. A 2D representation of what this looks like is shown in Figure 3.1 (a). This is a 256 x 256 grid of an empty control volume at time 0. From this, it can be seen that the bottom face is populated by a 0 Dirichlet boundary condition, the top by a 1 Dirichlet boundary condition and the walls with a zero flux. This plot is made by plotting the

output data in a data visualisation tool, in this case, Visit 2.13.0.

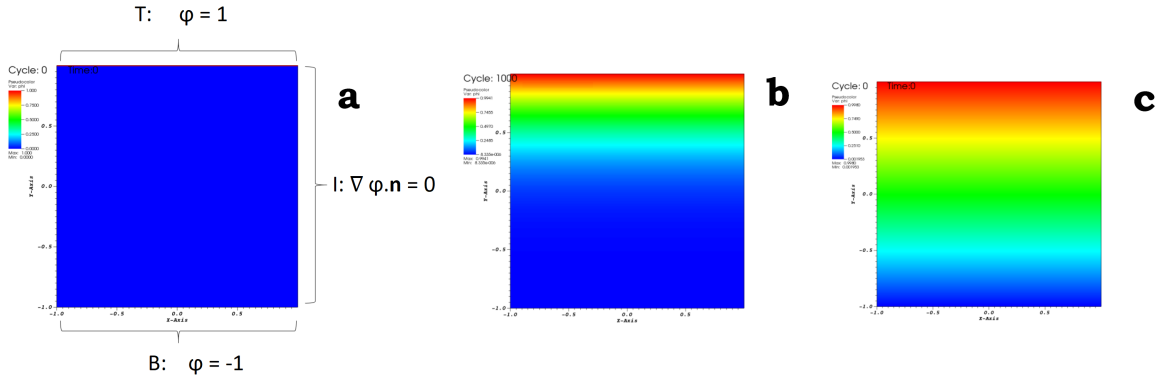

Figure 3.1: A 256 x 256 grid of a diffusive flow to demonstrate the boundary conditions specified, the quantity represented is the concentration. (a) has initial conditions of all cells equal to 0, (b) shows how the concentration map changes after 1,000 Jacobi solver cycles from an empty grid, (c) shows the initiation routine where initial conditions of the cells are set as a proportion of their y-axis (direction of flow) position.

Having initialised this problem, it is now possible to cycle the simulation to see how the flow through the control volume changes with solver cycles. The solution after cycling the simulation through 1,000 Jacobi solver cycles is shown in Figure 3.1 (b). It can be seen that the cells close to the top boundary have started to increase their value of concentration. This is due to the top boundary representing an inflow condition.

With more cycles, the top boundary inflow and bottom boundary outflow will balance, leading to a steady-state condition. However, in order to reach that situation, a number of cycles will need to be carried out. To avoid this and the unnecessary computation, a routine has been written to populate the initial cells called `init_phi_2d.f90`. This Fortran routine cycles through the cells and populates them with a value depending on their y-axis position, and this value is a proportion of one depending on their position. In this way, the solution reaches a steady-state condition from initialisation, and this can be seen in Figure 3.1 (c). However, it is important to note that this routine is just an initial guess for the solution, for very complex domains such as battery electrodes, a larger number of cycles is expected.

3.1.2 Solving for Diffusion

Having successfully run a diffusion problem through a fully conducting control volume, the next step is to incorporate the electrode microstructure. The output file from the post-processed data obtained in Section 4.1.2 is given in `.tiff` format. When examined, this is a list of grey-scale values that represent individual voxels. If the value is equal to 0, the voxel represents a porous space; if the value is equal to 255, then the voxel represents a solid. A script was written that opens up a target `.tiff` file, reads the filename in order to determine the pixel dimensions, and then populates a C++ data array with the appropriate values. This phase data is then used by the solver to determine the calculation performed; if the phase is of interest, the diffusion equation is solved, whereas non-conducting phases are ignored. The solver initialises using the fill routine discussed in Section 3.1.1 and then iterates until a solution with steady-state conditions is reached. The solution is finished when the residuals from the solver are reduced to practical tolerance limits. The solution to a 3D steady-state, single-axis diffusion problem based on real LFP electrode CT data, obtained in Section 4.3, displayed using Visit [248], can be seen in Figure 3.2 a. The dark blue represents the inlet condition, whilst the red represents the outflow. Figure 3.2 b shows the box decomposition of the domain, how it has been divided to be solved by parallel cores.

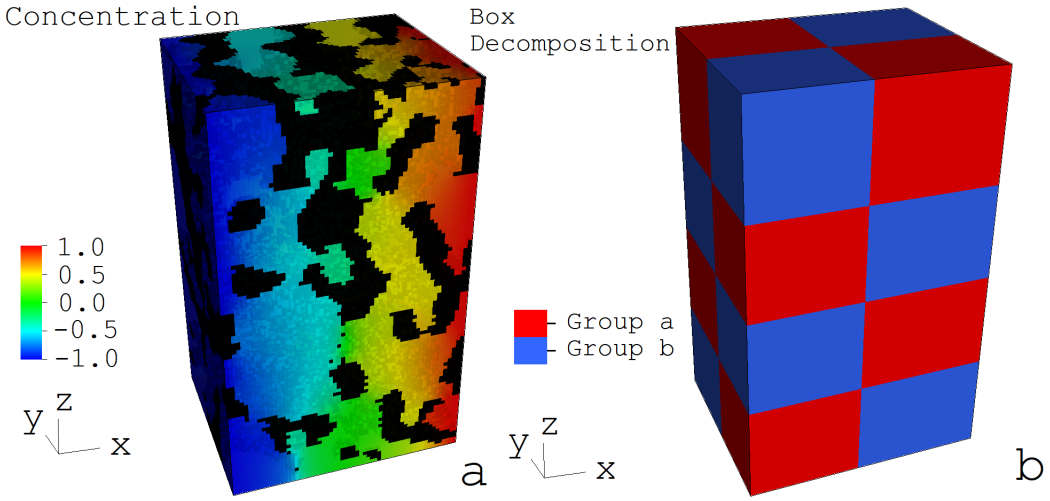

Figure 3.2: 3D visualisation of the concentration gradient (a) and box decomposition (b) across a lithium iron phosphate electrode microstructure.

3.2 Software Description

The full OpenImpala codebase, developed by the author during this PhD, contains over 4,000 lines of code, which precludes its complete inclusion in this thesis. Instead, code snippets for key routines: a data reader based on `.dat` files, Fortran-based cell initialisation and boundary conditions, and Hypre-based computation, are included in Appendix C. In this Section, an overview of the software architecture is presented and each of the software routines are described in pseudocode, as well as an example use case. The interested reader is referred to the publicly accessible Github repository for full access to the codebase: https://github.com/kramergroup/openImpala/releases/tag/v1.0.0. N.B. the code contained in this thesis is released as v1.0.0, development of the code is expected to continue so in the future there may be discrepancies between the routines described here and the main branch of the code.

3.2.1 Software Architecture

OpenImpala is built on the open-source software framework, AMReX, used to manage the distribution of boxed voxel domains. The boxes are sent to parallel compute processes and solved using the efficient parallel linear solver, Hypre. AMReX is based on regularity at the block/box level, as each is still logically rectangular, which allows the data to be stored internally as an array of contiguous blocks of memory in Fortran array order.

OpenImpala is made up of a number of C++ header (`.h`) and definition (`.cpp`) files, and Fortran (path.F90) files. The overall programme structure is shown in Figure 3.3. Example segmented image datasets are stored as .tiff files within the data folder. They are read by a C++ class defined in `TiffReader.cpp`, which depends on an opensource library, LibTiff [249], and AMReX [250]. `TiffReader.cpp` opens the associated .tiff file, reads the dataset, thresholds the data into a specified number of phases and then stores it as a MultiFab, a class native to AMReX. A MultiFab contains the array of stored boxes of data. A segmented electrode dataset loaded into the programme and then displayed using Visit can be seen in Figure 3.4. Once the dataset has been loaded into the programme, several different C++ functions can be called, such as `VolumeFraction.cpp`

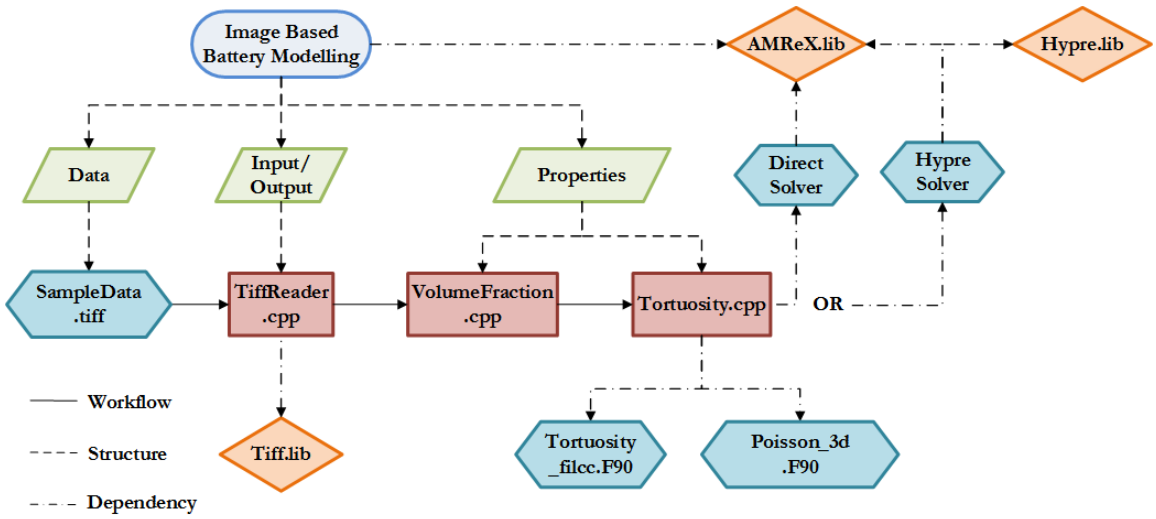

Figure 3.3: Flowchart to show the structure of the image-based battery modelling programme.

and `Tortuosity.cpp`, as detailed by the workflow path of Figure 3.3.

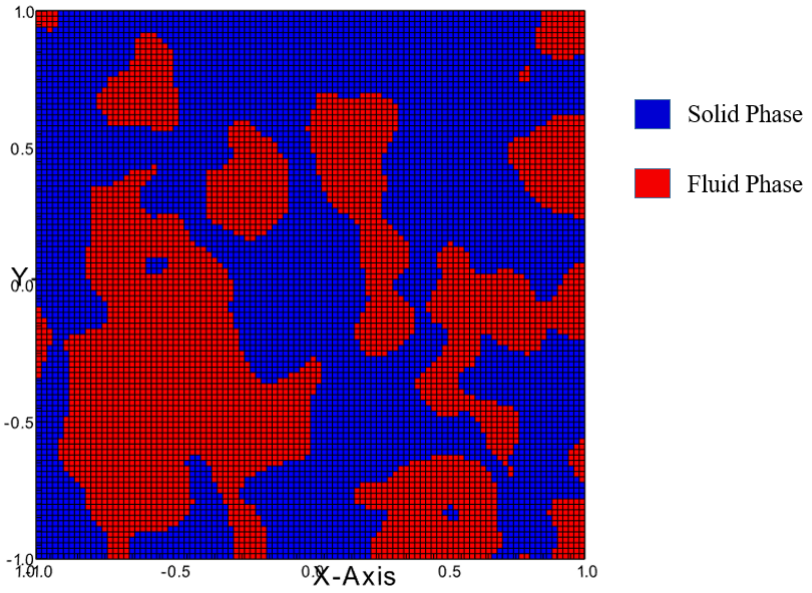

Figure 3.4: Picture to show segmented electrode data, as read from the associated .tiff, loaded into the programme.

3.2.2 Software Functionalities

`TiffReader.cpp` uses the open-source library, LibTiff, to interact with .tiff segmented image files. It contains a reader of .tiff slices used to create Fortran array box structures filled with thresholding data. Specified files are opened and the data is stored in For-

tran array format, which can then be used by other functions. It also has the capability to perform a simple thresholding algorithm, where a specified grey-scale value is set and used to segment the image data into a two-phase dataset. It is also possible to retrieve properties of the tiff file such as height, width and depth, which can then be used to inform the physical space required by the solver.

`TiffStackReader.cpp` and `DatReader.cpp` work in a similar way to `TiffReader.cpp`, but are used to read in a stack of separate .tiff files and a typical alternative file format, .dat, respectively.

`VolumeFraction.cpp` computes the volume fraction of a specified phase within a porous structure. Phases are indicated by integer, 32-bit, values stored within the MultiFab. `VolumeFraction.cpp` iterates over all the boxes stored within the MultiFab and counts the cells populated by the indicated phase, finally summing the counted cells to produce the volume fraction. This process can be easily parallelised by distributing the calculation by boxes across MPI threads, like those seen in Figure 3.2 b, which has already been done to store the data within the MultiFab. Although this calculation is not computationally expensive, `VolumeFraction.cpp` should introduce the reader to OpenImpala's structure and how to parallelise a calculation. These boxes can then be sent to different computational nodes before the master thread finally reduces the final result. This C++ function can be used to calculate a microstructure's porosity by selecting the void space as the phase of interest.

`Tortuosity.cpp` computes the tortuosity of a porous structure by solving the Laplace equation for diffusion for a given direction and phase, and uses this to calculate tortuosity factor, as shown in Equations 1.10 and 3.3. `Tortuosity.cpp` calls a Fortran routine `tortuosityfillcc.F90` that fills the Dirichlet boundary conditions at the opposing faces, perpendicular to the principal flow direction to create an inlet and outlet, similar to Figure 3.1 (c). These boundary conditions are implemented using the ghost cell technique, where an additional layer of voxels is added above the top face and below the bottom face and then populated with the boundary conditions [109]. This means the Dirichlet boundary condition is applied to the centre point of each voxel in

the layer above the top face, T , and the centre point of each voxel in the layer below the bottom face, B. It also fills the initial conditions across the computational domain by a linear gradient along the principal flow direction, stored as 64-bit doubles within a MultiFab. However, the routine only fills cells of the phase of interest, initialising all others to zero.

`Tortuosity.cpp` then calls `Poisson3d.F90` that solves the Laplace equation only for the phase of interest, ignoring the non-conducting phase. This is achieved by using a seven point stencil across the dataset that checks whether that cell and the adjacent cells are conductive, which includes it within the total computation, or non-conductive, which sets the value to 0 and ignores it for the adjacent calculations. OpenImpala can either use a basic implicit solver to ensure the robustness of the calculation or iterative solvers such as the Jacobi method [251] or generalised minimal residual (GMRES) method [252] to improve speed. OpenImpala can utilise solvers from the open-source library Hypre, including preconditioners for Flexible GMRES, to improve the calculation speed [253]. The solver starts with an initial guess, as detailed in Section 3.1.1, which drastically reduces the number of solves required in most typical cases. The solver iterates until the residuals are reduced to reasonable tolerance limits, set by the variable `EPS`, giving the final solution. There is a broader discussion about the relevance of 'flow-through' type tortuosity calculations for certain electrode microstructures, as discussed in [140].

`CathodeWrite.cpp` provides a writer of cathode parameter files. This class can be used to create files to interface with popular open-source DFN models: PyBamm [254] and DandeLiion [255]. This class takes calculated values from `VolumeFraction.cpp` and `Tortuosity.cpp` and writes them into specific files for the associated continuum models, .py for PyBamm and .txt for DandeLiion.

Each of these functions has an associated unit test, used to check correct functionality, specified by a `t` at the start of the filename. `tTiffReader.cpp` opens a sample .tiff file and asserts the dimensions are as expected, printing the output. `tDatReader.cpp` opens a sample .dat file and asserts the dimensions are as expected, printing the

output. `tVolumeFraction.cpp` opens a sample 2 phase segmented .tiff file and calculates the volume fraction of each phase, asserting the values obtained are correct. `tTortuosity.cpp` opens a sample two-phase segmented tiff file and calculates the effective diffusion and tortuosity in the x-direction, asserting the values calculated are as expected.

3.2.2.1 Pseudocode

OpenImpala is interacted with through `.cpp`, `.H` and `.F90` files. An example file is included which demonstrates how to calculate the steady-state diffusive flow and tortuosity through a lithium iron phosphate (LFP) electrode sample [130]. This could then, for example, be used to inform battery manufacturers of the performance of the electrode or be used to more accurately model the processes occurring inside that specific domain.

`Diffusion.cpp` calculates diffusion and tortuosity in the three cartesian directions, as well as volume fraction for a two-phase segmented dataset. The program opens a .tiff file from user input, read its data, and then calculate the following properties: volume fractions of the phase of interest, effective diffusivity and tortuosity in the x, y and z directions.

At runtime, an inputs file (`build/apps/inputs`) is used to define common variables that are used throughout the code. In this case, `FILENAME` links to the segmented image dataset that is to be analysed, `BOXSIZE` defines the number of voxels in one dimension that each box has (how the domain is decomposed to different parallel processes), `EPS` defines the tolerance limits set, and `DIRECTION` defines the direction of interest for the simulation. First, a number of Include calls are used to include open-source libraries, such as LibTiff, AMReX and Hypre, as well as the OpenImpala classes defined in Section 3.2.2, such as `TortuosityHypre.H` and `VolumeFraction.H`. Next, `DATAPATH` is used to define where the input files are stored. The main programme can then begin. The code parses the parameter values from the inputs file and stores the values, and then initialises a physical geometry and a multifab of phase values:

```
amrex::Geometry geom;
amrex::BoxArray ba;
amrex::DistributionMapping dm;
amrex::iMultiFab mf_phase;
```

opens up the `.tiff` or `.dat` file:

```
amrex::Print() << "tTiffReader - Reading file " <<
DATA_PATH + FILENAME << std::endl;
TiffReader reader(DATA_PATH + FILENAME);
```

creates a physical domain, `rb`:

```
amrex::RealBox rb({-1.0*fx,-1.0*fy,-1.0*fz}, {1.0*fx,1.0*fy,1.0*fz});
```

and populates the computational domain with values from the tiff file and thresholds it to the relevant phase. A volume fraction computation is performed using the class defined in Section 3.2.2:

```
VolumeFraction vf(mf_phase, 0);
```

where `mf_phase` is the multifab storing the phase information. A steady-state Fickian diffusion problem is then solved over the dataset in each of the cartesian directions, e.g. for the x-direction:

```
TortuosityHypre tortuosityx(geom,ba,dm,mf_phase,vf.value(),0,Direction::X
                            ,TortuosityHypre::SolverType::FlexGMRES);
```

where `geom` is the geometry object of the domain, `ba` the array of computational boxes used to split up the domain, and `dm` the distribution mapping of how the boxes are apportioned. Finally volume fraction, tortuosity and the total timing of the computation are printed for the user :

```
amrex::Print() << std::endl << " Volume Fraction: "
                  << amrex::Real(vf.value()) << std::endl;
amrex::Print() << " Tortuosity value: " << tau_value_x << std::endl;
amrex::Print() << std::endl << "Total run time (seconds) = "
                  << stop_time << std::endl; .
```

3.2.3 Research Impact

OpenImpala is a software framework utilising open-source libraries to efficiently manage and simulate large-scale image-based datasets. Coupled with appropriate computing architecture, further insight into macroscale heterogeneity, manufacturing defects and asymmetric microstructures could be revealed. The open-source nature of the software makes it widely accessible to research institutions and industry; a large number of similar softwares are expensive proprietary packages or, due to research exclusivity, act like "black boxes", making their comparison to similar tools difficult. OpenImpala could also be used to verify the accuracy of simplification methods such as representative elementary volumes, particle approximations, downsampling and pore network modelling. This first version of the software already provides valuable functionality, but the code's current speed and modular architecture would make it a suitable candidate to expand to multi-physics capability. The modular architecture is implemented through the use of separate C++ classes, that can be used when needed by the user. Allowing for this type of extensibility is a core design objective.

The code does bridge the gap between areas of multi-scale modelling in battery research, the first stage was calculating tortuosity with subsequent steps incorporating transient computations and multiphysics. With this in mind, parameterised electrode files for specific tomographies are produced by OpenImpala with compatibility for two popular continuum battery models: PyBamm [254] and DandeLiion [255]. These parameter files contain electrode properties such as porosity and tortuosity, and can then be used to inform a multi-physics model. It is expected that this will improve the accuracy of these continuum battery models by producing bespoke properties and characteristics for the as-manufactured electrodes. With the reduction in micro-computed tomography costs expected over the coming years, the method will find more widespread use and could be used as a metrology tool. Used with a fast-acting image-based modelling software, such as OpenImpala, this could provide bespoke results for as manufactured components; in this case, electrodes, but this could also be applied to other fields. OpenImpala is currently in use by the Engineering Materials group at the University of Southampton, where it was developed by the author during this PhD. Additionally, to the authors knowledge, it has been used at the Univer-

Nr.	Code metadata description	
C1	Current code version	v1.0.0
C2	Permanent link to code/repository	github.com/kramergroup/openImpala
C3	Legal Code License	BSD-3-Clause
C4	Code versioning system used	git
C5	Software code languages, tools,	AMReX, C++, Fortran, MPI
C6	Compilation requirements	GCC, Unix, AMReX, libTIFF, Hypre
C7	Link to developer documentation/manual	github.com/kramergroup/openImpala/blob/master/README.md
C8	Support email for questions	d.kramer@soton.ac.uk

Table 3.1: Code metadata.

sity of Manchester, University College London, Imperial College, Ghent University and Helmut Schmidt University. It is also currently being deployed as part of a pseudo-operando reconstruction, segmentation and simulation data processing pipeline at the United Kingdom's national synchrotron, the Diamond Light Source, to provide real time results to beamline operators and users, informing experimental design. It is currently being used as a way to bridge the gap between multi-scale modelling of Li-ion batteries but a wider audience is expected. A large amount of interest has been shown by the Image-Based Simulation group for Industry (IBSim-4i) due to the software's open and modular structure.

3.3 Scaling Analysis

3.3.1 AMReX

In order to understand the performance of AMReX on HPC systems, an investigation was carried out to determine how well AMReX scaled with an increasing number of CPU cores. This study was carried out without using code written for the battery model. For this, a compressible Navier Stokes (CNS) combustion example was chosen; this was due to the combustion taking place within a chamber that required the use of the embedded boundary approach [256], so represented a similar case to the battery model. The example was run on both a local desktop machine as well as making use of the University of Southampton supercomputer, Iridis4.

Figure 3.5 shows how the code scales with an increasing number of cores. The lo-

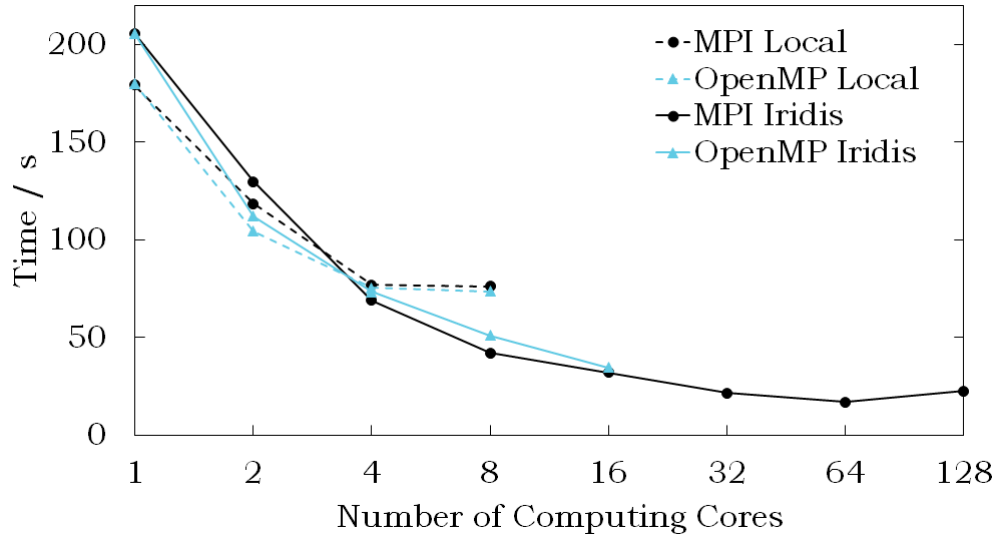

Figure 3.5: A graph to show how the time taken to solve the CNS combustion problem changed with the number of CPU cores (threads).

cal machine consists of an Intel Core i7-6700 3.40GHz quad-core with an 8MB cache and 16GB of DDR4 memory. It can be seen that for the locally run simulations (dotted lines), the code is only run up to a maximum of eight cores. It is also noted that there is no speedup between four and eight cores, this is because the local machine is only running a quad-core processor, so running additional instances of the programme does not provide any gain. Iridis4, however, consists of 750 computer nodes, each with dual 2.6 GHz Intel octa-core Sandybridge processors and 64 GB of memory. The number of instances on Iridis4 (solid lines) can therefore be much larger, in this case, up to 128, which only constitutes using eight nodes. Each increase in the number of threads provides a smaller return in time gained, and at 128 threads, a slowdown is actually observed; this is due to the overheads (messages being sent between nodes) increasing with the number of threads. If, as in this case, the problem is too small, then just increasing the number of threads does not improve the solution time. This example was run using both shared-memory parallelisation, OpenMP (blue lines) and distributed-memory parallelisation, MPI (black lines). OpenMP can only be run up to the maximum number of cores on a single node for Iridis, which is 16. It is noted that at lower numbers of threads, OpenMP outperforms MPI, whilst at higher numbers, MPI is faster. Further investigation of this is required in order to determine the best parallelisation method; it is possible that a combination of both, known as a hybrid approach, could provide the fastest solution times. Finally, at a single core, the local machine out-

performs Iridis; this is due to the local machine running a faster clock speed of 3.4 GHz in comparison to Iridis' 2.6 GHz.

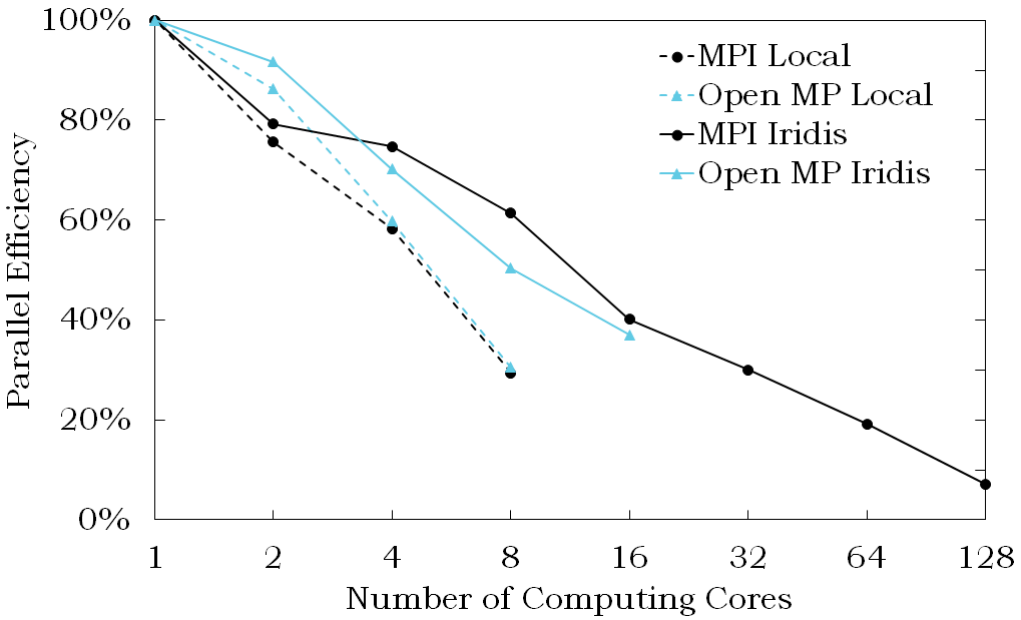

Figure 3.6: A graph to show the parallel efficiency achieved when solving the CNS combustion problem for a number of threads.

The graph in Figure 3.6 shows how the parallel efficiency varies with the number of computing cores. Parallel efficiency is defined as:

$$E = \frac{1}{P}\frac{t_{seq}}{t_p} \tag{3.4}$$

where E is the parallel efficiency, P is the number of cores being run on, t_{seq} is the runtime of the best sequential algorithm, and t_p is the runtime of the parallel algorithm [257, 258]. What can be seen from this graph is a reduction in computational efficiency with an increasing number of cores. This type of graph can be used to choose the most efficient combination of OpenMP and MPI cores; however, the problem size for this case is too small to provide reliable guidance for domain sizes of interest.

3.3.2 Basic Solver

Having shown that AMReX scales well on the supercomputer, the next step is to implement the finite difference iterative solver, as written by the author, on real electrode microstructure. The electrode microstructure used is a 2-phase segmented LFP elec-

trode dataset, made up of 100 x 100 x 100 voxels, and was obtained in Section 4.3. These tests were performed on Iridis5, a supercomputing cluster made of 464 compute nodes with dual 2.0 GHz Intel Skylake processors, giving 40 CPUs and 192 GB of DDR4 memory per node. The clock speed of these processors is slower than both Iridis4 and the desktop machine used in Section 3.3.1; however, the large memory available per node means large datasets can be loaded entirely, improving computation times. The scaling analysis was used to compare the performance of OpenMP and MPI solution times, the results of which can be seen in Figures 3.7 and 3.8.

Figure 3.7 shows that the MPI solution scales linearly with computing cores, showing very good scalability of the code. This is again confirmed by the parallel efficiency shown in Figure 3.8. It can be seen that at four computing cores, the parallel efficiency actually exceeds 100% (102%). This is known as super-linear speedup and is due to the cache effect, where the entire electrode dataset is stored within the cache memory of the CPU. This results in the CPU accessing the memory more quickly, meaning the solution time is improved. Comparing OpenMP and MPI, it is seen that MPI based parallelisation consistently outperforms OpenMP, with the exception of two cores. Further investigation is required whether a hybrid approach is suitable to improve the solution time.

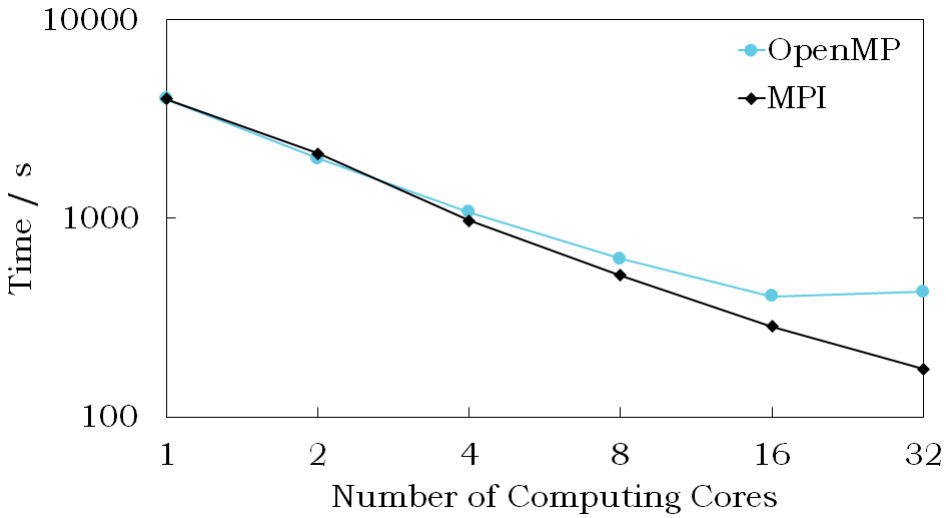

Figure 3.7: A graph to show how the time taken to solve the diffusion problem on an LFP 100 x 100 x 100 subvolume changes with the number of CPU cores (threads). This compares two different parallelisation methods, OpenMP and MPI.

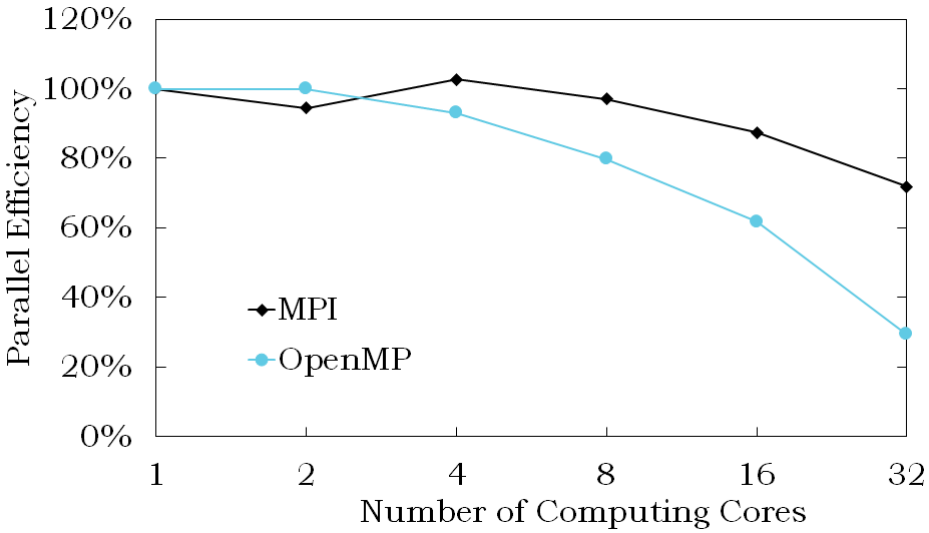

Figure 3.8: A graph to show the parallel efficiency achieved when solving the diffusion problem on an LFP 100 x 100 x 100 subvolume for a number of threads. This compares two different parallelisation methods, OpenMP and MPI.

3.3.3 Hypre Solver

In order to improve solution time, a Hypre based solver is also implemented. This test compares the simple finite-difference iterative solver to the Hypre solver. The electrode microstructure used is a 2-phase segmented LFP electrode dataset, made up of 100 x 100 x 100 voxels, and was obtained in Section 4.3. These tests were performed on Iridis5, using MPI for both parallelisations. The result can be seen in Figure 3.9. The Hypre solver performs the same calculation 220x faster than the equivalent basic finite-difference calculation, using the same computer architecture. The solver also continues to scale linearly up to 16 cores.

3.3.3.1 Efficient Box-Sizing

Weak scaling of the programme has also been investigated to explore the performance against a varying problem size [259]. Porespy was used to computationally generate test microstructures of varying resolutions. For a single-core, this was defined at 125 voxels^3 and a porosity of 0.5, giving a total dataset size of approximately 2 x 10^6. This dataset is then scaled depending on the number of cores, so two cores give a dataset size of approximately 4 x 10^6, four cores gives a dataset of 4 x 10^6 and so forth. The results of this scaling can be seen in Figure 3.10. It is seen that for this first test, the

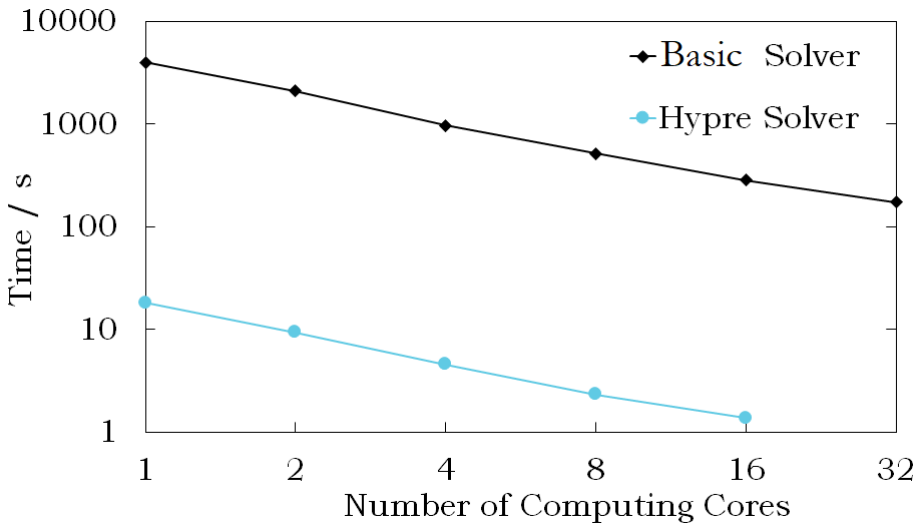

Figure 3.9: A graph to show how the time taken to solve the diffusion problem on an LFP 100 x 100 x 100 subvolume changes with the number of CPU cores (threads). This compares two different solvers, basic finite-difference methods and Hypre.

solution time performs as expected for a smaller number of cores but starts to vary between adjacent tests at higher numbers. This is due to how the program is dividing the computational domain into calculation boxes and shows the importance of this factor, a visualisation of this box decomposition can be seen in Figure 3.2 b. In order to quantify this, an equation is proposed, Equation 3.5, to calculate the efficient number of boxes to divide the computational domain into, in one dimension:

$$Bo_{1D} = \frac{\min(x)^3}{P} \quad Bo_{1D} \in Z \quad x \in Z \tag{3.5}$$

where x is the minimum integer that, when cubed, divides by the number of cores to give an integer and P is the number of computing cores used in the computation. When this equation is used to calculate the number of boxes required, a second set of results is obtained, also shown in Figure 3.10. From this, it can be seen that the simulation time of some of the tests has reduced by up to 12%. Additionally, the curve has started to asymptote to the horizontal at a higher number of computing cores.

The time taken to solve a diffusion problem in a single cartesian direction, x, across 7.8 x 10^6 voxels is shown in Figure 3.11. Here, the box-size used is varied, showing that the influence of this parameter on solution time is significant. The dotted line represents the size of the voxel domain in one dimension, above which only a single core

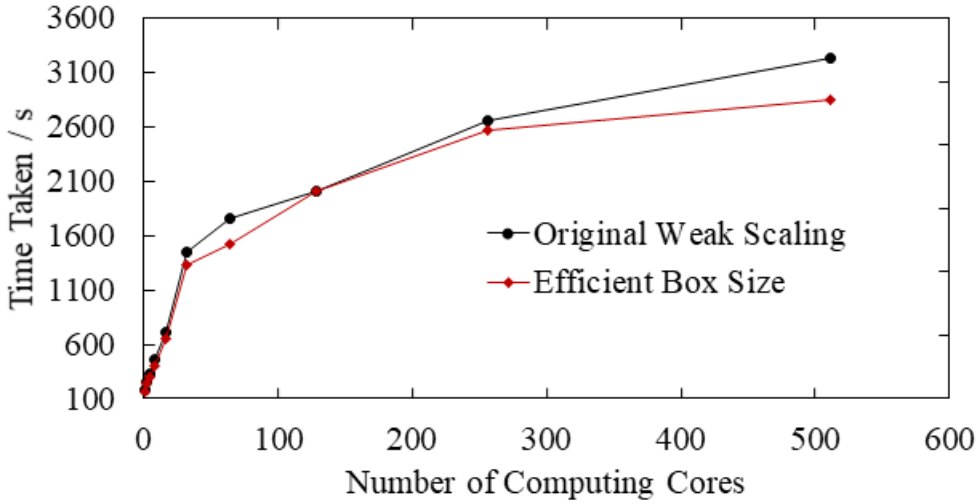

Figure 3.10: The time taken to solve the weak scaling diffusion problem, each core solving 2 x 10^6 voxels, comparing original and efficient box-sizing.

can solve the computational problem. The use of Equation 3.5 prevents the parameter from exceeding this value while reducing the computational time sufficiently.

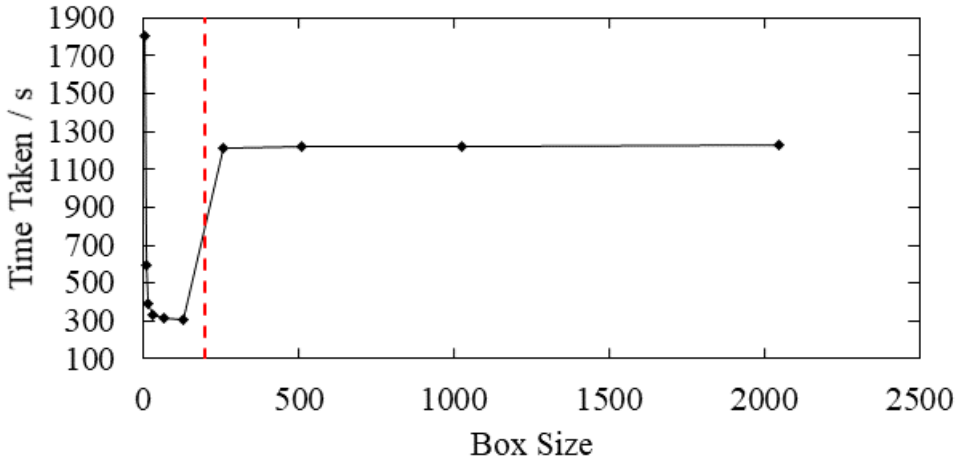

Figure 3.11: The time taken to solve the diffusion problem using four cores, across 7.8 x 10^6 voxels, varying box-size, dotted red line corresponds to the size of the voxel domain in one dimension.

3.3.4 Comparison with Other Software

The main novelty of OpenImpala is the code's ability to be highly parallelised on HPC systems; this, therefore, lends its use to larger-scale datasets. In this section, OpenImpala's results are compared to the performance of v1.0 of the popular open-source academic software, Taufactor. Taufactor was recently updated to v1.1, improving the performance of the solver. Porespy [260], an open-source microstructural generation programme, is used to computationally generate a test microstructure with a domain size of 600^3 voxels and a porosity of 0.5. This gives a total dataset size of 2.16×10^8 voxels. Dirichlet boundary conditions are used in the simulation direction, and reflective boundary conditions are employed along the sides. The choice of boundary conditions influences the calculated result, as discussed in [261, 262], potentially leading to systematic error depending on the sample volume. Work is ongoing to expand the boundary conditions available to the user. For OpenImpala, tests were run on an increasing number of computer cores, up to 512, to evaluate the strong scaling of the code [263, 264]. The simulations were run on the University of Southampton's HPC system, Iridis 5. This system consists of 464 compute nodes, comprising 40 cores per node (i.e. dual 2.0 GHz Intel Skylake processors) with 192 GB of DDR4 memory and InfiniBand interconnect.

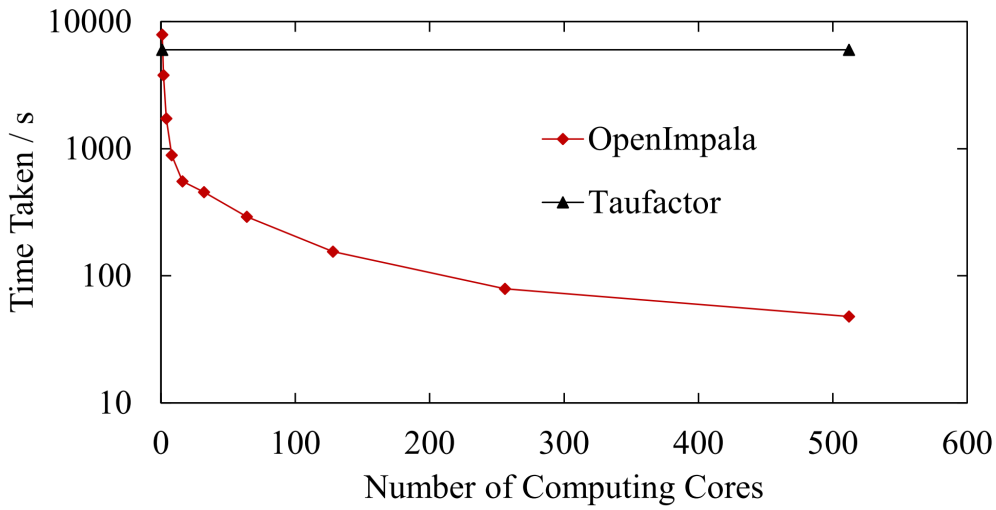

Figure 3.12: The time taken to solve a 2 x 10^8 voxel diffusion problem, comparing Taufactor and OpenImpala.

The results of this comparison simulation can be seen in Figure 3.12. The y-axis displays the time taken to solve the steady-state diffusion problem, and the x-axis the number of computing cores used; Taufactor timing (obtained using the same hardware) is displayed as a horizontal line as it is a single core software. It is seen that the scalability of OpenImpala results in a reduction of solution time at two or more cores when compared to Taufactor. It is also noted that a calculation that would have taken around 100 minutes on Taufactor can be performed in less than two minutes when performed on a suitable number of computing cores.

To further investigate the parallelisation of OpenImpala, parallel efficiency is shown in Figure 3.13 against the ideal performance. For two, four and eight computing cores, the parallel efficiency exceeds 100%. This is again super-linear speedup and is thought to result from the cache effect, where the entire dataset is stored within the cache memory of the CPU [265], resulting in the CPU accessing the memory more quickly, meaning the solution time is improved. It is also noted that the efficiency starts to stabilise at core sizes larger than 40. The stabilisation is thought to be due to the calculation becoming distributed across multiple nodes due to the HPC architecture of the test platform against the ideal performance. Finally, a speedup ratio plot is shown in Figure 3.14 to show the performance against an ideal case, where speedup is defined as:

$$S = \frac{t_{seq}}{t_p}. \tag{3.6}$$

3.4 Computational Validation

Having introduced the different methods of calculating tortuosity in Section 1.4. It is useful to understand the effect these different methods have on the value obtained. In [44], a set of Fontainebleau sandstone samples with porosities ranging from 8.61% to 24.50% are used to compare the results from each of the different image analysis methods, physical simulations and theoretical models. These seven different porosity samples can be seen in Figure 3.15, taken from [266]. They are 480 x 480 x 480 voxels with a voxel resolution of 5.7 µm, representing an equivalent 2.7 mm^3 physical volume. Geometrical and physical tortuosities are computed for the three principal directions,

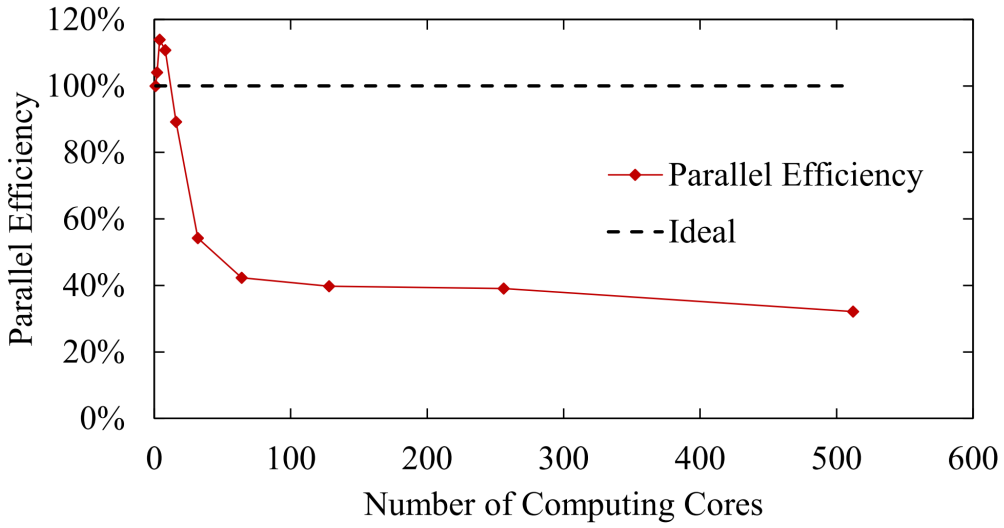

Figure 3.13: Parallel efficiency to solve 2 x 10^8 voxel diffusion problem compared to ideal performance.

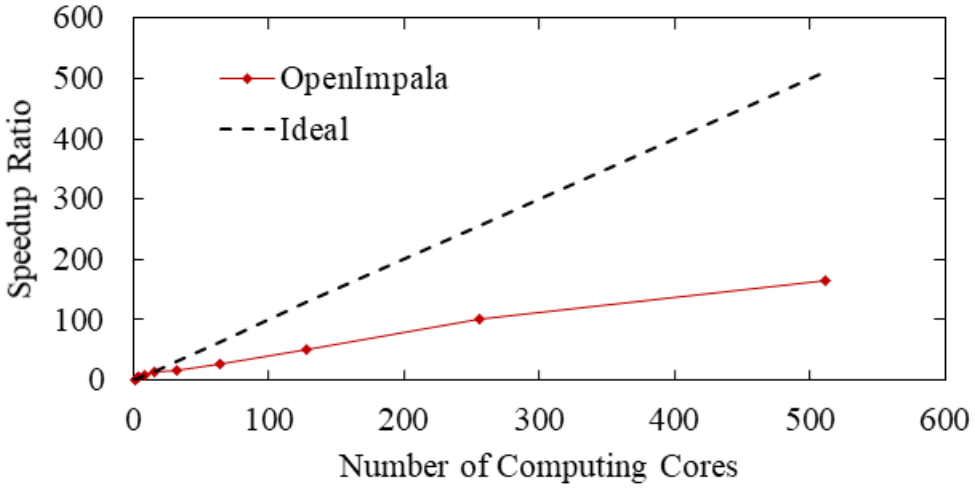

Figure 3.14: Speedup ratio against number of computing cores to solve 2 x 10^8 voxel diffusion problem compared to ideal performance.

for each REV, using the methods listed in Section 1.4. The sandstone is considered to be isotropic, and to minimise the sampling error, a characteristic tortuosity is obtained by averaging the directional tortuosities:

$$\frac{1}{\tau^2} = \frac{1}{3}\left(\frac{1}{\tau_x^2} + \frac{1}{\tau_y^2} + \frac{1}{\tau_z^2}\right) \tag{3.7}$$

where τ_x, τ_y and τ_z are tortuosities in the x, y and z directions, respectively.

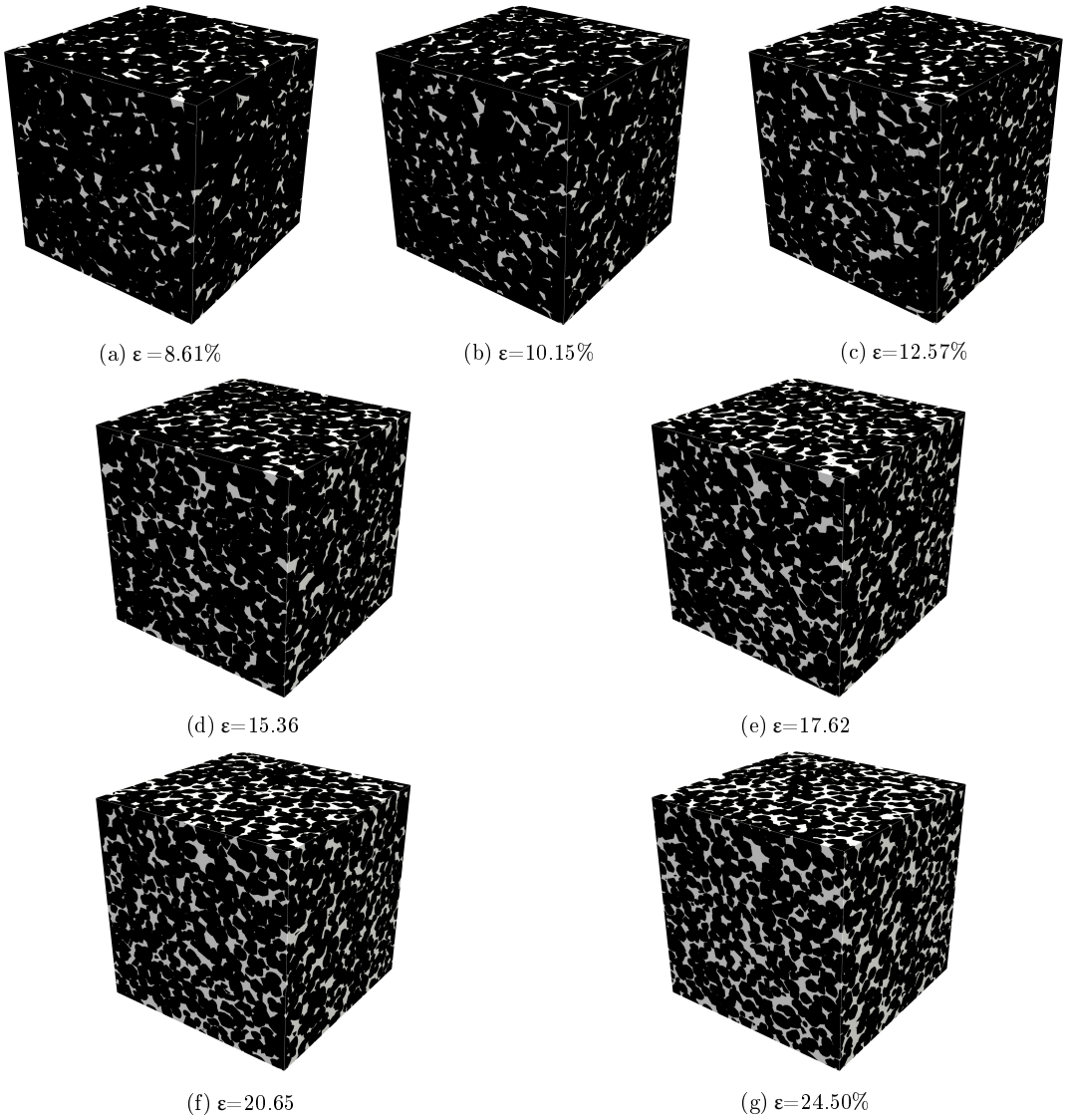

Figure 3.15: The 3D digital microstructures of Fontainebleau sandstone samples, pore space shown in white and solid-phase shown in black, reproduced with permission from Elsevier from [44].

The results of these 16 different methods can be seen in Figure 3.16; however, it is critical to note τ here is the square root of tortuosity compared to the other definitions in this thesis, due to the definitions given in [44]. There are notable discrepancies across these different methods, with significant variance present in samples with lower porosity. This is not surprising considering the variance in the definition of tortuosity already presented in Section 1.4; however, it is important to understand the context of what these results of tortuosity mean. The 'Diffusional FDM Simulation' is of particu-

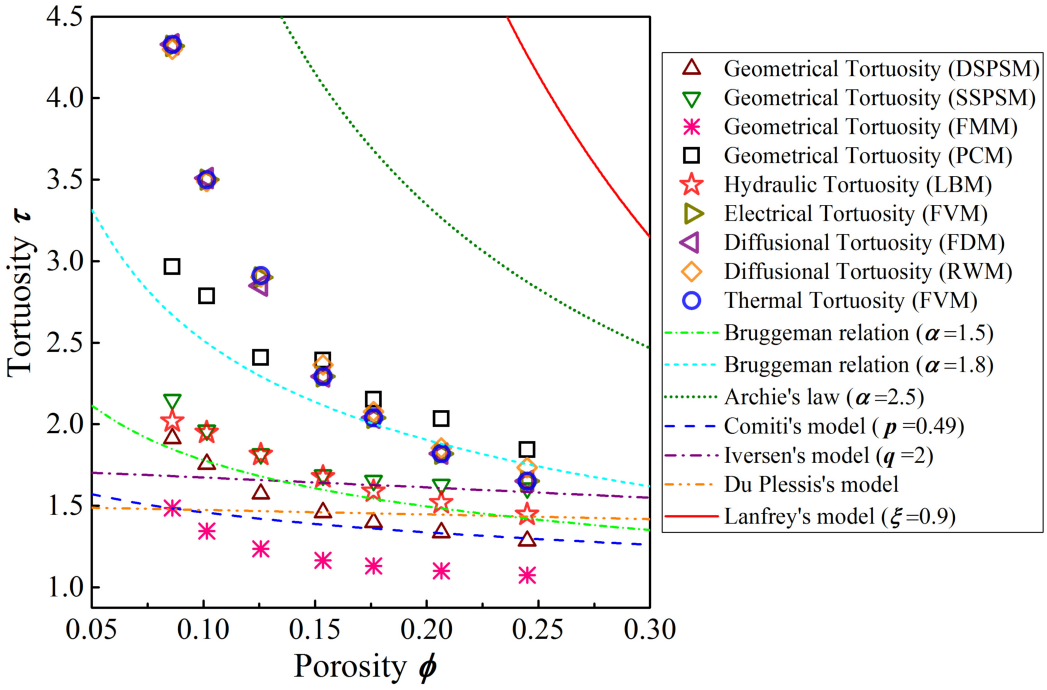

Figure 3.16: The tortuosity results calculated from 16 different image analysis methods, physical simulations and theoretical models for the seven Fontainebleau sandstone samples, reproduced with permission from Elsevier from [44], N.B. τ here is the square root of tortuosity compared to the other definitions in this thesis.

lar interest as this is the same method used by OpenImpala, and it is noted that there is good agreement between finite difference methods, finite volume methods and random walker methods. Finally, it is also noted that the choice of Bruggeman coefficient value has significant variance on the results calculated.

Taufactor was used in the calculation of these finite difference results, which then, therefore, provides an excellent benchmark to validate OpenImpala's performance against, in the broader context of these 16 different methods. The same Fontainebleau sandstone samples were used in these calculations; however, the Taufactor calculations were rerun to ensure the same computational setup was used between OpenImpala and Taufactor. The results of these simulations are shown in Figure 3.17, which includes two models of the Bruggeman exponent and Archie's law for context. It is seen that OpenImpala and Taufactor provide good agreement across the range of porosities. These results can be obtained in good agreement with other methods but, with a suitable computing architecture, at close to real time results. OpenImpala has the

potential of providing real time feedback to imaging scientists, during an operando experiment.

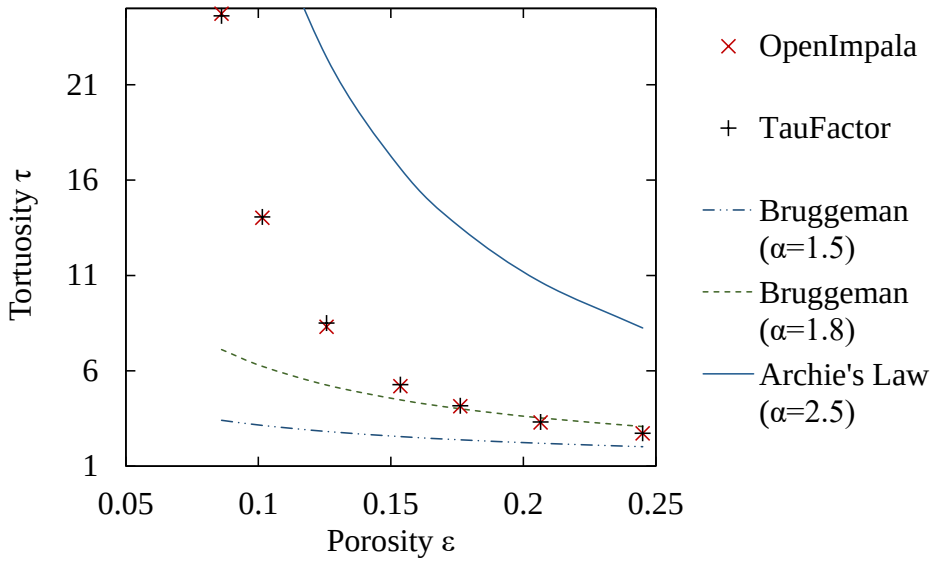

Figure 3.17: The tortuosity results calculated from OpenImpala, Taufactor, two Bruggeman exponents and Archie's law for the seven Fontainebleau sandstone samples.

3.5 Summary

This chapter has detailed the development of a data-driven, image-based modelling framework that is capable of modelling transport processes in Li-ion battery electrodes, called OpenImpala. Micro X-ray computed tomography is used to obtain 3D microstructural data from manufactured samples non-destructively. These 3D datasets are then used as the computational domain within a finite-differences-based model, in order to solve the diffusion equation directly on the CT obtained dataset. The code then calculates the equivalent homogenised transport coefficients for the given microstructure, which can then be used to create a parameter file for continuum models PyBamm and DandeLiion. The code has been shown to scale well with an increasing number of computational cores on distributed memory architectures, making it applicable to large datasets typical of tomography. OpenImpala is currently in use by multiple academic institutions, and is being deployed as part of an automated reconstruction, segmentation and simulation data pipeline at the UK's national synchrotron, the Diamond Light Source.

The code solves a diffusion problem across CT obtained electrode microstructure and calculates the tortuosity value. The code is based upon an open-source modelling framework, AMReX. The code reads in CT obtained segmented datasets, calculates volume fractions, and performs an iterative solution of the Laplace equation. The solver can either be a basic finite differences method or based upon the Hypre framework. The code has been shown to scale well with an increasing number of cores. The Hypre solver performs equivalent calculations 220x faster than the basic finite differences method. The Hypre solver has been shown to outperform Taufactor when used on two or more computing cores. The codes computations have been validated against results from Taufactor and have been shown to have good agreement.

3.5.1 Future Work

The next step in the development of the single physics model is to incorporate adaptive mesh refinement within the code to be able to model at a much higher fidelity due to the increased computational efficiency. The solvers presented in this section also need to be compared in terms of their error in order to fully characterise their performance. These results can be compared to experimental data from electrochemical impedance spectroscopy carried out on the same samples. The framework could be expanded to full multi-physics capability. This will be achieved by writing additional mathematical kernels to represent the physical fields present (thermal, electrical, electrochemical), possible due to the modular nature of the code inherent through the use of C++ classes. In order to achieve multi-physics capability, it will be necessary to perform transient simulations, this could be achieved be implementing an explicit time integrator such as forward Euler or a Runge-Kutta scheme. A key limitation to be aware of is that through the use of a voxel-based mesh, surface-averaged computations will be inaccurate at present. These could be addressed through the use of correction factors or through the use of the embedded boundary method.

The current development of AMReX has limited usage of embedded boundary approaches; it is only currently possible to draw simple shapes such as circles, walls or polygons. However, this feature is under continuous progress, and the functionality of the embedded boundary approach is improving with every release. This may present

an opportunity to collaborate with the authors over the development of a new tool within AMReX, a feature that allows geometry to be imported from data files and used as the embedded boundary structure. Whilst developing the tools in this thesis, bugs were found in the AMReX source code. These have now been committed to the open-source AMReX code and successfully merged; any future developments will continue to be communicated to the AMReX team.

Chapter 4

X-ray Computed Tomography of Electrodes

This Chapter details the experimental setup, postprocessing method and results for the imaging of various electrodes for electrochemical devices. Section 4.1.1 shows an initial experiment using the Zeiss Versa 510, imaging a titanium dioxide electrode for an aqueous aluminium ion battery. Section 4.2 shows the imaging of a lithium titanate compound electrode for a supercapacitor. Section 4.3 details the image-based analysis of various electrode image datasets using OpenImpala, the open-source software package developed in Chapter 3. Section 4.3.1 shows the image acquisition and subsequent resolution analysis of a lithium iron phosphate electrode. Section 4.3.2 shows the image analysis of a lithium nickel manganese cobalt oxide electrode particle. Section 4.3.3 details the process used to digitally modify a series of image datasets of a reticulated vitreous carbon electrode used in a soluble lead flow battery, and the subsequent simulations on these datasets. Finally, Section 4.4 summarises the findings of this Chapter.

4.1 Titanium Dioxide Electrode for Aqueous Aluminium Ion Battery

4.1.1 Experimental Setup

The first electrode to be imaged was an uncycled titanium dioxide sample on a carbon polymer substrate, originally made for an aluminium ion battery. The electrode ink was produced by mixing 87.5 wt% TiO_2 nanopowder, purchased from Sigma Aldrich, 5 wt% carbon black and 7.5 wt% Nafion in propanol and water. The ink contained TiO_2 with a nominal size of 25 nm particles; therefore, it will not be possible to resolve individual particles using the CT scanner but will instead see the structures that this ink forms. The inks were coated onto SIGRACELL PV15 carbon polymer (natural graphite and fluoropolymer composite), made by SGL and used to ensure a corrosion resistant current collector, and left to dry overnight. The mass loading was 6.7 mg cm^{-2}. Further details about the sample preparation is given in [267].

This sample was chosen as it provided a good opportunity to collaborate with other members of the centre for doctoral training (CDT), namely Alex Holland, who has been developing aluminium-ion batteries [267, 268]. Additionally, disassembling a Li-ion battery for the initial scans would require the use of a glove box and an inert environment; titanium dioxide is more stable and so would allow greater flexibility during setup. Finally, the actual titanium dioxide layer was approximately 20 µm, meaning it is a thinner film electrode than the equivalent Li-ion graphite, therefore thoroughly testing the capability of the Versa.

The scan was carried out with a 20x magnification lens, voxel dimensions of 964 x 995 x 971 and a pixel size of 481 nm; the total scan time was 16 hours captured using imaging settings of 50.0 kV and 50.0 µA. The dimensions gave a total voxel count of ~10^9. The image data is then reconstructed into a tomographic volume using a commercial Zeiss filtered back projection (FBP) algorithm, further details of which can be read in [269]. A single tomographic slice of the sample can be seen in Figure 4.1.

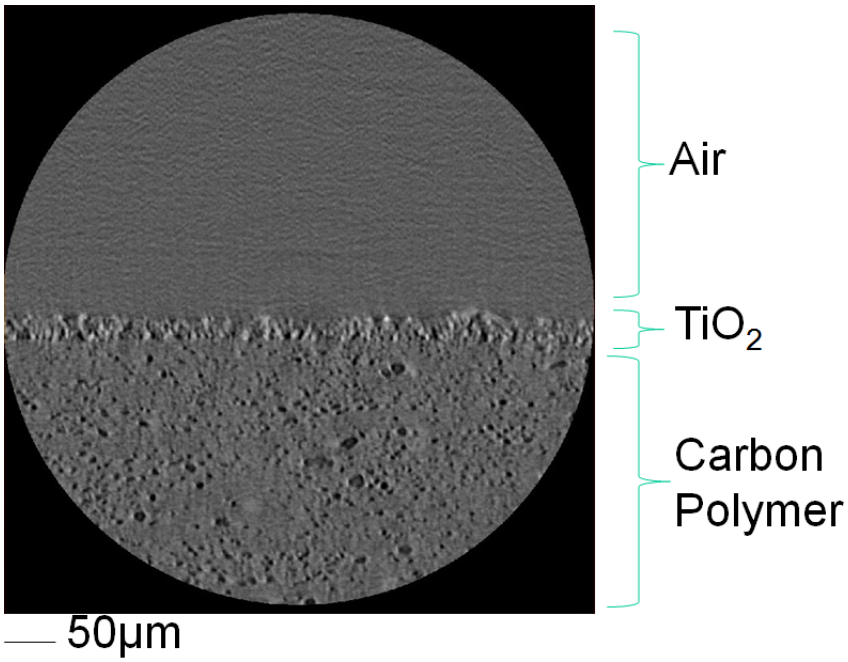

Figure 4.1: Individual tomographic slice of a TiO_2 layer on a carbon polymer substrate, voxel size of 481 nm

4.1.2 Post-processing Methods

The stack of 2D tomographies then needs to be stitched together into a thresholded data file that could be used as an input to the model. The first step was to specify the spacing between slices that is defined by the pixel dimensions originally used in the scan. Next, a number of post-processing techniques were carried out on the dataset using a piece of commercial software, Avizo. Noise and distortion are picked up by the scintillator during the scan, as detailed in Section 2.1.3.2, and needs to removed from the dataset. In Figure 4.1, artifacts can be seen in the air layer; this is due to some of the X-rays scattering away from the titanium dioxide and carbon polymer solid and being detected by the scintillator. In order to remove these artefacts as well as others within the solid matrices, a filter must be applied.

Within image processing, anisotropic diffusion filtering has been shown to provide good clean-up results without removing the original detail [270]; however, it comes at a relatively high computational cost [271]. Anisotropic diffusion filtering works by creating a family of parameterised images, with each resulting image being a combination of the original and an isotropic Gaussian filtered image that depends on the local content. In this way, the filter does not remove significant portions of the edge, line and

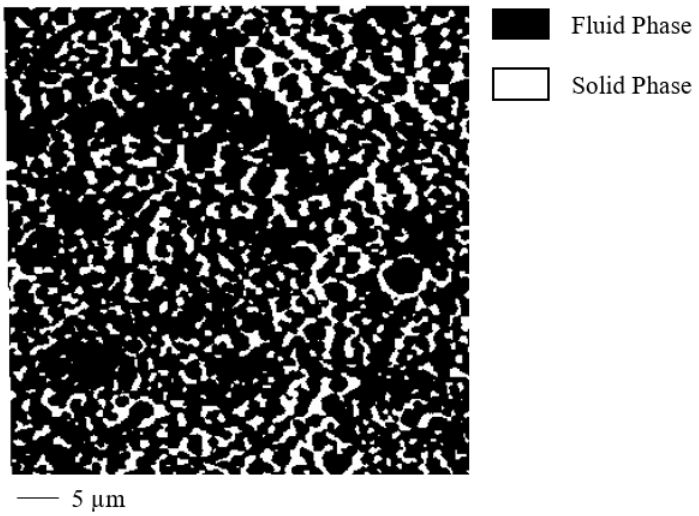

Figure 4.2: Segmented TiO_2 against the void sample, voxel size of 481 nm.

details that are important to the interpretation of the image, but still smooths out the artifacts that were originally detected [271]. As the dataset is being used as an input to a computational model, obtaining a sufficiently accurate tomography is very relevant; for this reason, anisotropic diffusion filtering was chosen.

With the image having been filtered, it is next thresholded based on the greyscale values held within each voxel location. These grayscale values represent the amount of attenuation the X-ray beam has undergone, and therefore, the material that is present. Using a histogram of the entire image, it is possible to separate out individual materials; in this case, the titanium dioxide and carbon polymer substrate are of interest. This thresholding algorithm defines the voxel in the image either as solid, if the grayscale value is less than a defined constant, or as pore, if the grayscale value is greater than that constant. Finally, smaller micropores and any remaining microparticles are removed from the dataset via a simple volume greater than/less than algorithm. This algorithm counts adjacent voxels of the same phase to discretise the image into bodies, any body consisting of two voxels or less is removed.

This value was chosen as the information contained within them is not sufficient to evaluate the fidelity of features that are of a similar size to the CT data voxels [211]; they are therefore changed to the bulk material surrounding them. A sample showing the segmented result can be seen in Figure 4.2, a final volumetric rendering of the post-

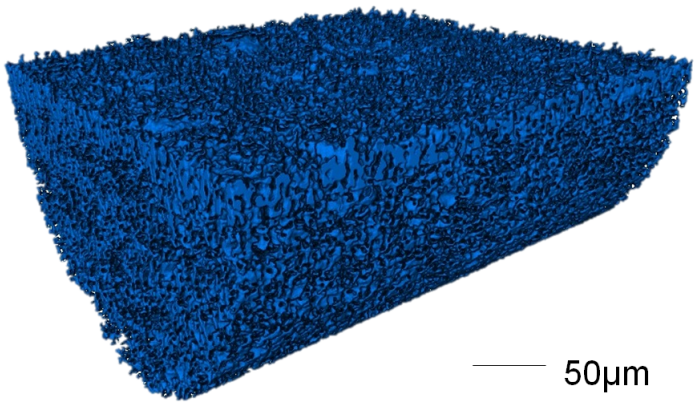

Figure 4.3: Volumetric rendering of a thresholded TiO_2 layer on a carbon polymer substrate, ~10^8 voxels, size of 481 nm

processed dataset can be seen in Figure 4.3.

In summary, this section has demonstrated the X-ray tomographic imaging process of a titanium dioxide electrode for an aqueous aluminium-ion battery. With this methodology demonstrated, it can now be applied to other electrochemical devices to further understand the influence of electrode morphology. A summary of the post-processing methodology is shown in Figure 4.4.

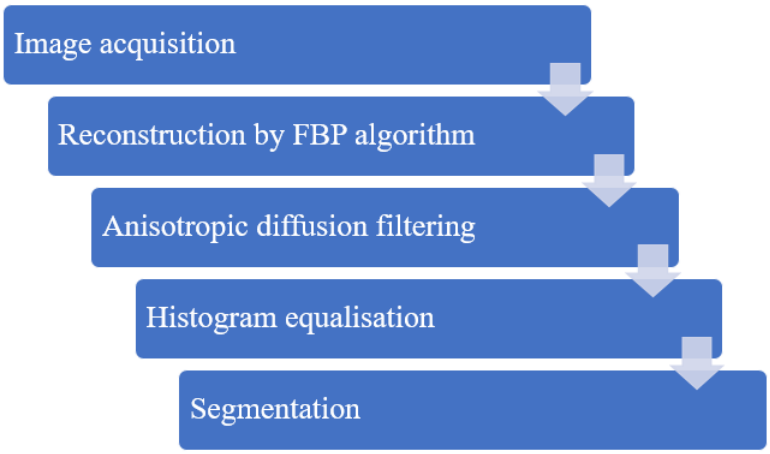

Figure 4.4: Flowchart to show the post-processing steps taken in Avizo.

4.2 Lithium Titanate/Pyrenecarboxylic Acid Decorated Carbon Nanotubes Supercapacitor Electrode

This section is a modified version of the authors contribution to "Lithium titanate/pyrenecarboxylic acid decorated carbon nanotubes hybrid-Alginate gel supercapacitor." published in "Electrochimica Acta 309 (2019): 253-263" by "Manoranjan Ojha, James Le Houx, Radha Mukkabla, Denis Kramer, Richard George Andrew Wills, and Melepurath Deepa".

4.2.1 Experimental Setup

Lithium titanate has been used extensively as an intercalation type anode in Li-ion batteries. This is due to it undergoing negligible volume change during the Li-ion intercalation/deintercalation process resulting in a long cycle life. However, it has not been widely used within supercapacitors. Supercapacitors are high power, low energy electrochemical devices that can sustain very high cycle lives. Manoranjan Ojha at the Indian Institute of Technology Hyderabad developed an asymmetric supercapacitor, containing a hybrid of lithium titanate ($Li_4Ti_5O_{12}$) with 1-pyrenecarboxylic acid decorated multi-walled carbon nanotubes (LTO/PCA@CNTs) as one of the electrodes. The LTO/PCA@CNTs material was coated over a nickel (Ni) foam during fabrication which then enables a supercapacitor cell to be manufactured.

Samples of the LTO/PCA@CNTs Ni foam electrodes were received from Hyderabad so that X-ray CT analysis could be performed. This analysis was performed in order to understand the interaction between the LTO/PCA@CNTs electrode material and the Ni foam substrate, and to see the bulk structure of the material. The sample was cut to a cylinder shape through the use of a scalpel and then mounted to the top of a 3mm diameter aluminium rod; it was held in place by epoxy to prevent movement through the scan. The scans were carried out using the Zeiss 160 kVp Versa 510 at the University of Southampton. Further details about the sample preparation can be seen in [125].

4.2.2 Results and Discussion

The image data is then reconstructed into a tomographic volume using a commercial Zeiss filtered back projection algorithm. The CT images are shown in Figures 4.5a, b, c and d. Figure 4.5a is captured using a 4x magnification lens, which corresponds to an individual voxel dimension of 3358 nm, the reconstructed pixel dimensions are 992 x 1015 x 1001. The imaging settings were 80.0 kV and 88.0 µA. From this image, the Ni foam can be seen, and the structure is made up of a highly porous network of Ni branches and nodes. The accessible pores formed by the branch and node structure of the foam are in the scale of hundreds of µm and are misaligned across the depth of the foam layers. Figures 4.5b, c and d are captured using a 40x magnification lens, giving an individual voxel dimension of 397 nm, and the reconstructed pixel dimensions are 992 x 1015 x 1005, captured using imaging settings of 50.0 kV and 50.0 µA.

In Figure 4.5b, a single Ni branch has been enhanced in order to ascertain more detail. It can be seen that the Ni branch is made of a thin-walled structure and is hollow, which is presumed to be a relic of the foam manufacturing process. The hollow areas within the Ni branches are isolated, are not accessible for LTO/PCA@CNTs deposition and do not add to the porosity of the foam. The LTO/PCA@CNTs material is visible on the surface of the branch as a deposited structure and is highlighted within the red boundaries in Figures 4.5c and d. Figures 4.5c and d show an individual tomographic slice of the 40x scan. From these images, it is more evident that the Ni foam is made of a thin-walled structure and the deposited area can be viewed in more detail. Agglomerations have formed on the surface of the Ni fibre, which are the deposits of the LTO/PCA@CNTs hybrid. The LTO/PCA@CNTs material was distributed throughout the foam pores with uniform contact to the Ni surfaces.

This is the first time this material has been imaged, and this work is published here [125]. It can be seen in Figure 4.5c and d that a large amount of streaking from the X-rays scattering off the Ni foam substrate is observed; this was removed during post-processing and is no longer visible in the volumetric renderings, as seen in Figure 4.5b.

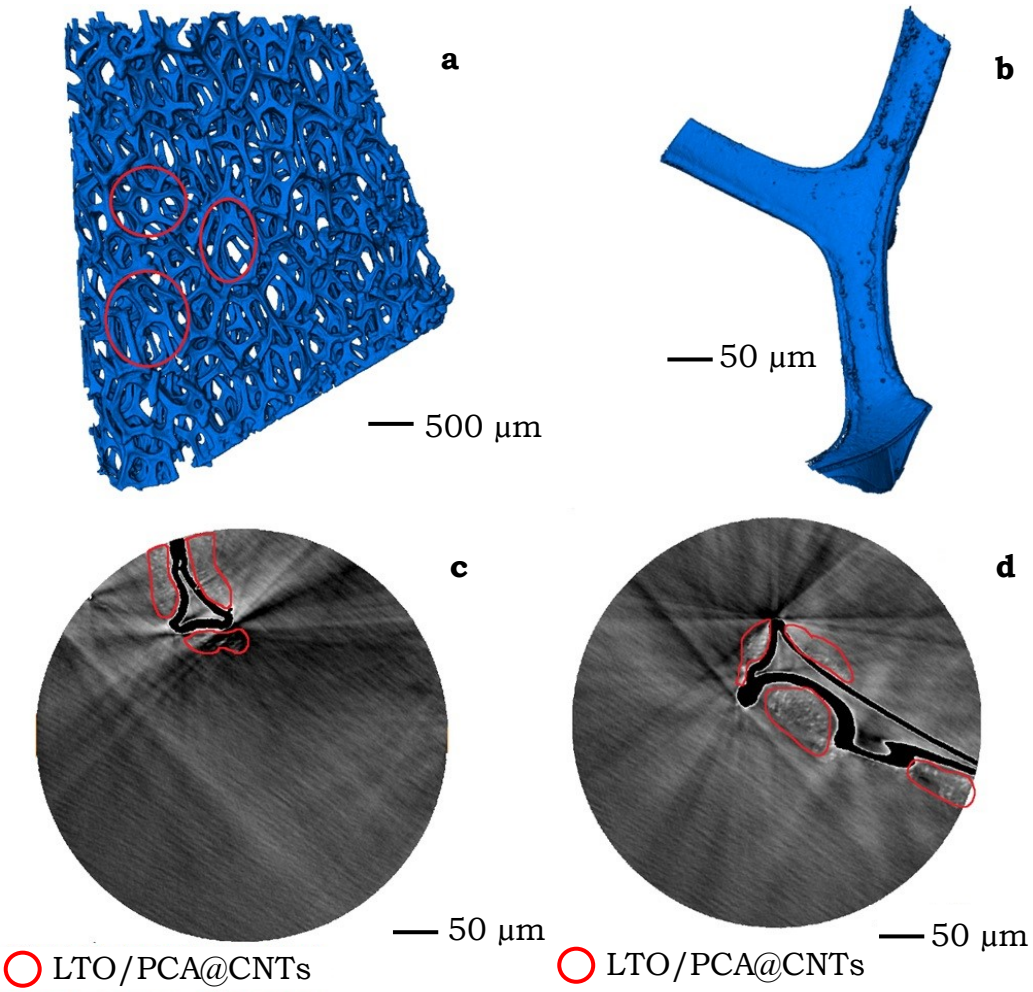

Figure 4.5: Tomography images of the LTO/PCA@CNTs electrode, volumetric rendering with voxel dimensions of (a) 3790 nm and (b) 397 nm, and two orthographic slices at 397 nm voxel dimensions detailing the location of the electrode material (c) and (d).

4.3 Image-Based Modelling Using OpenImpala

One of the remaining challenges in the field, outlined in [165], is to fully characterise the effects that image resolution has on structural and transport properties, such as porosity and effective tortuosity. First investigations regarding the effect of image resolution on the results of the simulation can be found in [105]; however, a more rigorous study is required to fully characterise the effects. Imaging the same electrode sample at a number of resolutions, at the same point in space and with the same overall dimensions would allow a direct comparison of the effect of image resolution. This section sets out to improve this understanding.

Finite element-based models have been used extensively to simulate Li-ion batteries, [111] however, they have been shown to be computationally expensive to mesh the image data. Finite difference/volume schemes use a regularly discretised mesh and are usually faster to implement, as the voxel dataset can be used directly, but they can result in approximation errors. This work uses an open-source, data-driven, image-based modelling framework, OpenImpala, that is capable of modelling transport processes in Li-ion battery electrodes. OpenImpala uses a finite difference scheme to solve transport equations directly on the imaged microstructure, solving for effective diffusion, tortuosity and porosity.

Electrode microstructural image data is obtained experimentally using micro-CT at two resolutions. Image data is also generated computationally using level set functions based on tomographic data. These datasets are then used to compare geometric parameters as calculated by OpenImpala [272].

4.3.1 X-Ray Tomography of Lithium Iron Phosphate Electrodes

This section is a modified version of the authors contribution to "Effect of Tomography Resolution on Calculation of Microstructural Properties for Lithium Ion Porous Electrodes." published in "ECS Transactions 97, no. 7 (2020): 255" by "James Le Houx, Markus Osenberg, Matthias Neumann, Joachim R. Binder, Volker Schmidt, Ingo Manke, Thomas Carraro, and Denis Kramer".

4.3.1.1 Sample Preparation

Lithium iron phosphate (LFP) is used extensively as a battery cathode material, finding commercial use in a number of applications such as electric vehicles, utility-scale stationary energy storage applications and backup power. At the University of Southampton, there is the capability to manufacture both coin and pouch cells using this material. The full methodology for the manufacture of a standard pouch cell is given in Figure 4.6. The material is mixed into a slurry with a conductive binder using a planetary mixer at 2000 rpm and then sonicated for one hour. For the cathode, the resulting inks are coated onto an aluminium current collector using a doctor blade, whilst the anode is coated onto a copper current collector. The electrodes are then cut into shape using an electrode die cutter. Finally they are calendered, a process where a series of hard pressure rollers are used to smooth the sheet of electrode material across the current collector. The electrodes can then be studied ex-situ using X-ray CT to understand their morphology, however, for completeness, the full pouch cell manufacturing process is included here [273].

The calendared electrodes are then wrapped in a commercially available glass microfiber separator (Whatman, 0.25 mm thick), ensuring that there is a layer of separator between any two adjacent electrodes to prevent short circuits. Nickel tabs are then ultrasonically welded onto the eneds of the electrodes to connect them in parallel. A typical pouch cell from this process contains 3 individual cells (6 electrodes in total), with a total pouch cell interior thickness of around 5 mm. The outer case of the pouch cell is formed using a cup-forming press from a polymer laminated aluminium-foil and the interior assembly sealed in the cup on three edges by applying a heat of 180-200 °C. The fourth, open side is then used to inject the electrolyte through a pipette to a volume of 15 ml inside a dry box, the cell is then agitated and left to stand to remove bubbles. Lastly, the fourth edge of the pouch cell is sealed under vacuum to remove all air and seal the cell.

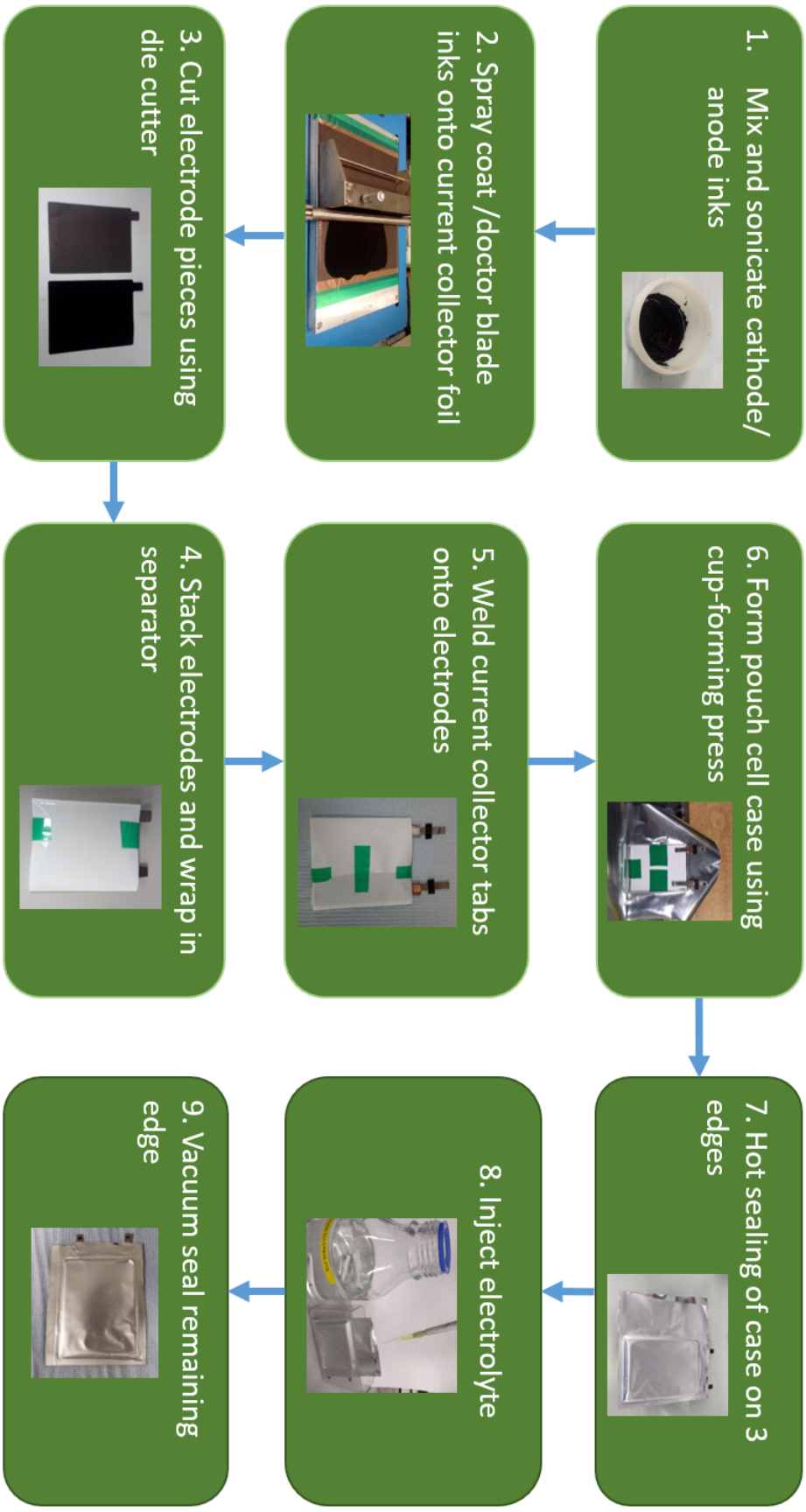

Figure 4.6: Nine-step procedure for manufacturing pouch cells [273].

Figure 4.7: Experimental setup for mounting the lithium iron phosphate electrode sample.

4.3.1.2 Experimental Setup

A single electrode from this process is approximately 40 µm in thickness; therefore, if the sample were directly mounted onto the aluminium rod, as was the case for the lithium titanate sample in Section 4.2, a large amount of beam scattering would be present from the aluminium. Instead, the electrode was rolled into a tube and then mounted on top of the aluminium rod, held in place by epoxy, as seen in Figure 4.7. This allowed the scintillator and beam source distance to be reduced to the diameter of the mounting rod, and also moved the focal point away from the highly scattering aluminium, improving image quality.

Two scans were performed using the Zeiss 160 kVp Versa 510 at the University of Southampton. The first with a 15 s exposure time and 2401 projections across an image angle of ±180°, using a 20-fold optical magnification to capture a voxel size of 801 nm. This gave voxel dimensions of 888 x 995 x 973 for the full volume. The second with a 50 s exposure and 3201 projections, using a 40-fold optical magnification to capture a voxel size of 400 nm giving a full reconstruction volume of 1784 x 1994 x 1948 voxels. Both used a voltage of 80 kV and a power of 6 W, the power was slightly higher than usual in order to better resolve the image. The two scans were both carried out on the same sample and using the same focal point; this is so they could be used as a direct comparison to see how porosity and tortuosity values changed with spatial resolution.

4.3.1.3 Comparison of the Effect of Resolution

The results of the reconstructed scans can be seen in Figure 4.8. Subfigure 4.8 (a) shows an overall scan of the electrode from the top view at a coarser resolution, and this image is then used to find a region of interest to perform subsequent scans. Subfigure 4.8 (b) shows a single tomographic slice from the 801 nm scan; the LFP electrode can be seen coated onto the aluminium current collector, and this scan was used to select a sub-volume for further analysis. This equivalent sub-volume for both resolution scans was then used to directly compare the impact of scan resolution on the properties obtained.

Subfigures 4.8 (c) and (d) show the raw image data at 801 nm and 400 nm voxel size, respectively. This raw image data is then post-processed using an anisotropic diffusion filter, as detailed in Section 4.1.2, and the greyscale data is equalised across the histogram to produce more refined peaks and troughs. The results of this post-processing are shown in Subfigures 4.8 (e) and (f). Finally, this data is segmented into two phases, solid and pore, using a simple interactive thresholding algorithm to produce Subfigures 4.8 (g) and (h).

This post-processing was carried out using the commercial software package, Avizo. Comparing Subfigures 4.8 (g) and (h) visually, it is possible to see a difference in the detail of the images. Large pores and regions of solid are still present in the 801 nm scan; however, a significant amount of detail has been lost by using a coarser resolution. In order to quantify this, six sub-volumes were taken from both resolutions and these twelve datasets were used to calculate porosity and tortuosity. Tortuosity in this chapter refers to effective tortuosity, as opposed to geodesic tortuosity, and is calculated in each direction for each sub-volume dataset using OpenImpala run on the University of Southampton's HPC system Iridis, by:

$$\tau = \epsilon \frac{D}{D_{eff}} \tag{4.1}$$

where ϵ is the volume fraction of the conducting phase, D is the intrinsic diffusivity

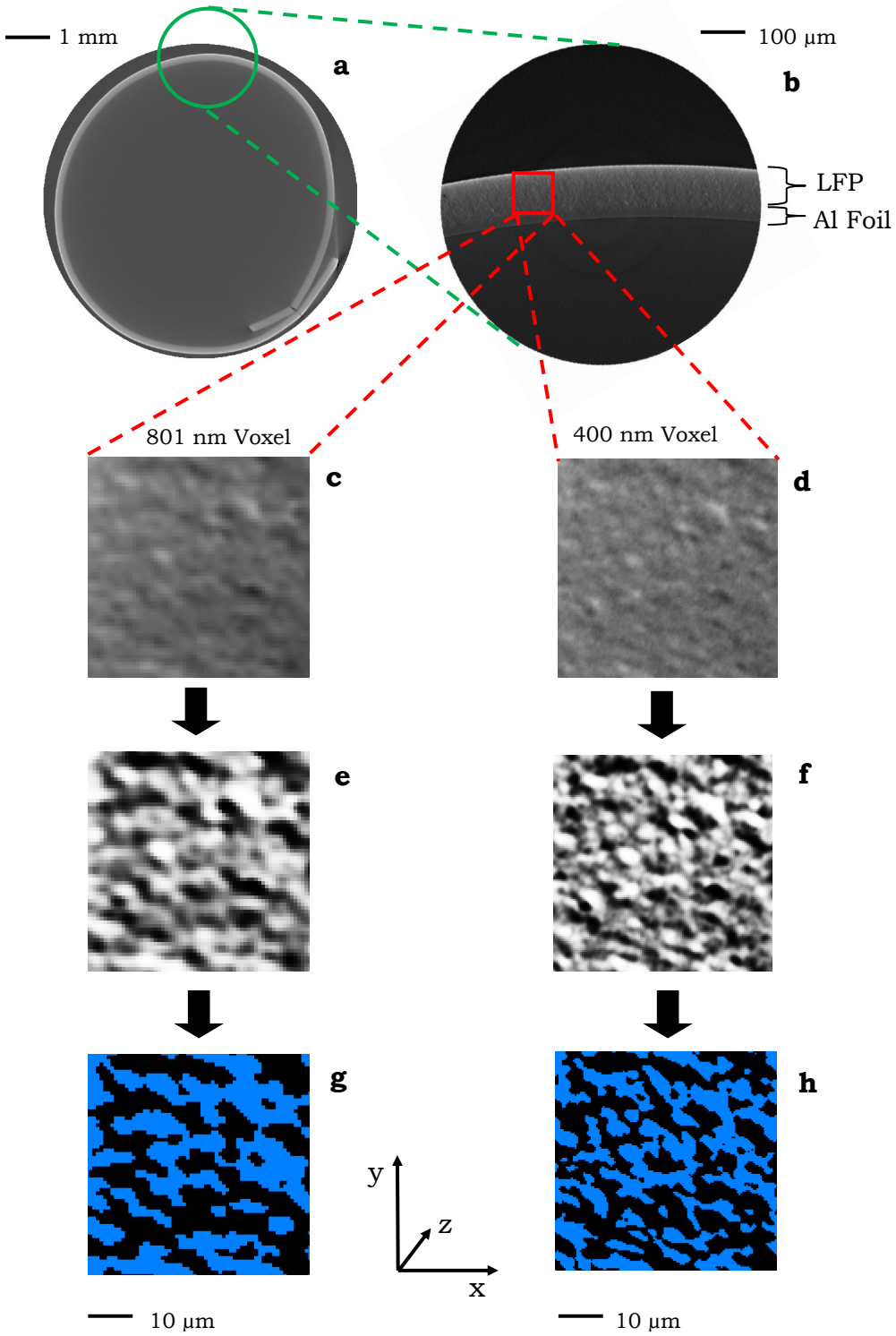

Figure 4.8: CT of an LFP electrode detailing (a) the mounting, (b) the region of interest; 801 nm voxel scans of (c) raw data, (e) equalised and filtered data, and (g) 2-phase thresholded data; and 400 nm voxel scans of (d) raw data, (f) equalised and filtered data, and (h) 2-phase thresholded data

of the conducting phase and D_{eff} is the effective diffusivity through the conducting phase where the complementary phase is insulating [109, 173]. Another value for the tortuosity can also be calculated using the Bruggeman relationship, given by:

$$\tau = \epsilon^{1-\alpha} \qquad \text{(1.2 revisited)}$$

where τ is the tortuosity, ϵ is the porosity, and α is the Bruggeman exponent, usually assumed to be 1.5 [124]. In order to compare these values, direction-averaged values of tortuosity are obtained for each data sub-volume; the results of these can be seen in Figure 4.9. The Bruggeman relationship significantly underestimates the tortuosity in comparison to CT-based values, which is consistent with observations made in the literature. It is also noted that the 400 nm scan corresponds to a smaller value for the tortuosity in comparison to the other CT-based values, which is again in agreement with the literature [105]. Shearing et al. state in [105] that 'the improvements in scan resolution reveal smaller pore geometries that contribute to higher porosity, improved connectivity and a corresponding lower tortuosity'. Finally, it is noted that there is a more significant variance in values across the six datasets for the 801 nm resolution when compared to the 400 nm. This variance might be due to the scan resolutions inability to resolve all features. Detailed results of these calculations are given in Table 4.1.

For the samples investigated, the tortuosity was found to vary in all three directions. It is especially noted that for the 400 nm scans, the tortuosity in the y-direction is consistently at a lower value (an average of 1.52 compared to 1.87 and 1.72 in the x- and z-direction, respectively). It is conceivable that this result may be due to the processing steps used to manufacture the electrode, e.g. calendering where the pores in the x- and z-directions would be reduced in size; however, further investigation is required to confirm this hypothesis.

4.3.1.4 Three Phase Segmentation Techniques

The previous analyses looked at segmenting the electrode data into two phases, solid and liquid, in order to determine the tortuosity of the electrolyte phase. However, the

Table 4.1: Tortuosity values calculated for six sub-volumes from two-resolution X-ray tomography scans of an LFP electrode.

Voxel Volume			63 x 63 x 63			Voxel Size		801 nm	
Sample Set	1			2			3		
Direction	x	y	z	x	y	z	x	y	z
D^{eff}	0.289	0.351	0.353	0.296	0.346	0.329	0.285	0.353	0.314
Tortuosity	2.07	1.70	1.69	2.00	1.71	1.80	2.05	1.65	1.86
Direction Averaged Tortuosity	1.82			1.84			1.85		
Phase Volume	59.6%			59.2%			58.4%		
Bruggeman	1.30			1.30			1.31		
Sample Set	4			5			6		
Direction	x	y	z	x	y	z	x	y	z
D^{eff}	0.291	0.374	0.339	0.280	0.349	0.332	0.283	0.340	0.340
Tortuosity	2.04	1.59	1.75	2.10	1.69	1.78	2.08	1.73	1.73
Direction Averaged Tortuosity	1.79			1.86			1.85		
Phase Volume	59.3%			59.0%			58.9%		
Bruggeman	1.30			1.30			1.30		

Voxel Volume			125 x 126 x 126			Voxel Size		400 nm	
Sample Set	1			2			3		
Direction	x	y	z	x	y	z	x	y	z
D^{eff}	0.333	0.384	0.365	0.323	0.405	0.344	0.315	0.403	0.346
Tortuosity	1.83	1.59	1.67	1.87	1.49	1.76	1.91	1.49	1.74
Direction Averaged Tortuosity	1.70			1.71			1.71		
Phase Volume	60.9%			60.4%			60.2%		
Bruggeman	1.28			1.29			1.29		
Sample Set	4			5			6		
Direction	x	y	z	x	y	z	x	y	z
D^{eff}	0.314	0.405	0.357	0.318	0.402	0.347	0.336	0.384	0.362
Tortuosity	1.93	1.50	1.70	1.89	1.50	1.74	1.81	1.59	1.68
Direction Averaged Tortuosity	1.71			1.71			1.69		
Phase Volume	60.7%			60.3%			60.9%		
Bruggeman	1.28			1.29			1.28		

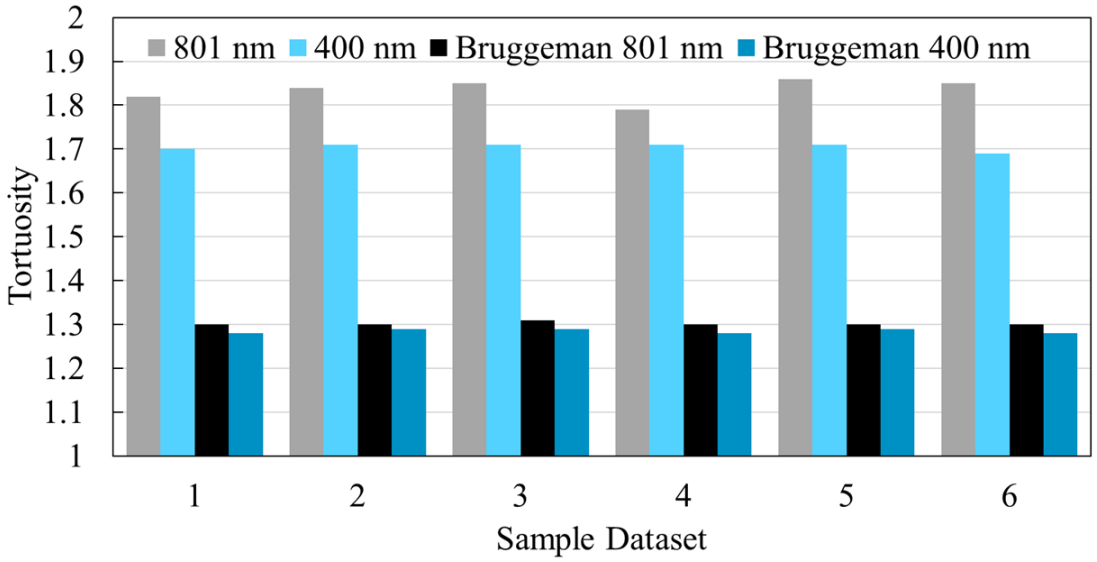

Figure 4.9: Graph to show the variance of tortuosity factor calculated for two resolution scans, 400 nm and 801 nm, and through using the Bruggeman relationship across six data samples.

electrode consists of three distinct phases: electrolyte, active particle and binder with conductive carbon. In order to segment these data into three phases, more refined thresholding algorithms are required. Using the 400 nm filtered and equalised data from Figure 4.8 (f), two different methods are applied.

The first, auto-thresholding, uses the image histogram to separate the voxel classes statistically. The second, watershed thresholding, simulates the flooding of a set of labelled regions of the image until the regions reach the watershed lines. This process is detailed in Figure 4.10. These two methods were both applied to the same dataset giving two distinct results, Figure 4.11.

There is a significant difference in the result of these two segmentation algorithms, auto-thresholding results in some very small active particles due to the dependence of the method on statistical greyscale values. Conversely, watershed thresholding results in larger conglomerations of active particle held together by regions of the conductive binder. As the electrodes are structurally made of active particle 'islands', held together by 'bridges' of conductive binder, auto-thresholding should give a more accurate result, however, there is not enough data within the image to properly differentiate

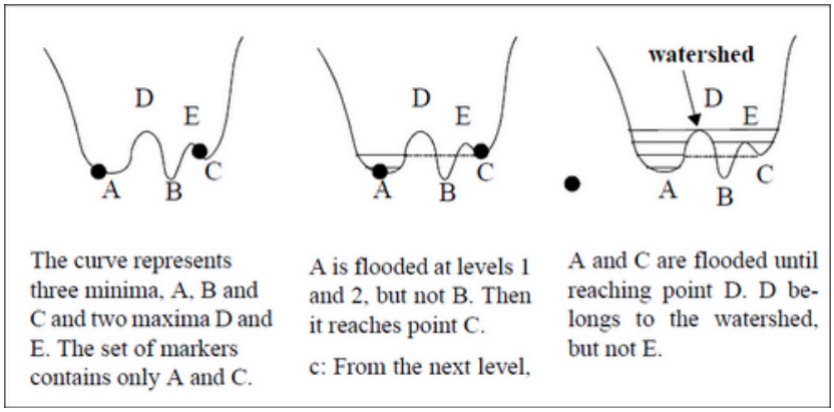

Figure 4.10: Figure to show the operation of the watershed algorithm [274].

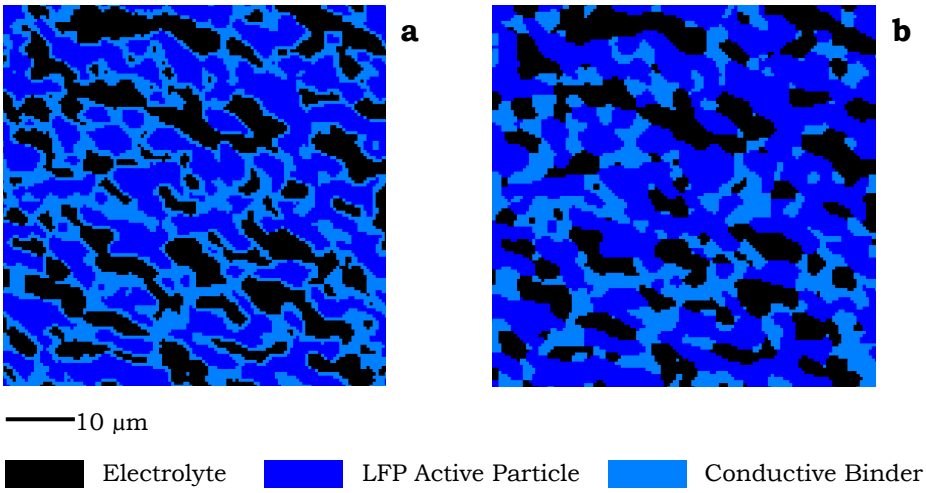

Figure 4.11: Subvolume of a CT of an LFP electrode with a voxel size of 400 nm, detailing two different 3-phase segmentation techniques (a) auto-thresholding and (b) watershed thresholding.

between the three phases. One way to improve the quality of the image dataset is to make use of correlated multi-modal imaging and combine two different techniques, as outlined in Section 1.5.2.2. .

4.3.2 Lithium Nickel Manganese Cobalt Oxide Structured Particles

This section is a modified version of the authors contribution to "Effect of Tomography Resolution on Calculation of Microstructural Properties for Lithium Ion Porous Electrodes." published in "ECS Transactions 97, no. 7 (2020): 255" by "James Le Houx, Markus Osenberg, Matthias Neumann, Joachim R. Binder, Volker Schmidt, Ingo Manke, Thomas

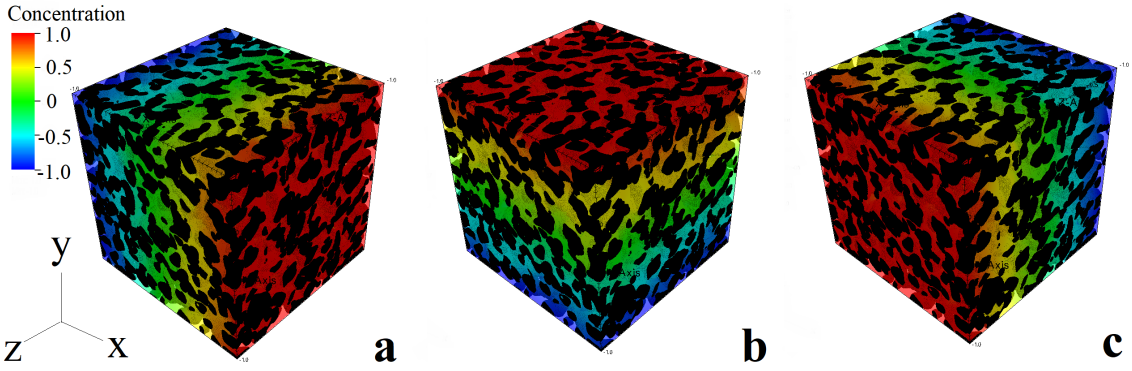

Figure 4.12: Concentration plots of 499 voxel cubic dataset for (a) x-, (b) y-, and (c) z-directions.

Carraro, and Denis Kramer".

4.3.2.1 Comparison of the Effect of Resolution

This experiment uses a level-set defined model of the geometry, as outlined in [275], based on tomographic data, that can be used to compute the tortuosity with different resolutions. The preparation for these image datasets are included in Appendix B for completeness of the work but to be clear, the work included in Appendix B was not carried out by the author. The tomographic image datasets are of a lithium nickel manganese cobalt oxide (NMC) microstructural particle. In this thesis, two datasets have been reconstructed from the same microstructure with volume $5\,\mu m^3$, using two resolutions: a 499 cubic voxel set with voxel size 10 nm and a 998 cubic voxel set with voxel size 5 nm. These datasets are then used as the computational domain in Section 4.3.2.1.

Concentration plots of the steady-state diffusion calculation of the 499 cubic voxels set in the x, y and z directions are shown in Figure 4. OpenImpala is an easily parallelisable code written specifically for high-performance computing, allowing large image datasets to be used to compute effective transport parameters. The simulations were run on the University of Southampton's HPC system, Iridis 5. This consists of 464 compute nodes, of 40 cores per node, running dual 2.0 GHz Intel Skylake processors with 192 Gb of DDR4 memory. The calculations for the 499 voxel set that would have pre-

Table 4.2: Tortuosity calculated for both pore and material phases based on two resolutions of a single active NMC particle.

	Pore Phase						Material Phase					
Voxel Volume	499 x 499 x 499			998 x 998 x 998			499 x 499 x 499			998 x 998 x 998		
Direction	x	y	z	x	y	z	x	y	z	x	y	z
D^{eff}	0.179	0.200	0.194	0.188	0.214	0.210	0.333	0.335	0.343	0.348	0.344	0.361
Tortuosity	2.12	1.90	1.96	2.02	1.77	1.81	1.86	1.85	1.85	1.78	1.80	1.72
Direction Averaged Tortuosity	2.00			1.87			1.86			1.77		
Phase Volume	38.0%			38.0%			62.0%			62.0%		
Bruggeman	1.62			1.62			1.27			1.27		

viously taken hours and days to solve, can now be solved in around 2 minutes with suitable computing architecture using OpenImpala. Furthermore, large scale datasets typical of modern tomography, 10^9 voxels, can be analysed to obtain more representative effective diffusion coefficients.

The results of the calculations can be seen in Table 4.2. The pore phase and solid phase of both resolution datasets were analysed in each direction. Since both data sets were obtained by the same level set model, the same phase volumes for the two resolutions were expected. For the solid phase, similar values for direction averaged tortuosity and phase volume are calculated to the micro-CT values obtained in Table 4.1. Additionally, the trend of decreasing tortuosity with an improved resolution is noted.

4.3.3 Reticulated Vitreous Carbon Electrodes for a Soluble Lead Flow Battery

This section is a modified version of the authors contribution to "The soluble lead flow battery: Image-based modelling of porous carbon electrodes" published in "Journal of Energy Storage 52:104791 (2022)" by "Fraser, Ewan, James Le Houx, Luis Fernando Arenas, Ranga Dinesh Koralage and Richard Wills".

This Section simulates the behaviour of the soluble lead flow battery when reticulated vitreous carbon (RVC) electrodes are used. The arrangement of the flow battery is such that there is a porous, foam-like carbon electrode, which the liquid electrolyte

flows past by means of a pump. As the battery is charged solid Pb is deposited at the negative electrode and solid PbO_2 is deposited at the positive electrode. During discharge, the solid deposits are dissolved back into the electrolyte as Pb^{2+} ions. This multiphase interaction between electrode and electrolyte is key to the operation of the battery, especially as the morphology evolves during charge/discharge cycles. The open-source software OpenImpala is used to predict the macro-homogeneous properties of RVC from computed tomography data of various grades of RVC. The process is repeated on digitally manipulated datasets where a voxel dilation technique has been used to estimate the geometry of RVC electrodes with a range of thicknesses of deposited material. These macro-homogeneous properties can then be used to inform other scales of battery modelling.

4.3.3.1 Image Data Preparation

The raw CT data was obtained from work by Arenas et al [276], which used a Nikon/X-Tek XTH 225 instrument, with an isotropic resolution of 9.6 µm per voxel and a detector size of 2000 x 2000 pixels. The data for scans of 10, 30, 45, 80 and 100 ppi(pores per inch) was binarised into two constituent phases, solid and porous volume, and cropped into a cuboid domain of dimensions 1072 x 1104 x 1296. An isometric view of a slice of the segmented 100 ppi data is shown in Figure 4.13.

For each grade of RVC, the morphology of the porous electrodes was virtually modified [277] by voxel dilation of the solid domain of the RVC CT dataset in the open-source software ImageJ [278]. This virtual dilation was performed to see the effect of deposit accumulation on the transport processes of the porous electrode. Each dataset was dilated by a single voxel and then further dilated until the following specified total solid volume fraction were reached: 0.1, 0.2, 0.3, 0.5 and 0.8. Both the original and newly dilated datasets had the raw greyscale values multiplied by 0.5 to achieve an electrolyte phase of 0 and a solid phase of 127. The original dataset was then added to each of the dilated datasets to achieve a three-phase segmented dataset with RVC holding a value of 255, the artificial electrode deposit 127 and the electrolyte 0.

For each of these 35 datasets, values for both the porosity and tortuosity were cal-

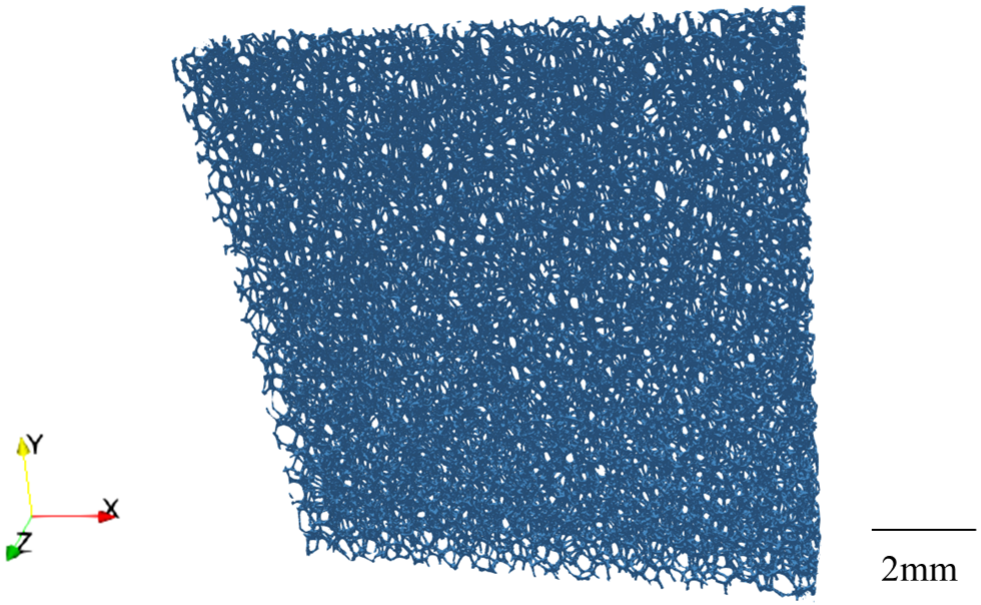

Figure 4.13: Isometric view of a slice of the thresholded 100 ppi RVC CT data.

culated using the open-source software, OpenImpala [272]. These calculations were performed in the x-direction, as previous work by Arenas et al., [276], has shown each RVC grade to have good isotropy. Tortuosity in this case refers to effective tortuosity, not geodesic tortuosity [130] and is calculated by solving a steady-state Fickian diffusion problem as shown in Equation 1.9. The computations were performed on the University of Southampton's supercomputer, Iridis 5.

4.3.3.2 Simulation Results

Figure 4.14 shows the steady-state diffusion gradients for each of the seven datasets of the 100 ppi RVC sample. From visual inspection, it can be seen that at higher levels of lead compound deposition, pathways throughout the domain have been closed off, leading to more contorted diffusion paths. Additionally, the closing of transport paths could lead to areas of the solid fraction being inaccessible on discharge, reducing ion transport. Therefore, the management of lead compound accumulation in the porous electrode is a key component in the correct operation of the soluble lead flow battery.

Figure 4 shows the complete plot of results from the image analysis. Effective tortuosity values are plotted against solid volume fraction for each of the RVC grades. There

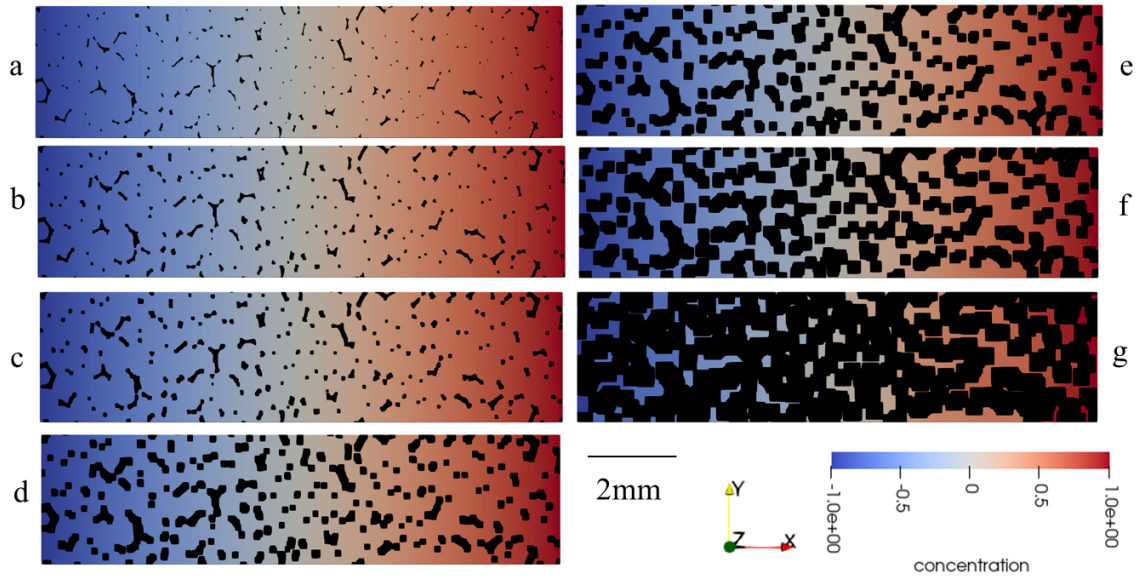

Figure 4.14: Steady-state diffusion profiles for the 100 ppi RVC sample at each deposition: (a) clean, (b) one voxel dilation, (c) 90% porosity, (d) 80% porosity, (e) 70% porosity, (f) 50% porosity and (g) 20% porosity. Flow is from left to right and these are 2D representative strips of the full datasets.

is a general trend of tortuosity increasing as lead is accumulated on the electrode, with a significant increase apparent at values of 80% solid, likely due to the closing of transport paths. Additionally, standard deviation across the grades increases with tortuosity. At low levels of deposition, the value of tortuosity is found to be similar across the grades of RVC, which is in agreement with [276]. However, as the solid fraction increases, discrepancies between the different grades become more significant. This is a key result. At low levels of deposition, the morphology of the RVC electrode appears to have little effect on transport processes, but as lead compounds are accumulated, the structure becomes increasingly important.

Furthermore, the 80 ppi grade has a significantly higher value of tortuosity, 15.2, at a solid volume fraction of 80%. The specific morphology of this grade has resulted in a highly contorted diffusion path. When designing electrodes for use in the soluble lead flow battery, it is important to consider the effect of morphology on both the transport processes occurring in a fully discharged state, as well as in the fully charged state when lead compound accumulation is higher.

The tortuosity and porosity values obtained through these methods are then used

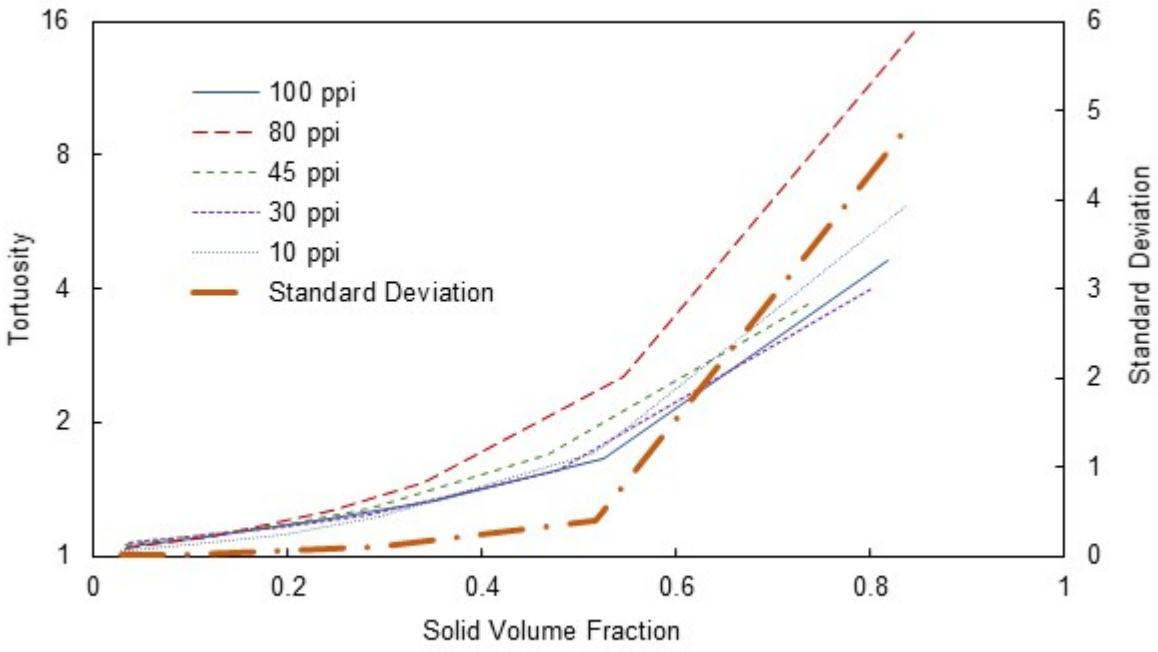

Figure 4.15: Graph to show how the tortuosity of the RVC samples varies depending on the solid volume fraction and ppi value. The standard deviation between results is shown to significantly increase at higher lead deposition (i.e. 80% solid volume fraction).

as values in a lookup table for a numerical model to represent the varying conditions throughout charge/discharge more accurately. Further details of this numerical model are provided in Appendix D. At each timestep, the volume fraction is taken, and a linear interpolation function is used with the lookup table to determine the corresponding values of tortuosity and porosity, demonstrating how OpenImpala can be used to link the methods of multi-scale modelling together.

4.4 Summary

In this chapter, a workflow for two-phase segmentation of electrodes has been presented: imaging the electrode using CT imagery, post-processing the data using anisotropic diffusion filters and equalising the histogram, and finally segmentation into two distinct phases. This technique has been applied to three electrode materials: titanium dioxide, lithium titanate and lithium iron phosphate. Titanium dioxide provided a thin film electrode to thoroughly test the capability of the Zeiss Versa 510 located at the University of Southampton. Lithium titanate ($Li_4Ti_5O_{12}$) with 1-pyrenecarboxylic acid decorated multi-walled carbon nanotubes (LTO/PCA@CNTs) was analysed in order to determine the distribution of electrode material across the nickel foam substrate, this is the first time this material has been imaged, and this work is currently in publication.

In this chapter, effective diffusion coefficients of a porous LFP electrode have been computed using tomographic data. The computed tortuosity has been compared to the tortuosity obtained by the Bruggeman formula. It is found that the Bruggeman formula significantly underestimates the tortuosity compared to the OpenImpala calculated results for the case study. Furthermore, a comparison of resolution study was carried out to see how this affects results obtained.

Regarding the LFP electrode, it is found that there is a more significant statistical variability in the data with finer resolution (801 nm), whereas the coarser resolution (400 nm) results have a much smaller standard deviation. In both case studies, a finer resolution leads to a reduction of the tortuosity.

Electrochemical Device	Sample Synthesis	X-ray CT	Post-processing	Image-based Modelling
Titanium Dioxide Electrode for Aluminium Ion Battery	No	Yes	Yes	No
Lithium Titanate Electrode for Supercapacitor	No	Yes	Yes	No
Lithium Iron Phosphate Electrode for Lithium Ion Battery	Yes	Yes	Yes	Yes
Lithium Nickel Manganese Cobalt Oxide for Lithium Ion Battery	No	No	No	Yes
Reticulated Vitreous Carbon Electrodes for Soluble Lead Flow Battery	No	No	Yes	Yes

Table 4.3: Table to clarify the authors contributions to the different experiments contained within this chapter.

This Section has also used OpenImpala to predict the macro-homogeneous properties of RVC for a soluble lead flow battery from computed tomography data of various grades of RVC. The process is repeated on digitally manipulated datasets where a voxel dilation technique has been used to estimate the geometry of RVC electrodes with a range of thicknesses of deposited material. These macro-homogeneous properties can then be used to inform other scales of battery modelling.

This work has made use of a single-physics, image-driven computational model, OpenImpala, and applied it in the study of transport processes in various electrochemical devices. A summary of the authors contributions to each of these experiments is given in Table 4.3. The 998 voxel data set of the single-particle has also been used to show the capability of the implementation to deal with large data sets typical of modern tomography. In future works, this code can be used to analyse larger electrode reference volume elements. Allowing the study of microstructural properties of porous electrodes with a precision not yet shown.

4.4.1 Future Work

X-ray tomography in conjunction with image-based modelling could be used to analyse a number of different electrochemical systems to better understand the effect of structure. A number of different systems have been investigated in this Chapter. A possible future direction is to investigate the digital modification of image datasets,

like that seen in Section 4.3.3, in order to create a series of virtual datasets. Each of these could then be used as the computational domain for an image based model, and these simulations could all be run to predict the optimal electrode microstructure for a specific parameter. This digital microstructure could then be manufactured by means of selective powder deposition, or laser drilling, closing the loop between experimentation, imaging and computation.

Chapter 5

Summary and Conclusions

5.1 Summary

Chapter 1 highlights the importance of Li-ion batteries to the automotive, consumer electronics and energy industries. Providing more suitable solutions to thermal runaway is highlighted as a key challenge. The author's research group are exploring using PTCR materials as additives to the electrodes to mitigate the thermal runaway effect, however, modelling is required to understand the effects on the operation of the battery. Newman pseudo-2D models are widespread in their use. However, they do not predict phenomena related to the inhomogeneous structure of the electrode. Homogenisation models can only solve on small volumes of the electrode due to the large computational load required to solve the associated equations. Finite element image-based models require the use of representative elementary volumes as they are inherently hard to parallelise. There is, therefore, a need for an image-based single-physics code that scales well with an increasing number of computational cores.

Chapter 2 presents an overview of the experimental methodologies used throughout this thesis. X-ray computed tomography (CT) is a radiographic experimental technique used to image volumetric detail in three dimensions. The relatively good penetration of X-rays permits the nondestructive imaging of the internal structure of materials. An image artifact is a part of the image data that does not represent the physical structure of the test sample. There are a wide range of possible image artifacts associated with CT imaging, such as: radiation scatter, statistical noise, edge streaks

and beam hardening. Reducing/removing each of these artefacts requires the careful balancing of experimental parameters in order to improve image quality. A representative elementary volume (REV) is the smallest volume over which a computation or measurement can be made that is representative of the whole volume. The finite differences method (FDM) is a differential scheme that is an approximation of a Taylor series expansion. FDM methods are usually run in regular, discretised cube meshes. Meaning they are less computationally intensive to implement during the meshing stage but can bring about an approximation of the error due to the differences method. AMReX is block-structured adaptive mesh software framework. Through using more computationally efficient adaptive mesh regimes, implementing a hybrid OpenMP/MPI parallel approach and by developing the framework from the ground up, AMReX-based solvers have been shown to reach a solution up to 200 times faster than Chombo using the same number of processors.

Chapter 3 presents a single-physics image-based model (OpenImpala) that has been developed. The code solves for diffusion across CT obtained electrode microstructure and calculates the tortuosity factor. The code reads in CT obtained segmented datasets, calculates volume fractions for the phases, and performs an iterative solution of the diffusion equation. Two solvers are used: a basic finite differences method or a solver based on the Hypre framework. Both solvers are shown to scale well with an increasing number of computational cores. The Hypre based solver performs equivalent calculations 220x faster than the basic finite differences method. The Hypre solver has been shown to outperform Taufactor when used on two or more computing cores. This chapter has detailed the development of a data-driven, image-based modelling framework that is capable of modelling transport processes in Li-ion battery electrodes called OpenImpala. Micro X-ray computed tomography is used to obtain 3D microstructural data from manufactured samples non-destructively. These 3D datasets are then used as the computational domain within a finite-differences-based model, in order to solve the diffusion equation directly on the CT obtained dataset. The code then calculates the equivalent homogenised transport coefficients for the given microstructure, which can then be used to create a parameter file for continuum models PyBamm and DandeLiion. The code has been shown to scale well with an in-

creasing number of computational cores on distributed memory architectures, making it applicable to large datasets typical of tomography.

Chapter 4 presents a workflow for the two-phase segmentation of electrodes. This method images the electrode using CT imagery, post-processes the data by applying an anisotropic diffusion filter and segments it into two distinct phases, solid and liquid. This method is applied to three electrode materials: titanium dioxide, lithium titanate and lithium iron phosphate. This is the first time the LTO/PCA@CNTs material has been imaged and the work is currently in publication. The effects of scan resolution were studied using lithium iron phosphate. It was found that CT imaged electrodes consistently produce higher values of tortuosity compared to the Bruggeman values. Furthermore, improved resolution scans result in lower tortuosity values. The author believes this is due to smaller pore geometries being resolved, resulting in greater connectivity of the phases. Finally, an increase of tortuosity is recorded in the x and z directions. It is hypothesised this is a result of the calendaring process used during the manufacture of the electrode. This Chapter has also used OpenImpala to predict the macro-homogeneous properties of reticulated vitreous carbon (RVC) electrodes for a soluble lead flow battery from computed tomography data of various grades of RVC. The process is repeated on digitally manipulated datasets where a voxel dilation technique has been used to estimate the geometry of RVC electrodes with a range of thicknesses of deposited material. These macro-homogeneous properties can then be used to inform other scales of battery modelling.

In summary, the overall contribution of the work contained in this thesis is the development of a novel parallelisable image-based modelling framework, OpenImpala, its validation and performance testing, and the application of the framework to transport processes in multiple electrochemical case studies, including lithium-ion battery electrodes, a lithium titanate supercapacitor, aluminum ion electrodes and a soluble lead flow battery, demonstrating its importance and versatility to energy storage research.

5.2 Future Work

The next step in the development of the single physics model is to incorporate adaptive mesh refinement within the code to reduce the computational resource required. The solvers presented in this section also need to be compared in terms of their error in order to fully characterise their performance. These results can be compared to experimental data from electrochemical impedance spectroscopy carried out on the same samples. The framework could be expanded to full multi-physics capability. This will be achieved by writing additional mathematical kernels to represent the physical fields present (thermal, electrical, electrochemical), possible due to the modular nature of the code.

A possible approach to reduce computational resource is to use an embedded boundary method. The current development of AMReX has limited usage of embedded boundary approaches; it is only currently possible to draw simple shapes such as circles, walls or polygons. However, this feature is under continuous progress, and the functionality of the embedded boundary approach is improving with every release. This may present an opportunity to collaborate with the authors over the development of a new tool within AMReX, a feature that allows geometry to be imported from data files and used as the embedded boundary structure. Whilst developing the tools in this thesis, bugs were found in the AMReX source code. These have now been committed to the open-source AMReX code and successfully merged; any future developments will continue to be communicated to the AMReX team.

Having established a working imaging method to capture the electrode microstructure, the next step is to image an electrode that has been cycled to failure. Due to the intercalation of the ions, significant change should be witnessed. This will manifest itself as a change in tortuosity and porosity of the material and should therefore be quantifiable. Additionally, further work is required to investigate three-phase segmentation techniques to determine the most appropriate. A comparison of three separate techniques: Trainable Weka Segmentation, auto-thresholding and watershed thresholding is required. These results will be compared to other imaging techniques, such as SEM, as well as experimental results. Finally, quantifying the accuracy of these scans

using the method detailed in section 2.1.3.3 is required to give greater insight to the limitations of the process.

X-ray tomography in conjunction with image-based modelling could be used to analyse a number of different electrochemical systems to better understand the effect of structure. A number of different systems have been investigated in this Chapter. A possible future direction is to investigate the digital modification of image datasets, like that seen in Section 4.3.3, in order to create a series of virtual datasets. Each of these could then be used as the computational domain for an image based model, and these simulations could all be run to predict the optimal electrode microstructure for a specific parameter. This digital microstructure could then be manufactured by means of selective powder deposition, or laser drilling, closing the loop between experimentation, imaging and simulation.

References

[1] W. Chen, J. Liang, Z. Yang, and G. Li, "A review of lithium-ion battery for electric vehicle applications and beyond," *Energy Procedia*, vol. 158, pp. 4363–4368, 2019, Innovative Solutions for Energy Transitions, ISSN: 1876-6102. DOI: https://doi.org/10.1016/j.egypro.2019.01.783. [Online]. Available: https://www.sciencedirect.com/science/article/pii/S1876610219308215.

[2] I. Burch and J. Gilchrist, "Survey of global activity to phase out internal combustion engine vehicles," *Center of Climate Protection: Santa Rosa, CA, USA*, 2018.

[3] X. Xu, Z. Wei, Q. Ji, C. Wang, and G. Gao, "Global renewable energy development: Influencing factors, trend predictions and countermeasures," *Resources Policy*, vol. 63, p. 101 470, 2019.

[4] IPCC, *Climate Change 2021: The Physical Science Basis. Contribution of Working Group I to the Sixth Assessment Report of the Intergovernmental Panel on Climate Change*. Cambridge, United Kingdom and New York, NY, USA: Cambridge University Press, 2021.

[5] H. Vella, "Ten steps to net zero: As the goal to reach net zero in the uk rapidly approaches, we examine boris johnson's 10-point plan for a green industrial revolution," *Engineering & Technology*, vol. 16, no. 1, pp. 20–25, 2021.

[6] S. Vazquez, S. M. Lukic, E. Galvan, L. G. Franquelo, and J. M. Carrasco, "Energy storage systems for transport and grid applications," *IEEE Transactions on Industrial Electronics*, vol. 57, no. 12, pp. 3881–3895, 2010.

[7] P. Denholm, E. Ela, B. Kirby, and M. Milligan, "The role of energy storage with renewable electricity generation," *National Renewable Energy Laboratory*, 2010.

[8] A. Züttel, A. Borgschulte, and L. Schlapbach, *Hydrogen as a future energy carrier*. John Wiley & Sons, 2011.

[9] G. Marbán and T. Valdés-Solís, "Towards the hydrogen economy?" *Int. J. Hydrogen Energy*, vol. 32, no. 12, pp. 1625–1637, 2007.

[10] A. Poullikkas, "Sustainable options for electric vehicle technologies," *Renewable and Sustainable Energy Reviews*, vol. 41, pp. 1277–1287, 2015.

[11] M. Naumann, R. C. Karl, C. N. Truong, A. Jossen, and H. C. Hesse, "Lithium-ion battery cost analysis in pv-household application," *Energy Procedia*, vol. 73, pp. 37–47, 2015.

[12] D. Pratt, "Battery storage dominates national grid efr tender results," *Energy Storage News*, 2016.

[13] M. Koziol, "South australia announces tesla as back of world's largest battery," *The Sydney Morning Herald*, 2017.

[14] Q. Wang, P. Ping, X. Zhao, G. Chu, J. Sun, and C. Chen, "Thermal runaway caused fire and explosion of lithium ion battery," *Journal of power sources*, vol. 208, pp. 210–224, 2012.

[15] N. Williard, W. He, C. Hendricks, and M. Pecht, "Lessons learned from the 787 dreamliner issue on lithium-ion battery reliability," *Energies*, vol. 6, no. 9, pp. 4682–4695, 2013.

[16] Reuters in Montreal, "Lithium-ion batteries banned as cargo on passenger flights," *The Guardian*, 2016.

[17] F. Larsson, P. Andersson, and B.-E. Mellander, "Lithium-ion battery aspects on fires in electrified vehicles on the basis of experimental abuse tests," *Batteries*, vol. 2, no. 2, p. 9, 2016.

[18] L. Bunce, M. Harris, and M. Burgess, "Charge up then charge out? drivers' perceptions and experiences of electric vehicles in the uk," *Transportation Research Part A: Policy and Practice*, vol. 59, pp. 278–287, 2014.

[19] J. Christman, "The case of the burning laptops," *Journal of Case Studies*, vol. 30, no. 1, pp. 88–97, 2012.

[20] R. D. McKerracher, J. Guzman-Guemez, R. G. Wills, S. M. Sharkh, and D. Kramer, "Advances in prevention of thermal runaway in lithium-ion batteries," *Advanced Energy and Sustainability Research*, vol. 2, no. 5, p. 2 000 059, 2021.

[21] D. Kramer, "Improved lifetime performance and safety of electrochemical energy stores through functionalization of passive materials and components," *ISCF Wave*, 2016.

[22] K. M. Jensen, X. Yang, J. V. Laveda, W. G. Zeier, K. A. See, M. Di Michiel, B. C. Melot, S. A. Corr, and S. J. Billinge, "X-ray diffraction computed tomography for structural analysis of electrode materials in batteries," *Journal of The Electrochemical Society*, vol. 162, no. 7, A1310–A1314, 2015.

[23] F. Tariq, V. Yufit, M. Kishimoto, P. Shearing, S. Menkin, D. Golodnitsky, J. Gelb, E. Peled, and N. Brandon, "Three-dimensional high resolution x-ray imaging and quantification of lithium ion battery mesocarbon microbead anodes," *Journal of Power Sources*, vol. 248, pp. 1014–1020, 2014.

[24] S. J. Dillon and K. Sun, "Microstructural design considerations for li-ion battery systems," *Current Opinion in Solid State and Materials Science*, vol. 16, no. 4, pp. 153–162, 2012.

[25] M. Ebner, F. Geldmacher, F. Marone, M. Stampanoni, and V. Wood, "X-ray tomography of porous, transition metal oxide based lithium ion battery electrodes," *Advanced Energy Materials*, vol. 3, no. 7, pp. 845–850, 2013.

[26] J. Dunn, L. Gaines, J. Kelly, C. James, and K. Gallagher, "The significance of li-ion batteries in electric vehicle life-cycle energy and emissions and recycling's role in its reduction," *Energy & Environmental Science*, vol. 8, no. 1, pp. 158–168, 2015.

[27] A. A. Pesaran, "Battery thermal models for hybrid vehicle simulations," *Journal of power sources*, vol. 110, no. 2, pp. 377–382, 2002.

[28] R. Wright, J. Christophersen, C. Motloch, J. Belt, C. Ho, V. Battaglia, J. Barnes, T. Duong, and R. Sutula, "Power fade and capacity fade resulting from cycle-life testing of advanced technology development program lithium-ion batteries," *Journal of Power Sources*, vol. 119, pp. 865–869, 2003.

[29] P. Ramadass, B. Haran, R. White, and B. N. Popov, "Capacity fade of sony 18650 cells cycled at elevated temperatures: Part i. cycling performance," *Journal of power sources*, vol. 112, no. 2, pp. 606–613, 2002.

[30] S. A. Khateeb, S. Amiruddin, M. Farid, J. R. Selman, and S. Al-Hallaj, "Thermal management of li-ion battery with phase change material for electric scooters: Experimental validation," *Journal of Power Sources*, vol. 142, no. 1, pp. 345–353, 2005.

[31] J. Shim, R. Kostecki, T. Richardson, X. Song, and K. A. Striebel, "Electrochemical analysis for cycle performance and capacity fading of a lithium-ion battery cycled at elevated temperature," *Journal of power sources*, vol. 112, no. 1, pp. 222–230, 2002.

[32] V. Etacheri, R. Marom, R. Elazari, G. Salitra, and D. Aurbach, "Challenges in the development of advanced li-ion batteries: A review," *Energy & Environmental Science*, vol. 4, no. 9, pp. 3243–3262, 2011.

[33] J. Vetter, P. Novak, M. Wagner, C. Veit, K.-C. Möller, J. Besenhard, M. Winter, M. Wohlfahrt-Mehrens, C. Vogler, and A. Hammouche, "Ageing mechanisms in lithium-ion batteries," *Journal of power sources*, vol. 147, no. 1, pp. 269–281, 2005.

[34] C. R. Birkl, M. R. Roberts, E. McTurk, P. G. Bruce, and D. A. Howey, "Degradation diagnostics for lithium ion cells," *Journal of Power Sources*, vol. 341, pp. 373–386, 2017.

[35] M. Doyle and J. Newman, "The use of mathematical modeling in the design of lithium/polymer battery systems," *Electrochimica Acta*, vol. 40, no. 13-14, pp. 2191–2196, 1995.

[36] T. F. Fuller, M. Doyle, and J. Newman, "Simulation and optimization of the dual lithium ion insertion cell," *Journal of the Electrochemical Society*, vol. 141, no. 1, pp. 1–10, 1994.

[37] M. Doyle, T. F. Fuller, and J. Newman, "Modeling of galvanostatic charge and discharge of the lithium/polymer/insertion cell," *Journal of the Electrochemical society*, vol. 140, no. 6, p. 1526, 1993.

[38] S. A. Krachkovskiy, J. M. Foster, J. D. Bazak, B. J. Balcom, and G. R. Goward, "Operando mapping of li concentration profiles and phase transformations in graphite electrodes by magnetic resonance imaging and nuclear magnetic resonance spectroscopy," *The Journal of Physical Chemistry C*, vol. 122, no. 38, pp. 21 784–21 791, 2018.

[39] M. Ecker, T. K. D. Tran, P. Dechent, S. Käbitz, A. Warnecke, and D. U. Sauer, "Parameterisation of a physico-chemical model of a lithium-ion battery part i: Determination of parameters," *J. Electrochem. Soc*, vol. 162, no. 9, A1836–A1848, 2015.

[40] A. J. Louli, J. Li, S. Trussler, C. R. Fell, and J. R. Dahn, "Volume, pressure and thickness evolution of li-ion pouch cells with silicon-composite negative electrodes," *Journal of The Electrochemical Society*, vol. 164, no. 12, A2689–A2696, 2017. DOI: 10.1149/2.1691712jes. [Online]. Available: https://doi.org/10.1149/2.1691712jes.

[41] M. Ecker, S. Käbitz, I. Laresgoiti, and D. U. Sauer, "Parameterization of a physico-chemical model of a lithium-ion battery: Ii. model validation," *Journal of The Electrochemical Society*, vol. 162, no. 9, A1849, 2015.

[42] C.-H. Chen, F. Brosa Planella, K. O'Regan, D. Gastol, W. D. Widanage, and E. Kendrick, "Development of Experimental Techniques for Parameterization of Multi-scale Lithium-ion Battery Models," *Journal of The Electrochemical Society*, vol. 167, no. 8, p. 080 534, 2020. DOI: 10.1149/1945-7111/ab9050.

[43] F. Civan, *Porous media transport phenomena*. John Wiley & Sons, 2011.

[44] J. Fu, H. R. Thomas, and C. Li, "Tortuosity of porous media: Image analysis and physical simulation," *Earth-Science Reviews*, p. 103 439, 2020.

[45] A. Koponen, M. Kataja, and J. Timonen, "Permeability and effective porosity of porous media," *Physical Review E*, vol. 56, no. 3, p. 3319, 1997.

[46] L. W. Petersen, P. Moldrup, O. H. Jacobsen, and D. E. Rolston, "Relations between specific surface area and soil physical and chemical properties," *Soil Science*, vol. 161, no. 1, pp. 9–21, 1996.

[47] B. Münch and L. Holzer, "Contradicting geometrical concepts in pore size analysis attained with electron microscopy and mercury intrusion," *Journal of the American Ceramic Society*, vol. 91, no. 12, pp. 4059–4067, 2008.

[48] L. Holzer, D. Wiedenmann, B. Münch, L. Keller, M. Prestat, P. Gasser, I. Robertson, and B. Grobéty, "The influence of constrictivity on the effective transport properties of porous layers in electrolysis and fuel cells," *Journal of materials science*, vol. 48, no. 7, pp. 2934–2952, 2013.

[49] C. F. Berg, "Permeability description by characteristic length, tortuosity, constriction and porosity," *Transport in porous media*, vol. 103, no. 3, pp. 381–400, 2014.

[50] M. B. Clennell, "Tortuosity: A guide through the maze," *Geological Society, London, Special Publications*, vol. 122, no. 1, pp. 299–344, 1997.

[51] P. Adler, C. G. Jacquin, and J. Quiblier, "Flow in simulated porous media," *International Journal of Multiphase Flow*, vol. 16, no. 4, pp. 691–712, 1990.

[52] S. Prachayawarakorn and R. Mann, "Effects of pore assembly architecture on catalyst particle tortuosity and reaction effectiveness," *Catalysis today*, vol. 128, no. 1-2, pp. 88–99, 2007.

[53] T. Zielinski, "Inverse identification and microscopic estimation of parameters for models of sound absorption in porous ceramics," in *Proceedings of International Conference on Noise and Vibration Engineering (ISMA2012)/International Conference on Uncertainty in Structural Dynamics (USD2012)*, 2012, pp. 95–108.

[54] V. Karanikola, A. F. Corral, H. Jiang, A. E. Sáez, W. P. Ela, and R. G. Arnold, "Effects of membrane structure and operational variables on membrane distillation performance," *Journal of Membrane Science*, vol. 524, pp. 87–96, 2017.

[55] E. A. Botchwey, M. A. Dupree, S. R. Pollack, E. M. Levine, and C. T. Laurencin, "Tissue engineered bone: Measurement of nutrient transport in three-dimensional matrices," *Journal of Biomedical Materials Research Part A: An Official Journal of The Society for Biomaterials, The Japanese Society for Biomaterials, and The Australian Society for Biomaterials and the Korean Society for Biomaterials*, vol. 67, no. 1, pp. 357–367, 2003.

[56] F. Dolamore, C. Fee, and S. Dimartino, "Modelling ordered packed beds of spheres: The importance of bed orientation and the influence of tortuosity on dispersion," *Journal of Chromatography A*, vol. 1532, pp. 150–160, 2018.

[57] J. Kozeny, "Uber kapillare leitung der wasser in boden," *Royal Academy of Science, Vienna, Proc. Class I*, vol. 136, pp. 271–306, 1927.

[58] P. C. Carman, "Fluid flow through granular beds," *Trans. Inst. Chem. Eng.*, vol. 15, pp. 150–166, 1937.

[59] M. Barrande, R. Bouchet, and R. Denoyel, "Tortuosity of porous particles," *Analytical chemistry*, vol. 79, no. 23, pp. 9115–9121, 2007.

[60] A. T. Borujeni, N. Lane, K. Thompson, and M. Tyagi, "Effects of image resolution and numerical resolution on computed permeability of consolidated packing using lb and fem pore-scale simulations," *Computers & Fluids*, vol. 88, pp. 753–763, 2013.

[61] A. A. Garrouch, L. Ali, and F. Qasem, "Using diffusion and electrical measurements to assess tortuosity of porous media," *Industrial & engineering chemistry research*, vol. 40, no. 20, pp. 4363–4369, 2001.

[62] A. Weerts, D. Kandhai, W. Bouten, and P. Sloot, "Tortuosity of an unsaturated sandy soil estimated using gas diffusion and bulk soil electrical conductivity: Comparing analogy-based models and lattice–boltzmann simulations," *Soil Science Society of America Journal*, vol. 65, no. 6, pp. 1577–1584, 2001.

[63] D. Kramer, S. A. Freunberger, R. Flückiger, I. A. Schneider, A. Wokaun, F. N. Büchi, and G. G. Scherer, "Electrochemical diffusimetry of fuel cell gas diffusion layers," *Journal of Electroanalytical Chemistry*, vol. 612, no. 1, pp. 63–77, 2008.

[64] W. He, J. Zou, B. Wang, S. Vilayurganapathy, M. Zhou, X. Lin, K. H. Zhang, J. Lin, P. Xu, and J. H. Dickerson, "Gas transport in porous electrodes of solid oxide fuel cells: A review on diffusion and diffusivity measurement," *Journal of Power Sources*, vol. 237, pp. 64–73, 2013.

[65] S. Carniglia, "Construction of the tortuosity factor from porosimetry," *Journal of Catalysis*, vol. 102, no. 2, pp. 401–418, 1986.

[66] K. Yang, M. Li, N. N. Ling, E. F. May, P. R. Connolly, L. Esteban, M. B. Clennell, M. Mahmoud, A. El-Husseiny, A. R. Adebayo, *et al.*, "Quantitative tortuosity measurements of carbonate rocks using pulsed field gradient nmr," *Transport in Porous Media*, vol. 130, no. 3, pp. 847–865, 2019.

[67] V. D. Bruggeman, "Berechnung verschiedener physikalischer konstanten von heterogenen substanzen. i. dielektrizitätskonstanten und leitfähigkeiten der mischkörper aus isotropen substanzen," *Annalen der physik*, vol. 416, no. 7, pp. 636–664, 1935.

[68] G. E. Archie *et al.*, "The electrical resistivity log as an aid in determining some reservoir characteristics," *Transactions of the AIME*, vol. 146, no. 01, pp. 54–62, 1942.

[69] J. Comiti and M. Renaud, "A new model for determining mean structure parameters of fixed beds from pressure drop measurements: Application to beds packed with parallelepipedal particles," *Chemical Engineering Science*, vol. 44, no. 7, pp. 1539–1545, 1989, ISSN: 0009-2509. DOI: https://doi.org/10.1016/0009-2509(89)80031-4. [Online]. Available: https://www.sciencedirect.com/science/article/pii/0009250989800314.

[70] N. Iversen and B. B. Jørgensen, "Diffusion coefficients of sulfate and methane in marine sediments: Influence of porosity," *Geochimica et Cosmochimica Acta*, vol. 57, no. 3, pp. 571–578, 1993.

[71] J. P. Du Plessis and J. H. Masliyah, "Flow through isotropic granular porous media," *Transport in porous media*, vol. 6, no. 3, pp. 207–221, 1991.

[72] P.-Y. Lanfrey, Z. Kuzeljevic, and M. Dudukovic, "Tortuosity model for fixed beds randomly packed with identical particles," *Chemical Engineering Science*, vol. 65, no. 5, pp. 1891–1896, 2010.

[73] B. Ghanbarian, A. G. Hunt, R. P. Ewing, and M. Sahimi, "Tortuosity in porous media: A critical review," *Soil science society of America journal*, vol. 77, no. 5, pp. 1461–1477, 2013.

[74] B. Tjaden, D. J. Brett, and P. R. Shearing, "Tortuosity in electrochemical devices: A review of calculation approaches," *International Materials Reviews*, vol. 63, no. 2, pp. 47–67, 2018.

[75] L. Pisani, "Simple expression for the tortuosity of porous media," *Transport in Porous Media*, vol. 88, no. 2, pp. 193–203, 2011.

[76] D.-W. Chung, M. Ebner, D. R. Ely, V. Wood, and R. E. García, "Validity of the bruggeman relation for porous electrodes," *Modelling and Simulation in Materials Science and Engineering*, vol. 21, no. 7, p. 074 009, 2013.

[77] J. Lai, G. Wang, Z. Wang, J. Chen, X. Pang, S. Wang, Z. Zhou, Z. He, Z. Qin, and X. Fan, "A review on pore structure characterization in tight sandstones," *Earth-Science Reviews*, vol. 177, pp. 436–457, 2018.

[78] S. Schlüter, A. Sheppard, K. Brown, and D. Wildenschild, "Image processing of multiphase images obtained via x-ray microtomography: A review," *Water Resources Research*, vol. 50, no. 4, pp. 3615–3639, 2014.

[79] P. R. Munroe, "The application of focused ion beam microscopy in the material sciences," *Materials characterization*, vol. 60, no. 1, pp. 2–13, 2009.

[80] P. Stutzman, "Scanning electron microscopy imaging of hydraulic cement microstructure," *Cement and Concrete Composites*, vol. 26, no. 8, pp. 957–966, 2004.

[81] S. Ringer and K. Hono, "Microstructural evolution and age hardening in aluminium alloys: Atom probe field-ion microscopy and transmission electron microscopy studies," *Materials characterization*, vol. 44, no. 1-2, pp. 101–131, 2000.

[82] F. Javadpour *et al.*, "Nanopores and apparent permeability of gas flow in mudrocks (shales and siltstone)," *Journal of Canadian Petroleum Technology*, vol. 48, no. 08, pp. 16–21, 2009.

[83] L. M. Anovitz and D. R. Cole, "Characterization and analysis of porosity and pore structures," *Reviews in Mineralogy and geochemistry*, vol. 80, no. 1, pp. 61–164, 2015.

[84] P. Adler, *Porous media: geometry and transports*. Elsevier, 2013.

[85] J. Thovert, J. Salles, and P. Adler, "Computerized characterization of the geometry of real porous media: Their discretization, analysis and interpretation," *Journal of microscopy*, vol. 170, no. 1, pp. 65–79, 1993.

[86] C. J. Gommes, A.-J. Bons, S. Blacher, J. H. Dunsmuir, and A. H. Tsou, "Practical methods for measuring the tortuosity of porous materials from binary or gray-tone tomographic reconstructions," *AIChE Journal*, vol. 55, no. 8, pp. 2000–2012, 2009.

[87] A. Cecen, E. Wargo, A. Hanna, D. Turner, S. Kalidindi, and E. Kumbur, "3-d microstructure analysis of fuel cell materials: Spatial distributions of tortuosity, void size and diffusivity," *Journal of The Electrochemical Society*, vol. 159, no. 3, B299, 2012.

[88] E. Wargo, T. Kotaka, Y. Tabuchi, and E. Kumbur, "Comparison of focused ion beam versus nano-scale x-ray computed tomography for resolving 3-d microstructures of porous fuel cell materials," *Journal of Power Sources*, vol. 241, pp. 608–618, 2013.

[89] S. Litster, W. Epting, E. Wargo, S. Kalidindi, and E. Kumbur, "Morphological analyses of polymer electrolyte fuel cell electrodes with nano-scale computed tomography imaging," *Fuel Cells*, vol. 13, no. 5, pp. 935–945, 2013.

[90] O. Stenzel, O. Pecho, L. Holzer, M. Neumann, and V. Schmidt, "Predicting effective conductivities based on geometric microstructure characteristics," *AIChE Journal*, vol. 62, no. 5, pp. 1834–1843, 2016.

[91] Y. San Wu, L. J. van Vliet, H. W. Frijlink, and K. van der Voort Maarschalk, "The determination of relative path length as a measure for tortuosity in compacts using image analysis," *european journal of pharmaceutical sciences*, vol. 28, no. 5, pp. 433–440, 2006.

[92] J. Montes, F. Cuevas, and J. Cintas, "Electrical and thermal tortuosity in powder compacts," *Granular Matter*, vol. 9, no. 6, pp. 401–406, 2007.

[93] W. B. Lindquist, S.-M. Lee, D. A. Coker, K. W. Jones, and P. Spanne, "Medial axis analysis of void structure in three-dimensional tomographic images of porous media," *Journal of Geophysical Research: Solid Earth*, vol. 101, no. B4, pp. 8297–8310, 1996.

[94] M. Axelsson and S. Svensson, "3d pore structure characterisation of paper," *Pattern Analysis and Applications*, vol. 13, no. 2, pp. 159–172, 2010.

[95] W. C. Sun, J. E. Andrade, and J. W. Rudnicki, "Multiscale method for characterization of porous microstructures and their impact on macroscopic effective permeability," *International Journal for Numerical Methods in Engineering*, vol. 88, no. 12, pp. 1260–1279, 2011.

[96] N. O. Shanti, V. W. Chan, S. R. Stock, F. De Carlo, K. Thornton, and K. T. Faber, "X-ray micro-computed tomography and tortuosity calculations of percolating pore networks," *Acta Materialia*, vol. 71, pp. 126–135, 2014.

[97] R. I. Al-Raoush and I. T. Madhoun, "Tort3d: A matlab code to compute geometric tortuosity from 3d images of unconsolidated porous media," *Powder technology*, vol. 320, pp. 99–107, 2017.

[98] E. Brun, J. Vicente, F. Topin, and R. Occelli, "Imorph: A 3d morphological tool to fully analyse all kind of cellular materials," *Cellular Metals for Structural and Functional Applications*, 2008.

[99] P. S. Jørgensen, K. V. Hansen, R. Larsen, and J. R. Bowen, "Geometrical characterization of interconnected phase networks in three dimensions," *Journal of microscopy*, vol. 244, no. 1, pp. 45–58, 2011.

[100] S. Pardo-Alonso, J. Vicente, E. Solórzano, M. Á. Rodriguez-Perez, and D. Lehmhus, "Geometrical tortuosity 3d calculations in infiltrated aluminium cellular materials," *Procedia Materials Science*, vol. 4, pp. 145–150, 2014.

[101] Y.-c. K. Chen-Wiegart, R. DeMike, C. Erdonmez, K. Thornton, S. A. Barnett, and J. Wang, "Tortuosity characterization of 3d microstructure at nano-scale for energy storage and conversion materials," *Journal of Power Sources*, vol. 249, pp. 349–356, 2014.

[102] O. O. Taiwo, D. P. Finegan, D. S. Eastwood, J. L. Fife, L. D. Brown, J. A. Darr, P. D. Lee, D. J. Brett, and P. R. Shearing, "Comparison of three-dimensional analysis and stereological techniques for quantifying lithium-ion battery electrode microstructures," *Journal of microscopy*, vol. 263, no. 3, pp. 280–292, 2016.

[103] D. Gostovic, z. J. Smith, D. Kundinger, K. Jones, and E. Wachsman, "Three-dimensional reconstruction of porous lscf cathodes," *Electrochemical and Solid State Letters*, vol. 10, no. 12, B214, 2007.

[104] J. Desrues, G. Viggiani, and P. Besuelle, *Advances in X-ray Tomography for Geomaterials*. John Wiley & Sons, 2010, vol. 118.

[105] P. R. Shearing, N. Brandon, J. Gelb, R. Bradley, P. Withers, A. Marquis, S. Cooper, and S. Harris, "Multi length scale microstructural investigations of a commercially available li-ion battery electrode," *Journal of The Electrochemical Society*, vol. 159, no. 7, A1023–A1027, 2012.

[106] Ł. D. Kaczmarek, Y. Zhao, H. Konietzky, T. Wejrzanowski, and M. Maksimczuk, "Numerical approach in recognition of selected features of rock structure from hybrid hydrocarbon reservoir samples based on microtomography," *Studia Geotechnica et Mechanica*, vol. 39, no. 1, pp. 13–26, 2017.

[107] W. Sobieski, M. Matyka, J. Gołembiewski, and S. Lipiński, "The path tracking method as an alternative for tortuosity determination in granular beds," *Granular Matter*, vol. 20, no. 4, p. 72, 2018.

[108] R. Lemaitre and P. Adler, "Fractal porous media iv: Three-dimensional stokes flow through random media and regular fractals," *Transport in Porous Media*, vol. 5, no. 4, pp. 325–340, 1990.

[109] S. Cooper, A. Bertei, P. Shearing, J. Kilner, and N. Brandon, "Taufactor: An open-source application for calculating tortuosity factors from tomographic data," *SoftwareX*, vol. 5, pp. 203–210, 2016.

[110] J. R. Wilson, W. Kobsiriphat, R. Mendoza, H.-Y. Chen, J. M. Hiller, D. J. Miller, K. Thornton, P. W. Voorhees, S. B. Adler, and S. A. Barnett, "Three-dimensional reconstruction of a solid-oxide fuel-cell anode," *Nature materials*, vol. 5, no. 7, pp. 541–544, 2006.

[111] A. G. Kashkooli, S. Farhad, D. U. Lee, K. Feng, S. Litster, S. K. Babu, L. Zhu, and Z. Chen, "Multiscale modeling of lithium-ion battery electrodes based on nano-scale x-ray computed tomography," *Journal of Power Sources*, vol. 307, pp. 496–509, 2016.

[112] T. Hutzenlaub, A. Asthana, J. Becker, D. Wheeler, R. Zengerle, and S. Thiele, "Fib/sem-based calculation of tortuosity in a porous licoo2 cathode for a li-ion battery," *Electrochemistry Communications*, vol. 27, pp. 77–80, 2013.

[113] S. Peng, F. Marone, and S. Dultz, "Resolution effect in x-ray microcomputed tomography imaging and small pore's contribution to permeability for a berea sandstone," *Journal of hydrology*, vol. 510, pp. 403–411, 2014.

[114] D. P. Finegan, S. J. Cooper, B. Tjaden, O. O. Taiwo, J. Gelb, G. Hinds, D. J. Brett, and P. R. Shearing, "Characterising the structural properties of polymer separators for lithium-ion batteries in 3d using phase contrast x-ray microscopy," *Journal of Power Sources*, vol. 333, pp. 184–192, 2016.

[115] N. R. Backeberg, F. Iacoviello, M. Rittner, T. M. Mitchell, A. P. Jones, R. Day, J. Wheeler, P. R. Shearing, P. Vermeesch, and A. Striolo, "Quantifying the anisotropy and tortuosity of permeable pathways in clay-rich mudstones using models based on x-ray tomography," *Scientific Reports*, vol. 7, no. 1, pp. 1–12, 2017.

[116] H. Iwai, N. Shikazono, T. Matsui, H. Teshima, M. Kishimoto, R. Kishida, D. Hayashi, K. Matsuzaki, D. Kanno, M. Saito, *et al.*, "Quantification of sofc anode microstructure based on dual beam fib-sem technique," *Journal of Power Sources*, vol. 195, no. 4, pp. 955–961, 2010.

[117] H. Ostadi, P. Rama, Y. Liu, R. Chen, X. Zhang, and K. Jiang, "3d reconstruction of a gas diffusion layer and a microporous layer," *Journal of Membrane Science*, vol. 351, no. 1-2, pp. 69–74, 2010.

[118] Y. Nakashima and Y. Watanabe, "Estimate of transport properties of porous media by microfocus x-ray computed tomography and random walk simulation," *Water Resources Research*, vol. 38, no. 12, pp. 8–1, 2002.

[119] Y. Nakashima and S. Kamiya, "Mathematica programs for the analysis of three-dimensional pore connectivity and anisotropic tortuosity of porous rocks using x-ray computed tomography image data," *Journal of Nuclear Science and Technology*, vol. 44, no. 9, pp. 1233–1247, 2007.

[120] M. Kishimoto, H. Iwai, K. Miyawaki, M. Saito, and H. Yoshida, "Improvement of the sub-grid-scale model designed for 3d numerical simulation of solid oxide fuel cell electrodes using an adaptive power index," *Journal of power sources*, vol. 223, pp. 268–276, 2013.

[121] T. Tranter, M. Kok, M. Lam, and J. Gostick, "Pytrax: A simple and efficient random walk implementation for calculating the directional tortuosity of images," *SoftwareX*, vol. 10, p. 100 277, 2019.

[122] R. B. Bird, "Transport phenomena," *Appl. Mech. Rev.*, vol. 55, no. 1, R1–R4, 2002.

[123] P. Pietsch and V. Wood, "X-ray tomography for lithium ion battery research: A practical guide," *Annual Review of Materials Research*, vol. 47, pp. 451–479, 2017.

[124] P. Shearing, L. Howard, P. S. Jørgensen, N. Brandon, and S. Harris, "Characterization of the 3-dimensional microstructure of a graphite negative electrode from a li-ion battery," *Electrochemistry communications*, vol. 12, no. 3, pp. 374–377, 2010.

[125] M. Ojha, J. Le Houx, R. Mukkabla, D. Kramer, R. G. A. Wills, and M. Deepa, "Lithium titanate/pyrenecarboxylic acid decorated carbon nanotubes hybrid-alginate gel supercapacitor," *Electrochimica Acta*, vol. 309, pp. 253–263, 2019.

[126] C. Ziegler, S. Thiele, and R. Zengerle, "Direct three-dimensional reconstruction of a nanoporous catalyst layer for a polymer electrolyte fuel cell," *Journal of Power Sources*, vol. 196, no. 4, pp. 2094–2097, 2011.

[127] H. Ostadi, M. Malboubi, P. Prewett, and K. Jiang, "3d reconstruction of a micro pipette tip," *Microelectronic engineering*, vol. 86, no. 4-6, pp. 868–870, 2009.

[128] P. Sedigh Rahimabadi, M. Khodaei, and K. R. Koswattage, "Review on applications of synchrotron-based x-ray techniques in materials characterization," *X-Ray Spectrometry*, vol. 49, no. 3, pp. 348–373, 2020.

[129] V. Cnudde and M. N. Boone, "High-resolution x-ray computed tomography in geosciences: A review of the current technology and applications," *Earth-Science Reviews*, vol. 123, pp. 1–17, 2013.

[130] J. Le Houx, M. Osenberg, M. Neumann, J. R. Binder, V. Schmidt, I. Manke, T. Carraro, and D. Kramer, "Effect of tomography resolution on calculation of microstructural properties for lithium ion porous electrodes," *ECS Transactions*, vol. 97, no. 7, p. 255, 2020.

[131] C.-W. Wang and A. M. Sastry, "Mesoscale modeling of a li-ion polymer cell," *Journal of the Electrochemical Society*, vol. 154, no. 11, A1035–A1047, 2007.

[132] G. B. Less, J. H. Seo, S. Han, A. M. Sastry, J. Zausch, A. Latz, S. Schmidt, C. Wieser, D. Kehrwald, and S. Fell, "Micro-scale modeling of li-ion batteries: Parameterization and validation," *Journal of The Electrochemical Society*, vol. 159, no. 6, A697–A704, 2012.

[133] D. Kehrwald, P. R. Shearing, N. P. Brandon, P. K. Sinha, and S. J. Harris, "Local tortuosity inhomogeneities in a lithium battery composite electrode," *Journal of The Electrochemical Society*, vol. 158, no. 12, A1393–A1399, 2011.

[134] M. Ebner, F. Marone, M. Stampanoni, and V. Wood, "Visualization and quantification of electrochemical and mechanical degradation in li ion batteries," *Science*, vol. 342, no. 6159, pp. 716–720, 2013.

[135] C. Lim, B. Yan, L. Yin, and L. Zhu, "Simulation of diffusion-induced stress using reconstructed electrodes particle structures generated by micro/nano-ct," *Electrochimica Acta*, vol. 75, pp. 279–287, 2012.

[136] B. Yan, C. Lim, L. Yin, and L. Zhu, "Three dimensional simulation of galvanostatic discharge of licoo2 cathode based on x-ray nano-ct images," *Journal of The Electrochemical Society*, vol. 159, no. 10, A1604–A1614, 2012.

[137] B. Yan, C. Lim, and L. Yin, "Simulation of heat generation in a reconstructed licoo2 cathode during galvanostatic discharge," *Electrochimica Acta*, vol. 100, pp. 171–179, 2013.

[138] V. Wood, "X-ray tomography for battery research and development," *Nature Reviews Materials*, vol. 3, no. 9, pp. 293–295, 2018.

[139] F. Sun, X. He, X. Jiang, M. Osenberg, J. Li, D. Zhou, K. Dong, A. Hilger, X. Zhu, R. Gao, *et al.*, "Advancing knowledge of electrochemically generated lithium microstructure and performance decay of lithium ion battery by synchrotron x-ray tomography," *Materials today*, vol. 27, pp. 21–32, 2019.

[140] T.-T. Nguyen, A. Demortière, B. Fleutot, B. Delobel, C. Delacourt, and S. J. Cooper, "The electrode tortuosity factor: why the conventional tortuosity factor is not well suited for quantifying transport in porous Li-ion battery electrodes and

what to use instead," *npj Computational Materials*, vol. 6, no. 1, Aug. 2020. DOI: 10.1038/s41524-020-00386-4. [Online]. Available: https://doi.org/10.1038%2Fs41524-020-00386-4.

[141] L. Shen and Z. Chen, "Critical review of the impact of tortuosity on diffusion," *Chemical Engineering Science*, vol. 62, no. 14, pp. 3748–3755, 2007.

[142] C. Kalyvas, "The impact of diffusion on solid oxide fuel cell anode performance," *Imperial College*, 2004.

[143] J. Conder, C. Marino, P. Novák, and C. Villevieille, "Do imaging techniques add real value to the development of better post-li-ion batteries?" *Journal of Materials Chemistry A*, vol. 6, no. 8, pp. 3304–3327, 2018.

[144] S. R. Daemi, C. Tan, T. Volkenandt, S. J. Cooper, A. Palacios-Padros, J. Cookson, D. J. Brett, and P. R. Shearing, "Visualizing the carbon binder phase of battery electrodes in three dimensions," *ACS Applied Energy Materials*, vol. 1, no. 8, pp. 3702–3710, 2018.

[145] D. S. Eastwood, P. M. Bayley, H. J. Chang, O. O. Taiwo, J. Vila-Comamala, D. J. Brett, C. Rau, P. J. Withers, P. R. Shearing, C. P. Grey, *et al.*, "Three-dimensional characterization of electrodeposited lithium microstructures using synchrotron x-ray phase contrast imaging," *Chemical communications*, vol. 51, no. 2, pp. 266–268, 2015.

[146] V. Vanpeene, A. Etiemble, A. Bonnin, E. Maire, and L. Roué, "In-situ x-ray tomographic study of the morphological changes of a si/c paper anode for li-ion batteries," *Journal of Power Sources*, vol. 350, pp. 18–27, 2017.

[147] S. J. Cooper, M. Kishimoto, F. Tariq, R. S. Bradley, A. J. Marquis, N. P. Brandon, J. A. Kilner, and P. R. Shearing, "Microstructural analysis of an lscf cathode using in situ tomography and simulation," *ECS Transactions*, vol. 57, no. 1, pp. 2671–2678, 2013.

[148] S.-M. Bak, Z. Shadike, R. Lin, X. Yu, and X.-Q. Yang, "In situ/operando synchrotron-based x-ray techniques for lithium-ion battery research," *NPG Asia Materials*, vol. 10, no. 7, pp. 563–580, 2018.

[149] D. P. Finegan, M. Scheel, J. B. Robinson, B. Tjaden, M. Di Michiel, G. Hinds, D. J. Brett, and P. R. Shearing, "Investigating lithium-ion battery materials during overcharge-induced thermal runaway: An operando and multi-scale x-ray ct study," *Physical Chemistry Chemical Physics*, vol. 18, no. 45, pp. 30 912–30 919, 2016.

[150] D. P. Finegan, M. Scheel, J. B. Robinson, B. Tjaden, I. Hunt, T. J. Mason, J. Millichamp, M. Di Michiel, G. J. Offer, G. Hinds, *et al.*, "In-operando high-speed tomography of lithium-ion batteries during thermal runaway," *Nature communications*, vol. 6, no. 1, pp. 1–10, 2015.

[151] D. P. Finegan, E. Darcy, M. Keyser, B. Tjaden, T. M. Heenan, R. Jervis, J. J. Bailey, R. Malik, N. T. Vo, O. V. Magdysyuk, *et al.*, "Characterising thermal runaway within lithium-ion cells by inducing and monitoring internal short circuits," *Energy & Environmental Science*, vol. 10, no. 6, pp. 1377–1388, 2017.

[152] D. P. Finegan, E. Darcy, M. Keyser, B. Tjaden, T. M. Heenan, R. Jervis, J. J. Bailey, N. T. Vo, O. V. Magdysyuk, M. Drakopoulos, *et al.*, "Identifying the cause of rupture of li-ion batteries during thermal runaway," *Advanced Science*, vol. 5, no. 1, p. 1 700 369, 2018.

[153] S. Müller, M. Lippuner, M. Verezhak, V. De Andrade, F. De Carlo, and V. Wood, "Multimodal nanoscale tomographic imaging for battery electrodes," *Advanced Energy Materials*, p. 1 904 119, 2020.

[154] F. Pfeiffer, "X-ray ptychography," *Nature Photonics*, vol. 12, no. 1, pp. 9–17, 2018.

[155] J. M. Rodenburg, "Ptychography and related diffractive imaging methods," *Advances in imaging and electron physics*, vol. 150, pp. 87–184, 2008.

[156] S. Latham, T. Varslot, A. Sheppard, *et al.*, "Image registration: Enhancing and calibrating x-ray micro-ct imaging," *Proc. of the Soc. Core Analysts, Abu Dhabi, UAE*, pp. 1–12, 2008.

[157] R. F. Ziesche, T. Arlt, D. P. Finegan, T. M. Heenan, A. Tengattini, D. Baum, N. Kardjilov, H. Markötter, I. Manke, W. Kockelmann, *et al.*, "4d imaging of lithium-batteries using correlative neutron and x-ray tomography with a virtual unrolling technique," *Nature communications*, vol. 11, no. 1, pp. 1–11, 2020.

[158] N. Kardjilov, I. Manke, A. Hilger, M. Strobl, and J. Banhart, "Neutron imaging in materials science," *Materials Today*, vol. 14, no. 6, pp. 248–256, 2011.

[159] I. S. Anderson, R. L. McGreevy, and H. Z. Bilheux, "Neutron imaging and applications," *Springer Science+ Business Media, LLC*, vol. 2209, pp. 987–, 2009.

[160] J. B. Siegel, X. Lin, A. G. Stefanopoulou, D. S. Hussey, D. L. Jacobson, and D. Gorsich, "Neutron imaging of lithium concentration in lfp pouch cell battery," *Journal of the Electrochemical Society*, vol. 158, no. 5, A523, 2011.

[161] X. Lu, A. Bertei, D. P. Finegan, C. Tan, S. R. Daemi, J. S. Weaving, K. B. O'Regan, T. M. Heenan, G. Hinds, E. Kendrick, *et al.*, "3d microstructure design of lithium-ion battery electrodes assisted by x-ray nano-computed tomography and modelling," *Nature Communications*, vol. 11, no. 1, pp. 1–13, 2020.

[162] J.-W. Buurlage, F. Marone, D. M. Pelt, W. J. Palenstijn, M. Stampanoni, K. J. Batenburg, and C. M. Schlepütz, "Real-time reconstruction and visualisation towards dynamic feedback control during time-resolved tomography experiments at tomcat," *Scientific Reports*, vol. 9, no. 1, pp. 1–11, 2019.

[163] A. A. Franco, "Multiscale modelling and numerical simulation of rechargeable lithium ion batteries: Concepts, methods and challenges," *Rsc Advances*, vol. 3, no. 32, pp. 13 027–13 058, 2013.

[164] A. Jokar, B. Rajabloo, M. Désilets, and M. Lacroix, "Review of simplified pseudo-two-dimensional models of lithium-ion batteries," *Journal of Power Sources*, vol. 327, pp. 44–55, 2016.

[165] J. Le Houx and D. Kramer, "Physics based modelling of porous lithium ion battery electrodes—a review," *Energy Reports*, vol. 6, pp. 1–9, 2020.

[166] J. Newman and W. Tiedemann, "Porous-electrode theory with battery applications," *AIChE Journal*, vol. 21, no. 1, pp. 25–41, 1975.

[167] V. Chabot, S. Farhad, Z. Chen, A. S. Fung, A. Yu, and F. Hamdullahpur, "Effect of electrode physical and chemical properties on lithium-ion battery performance," *International Journal of Energy Research*, vol. 37, no. 14, pp. 1723–1736, 2013.

[168] A. Gupta, J. H. Seo, X. Zhang, W. Du, A. M. Sastry, and W. Shyy, "Effective transport properties of limn2o4 electrode via particle-scale modeling," *Journal of The Electrochemical Society*, vol. 158, no. 5, A487–A497, 2011.

[169] H. A. Lorentz, "Ueber die beziehung zwischen der fortpflanzungsgeschwindigkeit des lichtes und der körperdichte," *Annalen der Physik*, vol. 245, no. 4, pp. 641–665, 1880.

[170] L. Lorenz, "Ueber die refractionsconstante," *Annalen der Physik*, vol. 247, no. 9, pp. 70–103, 1880.

[171] B. Tjaden, S. J. Cooper, D. J. Brett, D. Kramer, and P. R. Shearing, "On the origin and application of the bruggeman correlation for analysing transport phenomena in electrochemical systems," *Current Opinion in Chemical Engineering*, vol. 12, pp. 44–51, 2016.

[172] N. Epstein, "On tortuosity and the tortuosity factor in flow and diffusion through porous media," *Chemical engineering science*, vol. 44, no. 3, pp. 777–779, 1989.

[173] O. Wiener, "Die theorie des mischkorpers fur das feld der stationaren stromung," *Abhandlungen der Sachsischen Gesellschaft der Akademischen Wissenschaften in Mathematik und Physik*, vol. 32, pp. 507–604, 1912.

[174] G. Richardson, G. Denuault, and C. Please, "Multiscale modelling and analysis of lithium-ion battery charge and discharge," *Journal of Engineering Mathematics*, vol. 72, no. 1, pp. 41–72, 2012.

[175] M. Landstorfer and T. Jacob, "Mathematical modeling of intercalation batteries at the cell level and beyond," *Chemical Society Reviews*, vol. 42, no. 8, pp. 3234–3252, 2013.

[176] M. Landstorfer, "Boundary conditions for electrochemical interfaces," *Journal of The Electrochemical Society*, vol. 164, no. 11, E3671–E3685, 2017.

[177] A. Gully, H. Liu, S. Srinivasan, A. Sethurajan, S. Schougaard, and B. Protas, "Effective transport properties of porous electrochemical materials—a homogenization approach," *Journal of The Electrochemical Society*, vol. 161, no. 8, E3066–E3077, 2014.

[178] U. Hornung, *Homogenization and porous media*. Springer Science & Business Media, 1996, vol. 6.

[179] M. M. Dias and A. C. Payatakes, "Network models for two-phase flow in porous media part 1. immiscible microdisplacement of non-wetting fluids," *Journal of Fluid Mechanics*, vol. 164, pp. 305–336, 1986.

[180] H. Dong and M. J. Blunt, "Pore-network extraction from micro-computerized-tomography images," *Physical review E*, vol. 80, no. 3, p. 036 307, 2009.

[181] J. Hinebaugh, Z. Fishman, and A. Bazylak, "Unstructured pore network modeling with heterogeneous pemfc gdl porosity distributions," *Journal of The Electrochemical Society*, vol. 157, no. 11, B1651, 2010.

[182] M. J. Blunt, B. Bijeljic, H. Dong, O. Gharbi, S. Iglauer, P. Mostaghimi, A. Paluszny, and C. Pentland, "Pore-scale imaging and modelling," *Advances in Water resources*, vol. 51, pp. 197–216, 2013.

[183] J. Gostick, M. Aghighi, J. Hinebaugh, T. Tranter, M. A. Hoeh, H. Day, B. Spellacy, M. H. Sharqawy, A. Bazylak, A. Burns, *et al.*, "Openpnm: A pore network modeling package," *Computing in Science & Engineering*, vol. 18, no. 4, pp. 60–74, 2016.

[184] Y.-H. Tseng and J. H. Ferziger, "A ghost-cell immersed boundary method for flow in complex geometry," *Journal of computational physics*, vol. 192, no. 2, pp. 593–623, 2003.

[185] T. Allahviranloo, "Successive over relaxation iterative method for fuzzy system of linear equations," *Applied mathematics and computation*, vol. 162, no. 1, pp. 189–196, 2005.

[186] B. Vijayaraghavan, D. R. Ely, Y.-M. Chiang, R. Garcia-Garcia, and R. E. Garcia, "An analytical method to determine tortuosity in rechargeable battery electrodes," *Journal of The Electrochemical Society*, vol. 159, no. 5, A548, 2012.

[187] D.-W. Chung, P. R. Shearing, N. P. Brandon, S. J. Harris, and R. E. García, "Particle size polydispersity in li-ion batteries," *Journal of The Electrochemical Society*, vol. 161, no. 3, A422–A430, 2014.

[188] M. Ebner and V. Wood, "Tool for tortuosity estimation in lithium ion battery porous electrodes," *Journal of The Electrochemical Society*, vol. 162, no. 2, A3064, 2014.

[189] D. Mohanty, E. Hockaday, J. Li, D. Hensley, C. Daniel, and D. Wood III, "Effect of electrode manufacturing defects on electrochemical performance of lithium-ion batteries: Cognizance of the battery failure sources," *Journal of Power Sources*, vol. 312, pp. 70–79, 2016.

[190] C. Huang and P. S. Grant, "Coral-like directional porosity lithium ion battery cathodes by ice templating," *Journal of Materials Chemistry A*, vol. 6, no. 30, pp. 14 689–14 699, 2018.

[191] M. Green, E. Fielder, B. Scrosati, M. Wachtler, and J. S. Moreno, "Structured silicon anodes for lithium battery applications," *Electrochemical and Solid State Letters*, vol. 6, no. 5, A75, 2003.

[192] Q. Xiong, T. G. Baychev, and A. P. Jivkov, "Review of pore network modelling of porous media: Experimental characterisations network constructions and applications to reactive transport," *Journal of Contaminant Hydrology*, vol. 192, pp. 101–117, Sep. 2016. DOI: 10.1016/j.jconhyd.2016.07.002. [Online]. Available: https://doi.org/10.1016%2Fj.jconhyd.2016.07.002.

[193] J. I. Goldstein, D. E. Newbury, J. R. Michael, N. W. Ritchie, J. H. J. Scott, and D. C. Joy, *Scanning electron microscopy and X-ray microanalysis*. Springer, 2017.

[194] D. Chen, S. Indris, M. Schulz, B. Gamer, and R. Monig, "In situ scanning electron microscopy on lithium-ion battery electrodes using an ionic liquid," *Journal of Power Sources*, vol. 196, no. 15, pp. 6382–6387, 2011.

[195] D. J. Miller, C. Proff, J. Wen, D. P. Abraham, and J. Bareno, "Observation of microstructural evolution in li battery cathode oxide particles by in situ electron microscopy," *Advanced Energy Materials*, vol. 3, no. 8, pp. 1098–1103, 2013.

[196] C.-Y. Chen, T. Sano, T. Tsuda, K. Ui, Y. Oshima, M. Yamagata, M. Ishikawa, M. Haruta, T. Doi, M. Inaba, *et al.*, "In situ scanning electron microscopy of silicon anode reactions in lithium-ion batteries during charge/discharge processes," *Scientific reports*, vol. 6, no. 1, pp. 1–9, 2016.

[197] D. B. Williams and C. B. Carter, "The transmission electron microscope," in *Transmission electron microscopy*, Springer, 1996, pp. 3–17.

[198] L. A. Giannuzzi *et al.*, *Introduction to focused ion beams: instrumentation, theory, techniques and practice*. Springer Science & Business Media, 2004.

[199] American Society for Testing and Materials, *ASTM 1441: Standard Guide for Computed Tomography (CT)*. ASTM International, 2005.

[200] G. F. Knoll, *Radiation detection and measurement*. John Wiley & Sons, 2010.

[201] J. Hsieh, *Computed tomography: principles, design, artifacts, and recent advances*. SPIE press, 2003, vol. 114.

[202] A. C. Kak, M. Slaney, and G. Wang, "Principles of computerized tomographic imaging," *Medical Physics*, vol. 29, no. 1, pp. 107–107, 2002.

[203] J. Rueckel, M. Stockmar, F. Pfeiffer, and J. Herzen, "Spatial resolution characterization of a x-ray microct system," *Applied Radiation and Isotopes*, vol. 94, pp. 230–234, 2014.

[204] P. M. Joseph and R. D. Spital, "The effects of scatter in x-ray computed tomography," *Medical physics*, vol. 9, no. 4, pp. 464–472, 1982.

[205] G. Davis and J. Elliott, "Artefacts in x-ray microtomography of materials," *Materials science and technology*, vol. 22, no. 9, pp. 1011–1018, 2006.

[206] A. Britten, M. Crotty, H. Kiremidjian, A. Grundy, and E. Adam, "The addition of computer simulated noise to investigate radiation dose and image quality in images with spatial correlation of statistical noise: An example application to x-ray ct of the brain," *The British journal of radiology*, vol. 77, no. 916, pp. 323–328, 2004.

[207] B. De Man, J. Nuyts, P. Dupont, G. Marchal, and P. Suetens, "Metal streak artifacts in x-ray computed tomography: A simulation study," *IEEE Transactions on Nuclear Science*, vol. 46, no. 3, pp. 691–696, 1999.

[208] J. Miles, M. Mavrogordato, I. Sinclair, D. Hinton, R. Boardman, and G. Earl, "The use of computed tomography for the study of archaeological coins," *Journal of Archaeological Science: Reports*, vol. 6, pp. 35–41, 2016.

[209] F. Leonard, S. Tammas-Williams, P. B. Prangnell, I. Todd, and P. J. Withers, "Assessment by x-ray ct of the effects of geometry and build direction on defects in titanium alm parts," in *Conference on industrial computed tomography (iCT)*, 2012, pp. 19–21.

[210] P. Shearing, R. Bradley, J. Gelb, S. Lee, A. Atkinson, P. Withers, and N. Brandon, "Using synchrotron x-ray nano-ct to characterize sofc electrode microstructures in three-dimensions at operating temperature," *Electrochemical and Solid State Letters*, vol. 14, no. 10, B117, 2011.

[211] R. A. Ketcham and J. Hildebrandt, "Characterizing, measuring, and utilizing the resolution of ct imagery for improved quantification of fine-scale features," *Nuclear Instruments and Methods in Physics Research Section B: Beam Interactions with Materials and Atoms*, vol. 324, pp. 80–87, 2014.

[212] American Society for Testing and Materials, *ASTM 1695: Standard Test Method for Measurement of Computed Tomography (CT) System Performance*. ASTM International, 2006.

[213] M. Maga, J. Kappelman, T. M. Ryan, and R. A. Ketcham, "Preliminary observations on the calcaneal trabecular microarchitecture of extant large-bodied hominoids," *American Journal of Physical Anthropology: The Official Publication of the American Association of Physical Anthropologists*, vol. 129, no. 3, pp. 410–417, 2006.

[214] R. A. Ketcham, D. T. Slottke, and J. M. Sharp Jr, "Three-dimensional measurement of fractures in heterogeneous materials using high-resolution x-ray computed tomography," *Geosphere*, vol. 6, no. 5, pp. 499–514, 2010.

[215] R. A. Ketcham, "Accurate three-dimensional measurements of features in geological materials from x-ray computed tomography data," *Advances in X-ray tomography for geomaterials*, pp. 143–148, 2006.

[216] R. A. Johns, J. S. Steude, L. M. Castanier, and P. V. Roberts, "Nondestructive measurements of fracture aperture in crystalline rock cores using x ray computed tomography," *Journal of Geophysical Research: Solid Earth*, vol. 98, no. B2, pp. 1889–1900, 1993.

[217] M. Van Geet and R. Swennen, "Quantitative 3d-fracture analysis by means of microfocus x-ray computer tomography (micro-ct): An example from coal," *Geophysical Research Letters*, vol. 28, no. 17, pp. 3333–3336, 2001.

[218] S. Wolter, A. Loschberger, T. Holm, S. Aufmkolk, M.-C. Dabauvalle, S. Van De Linde, and M. Sauer, "Rapi d storm: Accurate, fast open-source software for localization microscopy," *Nature methods*, vol. 9, no. 11, pp. 1040–1041, 2012.

[219] D. Sage, L. Donati, F. Soulez, D. Fortun, G. Schmit, A. Seitz, R. Guiet, C. Vonesch, and M. Unser, "Deconvolutionlab2: An open-source software for deconvolution microscopy," *Methods*, vol. 115, pp. 28–41, 2017.

[220] R. Hill, "Elastic properties of reinforced solids: Some theoretical principles," *Journal of the Mechanics and Physics of Solids*, vol. 11, no. 5, pp. 357–372, 1963.

[221] B. Jones and Y. Feng, "Effect of image scaling and segmentation in digital rock characterisation," *Computational Particle Mechanics*, vol. 3, no. 2, pp. 201–213, 2016.

[222] I. Arganda-Carreras, V. Kaynig, C. Rueden, K. W. Eliceiri, J. Schindelin, A. Cardona, and H. Sebastian Seung, "Trainable weka segmentation: A machine learning tool for microscopy pixel classification," *Bioinformatics*, vol. 33, no. 15, pp. 2424–2426, 2017.

[223] Mu-Vis. (2019). "Zeiss 160 kvp versa 510," [Online]. Available: https://www.southampton.ac.uk/muvis/about/equipment/versa.page (visited on 03/30/2019).

[224] G. Dhatt, E. LefranÃ, G. Touzot, *et al.*, *Finite element method*. John Wiley & Sons, 2012.

[225] N. Ottosen, H. Petersson, and N. Saabye, "Introduction to the finite element method, 1992," *Dorchester, UK: Prentice Hall Europe*,

[226] O. A. Ladyzhenskaya, "The method of finite differences," in *The Boundary Value Problems of Mathematical Physics*, Springer, 1985, pp. 212–307.

[227] P. Colella, D. Graves, T. Ligocki, D. Martin, D. Modiano, D. Serafini, and B. Van Straalen, "Chombo software package for amr applications design document," *Chombo*, 2009.

[228] P. Colella, "Ebchombo software package for cartesian grid, embedded boundary applications," *Chombo*, 2014.

[229] M. Kupiainen and B. Sjögreen, "A cartesian embedded boundary method for the compressible navier-stokes equations," *Journal of Scientific Computing*, vol. 41, no. 1, pp. 94–117, 2009.

[230] R. Gladstone, V. Lee, A. Vieli, and A. Payne, "Grounding line migration in an adaptive mesh ice sheet model," *Journal of Geophysical Research: Earth Surface*, vol. 115, no. F4, 2010.

[231] D. Trebotich, M. F. Adams, S. Molins, C. I. Steefel, and C. Shen, "High-resolution simulation of pore-scale reactive transport processes associated with carbon sequestration," *Computing in Science & Engineering*, vol. 16, no. 6, pp. 22–31, 2014.

[232] K. Bergman, S. Borkar, D. Campbell, W. Carlson, W. Dally, M. Denneau, P. Franzon, W. Harrod, K. Hill, J. Hiller, *et al.*, "Exascale computing study: Technology challenges in achieving exascale systems," *Defense Advanced Research Projects Agency Information Processing Techniques Office (DARPA IPTO), Tech. Rep*, vol. 15, 2008.

[233] Lawrence Berkley National Laboratory, "Ecp co-design center achieves orders of magnitude speed-up in latest software release," *HPC Wire*, 2017.

[234] M. J. Berger and J. Oliger, "Adaptive mesh refinement for hyperbolic partial differential equations," *Journal of computational Physics*, vol. 53, no. 3, pp. 484–512, 1984.

[235] A. Almgren, "Introduction to block-structured adaptive mesh refinement (amr)," *Lawrence Berkeley National Laboratory Presentation*, 2016.

[236] C. J. Budd, W. Huang, and R. D. Russell, "Adaptivity with moving grids," *Acta Numerica*, vol. 18, pp. 111–241, 2009.

[237] P. Diez and A. Huerta, "A unified approach to remeshing strategies for finite element h-adaptivity," *Computer Methods in Applied Mechanics and Engineering*, vol. 176, no. 1-4, pp. 215–229, 1999.

[238] AMReX Development Team. (2019). "Amrex documentation," [Online]. Available: https://amrex-codes.github.io/amrex/docs_html/Basics.html (visited on 11/02/2019).

[239] A. Geist, W. Gropp, S. Huss-Lederman, A. Lumsdaine, E. Lusk, W. Saphir, T. Skjellum, and M. Snir, "Mpi-2: Extending the message-passing interface," in *European Conference on Parallel Processing*, Springer, 1996, pp. 128–135.

[240] W. D. Gropp, W. Gropp, E. Lusk, and A. Skjellum, *Using MPI: portable parallel programming with the message-passing interface*. MIT press, 1999, vol. 1.

[241] L. Dagum and R. Menon, "Openmp: An industry standard api for shared-memory programming," *IEEE computational science and engineering*, vol. 5, no. 1, pp. 46–55, 1998.

[242] N. Zhou, Y. Georgiou, M. Pospieszny, L. Zhong, H. Zhou, C. Niethammer, B. Pejak, O. Marko, and D. Hoppe, "Container orchestration on hpc systems through kubernetes," *Journal of Cloud Computing*, vol. 10, no. 1, pp. 1–14, 2021.

[243] C. Boettiger, "An introduction to docker for reproducible research," *ACM SIGOPS Operating Systems Review*, vol. 49, no. 1, pp. 71–79, 2015.

[244] G. M. Kurtzer, V. Sochat, and M. W. Bauer, "Singularity: Scientific containers for mobility of compute," *PloS one*, vol. 12, no. 5, e0177459, 2017.

[245] J. C. Ferguson, F. Panerai, A. Borner, and N. N. Mansour, "PuMA: the Porous Microstructure Analysis software," *SoftwareX*, vol. 7, pp. 81–87, Jan. 2018. DOI: 10.1016/j.softx.2018.03.001. [Online]. Available: https://doi.org/10.1016%2Fj.softx.2018.03.001.

[246] B. Callow, I. Falcon-Suarez, H. Marin-Moreno, J. M. Bull, and S. Ahmed, "Optimal X-ray micro-CT image based methods for porosity and permeability quantification in heterogeneous sandstones," *Geophysical Journal International*, vol. 223, no. 2, pp. 1210–1229, Jun. 2020. DOI: 10.1093/gji/ggaa321. [Online]. Available: https://doi.org/10.1093%2Fgji%2Fggaa321.

[247] A. Fick, "V. on liquid diffusion," *The London, Edinburgh, and Dublin Philosophical Magazine and Journal of Science*, vol. 10, no. 63, pp. 30–39, 1855.

[248] H. Childs, "Visit: An end-user tool for visualizing and analyzing very large data," 2012.

[249] S. Leffler. (2003). "LibTIFF–TIFF Library and Utilities." Online, Accessed: 28/03/2021, [Online]. Available: remotesensing.org/libtiff (visited on 03/28/2021).

[250] W. Zhang, A. Almgren, V. Beckner, J. Bell, J. Blaschke, C. Chan, M. Day, B. Friesen, K. Gott, D. Graves, M. Katz, A. Myers, T. Nguyen, A. Nonaka, M. Rosso, S. Williams, and M. Zingale, "AMReX: a framework for block-structured adaptive mesh refinement," *Journal of Open Source Software*, vol. 4, no. 37, p. 1370, May 2019. DOI: 10.21105/joss.01370. [Online]. Available: https://doi.org/10.21105%2Fjoss.01370.

[251] X. I. Yang and R. Mittal, "Acceleration of the jacobi iterative method by factors exceeding 100 using scheduled relaxation," *Journal of Computational Physics*, vol. 274, pp. 695–708, 2014.

[252] Y. Saad, "A flexible inner-outer preconditioned gmres algorithm," *SIAM Journal on Scientific Computing*, vol. 14, no. 2, pp. 461–469, 1993.

[253] R. D. Falgout and U. M. Yang, "Hypre: A library of high performance preconditioners," in *International Conference on Computational Science*, Springer, 2002, pp. 632–641.

[254] V. Sulzer, S. G. Marquis, R. Timms, M. Robinson, and S. J. Chapman, "Python battery mathematical modelling (pybamm)," 2020.

[255] G. W. Richardson, J. M. Foster, R. Ranom, C. P. Please, and A. M. Ramos, "Charge transport modelling of lithium ion batteries," *arXiv preprint arXiv:2002.00806*, 2020.

[256] A. Nonaka, M. S. Day, and J. B. Bell, "A conservative, thermodynamically consistent numerical approach for low mach number combustion. part i: Single-level integration," *Combustion Theory and Modelling*, vol. 22, no. 1, pp. 156–184, 2018.

[257] A. Grama, V. Kumar, A. Gupta, and G. Karypis, *Introduction to parallel computing*. Pearson Education, 2003.

[258] I. G. Angus, G. C. Fox, J. S. Kim, and D. W. Walker, "Solving problems on concurrent processors.," *Volume 2: Software for Concurrent Processors*, 1990.

[259] J. L. Gustafson, "Reevaluating amdahl's law," *Communications of the ACM*, vol. 31, no. 5, pp. 532–533, 1988.

[260] J. T. Gostick, Z. A. Khan, T. G. Tranter, M. D. Kok, M. Agnaou, M. Sadeghi, and R. Jervis, "Porespy: A python toolkit for quantitative analysis of porous media images," *Journal of Open Source Software*, vol. 4, no. 37, p. 1296, 2019.

[261] F. L. Usseglio-Viretta, A. Colclasure, A. N. Mistry, K. P. Y. Claver, F. Pouraghajan, D. P. Finegan, T. M. Heenan, D. Abraham, P. P. Mukherjee, D. Wheeler, *et al.*, "Resolving the discrepancy in tortuosity factor estimation for li-ion battery electrodes through micro-macro modeling and experiment," *Journal of The Electrochemical Society*, vol. 165, no. 14, A3403, 2018.

[262] J. Laurencin, R. Quey, G. Delette, H. Suhonen, P. Cloetens, and P. Bleuet, "Characterisation of solid oxide fuel cell ni–8ysz substrate by synchrotron x-ray nano-tomography: From 3d reconstruction to microstructure quantification," *Journal of Power Sources*, vol. 198, pp. 182–189, 2012.

[263] G. M. Amdahl, "Validity of the single processor approach to achieving large scale computing capabilities," in *Proceedings of the April 18-20, 1967, spring joint computer conference*, 1967, pp. 483–485.

[264] M. D. Hill and M. R. Marty, "Amdahl's law in the multicore era," *Computer*, vol. 41, no. 7, pp. 33–38, 2008.

[265] V. Donaldson, F. Berman, and R. Paturi, "Program speedup in a heterogeneous computing network," *Journal of Parallel and Distributed Computing*, vol. 21, no. 3, pp. 316–322, 1994.

[266] C. F. Berg, *Fontainebleau 3d models*, http://www.digitalrocksportal.org/projects/57, 2016. DOI: doi:10.17612/P75P4P.

[267] A. Holland, R. Mckerracher, A. Cruden, and R. Wills, "An aluminium battery operating with an aqueous electrolyte," *Journal of Applied Electrochemistry*, vol. 48, no. 3, pp. 243–250, 2018.

[268] A. Holland, R. McKerracher, A. Cruden, and R. Wills, "Tio2 nanopowder as a high rate, long cycle life electrode in aqueous aluminium electrolyte," *Materials today energy*, vol. 10, pp. 208–213, 2018.

[269] X. Pan, E. Y. Sidky, and M. Vannier, "Why do commercial ct scanners still employ traditional, filtered back-projection for image reconstruction?" *Inverse problems*, vol. 25, no. 12, p. 123 009, 2009.

[270] C. Tsiotsios and M. Petrou, "On the choice of the parameters for anisotropic diffusion in image processing," *Pattern recognition*, vol. 46, no. 5, pp. 1369–1381, 2013.

[271] J. Weickert, *Anisotropic diffusion in image processing*. Teubner Stuttgart, 1998, vol. 1.

[272] J. Le Houx and D. Kramer, "Openimpala: Open source image based parallisable linear algebra solver," *SoftwareX*, vol. 15, p. 100 729, 2021.

[273] R. McKerracher, "EPSRC impact acceleration account project report," *EPSRC IAA*, 2018.

[274] Z. Konrad, "User's guide–avizo," 2017.

[275] J. Feinauer, A. Spettl, I. Manke, S. Strege, A. Kwade, A. Pott, and V. Schmidt, "Structural characterization of particle systems using spherical harmonics," *Materials Characterization*, vol. 106, pp. 123–133, 2015.

[276] L. F. Arenas, R. P. Boardman, C. P. de León, and F. C. Walsh, "X-ray computed micro-tomography of reticulated vitreous carbon," *Carbon*, vol. 135, pp. 85–94, 2018.

[277] J. Le Houx and D. Kramer, "X-ray tomography for lithium ion battery electrode characterisation—a review," *Energy Reports*, vol. 7, pp. 9–14, 2021.

[278] C. A. Schneider, W. S. Rasband, and K. W. Eliceiri, "Nih image to imagej: 25 years of image analysis," *Nature methods*, vol. 9, no. 7, pp. 671–675, 2012.

[279] J. Schindelin, I. Arganda-Carreras, E. Frise, V. Kaynig, M. Longair, T. Pietzsch, S. Preibisch, C. Rueden, S. Saalfeld, B. Schmid, *et al.*, "Fiji: An open-source platform for biological-image analysis," *Nature methods*, vol. 9, no. 7, pp. 676–682, 2012.

[280] A. Spettl, R. Wimmer, T. Werz, M. Heinze, S. Odenbach, C. Krill III, and V. Schmidt, "Stochastic 3d modeling of ostwald ripening at ultra-high volume fractions of the coarsening phase," *Modelling and Simulation in Materials Science and Engineering*, vol. 23, no. 6, p. 065 001, 2015.

Appendix A

Glossary

Block Structured Adaptive Mesh Refinement (AMR) Cover regions requiring higher resolution with finer grid

Bruggeman Correlation Correlates tortuosity factors of porous media with their porosity

Butler-Volmer Equation Describes how the electrical current on an electrode depends on the electrode potential

Checkerboarding Method where the voxels of a volume array are divided into vectorised subdomains (only applied to the conducting phase)

Concurrent Coupling Real time coupling of a multiscale model to solve state variables

Dirichlet Boundaries Fixed boundary condition problems

Fick's Laws First law relates the diffusive flux to the concentration under the assumption of steady state. Second law predicts how diffusion causes the concentration to change with time

Focused Ion Beam (FIB) FIB is a technique used for the analysis of microstructure, similar to SEM, however it uses a focused beam of ions not electrons

Ghost Node Concept The ghost node is used to calculate across adjacent voxels by providing a node that can be used to calculate edge node values. However the ghost node does not appear in the final solution

Jacobi Method An algorithm for determining the solutions of a diagonally dominant system of linear equations; each diagonal element is solved for and an approximate value is plugged in, this process iterate until the solution converges

Knudsen Interactions The Knudsen number is a dimensionless number defined as the ratio of the molecular mean free path length to a representative physical length scale. It becomes relevant when the scale length of the system is comparable to or smaller than the mean free path of the particles e.g. a long pore with a narrow diameter where the molecules frequently collide with the pore wall

Marching Cubes A computer graphics algorithm used to smooth a voxel field into a polygonal mesh

Newman Pseudo 2D Physics based model assuming homogeneous electrode structure, using the Bruggeman Correlation

Over Relaxation Method Derived by extrapolating the Jacobi method, it takes the form of a weighted average between the previous iterate and the computed Jacobi iterate successively for each component

Representative Elementary Volume (REV) The smallest volume over which a measurement can be made that will yield a value representative of the whole

Simpleware Commercial software package used to generate models from 3D image data

Spatial Resolution A term used to refer to the ability of an imaging method to differentiate between two objects

Tortuosity A measure of the geometric complexity of a porous medium. The ratio that characterises the convoluted pathways of fluid diffusion and electrical conduction through porous media

Voxel A voxel represents a value on a regular grid in 3D space. Voxels are used to describe 3D resolution as a voxel is similar to the word pixel. 'Vo' meaning volume and 'el' meaning element

Appendix B

FIB/SEM Tomography Experimental Setup

B.1 FIB/SEM Tomography of a Lithium Nickel Manganese Cobalt Oxide Structured Particle

The electrodes used in this section were manufactured by Joachim R. Binder at Karlsruhe Institute of Technology, imaged by Markus Osenberg at Technische Universität Berlin and post-processed by Matthias Neumann at Ulm University. These image datasets are then used as the computational domain for OpenImpala in Section 4.3.2.1. The preparation for these image datasets are included in this appendix for completeness of the work but to be clear, this section of work was not carried out by the author.

B.1.1 Experimental Setup

Like LFP, Lithium Nickel Manganese Cobalt Oxide (NMC) is another typical composition used in many applications. NMC based batteries are, for example, widely used in the automotive industry, power tools or e-bikes. To achieve high power densities, it is crucial that the electrolyte can reach as much active material as possible. Therefore, a high material surface is desirable. The material, produced at the Karlsruher Institute of Technology, is shown in Figure B.1 and designed with high power applications in mind and consequently is highly hierarchically structured. The active material was first ground from pristine $Li(Ni_{1/3}Mn_{1/3}Co_{1/3})O_2$ powder (NM-3100, Toda America),

next it was spray-dried and finally calcined at 850°C.

The FIB/SEM tomography was performed at Helmholtz-Zentrum Berlin by Markus Osenberg, using a Zeiss Crossbeam 340 equipped with a Gemini I VP column. For the serial section milling, the ion gun was operated at 30 kV with a gallium ion current of 300 pA. After each milling step, an SEM image was captured under an angle of 54°. The electron gun was operated at 2 kV. The pixel size was synchronised to the milling depth resulting in an isotropic voxel size of 10 nm.

B.1.2 3D data segmentation and reconstruction

The raw volume data was drift corrected by utilising image features that were not part of the milled surface. As these features have not been destroyed during the milling process, they were suitable for drift correction and could be tracked and stabilised. After stabilisation, the dataset was cropped, removing all parts that have not been ion milled, such as the preprocessed outer areas. For intensity normalisation, the data set was duplicated, and a minimum filter with a filter radius larger than the primary particles was applied. The filtered data set was further blurred, resulting in a gradient mask reflecting the intensity fading of the milled surface area in the original data set. After subtracting the intensity mask from the original data set, a Niblack local threshold was applied, resulting in the final binary reconstruction. All reconstruction steps have been performed using the freeware Fiji [279], by Markus Osenberg. The reconstructed final volume size measured 20x20x20 μm^3.

Figure B.1 shows a FIB/SEM tomographic reconstruction of a single NMC cathode battery particle. FIB/SEM tomography allows slicewise cuts through a complete particle with a spatial resolution of a few nanometers. Figure B.1 (a) shows an overview of the NMC electrode location where a single NMC particle was chosen. Figure B.1 (b) shows 2D a cut through several particles. From the particle in the centre, a complete 3D data set was created (Figures B.1 (c) and (d)). It contains all structural information of the NMR particle with a spatial resolution of roughly 10 nm.

NMC particle sizes are typically between a few µm and 30 µm. For this study, parti-

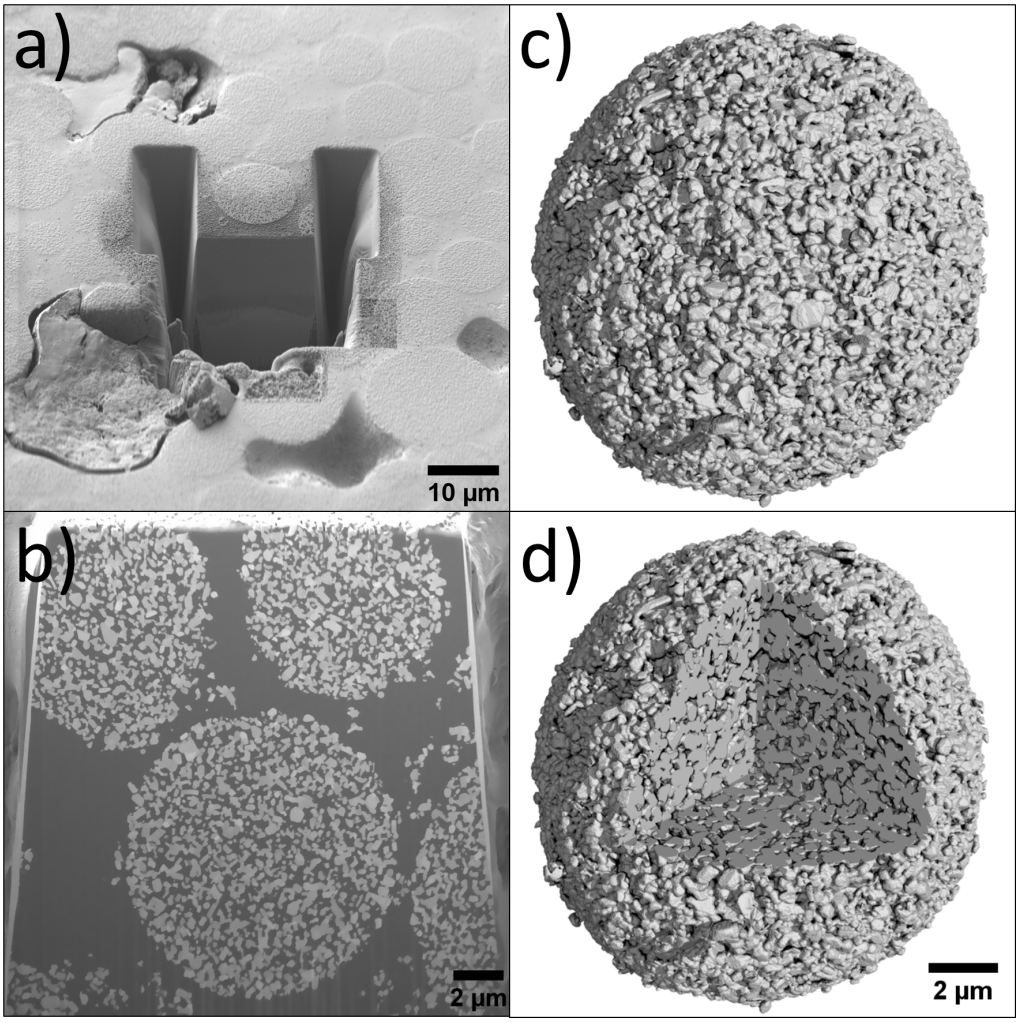

Figure B.1: FIB/SEM tomography performed on an NMC cathode particle showing (a) the preprocessed area on the sample before the serial section tomography is performed, (b) one slice of the serial section during the measuring process, (c) a 3D render of one of the tomographed NMC cathode particles and (d) the same particle but with one-eighth of the material virtually removed to reveal its inner structure.

cles of typical sizes around 4-8 µm have been chosen. These particles consist of much smaller primary particles with sizes around 20-150 nm (see Figure 3). Therefore, a measurement technique like FIB/SEM tomography with a spatial resolution of about 10 nm is ideally suited to create 3D data sets that contain all the necessary information for realistic simulation studies.

After binarisation of image data, a voxel representation of the pore phase and the solid phase is obtained. To perform the numerical study shown here, the geometry of the porous microstructure of the single NMC particle has been represented by level set functions as described below. For the tortuosity computation, the solid phase has been represented by a union of voxelised particles using the watershed algorithm described in [280]. Then, each voxelised particle undergoes a smoothing process, where it is analytically described by so-called spherical harmonics functions [275]. The analytical representation of the pore phase is then given by the complement of the union of particles. The idea is to define a model of the geometry, based on tomographic data, that can be used to compute the tortuosity with different resolutions. Two datasets have been reconstructed from the same microstructure with volume $5\,\mu m^3$, using two resolutions: a 499 cubic voxel set with voxel size 10 nm and a 998 cubic voxel set with voxel size 5 nm. These datasets are then used as the computational domain in Section 4.3.2.1.

Appendix C

OpenImpala Source Code

Key sections of the OpenImpala code are contained here, including Dat based file input, Fortran based initialisation routines and a snippet of the main Hypre based computation. The full code contains over 4,000 lines so for the sake of brevity, the interested reader is referred to the publicly accessible Github repository: https://github.com/kramergroup/openImpala/releases/tag/v1.0.0. N.B. the code contained in this thesis is released as v1.0.0, development of the code is expected to continue in the future.

C.1 TortuosityHypre Calculation

```
amrex::Real TortuosityHypre::value(const bool refresh)
{
    if (refresh || m_first_call)
    {
      m_first_call = false;
      solve();
    }

    amrex::Real fluxlo = 0.0;
    amrex::Real fluxhi = 0.0;
    amrex::Real phisumlo = 0.0;
    amrex::Real phisumhi = 0.0;
```

```
13      int num_phase_cells_0 = 0;
14      int num_phase_cells_1 = 0;
15      int num_phase_cells_2 = 0;
16      int num_phase_cells_3 = 0;
17
18      // Iterate over all boxes and count cells with value=m_phase
19      if ( m_dir==0)
20      {
21      for (amrex::MFIter mfi(m_mf_phase); mfi.isValid(); ++mfi) // Loop
         ↪  over grids
22      {
23        const amrex::Box& box = mfi.validbox();
24        const amrex::IArrayBox& phase_fab = m_mf_phase[mfi];
25        const amrex::FArrayBox& phi_fab = m_mf_phi[mfi];
26
27        // Obtain Array4 from FArrayBox.  We can also do
28        //     Array4<Real> const& a = mf.array(mfi);
29        amrex::Array4<int const> const& phase_fab_4 =
           ↪  phase_fab.array();
30        amrex::Array4<amrex::Real const> const& phi_fab_4 =
           ↪  phi_fab.array();
31
32        size_t idx;
33        // Iterate over all cells in Box and threshold
34        const auto lo = lbound(box);
35        const auto hi = ubound(box);
36
37
38        // Sum all concentration values for each slice in x direction
39        const auto domain_min_x = m_geom.Domain().loVect()[0];
40        if ( lo.x == domain_min_x) {
41              for (int y = lo.y; y <= hi.y; ++y) {
```

```
42                for (int z = lo.z; z <= hi.z; ++z) {
43                  if ( phase_fab_4(lo.x,y,z) == m_phase &&
                     ↪  phase_fab_4(lo.x+1,y,z) == m_phase ) {
44                    phisumlo += phi_fab_4(lo.x+1,y,z) -
                       ↪  phi_fab_4(lo.x,y,z);
45                    num_phase_cells_0 += 1;
46                  }
47                }
48          }
49        }
50
51        const auto domain_max_x = m_geom.Domain().hiVect()[0];;
52        if ( hi.x == domain_max_x) {
53              for (int y = lo.y; y <= hi.y; ++y) {
54                for (int z = lo.z; z <= hi.z; ++z) {
55                  if ( phase_fab_4(hi.x,y,z) == m_phase &&
                     ↪  phase_fab_4(hi.x-1,y,z) == m_phase ) {
56                    phisumhi += phi_fab_4(hi.x,y,z) -
                       ↪  phi_fab_4(hi.x-1,y,z);
57                    num_phase_cells_1 += 1;
58                  }
59                }
60          }
61        }
62
63      }
64    }
65
66
67    else if ( m_dir==1)
68    {
```

```
69  for (amrex::MFIter mfi(m_mf_phase); mfi.isValid(); ++mfi) // Loop
     ↪  over grids
70  {
71    const amrex::Box& box = mfi.validbox();
72    const amrex::IArrayBox& phase_fab = m_mf_phase[mfi];
73    const amrex::FArrayBox& phi_fab = m_mf_phi[mfi];
74
75    // Obtain Array4 from FArrayBox.  We can also do
76    //     Array4<Real> const& a = mf.array(mfi);
77    amrex::Array4<int const> const& phase_fab_4 = phase_fab.array();
78    amrex::Array4<amrex::Real const> const& phi_fab_4 =
       ↪  phi_fab.array();
79
80    size_t idx;
81    // Iterate over all cells in Box and threshold
82    const auto lo = lbound(box);
83    const auto hi = ubound(box);
84
85
86    // Sum all concentration values for each slice in y direction
87    const auto domain_min_y = m_geom.Domain().loVect()[1];
88    if ( lo.y == domain_min_y) {
89          for (int x = lo.x; x <= hi.x; ++x) {
90            for (int z = lo.z; z <= hi.z; ++z) {
91              if ( phase_fab_4(x,lo.y,z) == m_phase &&
                 ↪  phase_fab_4(x,lo.y+1,z) == m_phase ) {
92                phisumlo += phi_fab_4(x,lo.y+1,z) -
                   ↪  phi_fab_4(x,lo.y,z);
93                num_phase_cells_0 += 1;
94            }
95          }
96      }
```

```
97      }
98
99      const auto domain_max_y = m_geom.Domain().hiVect()[1];;
100     if ( hi.y == domain_max_y) {
101           for (int x = lo.x; x <= hi.x; ++x) {
102             for (int z = lo.z; z <= hi.z; ++z) {
103               if ( phase_fab_4(x,hi.y,z) == m_phase &&
                  ↪  phase_fab_4(x,hi.y-1,z) == m_phase ) {
104                 phisumhi += phi_fab_4(x,hi.y,z) -
                    ↪  phi_fab_4(x,hi.y-1,z);
105                 num_phase_cells_1 += 1;
106             }
107           }
108       }
109     }
110
111   }
112 }
113
114 else if ( m_dir==2)
115 {
116 for (amrex::MFIter mfi(m_mf_phase); mfi.isValid(); ++mfi) // Loop
    ↪  over grids
117 {
118   const amrex::Box& box = mfi.validbox();
119   const amrex::IArrayBox& phase_fab = m_mf_phase[mfi];
120   const amrex::FArrayBox& phi_fab = m_mf_phi[mfi];
121
122   // Obtain Array4 from FArrayBox.  We can also do
123   //     Array4<Real> const& a = mf.array(mfi);
124   amrex::Array4<int const> const& phase_fab_4 = phase_fab.array();
```

```
125   amrex::Array4<amrex::Real const> const& phi_fab_4 =
       ↪ phi_fab.array();
126
127   size_t idx;
128   // Iterate over all cells in Box and threshold
129   const auto lo = lbound(box);
130   const auto hi = ubound(box);
131
132
133   // Sum all concentration values for each slice in x direction
134   const auto domain_min_z = m_geom.Domain().loVect()[2];
135   if ( lo.z == domain_min_z) {
136         for (int x = lo.x; x <= hi.x; ++x) {
137           for (int y = lo.y; y <= hi.y; ++y) {
138             if ( phase_fab_4(x,y,lo.z) == m_phase &&
                 ↪ phase_fab_4(x,y,lo.z+1) == m_phase ) {
139               phisumlo += phi_fab_4(x,y,lo.z+1) -
                   ↪ phi_fab_4(x,y,lo.z);
140               num_phase_cells_0 += 1;
141             }
142         }
143     }
144   }
145
146   const auto domain_max_z = m_geom.Domain().hiVect()[2];;
147   if ( hi.z == domain_max_z) {
148         for (int x = lo.x; x <= hi.x; ++x) {
149           for (int y = lo.y; y <= hi.y; ++y) {
150             if ( phase_fab_4(x,y,hi.z) == m_phase &&
                 ↪ phase_fab_4(x,y,hi.z-1) == m_phase ) {
151               phisumhi += phi_fab_4(x,y,hi.z) -
                   ↪ phi_fab_4(x,y,hi.z-1);
```

```
152                 num_phase_cells_1 += 1;
153               }
154             }
155         }
156     }
157
158 }
159 }
160
161     // Reduce parallel processes
162     if (!refresh) {
163       amrex::ParallelAllReduce::Sum(phisumlo,
          ↪  amrex::ParallelContext::CommunicatorSub());
164       }
165
166     if (!refresh) {
167       amrex::ParallelAllReduce::Sum(phisumhi,
          ↪  amrex::ParallelContext::CommunicatorSub());
168       }
169
170     // Total problem length each direction
171     auto length_x = m_geom.ProbLength(0);
172     auto length_y = m_geom.ProbLength(1);
173     auto length_z = m_geom.ProbLength(2);
174
175     // Cell size in each direction
176     amrex::Real dx = m_geom.CellSize(0);
177     amrex::Real dy = m_geom.CellSize(1);
178     amrex::Real dz = m_geom.CellSize(2);
179
180     // Number of cells in each direction
181     auto num_cell_x = length_x/dx;
```

```
182     auto num_cell_y = length_y/dy;
183     auto num_cell_z = length_z/dz;
184
185     // Compute flux between adjacent slices
186     fluxlo = phisumlo / dx * (dy*dz);
187     fluxhi = phisumhi / dx * (dy*dz);
188
189     // Compute maximum flux as max_flux = (phi(left) -
        ↪ phi(right))*(b*c)/a
190     amrex::Real flux_max=0.0;
191
192     if ( m_dir==0) {
193       flux_max = (m_vhi-m_vlo) / length_x * (length_y*length_z);
194     }
195
196     else if ( m_dir==1) {
197       flux_max = ((m_vhi-m_vlo) / length_x * (length_y*length_z)) *
          ↪ ((num_cell_x*num_cell_x) / (num_cell_y*num_cell_y));
198     }
199
200     else if ( m_dir==2) {
201       flux_max = ((m_vhi-m_vlo) / length_x * (length_y*length_z)) *
          ↪ ((num_cell_x*num_cell_x) / (num_cell_z*num_cell_z));
202     }
203
204     // Compute Volume Fractions
205
206     amrex::Real rel_diffusivity = (fluxlo+fluxhi)/2.0/flux_max;
207
208     amrex::Real tau = m_vf / rel_diffusivity;
209
210     // Print all of fluxvect values
```

```
211     amrex::Print() << std::endl << " Relative Effective Diffusivity
        ↪  (D_eff / D): "
212                    << rel_diffusivity << std::endl ;
213
214     amrex::Print() << " Check difference between top and bottom
        ↪  fluxes is nil: " << abs(fluxlo - fluxhi) << std::endl;
215
216     return tau;
217
218
219 }
```

C.2 Dat File Input Routine

```
1  #include "DatReader.H"
2  #include <fstream>
3
4  #include <AMReX.H>
5  #include <AMReX_IntVect.H>
6  #include <AMReX_iMultiFab.H>
7
8  DatReader::DatReader( std::string const& filename) :
   ↪  m_filename(filename)
9  {
10   readDatFile();
11 }
12
13 void DatReader::readDatFile()
14 {
15   std::ifstream file(m_filename.c_str());
16   if (file.is_open()) {
17     std::string line;
```

```
18      int counter=0;
19      // Read one line at a time into the variable line:
20      while(std::getline(file, line))
21      {
22          std::stringstream  lineStream(line);
23
24          uint32_t value;
25          // Read an integer at a time from the line
26          while(lineStream >> value)
27          {
28            if (counter ==0){
29              m_width=value;
30            }
31            else if (counter ==1){
32              m_height=value;
33            }
34            else if (counter ==2){
35              m_depth=value;
36            }
37            else
38            {
39              // Add the integers from a line to a 1D array (vector)
40              m_raw.push_back(value);
41            }
42            counter++;
43          }
44
45      }
46      file.close();
47  }
48
49  }
```

```
50
51 uint32_t DatReader::depth()
52 {
53   return m_depth;
54 }
55
56 uint32_t DatReader::height()
57 {
58   return m_height;
59 }
60
61 uint32_t DatReader::width()
62 {
63   return m_width;
64 }
65
66 amrex::Box DatReader::box()
67 {
68   amrex::Box box(amrex::IntVect{0,0,0},
    ↪  amrex::IntVect{m_width-1,m_height-1,m_depth-1});
69   return box;
70 }
71
72 void DatReader::threshold(const uint32_t threshold, amrex::iMultiFab&
    ↪  mf)
73 {
74
75   for (amrex::MFIter mfi(mf); mfi.isValid(); ++mfi) // Loop over
    ↪  grids
76   {
77     const amrex::Box& box = mfi.validbox();
78     amrex::IArrayBox& fab = mf[mfi];
```

```
79
80      size_t idx;
81      // Iterate over all cells in Box and threshold
82      for (amrex::BoxIterator bit(box); bit.ok(); ++bit)
83      {
84        idx = bit()[0] + bit()[1]*m_width + bit()[2]*m_height*m_width;
85        // bit() returns IntVect
86        fab(bit(),0) = (m_raw[idx] < threshold);
87      }
88    }
89
90  }
```

C.3 Fortran Cell Initialisation

```
1   module tortuosity_filcc_module
2
3     use amrex_fort_module, only : amrex_real, amrex_spacedim
4     use amrex_bc_types_module
5     use amrex_constants_module
6
7     implicit none
8
9     interface tortuosity_filcc
10       module procedure tortuosity_filct
11       module procedure tortuosity_filbc
12       module procedure tortuosity_filic
13    end interface tortuosity_filcc
14
15    integer, parameter :: direction_x = 0
16    integer, parameter :: direction_y = 1
17    integer, parameter :: direction_z = 2
```

```
18
19    integer, parameter :: cell_type_blocked       = b'00000000'
20    integer, parameter :: cell_type_free          = b'00000001'
21
22    integer, parameter :: comp_phi = 1  ! fab component for
       ↪  concentration field
23    integer, parameter :: comp_ct  = 2  ! fab component for cell type
24
25    private
26    public :: tortuosity_filbc, tortuosity_filic
27
28  contains
29
30  ! ::: -----------------------------------------------------------
31  ! ::: This routine fills the cell type data structure for
32  ! ::: the tortuosity problem. Each cell is either blocked/free or
33  ! ::: has one or more boundaries.
34  ! :::
35  ! ::: INPUTS/OUTPUTS:
36  ! ::: q           <=  array to fill
37  ! ::: p            => array with phase indices
38  ! ::: domlo,domhi  => index extent of problem domain
39  ! ::: phase        => index of the active phase
40
41  ! ::: -----------------------------------------------------------
42
43     subroutine tortuosity_filct(q, q_lo, q_hi, q_ncomp, p, p_lo, p_hi,
       ↪  p_ncomp, &
44                                 domlo, domhi, phase) bind(c)
45
46
47        implicit none
```

```
48
49        integer,          intent(in   ) :: q_lo(3), q_hi(3)
50        integer,          intent(in   ) :: p_lo(3), p_hi(3)
51        integer,          intent(in   ) :: domlo(amrex_spacedim),
          ↪  domhi(amrex_spacedim)
52        integer,          intent(in   ) :: q_ncomp, p_ncomp
53        real(amrex_real), intent(inout) ::
          ↪  q(q_lo(1):q_hi(1),q_lo(2):q_hi(2),q_lo(3):q_hi(3),q_ncomp)
54        integer,          intent(in   ) ::
          ↪  p(p_lo(1):p_hi(1),p_lo(2):p_hi(2),p_lo(3):p_hi(3),p_ncomp)
55        integer,          intent(in   ) :: phase
56
57        ! Index variables
58        integer :: k, j, i
59
60        ! Domain indices
61        integer :: ilo, ihi, jlo, jhi, klo, khi
62        ilo = domlo(1)
63        ihi = domhi(1)
64        jlo = domlo(2)
65        jhi = domhi(2)
66        klo = domlo(3)
67        khi = domhi(3)
68
69        ! Iterate over all cells and fill in types
70        do k = klo, khi
71           do j = jlo, jhi
72              do i = ilo, ihi
73                 if (p(i,j,k,1) .eq. phase ) then
74                    q(i,j,k,comp_ct) = cell_type_free
75                 else
76                    q(i,j,k,comp_ct) = cell_type_blocked
```

```
77                end if
78             end do
79          end do
80       end do
81
82    end subroutine tortuosity_filct
83
84 ! ::: -----------------------------------------------------------
85 ! ::: This routine removes disconnected singular points from
86 ! ::: the phase MultiFab. It goes over the MultiFab and adjusts
87 ! ::: the phase information for voxels that are sourrounded by
88 ! ::: the other phase
89 ! :::
90 ! ::: INPUTS/OUTPUTS:
91 ! ::: q            => array with phase indices
92 ! ::: bxlo,bxhi    => valid index extenf of box
93 ! ::: domlo,domhi  => index extent of problem domain
94 ! ::: -----------------------------------------------------------
95 subroutine tortuosity_remspot(q, q_lo, q_hi, ncomp, bxlo, bxhi,
   ↪  domlo, domhi) bind(c)
96
97    implicit none
98
99    integer,          intent(in   ) :: q_lo(3), q_hi(3), domlo(3),
   ↪  domhi(3), bxlo(3), bxhi(3)
100   integer,          intent(in   ) :: ncomp
101   integer,          intent(inout) ::
      ↪  q(q_lo(1):q_hi(1),q_lo(2):q_hi(2),q_lo(3):q_hi(3),ncomp)
102
103   integer :: i,j,k      ! running indices
104   integer :: p(7)       ! array to hold the phase information for a
      ↪  seven point stencil
```

```
105
106     do k = bxlo(3), bxhi(3)
107        do j = bxlo(2), bxhi(2)
108           do i = bxlo(1), bxhi(1)
109
110              p(1) = q(i,j,k,1)
111
112              ! Direction -x
113              if ( i == domlo(1) ) then
114                 p(2) = -1
115              else
116                 p(2) = q(i-1,j,k,1)
117              end if
118
119              ! Direction +x
120              if ( i == domhi(1) ) then
121                 p(3) = -1
122              else
123                 p(3) = q(i+1,j,k,1)
124              end if
125
126              ! Direction -y
127              if ( j == domlo(2) ) then
128                 p(4) = -1
129              else
130                 p(4) = q(i,j-1,k,1)
131              end if
132
133              ! Direction +y
134              if ( j == domhi(2) ) then
135                 p(5) = -1
136              else
```

```
137                p(5) = q(i,j+1,k,1)
138             end if
139
140             ! Direction -z
141             if ( k == domlo(3) ) then
142                p(6) = -1
143             else
144                p(6) = q(i,j,k-1,1)
145             end if
146
147             ! Direction +z
148             if ( k == domhi(3) ) then
149                p(7) = -1
150             else
151                p(7) = q(i,j,k+1,1)
152             end if
153
154             if ((p(1) == p(2)) .or. &
155                 (p(1) == p(3)) .or. &
156                 (p(1) == p(4)) .or. &
157                 (p(1) == p(5)) .or. &
158                 (p(1) == p(6)) .or. &
159                 (p(1) == p(7))) then
160                   ! Do nothing - point is connected
161             else
162                if (q(i,j,k,1) == 0) then
163                   q(i,j,k,1) = 1
164                else
165                   q(i,j,k,1) = 0
166                end if
167             end if
168
```

```
169           end do
170         end do
171       end do
172
173   end subroutine tortuosity_remspot
174
175
176   ! ::: -----------------------------------------------------------
177   ! ::: This routine fills the Dirichlet boundary conditions for
178   ! ::: the tortuosity problem. There are two Dirichlet conditions
179   ! ::: on opposing faces perpendicular to the principal flow
      ↪  direction.
180   ! :::
181   ! ::: INPUTS/OUTPUTS:
182   ! ::: q           <=  array to fill
183   ! ::: p            => array with phase indices
184   ! ::: domlo,domhi  => index extent of problem domain
185   ! ::: vlo,vhi      => values at the boundary
186   ! ::: bc            => array of boundary flags bc(SPACEDIM,lo:hi)
187   ! ::: -----------------------------------------------------------
188
189     subroutine tortuosity_filbc(q, q_lo, q_hi, ncomp, p, p_lo, p_hi,
        ↪  p_ncomp, &
190                                 domlo, domhi, vlo, vhi, bc) bind(c)
191
192       implicit none
193
194       integer,          intent(in   ) :: q_lo(3), q_hi(3)
195       integer,          intent(in   ) :: p_lo(3), p_hi(3)
196       integer,          intent(in   ) :: domlo(amrex_spacedim),
          ↪  domhi(amrex_spacedim)
197       integer,          intent(in   ) :: ncomp, p_ncomp
```

```
198     real(amrex_real), intent(in   ) :: vlo, vhi
199     real(amrex_real), intent(inout) ::
        ↪  q(q_lo(1):q_hi(1),q_lo(2):q_hi(2),q_lo(3):q_hi(3),ncomp)
200     integer,          intent(in   ) ::
        ↪  p(p_lo(1):p_hi(1),p_lo(2):p_hi(2),p_lo(3):p_hi(3),p_ncomp)
201     integer,          intent(in   ) :: bc(amrex_spacedim,2)
202
203     integer :: ilo, ihi, jlo, jhi, klo, khi
204     integer :: i, j, k, n
205     integer :: imin, imax, jmin, jmax, kmin, kmax
206
207     ilo = domlo(1)
208     ihi = domhi(1)
209     jlo = domlo(2)
210     jhi = domhi(2)
211     klo = domlo(3)
212     khi = domhi(3)
213
214     do n = 1, ncomp
215
216        if (q_lo(1) < ilo) then
217           imin = q_lo(1)
218           imax = min(q_hi(1),ilo-1)
219
220           if (bc(1,1) .eq. amrex_bc_ext_dir) then
221
222             do k = q_lo(3), q_hi(3)
223                do j = q_lo(2), q_hi(2)
224                   do i = imin, imax
225                      q(i,j,k,n) = vlo !!! +
                       ↪  1.0*(j-domhi(2))/domhi(2)*(k-domhi(3))/domhi(3)*(vhi-vl
226                   end do
```

```
227                end do
228              end do
229
230           end if
231
232        end if
233
234        if (q_hi(1) > ihi) then
235           imin = max(q_lo(1),ihi+1)
236           imax = q_hi(1)
237
238           if (bc(1,2) .eq. amrex_bc_ext_dir) then
239
240              do k = q_lo(3), q_hi(3)
241                 do j = q_lo(2), q_hi(2)
242                    do i = imin, imax
243                       q(i,j,k,n) = vhi
244                    end do
245                 end do
246              end do
247
248           end if
249
250        end if
251
252        if (q_lo(2) < jlo) then
253           jmin = q_lo(2)
254           jmax = min(q_hi(2),jlo-1)
255
256           if (bc(2,1) .eq. amrex_bc_ext_dir) then
257
258              do k = q_lo(3), q_hi(3)
```

```
259                do j = jmin, jmax
260                   do i = q_lo(1), q_hi(1)
261                      q(i,j,k,n) = vlo
262                   end do
263                end do
264             end do
265
266          end if
267
268       end if
269
270       if (q_hi(2) > jhi) then
271          jmin = max(q_lo(2),jhi+1)
272          jmax = q_hi(2)
273
274          if (bc(2,2) .eq. amrex_bc_ext_dir) then
275
276             do k = q_lo(3), q_hi(3)
277                do j = jmin, jmax
278                   do i = q_lo(1), q_hi(1)
279                      q(i,j,k,n) = vhi
280                   end do
281                end do
282             end do
283
284          end if
285
286       end if
287
288       if (q_lo(3) < klo) then
289          kmin = q_lo(3)
290          kmax = min(q_hi(3),klo-1)
```

```
291
292             if (bc(3,1) .eq. amrex_bc_ext_dir) then
293
294               do k = kmin, kmax
295                  do j = q_lo(2), q_hi(2)
296                     do i = q_lo(1), q_hi(1)
297                        q(i,j,k,n) = vlo
298                     end do
299                  end do
300               end do
301
302             end if
303
304          end if
305
306          if (q_hi(3) > khi) then
307             kmin = max(q_lo(3),khi+1)
308             kmax = q_hi(3)
309
310             if (bc(3,2) .eq. amrex_bc_ext_dir) then
311
312               do k = kmin, kmax
313                  do j = q_lo(2), q_hi(2)
314                     do i = q_lo(1), q_hi(1)
315                        q(i,j,k,n) = vhi
316                     end do
317                  end do
318               end do
319
320             end if
321
322          end if
```

```
323
324       end do
325
326     end subroutine tortuosity_filbc
327
328
329
330   ! ::: -----------------------------------------------------------
331   ! ::: This routine fills the initial conditions for
332   ! ::: the tortuosity problem. The problem is initialised by a
333   ! ::: linear gradient along the principal flow direction. The
334   ! ::: routine only fill cells of the phase of interest and
335   ! ::: initialises all other cells with zero.
336   ! :::
337   ! ::: INPUTS/OUTPUTS:
338   ! ::: q           <=  array to fill
339   ! ::: p            => array with phase indices
340   ! ::: domlo,domhi  => index extent of problem domain
341   ! ::: vlo,vhi      => values at the boundary
342   ! ::: phase        => index of the phase of interest
343   ! ::: dir          => principal flow direction (X=0, Y=1, Z=2)
344   ! ::: -----------------------------------------------------------
345
346     subroutine tortuosity_filic(q, q_lo, q_hi, ncomp, p, p_lo, p_hi,
      ↪  p_ncomp, &
347                                 lo, hi, domlo, domhi, vlo, vhi, phase,
                                     ↪  dir) bind(c)
348
349       implicit none
350
351       integer,          intent(in   ) :: q_lo(3), q_hi(3), p_lo(3),
    ↪  p_hi(3)
```

```
352     integer,          intent(in   ) :: lo(3), hi(3)
353     integer,          intent(in   ) :: domlo(amrex_spacedim),
         ↪  domhi(amrex_spacedim)
354     integer,          intent(in   ) :: ncomp, p_ncomp
355     real(amrex_real), intent(in   ) :: vlo, vhi
356     real(amrex_real), intent(inout) ::
         ↪  q(q_lo(1):q_hi(1),q_lo(2):q_hi(2),q_lo(3):q_hi(3),ncomp)
357     integer,          intent(in   ) ::
         ↪  p(p_lo(1):p_hi(1),p_lo(2):p_hi(2),p_lo(3):p_hi(3),p_ncomp)
358     integer,          intent(in   ) :: phase
359     integer,          intent(in   ) :: dir
360
361     integer :: ilo, ihi, jlo, jhi, klo, khi
362     integer :: i, j, k, n
363     integer :: imin, imax, jmin, jmax, kmin, kmax
364
365     ilo = domlo(1)
366     ihi = domhi(1)
367
368 #if AMREX_SPACEDIM >= 2
369     jlo = domlo(2)
370     jhi = domhi(2)
371 #endif
372
373 #if AMREX_SPACEDIM == 3
374     klo = domlo(3)
375     khi = domhi(3)
376 #endif
377
378     do n = 1, ncomp
379
380        if (dir .eq. direction_x) then
```

```
381
382           do k = lo(3), hi(3)
383              do j = lo(2), hi(2)
384                 do i = lo(1), hi(1)
385                    if (p(i,j,k,1) == phase) then
386                       q(i,j,k,n) = vlo +
    ↪  1.0*(i-domlo(1)+1)/(domhi(1)-domlo(1)+2) * (vhi-vlo)
387                    else
388                       q(i,j,k,n) = 0.0
389                    end if
390                 end do
391              end do
392           end do
393
394        end if
395
396  #if AMREX_SPACEDIM >= 2
397
398        if (dir .eq. direction_y) then
399
400           do k = lo(3), hi(3)
401              do j = lo(2), hi(2)
402                 do i = lo(1), hi(1)
403                    if (p(i,j,k,1) == phase) then
404                       q(i,j,k,n) = vlo +
    ↪  1.0*(j-domlo(2))/(domhi(2)-domlo(2)) * (vhi-vlo)
405                    else
406                       q(i,j,k,n) = 0.0
407                    end if
408                 end do
409              end do
410           end do
```

```
411
412         end if
413
414 #endif
415
416
417 #if AMREX_SPACEDIM == 3
418
419         if (dir .eq. direction_z) then
420
421            do k = lo(3), hi(3)
422               do j = lo(2), hi(2)
423                  do i = lo(1), hi(1)
424                     if (p(i,j,k,1) == phase) then
425                        q(i,j,k,n) = vlo +
    ↪  1.0*(k-domlo(3))/(domhi(3)-domlo(3)) * (vhi-vlo)
426                     else
427                        q(i,j,k,n) = 0.0
428                     end if
429                  end do
430               end do
431            end do
432
433         end if
434
435 #endif
436
437      end do
438
439   end subroutine tortuosity_filic
440
441 end module tortuosity_filcc_module
```

Appendix D

Soluble Lead Flow Battery Modelling

D.1 The Soluble Lead Flow Battery: Image-based modelling of porous carbon electrodes

Image datasets from RVC electrodes are used as the computational domain for OpenImpala in Section 4.3.3, in order to calculate geometric properties across a range of charging states. These results were then used as part of a lookup table in modelling work as seen in this Appendix, carried out by Ewan Fraser. The modelling of the soluble lead flow battery is included in this Appendix to demonstrate how OpenImpala can be used to link together different scales of modelling, but to be clear, only the work included in Section 4.3.3 was carried out by the author.

The soluble lead flow battery: Image-based modelling of porous carbon electrodes

E.J. Fraser[a], J.P. Le Houx[a†], L.F. Arenas[a‡], K.K.J. Ranga Dinesh[a] and R.G.A. Wills[a]*

[a]Energy Technology Research Group, Faculty of Engineering and Physical Sciences, University of Southampton, Southampton, SO17 1BJ (United Kingdom).

Abstract

A novel numerical modelling framework coupling physics-based model equations and image-based boundary conditions is developed to simulate the behaviour of the soluble lead flow battery when reticulated vitreous carbon (RVC) electrodes are used. Experimental results are presented to validate the model. The open-source software OpenImpala is used to predict the macro-homogeneous properties of RVC from computed tomography data of various grades of RVC. The process is repeated on manipulated datasets where a voxel dilation technique has been used to estimate the geometry of RVC electrodes with a range of thicknesses of electrodeposited material. The model predicts that with a region of free electrolyte dividing the electrodes, the electrolyte velocity is low within the electrodes. This is exacerbated by a build-up of deposit close to the inlet. By dividing the electrodes with only a porous separator, a deposit build-up is no longer seen, and the concentration within the electrodes is shown to be far more even. Finally, with an applied current density of 50 mA cm^{-2}, the overpotential is predicted to be reduced by over 100 mV when 100 ppi RVC electrodes are used instead of 10 ppi electrodes. An experimentally validated voltage efficiency of over 80 % is achieved.

Keywords: Image-based modelling; reticulated vitreous carbon; soluble lead flow battery; redox flow batteries; energy storage; porous electrodes

1 Introduction

With the increased adoption of intermittent electricity generation at the expense of traditional synchronous generation, the demand for energy storage is growing [1]. A recent study by Homan et al. has shown that the standard deviation of the Great Britain grid frequency has increased significantly since 2014 [2]. This increase is correlated with a growth in renewable energy penetration such as solar and wind. However, the intermittent nature of renewable energy indicates that a combination of different technologies will be required for electricity networks to remain stable. Battery energy storage is likely to play a significant role to tackle the intermittent nature of renewable electricity generation and utilisation [1]. Although lithium-ion batteries provide the majority of battery energy storage currently installed globally [3], decoupling, or partial decoupling, of energy and power means redox flow batteries can have a lower environmental impact [4] and may be more economical for high energy applications [5].

While vanadium redox flow batteries provide the vast majority of installed capacity [3], other technologies [6], such as the soluble lead flow battery (SLFB), provide significant advantages over the VRFB. Lead has an existing supply chain, and it has been proposed that the SLFB can fit into the current recycling system [7, 8]. The SLFB can also operate in an undivided configuration, removing the substantial cost of a membrane or microporous separator [9] and has a higher discharge cell potential than the VRFB [10]. Moreover, this chemistry has been subject to continued interest and research for nearly two decades, has achieved high cyclability [11, 12] and has been investigated at pre-pilot scale [10].

The main electrode reactions involved in the SLFB are:

Positive:

$$Pb^{2+} + 2H_2O \rightleftharpoons PbO_2 + 4H^+ + 2e^- \quad E^0 = +1.46\ V\ vs\ SHE \qquad (1.1)$$

Negative:

$$Pb^{2+} + 2e^- \rightleftharpoons Pb \qquad E^0 = -0.13\ V\ vs\ SHE \qquad (1.2)$$

Cell:

$$2Pb^{2+} + 2H_2O \rightleftharpoons Pb + PbO_2 + 4H^+ \quad E^0_{cell} = +1.59\ V \qquad (1.3)$$

Where solid Pb is deposited at the negative electrode and solid PbO_2 is deposited at the positive electrode respectively during the charging process. During discharge, the solid deposits are dissolved back into the electrolyte as Pb^{2+} ions.

The SLFB contains a two-step charging voltage profile from the second charge onwards, which is associated with the positive electrode. This suggests some irreversibility in the electrode reaction during discharge, which leads to a build-up of material on the electrode surface. It has been proposed that there is a reversible side reaction where PbO_2 is only partially reduced to

*Email: rgaw@soton.ac.uk (R.G.A. Wills)

† Current address: Diamond Light Source, Diamond House, Harwell Science and Innovation Campus, Fermi Ave, Didcot, OX11 0DE (United Kingdom)

‡ Current address: Institut für Chemische und Elektrochemische Verfahrenstechnik - Forschungszentrum Energiespeichertechnologien. Technische Universität Clausthal, Goslar, 38640 (Germany). Tel. +49 5323 72-8069.

Pb^{2+} during discharge, also forming a solid PbO_x with x<2 [13]. Shah et al. [14] propose a simplification of this side reaction to:

$$PbO + H_2O \rightleftharpoons PbO_2 + 2H^+ + 2e^- \quad E^0 = +0.28\,V\ vs\ SHE \quad (1.4)$$

This is the side reaction that has been adopted in many SLFB models since [15-19].

Indeed, numerical simulation has been a valuable tool in the development of SLFB, mainly through understanding the current distribution and its relation to the location of deposits. For instance, early work by Pletcher et al. [13] demonstrated that there was a negative correlation between current density and coulombic efficiency in the initial cell design. However, simulations of the SLFB have shown that the low reversibility of the positive electrode reaction can be mitigated by increasing the effective electrode area at the positive electrode; the overpotential of the cell is decreased significantly due to the decrease in local current density [18, 20].

Later, Oury et al. [20] investigated the combination of a honeycomb-shaped positive electrode and two planar negative electrodes. Although the 3D electrode offers a larger surface area, they found that the positive current distribution is heavily reliant on the thickness of the honeycomb, with a higher current occurring at the edges of the channels. Shorter channels gave a more homogeneous current distribution and reduced the electrode area, thereby increasing the current density. Two cells share a positive electrode in this arrangement, making it impossible to arrange them into a bipolar stack. The monopolar stacks required to use this concept are too expensive for further development.

Nandanwar and Kumar [18] have shown that using cylindrical electrodes with the positive electrode on the outside substantially decreases the overpotential of the positive electrode, improving the voltage and hence energy efficiency. Energy efficiency was improved from 66% with planar electrodes to 80% using cylindrical electrodes, although the current density increases as the centre of the cylinder is approached. However, cylindrical and tubular flow cells are notoriously difficult to scale up as bipolar configurations are not possible. High productivity can only be achieved by connecting a large number of individual cells, which demand more material and take up more space.

A bipolar stack is clearly advantageous due to the reduced complexity, more even current distribution and increased space efficiency [21]. As an increased electrode area, particularly at the positive electrode, has been shown experimentally and theoretically to be advantageous in the SLFB [10], yet the two arrangements previously simulated (honeycomb and tubular electrodes) have issues when considering scale-up. On the other hand, a number of experimental studies have shown the effectiveness of reticulated vitreous carbon (RVC) as an electrode material [22-26]. RVC can be combined with a conventional bipolar plate for use in the SLFB in a similar manner to how carbon felt electrodes are used in an all-vanadium redox flow battery.

RVC has good chemical stability, high volumetric porosity and high permeability, making it useful for electrochemical flow cells [27]. RVC is commercially manufactured in a number of different grades ranging from 10 ppi to 100 ppi (pores per inch). It can also act as a coarse scaffold for deposition lead (Pb) and lead dioxide (PbO_2), giving structural rigidity to the electrodes and extended surface area [23, 24]. This may allow for a greater thickness of electrode deposits, increasing the capacity of the SLFB for a given electrode area. Carbon felts, which are often used in other flow batteries, e.g. the VRFB, are unsuitable for use in the SLFB because the small pores in the material would quickly become blocked with deposited Pb or PbO_2.

Our previous paper highlighted the effect of deposit growth in a high capacity SLFB [28]. A similar methodology is used to numerically model and simulate a SLFB with porous RVC electrodes in this study. In our previous work, the geometry of the reaction chamber changed during charge and discharge with the formation of Pb and PbO_2 deposits. However, in this study, we employed a fixed geometry because RVC electrodes can be modelled as a single porous domain with changing porosity, tortuosity, and permeability as a function of state of charge.

The objective of this study is to propose a novel numerical modelling framework to simulate the characteristics of SLFB with the presence of RVC electrodes. In our approach, the physical properties of RVC electrodes are derived using image-based computer tomography data. The coupling approach of physics-based modelling and image-based boundary conditions for electrodes provides a novel modelling framework to

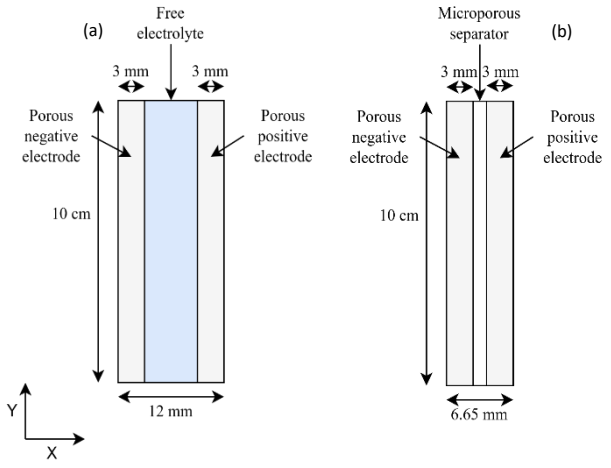

Figure 1: Schematic showing the geometry used to model the battery. (a) Electrolyte domain divided. (b) Microporous separator divided.

simulate SLFB with RVC electrodes. The paper is organised as follows. Section 2 described the experimental setup for validating the model, section 3 discusses the model setup, including governing equations, numerical details, and input data for calculations in section 4. Section 5 provides results and discussion, followed by conclusions.

2 Experimental setup

Experiments for validating the model were carried out in a flow cell with 4 cm × 2.5 cm electrodes. This cell consisted of acrylic flow frames, 1.5 mm (uncompressed) silicone foam gaskets, SGL carbon sigracell bipolar plates [29], 5 mm, 80 ppi RVC electrodes divided by an AmerSil FF60 microporous separator, copper foil current collectors, an insulating layer of hard norprene and 10 mm thick stainless steel endplates. The cell was held together with four M8 bolts, one in each corner. This also provided compression to maintain good contact between the RVC and the carbon-polymer plates. 400 cm^3 of electrolyte was circulated at a volumetric flow rate of 7 $cm^3\ s^{-1}$, corresponding to an average electrolyte velocity of approximately 2.3 $cm\ s^{-1}$ over plain bipolar pates.

The electrolyte consisted of 1 mol dm^{-3} methanesulfonic acid and 0.7 mol dm^{-3} lead methanesulfonate. Each cycle consisted of a charge for 1 hour followed by discharging until a 0.7 V cut-off voltage. Between each step, the cell was left at open circuit for 120 s.

3 Model setup

In this study, two configurations of the cell were used with slightly different geometry Figure 1 shows the geometry used in both configurations: Figure 1(a) shows the undivided configuration which includes two porous electrode domains separated by a 6 mm free electrolyte domain, and Figure 1(b) shows the divided configuration, which replaces the electrolyte domain with a microporous separator domain. The undivided configuration is similar to previous experimental studies that use RVC [22, 25, 26]. However, the divided configuration is suggested in this study as an alternative for improved cell performance. In a stack, this unit cell of a negative porous electrode, an electrolyte/separator domain, and a positive porous electrode would be divided by bipolar plates and current collectors at both ends of the stack. Neither of these is explicitly modelled; the boundary conditions simply imply their presence. The electrical resistance of these components and the interface between the plate and the RVC electrodes are expected to be small.

3.1 Governing Equations

In the free electrolyte domain, the flow is assumed to be laminar. The electrolyte velocity, $\boldsymbol{u}$ in m s^{-1}, is therefore described with the laminar form of the Navier-Stokes and continuity equations.

$$\rho\frac{\partial \boldsymbol{u}}{\partial t} + \rho(\boldsymbol{u}\cdot\nabla)\boldsymbol{u} = \nabla\cdot[-p + \mu\nabla\boldsymbol{u}] \qquad (3.1)$$

$$\nabla\cdot\boldsymbol{u} = 0 \qquad (3.2)$$

Where ρ is the electrolyte density in kg m^{-3}, p is pressure in Pa, and μ is dynamic viscosity in Pa s.

The electrolyte density and viscosity vary with its composition. Using Krishna et al.'s measurements, [30], viscosity in mPa s, μ_e, is related to concentrations, c, in mol dm^{-3} by equation 3.3 and electrolyte density in kg dm^{-3}, ρ_e, is related to concentration in mol dm^{-3} by equation 3.4.

$$\mu_e = 0.96 + 0.364\cdot c_{PbII} + 0.407\cdot {c_{PbII}}^2 + 0.262\cdot c_H \qquad (3.3)$$

$$\rho_e = 1.0 + 0.3\cdot c_{PbII} + 0.03\cdot c_H \qquad (3.4)$$

In the porous domains (RVC electrodes), the fluid flow is described using the Brinkman equations. These are an extension of Darcy's law which include dissipation of energy due to viscous shear forces, in a similar manner to Navier-Stokes but in porous media. The Brinkman equations become relevant at higher flow rates and are valid at high porosity [31]:

$$\frac{1}{\epsilon}\rho\frac{d\boldsymbol{u}}{dt} + \frac{1}{\epsilon}\rho(\boldsymbol{u}\cdot\nabla)\boldsymbol{u}\frac{1}{\epsilon} = -\nabla p + \mu\frac{1}{\epsilon}\nabla^2\boldsymbol{u} - \frac{\mu}{\kappa}\boldsymbol{u} \qquad (3.5)$$

Where ϵ is the porosity of the porous domain and κ is the permeability of the domain in m^2.

Permeability, κ, is calculated using the Kozeny-Carmen equation:

$$\kappa = \frac{\varepsilon^3}{c_\kappa \tau^2 {a_v}^2} \quad (3.6)$$

Where c_κ is the Kozeny constant, τ is tortuosity of the porous media and a_v is the surface area of the porous electrode.

Conservation of mass of each species gives:

$$\frac{\partial c_i}{\partial t} = -\nabla \cdot \boldsymbol{N_i} \quad (3.7)$$

Where the flux of species i (H^+, Pb^{2+}, $CH_3SO_3^-$) in mol m^{-2} s^{-1}, $\boldsymbol{N_i}$ is calculated using the Nernst-Planck equation.

$$\boldsymbol{N}_i = -D_{i,eff}\nabla c_i - z_i u_{m,i,eff} F c_i \nabla\phi + \boldsymbol{u} c_i \quad (3.8)$$

For species i, $D_{i,eff}$ is its effective diffusion coefficient in m^2 s^{-1}, c_i is its concentration in mol m^{-3}, z_i is its valence and $u_{m,i,eff}$ is its effective mobility in s mol kg^{-1}. ϕ is the electrolyte potential in V, F is Faraday's constant in C mol^{-1}.

The mobility, $u_{m,i}$ was such that the conductivity closely matches experimental measurements by Krishna et al. [30]. The method for calculating this is explained in a previous study [32].

In the porous electrode:

$$D_{i,eff} = F_d D_i \quad (3.9)$$

$$\sigma_{s,eff} = (1-\epsilon) F_s \sigma_s \quad (3.10)$$

Where F_d is the correction factor for diffusion and F_s is the correction factor for electrical conductivity. In the Bruggeman case, $F_d = \epsilon^{1.5}$ and $F_s = (1-\epsilon)^{1.5}$. $D_{i,eff}$ is the effective diffusion coefficient of species i in m^2 s^{-1}, ϵ is the electrode porosity and D_i is the diffusion coefficient of species i in m^2 s^{-1}. $\sigma_{s,eff}$ is the effective conductivity of the electrode and σ_s is the conductivity of the electrode both in S m^{-1}.

In the Free electrolyte, $D_{i,eff} = D_i$ and therefore, $u_{m,i,eff} = u_{m,i}$

3.2 Boundary conditions

A laminar inflow condition was prescribed by solving equation 3.11 for an average inlet velocity. The no-slip boundary condition was applied at the current collector surface.

$$-p_{in}\boldsymbol{n} = L_{in}\nabla_t \cdot \left(-p\boldsymbol{I} + \mu\frac{1}{\epsilon}\nabla_t \boldsymbol{u} - \frac{2}{3}\mu\frac{1}{\epsilon}(\nabla\cdot\boldsymbol{u})\boldsymbol{I}\right) \quad (3.11)$$

Where p_{in} is the inlet pressure, $\boldsymbol{n}$ is the normal vector, L_{in} is the inlet length, p is the local pressure, μ is viscosity, ϵ is the porosity, $\boldsymbol{u}$ is velocity, and $\boldsymbol{I}$ is the unity vector.

$$u = 0,\ v = 0 \quad (3.12)$$

At the outlet, pressure and diffusive fluxes and current density normal to the outlet boundary are equal to zero.

$$-D_i\nabla c_i \cdot \boldsymbol{n} = 0, \qquad \boldsymbol{j}\cdot\boldsymbol{n} = 0, \quad p = 0 \quad (3.13)$$

Inlet concentrations for each species were calculated assuming perfect mixing in the reservoir using an ordinary differential equation, equation 3.14.

$$c_{in,i} = \int \frac{L}{V}\left(\int_{outlet} \boldsymbol{N}_i \cdot \boldsymbol{n}\, dS - \int_{inlet} \boldsymbol{N}_i \cdot \boldsymbol{n}\, dS\right) dt \quad (3.14)$$

Where L is the width of the cell out of plane and V is the electrolyte reservoir volume.

The porosity of each electrode varied with volume of deposited material, i.e. state of charge. The change in porosity was calculated using Faraday's law, equation 3.15. 100% efficiency of the deposition reactions in the electrodes was assumed, and the deposits were considered to form as fully dense materials on the RVC surface with densities for Pb and PbO_2 as described in Table 2.

$$m_i = \frac{QM_i}{Fz} \quad (3.15)$$

Butler-Volmer kinetics were used, described by equation 3.16 and equation 3.17 for the negative and positive reactions, respectively. The positive side reaction uses a modified Bulter-Volmer equation to describe the kinetics, equation 3.18. To account for the availability of solid species in the reaction kinetics during discharge, when the solid surface concentration approached 0, the surface area in the porous domain tended to 0 during discharge. This represents the active surface area, as the discharge (dissolution) reaction only occurs at the surface of the deposits, not at the stripped RVC surface.

Negative electrode:

$$i_{loc} = Fk_{0,Pb}c_{Pb^{2+}}\left(e^{\left(\frac{\alpha_{o,neg}F\eta_{neg}}{RT}\right)} - e^{\left(\frac{-\alpha_{r,neg}F\eta_{neg}}{RT}\right)}\right) \quad (3.16)$$

$$i_v = \begin{cases} a_{v,neg} i_{loc} & c_{Pb} > 0 \\ 0 & c_{Pb} = 0\ during\ discharge \end{cases}$$

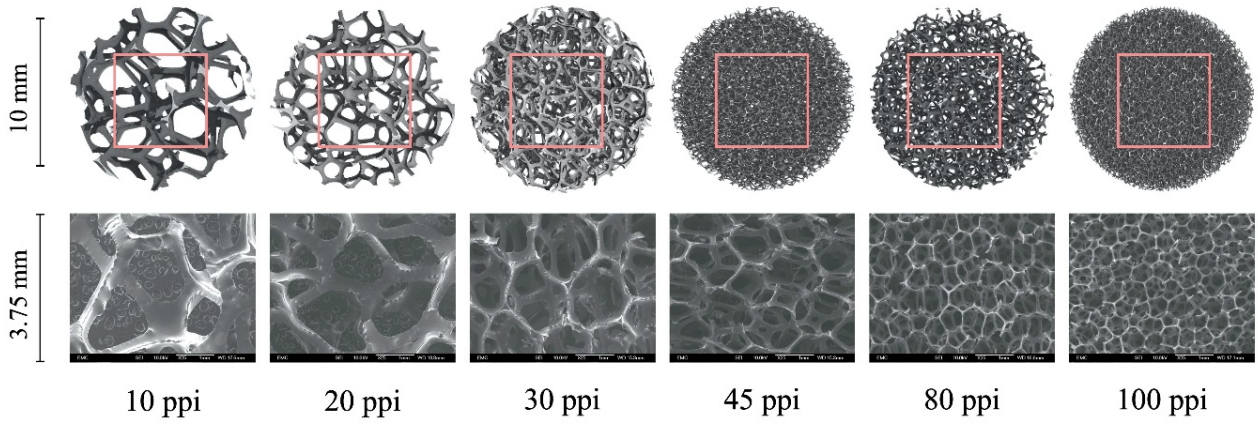

Figure 2: Thresholded top views and greyscale views of the RVC CT data for 10 ppi, 20 ppi, 30 ppi, 45 ppi, 80 ppi and 100 ppi. The datasets are cropped to the pink (lighter coloured) box of dimensions 1072 x 1104 x 1296.

Positive electrode:

Main reaction

$$i_{loc} = Fk_{0,PbO_2}c_{Pb^{2+}}\frac{c_{H^+}}{c_{H^+_{ref}}}\left(e^{\left(\frac{\alpha_{o,pos}F\eta_{pos}}{RT}\right)} - e^{\left(\frac{-\alpha_{r,pos}F\eta_{pos}}{RT}\right)}\right) \; c_{PbO2} > 0 \qquad (3.17)$$

Side reaction

$$i_{loc} = F\left(k_{f,PbO}c_{PbO}^2 e^{\left(\frac{F\eta_{pos}}{RT}\right)} - c_{H^+}c_{PbO_2}k_{b,PbO}e^{\left(\frac{F\eta_{pos}}{RT}\right)}\right)$$

$$i_v = a_{v,pos}i_{loc} \qquad (3.18)$$

Where i_{loc} is the local current density in A m^{-2}, $i_v$is the local volumetric current density in A m^{-3}, a_v is the surface area per unit volume in m^{-1}, $k_{0,Pb}$ and $k_{0,PbO_2}$are rate constants and $k_{f,PbO}$ is the forward rate constant for the side reaction, and $k_{b,PbO}$ is the backward rate constant for the side reaction in m s^{-1}, α is the transfer coefficient. Subscripts o and r represent the anodic (oxidation) and cathodic (reduction) reactions, and pos and neg denote positive and negative electrodes). η is the overpotential in V and is defined by equation 3.19.

$$\eta = \phi_s - \phi_l - E_{eq} \qquad (3.19)$$

ϕ_s is the electrode potential and ϕ_l is the electrolyte potential in V, and E_{eq} is the equilibrium potential in V, calculated at each electrode using the Nernst equation, equations 3.20a and 3.20b.

Negative $$E_{Eq} = E_0 + \frac{RT}{zF}ln\left(\frac{c_{Pb}}{c_{ref}}\right) \qquad (3.20a)$$

Positive $$E_{Eq} = E_0 - \frac{RT}{zF}ln\left(\frac{c_{Pb}}{c_{H^+}}\right) \qquad (3.20b)$$

Where E_0 is the reduction potential in V at the reference concentration, c_{ref} R is the universal gas constant in J K^{-1} mol^{-1}, T is the temperature in K.

The negative current collector is grounded:

$$\varphi = 0 \qquad (3.21)$$

At the positive current collector surface, an average current density is applied such that:

$$-\frac{\int_{\partial\Omega} i\cdot\boldsymbol{n}\, dS_+}{S_+} = i_{average} \qquad (3.22)$$

3.3 Initial conditions

Initial values for parameters used in the simulations are displayed in Table 1. Concentrations similar to those in the literature were chosen with corresponding values for density and viscosity [10]. The remaining initial values were selected to ensure consistency with the boundary conditions. To ensure non-conflicting boundary and initial conditions, several initial values were set to 0. The boundary conditions were then applied with a smoothed Heaviside function, which uses a piecewise 5th degree polynomial equation, applied over the first 1.5 s of the simulation.

Table 1: Initial conditions applied to the simulations of SLFBs.

Variable	Initial value	Unit
u	0	m s^{-1}
v	0	m s^{-1}
p	0	Pa
$cPbII_0$	700	mol m^{-3}
cH_0	1000	mol m^{-3}
ϕ_l	0	V
ϕ_s	0	V
$\phi_{s,+}$	0	V

$a_{v,10}$	620	m^{-1}
$a_{v,30}$	1400	m^{-1}
$a_{v,45}$	1450	m^{-1}
$a_{v,80}$	1700	m^{-1}
$a_{v,100}$	1450	m^{-1}
ε	0.97	-
μ_{e0}	1.6762	mPa s
ρ_{e0}	1.727	kg dm^{-3}

3.4 Parameters

Values of parameters used in the simulations are displayed in Table 2. The majority are as defined in our previous publications [28, 32].

Table 2: Parameters used in the solution of the simulated SLFBs.

Parameter	Value	Unit	Reference
A	0.51	$dm^{3/2}\ mol^{-1/2}$	[32]
B	3.29	$dm^{3/2}\ mol^{-1/2}$	[32]
b_1	3.52243	$dm^3\ mol^{-1}$	[32]
b_2	0.94331	$dm^3\ mol^{-1}$	[32]
b_3	0.18444	$dm^3\ mol^{-1}$	[32]
D_{PbII}	7e-10	$m^2\ s^{-1}$	[28]
D_H	9.3e-9	$m^2\ s^{-1}$	[28]
D_{CH3SO3}	1.33e-9	$m^2\ s^{-1}$	[32]
k^0_{Pb}	2.1e-7	$m\ s^{-1}$	[28]
k^0_{PbO2}	2.5e-7	$m\ s^{-1}$	[28]
k^0_b	4.5e-7	$mol\ m^{-2}\ s^{-1}$	[28]
k^0_f	0.002	$mol\ m^{-2}\ s^{-1}$	[28]
K	11.25	-	
ρ_{Pb}	11.337	kg dm^{-3}	[33]
ρ_{PbO2}	9.65	kg dm^{-3}	[33]
ρ_{PbO}	9.53	kg dm^{-3}	[33]
σ_{Pb}	4.69e6	$S\ m^{-1}$	[34]
σ_{PbO2}	8000*	$S\ m^{-1}$	[35]
σ_{RVC}	330	$S\ m^{-1}$	[36]
T	300	K	
z_{PbII}	2	-	
z_{H+}	1	-	
$z_{CH3SO3-}$	-1	-	

*Approximated constant value based on a mixture of α- and β- phases.

3.5 Numerical details

The equations were implemented and solved using COMSOL Multiphysics version 5.4. A Multifrontal Massively Parallel Sparse (MUMPS) direct solver was used for all simulations, and an implicit Backward Differentiation Formula (BDF) method was employed to control the time steps taken. First-order discretisation was employed for velocity and pressure, while linear discretisation was employed for concentration and potential fields. When compared with quadratic discretisation for concentrations and potential, a negligible difference was found.

Each domain was meshed using rectangular elements with 30 elements across the width of each electrode domain and 200 elements across the height of all domains. The elements were distributed symmetrically, with elements decreasing in size arithmetically such that the central elements were 30 times the size of the outer elements. A similar distribution was employed across the width of the electrode domains such that the inner elements were five times larger than the outer elements. Further boundary layer elements were used at the outer boundaries of the entire domain. The total number of elements ranged from approximately 13000 to 19000 depending on the problem solved.

4 Image data (CT)

4.1 Computational setup

Reticulated vitreous carbon electrode substrates were physically imaged to provide the scaffold geometries for the model. The raw CT data was obtained from work by Arenas et al., which used a Nikon/X-Tek XTH 225 instrument, with an isotropic resolution of 9.6 µm per voxel and a detector size of 2000 x 2000 pixels [36]. The data for scans of 10, 30, 45, 80 and 100 ppi (pores per inch) was binarised into two constituent phases, solid and porous volume, and cropped into a cuboid domain of dimensions 1072 x 1104 x 1296. Thresholded and greyscale views of 10 ppi, 20 ppi, 30 ppi, 45 ppi, 80 ppi and 100 ppi data is shown in Figure 2.

For each grade of RVC, the morphology of the porous electrodes was virtually modified [37] by voxel dilation of the solid domain of the RVC CT dataset in the open-source software ImageJ [38]. This virtual dilation was performed to see the effect of deposit accumulation on the transport processes of the porous electrode. The dilated volume corresponded to the volume of electrodeposited material, which is assumed to grow uniformly at all points of the porous substrate. Each dataset was dilated by a single voxel and then further dilated until the following specified total solid volume fractions were reached: 10%, 20%, 30%, 50% and 80%. Both the original and newly dilated datasets had the raw greyscale values multiplied by 0.5 to achieve an

electrolyte phase of 0 and a solid phase of 127. The original dataset was then added to each of the dilated datasets to achieve a three-phase segmented dataset with RVC holding a value of 255, the artificial electrode deposit 127 and the electrolyte 0.

For each of these 35 datasets, the porosity and tortuosity values were calculated using the open-source software, OpenImpala [39]. These calculations were performed in the *x*-direction, as previous work by Arenas et al. has shown each RVC grade to have good isotropy [36]. Tortuosity, in this case, refers to effective tortuosity, not geodesic tortuosity [40], and is calculated by solving a steady-state Fickian diffusion problem:

$$D^{eff} = D\,\frac{\varepsilon}{\tau} \qquad (4.1)$$

Where τ is the tortuosity, ε the volume fraction, D^{eff} the effective diffusivity of the conducting phase and D the intrinsic diffusivity [39]. The computations were performed on the University of Southampton's supercomputer, Iridis 5 [41].

The surface area for each dataset was calculated using the surface area analysis function in the ImageJ plugin BoneJ [42]. This approximates the surface area of the dataset by creating a surface mesh from the raster dataset and then calculates the surface area of the mesh.

5 Results and discussion

5.1 Virtual dilation

Figure 3 shows the steady-state diffusion gradients for each of the seven datasets of the 100 ppi RVC sample. From visual inspection, it can be seen that at higher levels of lead compound deposition, pathways throughout the domain have been closed off, leading to more contorted diffusion paths. Additionally, the closing of transport paths could lead to areas of the solid fraction being inaccessible on discharge, reducing ion transport. Therefore, the management of lead compound accumulation in the porous electrode is a key component in the correct operation of the soluble lead flow battery.

Figure 4 shows the complete plot of results from the image analysis. Effective tortuosity values are plotted against solid volume fraction for each of the RVC grades. There is a general trend of tortuosity increasing as lead is accumulated on the electrode, with a significant increase apparent at values of 80% solid, likely due to the closing of transport paths. Additionally, standard deviation across the grades increases with tortuosity. At low levels of deposition, the value of tortuosity is found to be similar across the grades of RVC, which is in agreement with Arenas et al. [36]. However, as the solid fraction increases, discrepancies between the different grades become more significant. This is a key result. At low levels of deposition, the morphology of the RVC electrode appears to have little effect

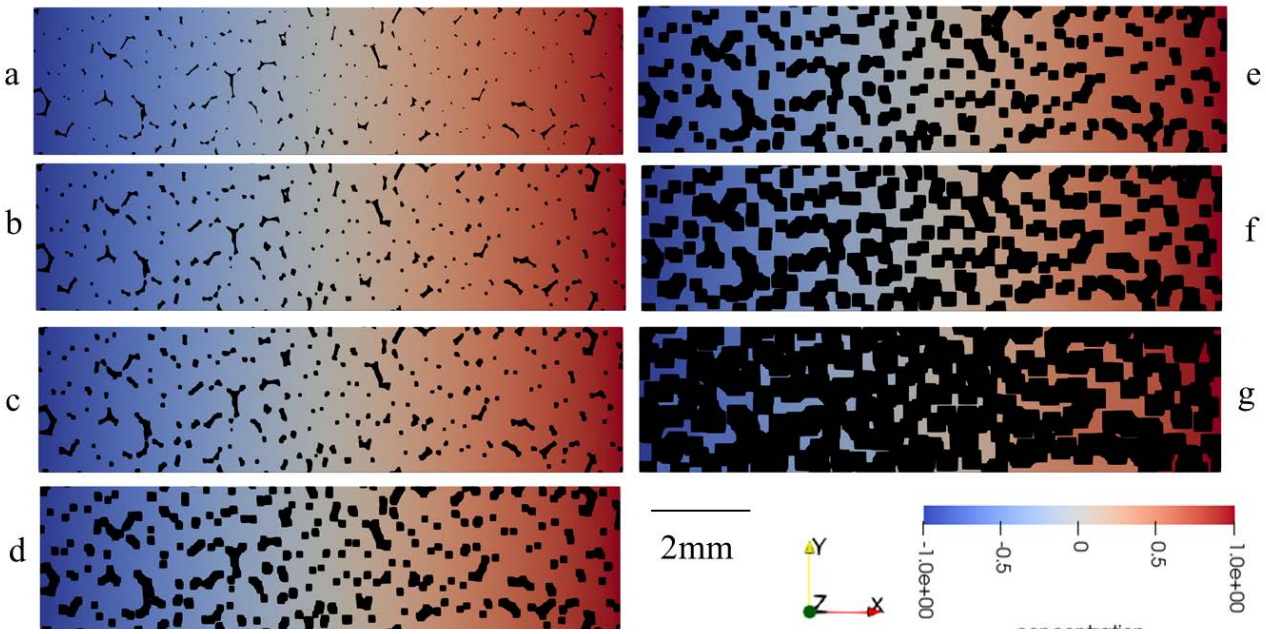

Figure 3: Steady-state diffusion profiles for the 100 ppi RVC sample at each deposition: (a) clean, (b) one voxel dilation, (c) 10% solid volume fraction, (d) 20% solid volume fraction, (e) 30% solid volume fraction, (f) 50% solid volume fraction and (g) 80% solid volume fraction. Flow is from left to right and these are 2D representative strips of the full datasets.

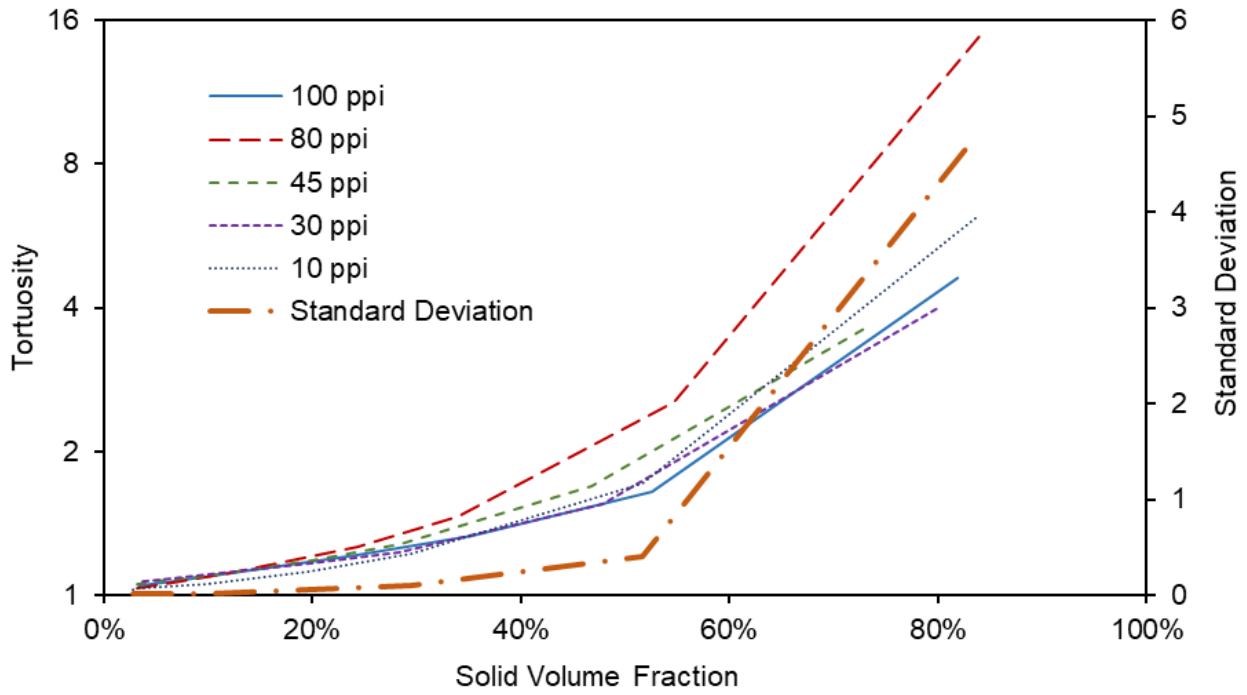

Figure 4: Graph to show how the tortuosity of the RVC samples varies depending on the solid volume fraction and ppi value. The standard deviation between results significantly increases at higher lead deposition (i.e. 80% solid volume fraction).

on transport processes, but as lead compounds are accumulated, the structure becomes increasingly important.

Furthermore, the 80 ppi grade has a significantly higher tortuosity value, ~15.2, at a solid volume fraction of 80%. The specific morphology of this grade has resulted in a very contorted diffusion path. When designing electrodes for use in the soluble lead flow battery, it is important to consider the effect of morphology on both the transport processes occurring in a fully discharged state, as well as in the fully charged state when lead compound accumulation is higher.

The tortuosity and porosity values obtained through these methods are then used as values in a lookup table for the numerical model to represent the varying conditions throughout charge/discharge more accurately. At each timestep, the volume fraction is taken, and a linear interpolation function is used with the lookup table to determine the corresponding values of tortuosity and porosity.

5.2 Undivided cell

Initially, the cell was set up with 3 mm RVC domains at the positive and negative electrodes, separated by a 6 mm electrolyte domain. See Figure 1a. The total gap between current collectors was 12 mm. For each grade of RVC described, an applied current density of 20, 30 and 50 mA cm^{-2} was applied at the positive current collector boundary for a duration of 1 hour. The cell was then discharged with the same applied current density until the cell voltage dropped to 1.3 V.

A value of 1.3 V was chosen as the discharge cut-off voltage because, after this point, the cell potential drops sharply [9]. While a lower cut-off voltage does not change the discharge time significantly, it added a significant amount of computational time due to the very short time-stepping

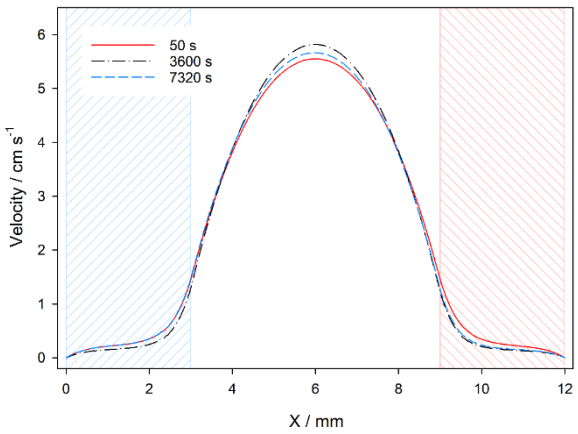

Figure 5: Velocity profile across the mid-height of the electrodes of the undivided cell using 10 ppi RVC and an applied current density of 20 mA cm^{-2}. While a roughly parabolic flow profile is seen within the electrolyte domain, a sharp decrease in velocity is seen within the porous electrodes. Peak flow velocity in the electrolyte domain changes by approximately 0.2 cm s^{-1} between charge and discharge. A much greater change in velocity is seen in the negative electrode between charge and discharge, where the velocity is generally greater overall. The negative (left, blue) and positive (right, red) electrodes domains are highlighted.

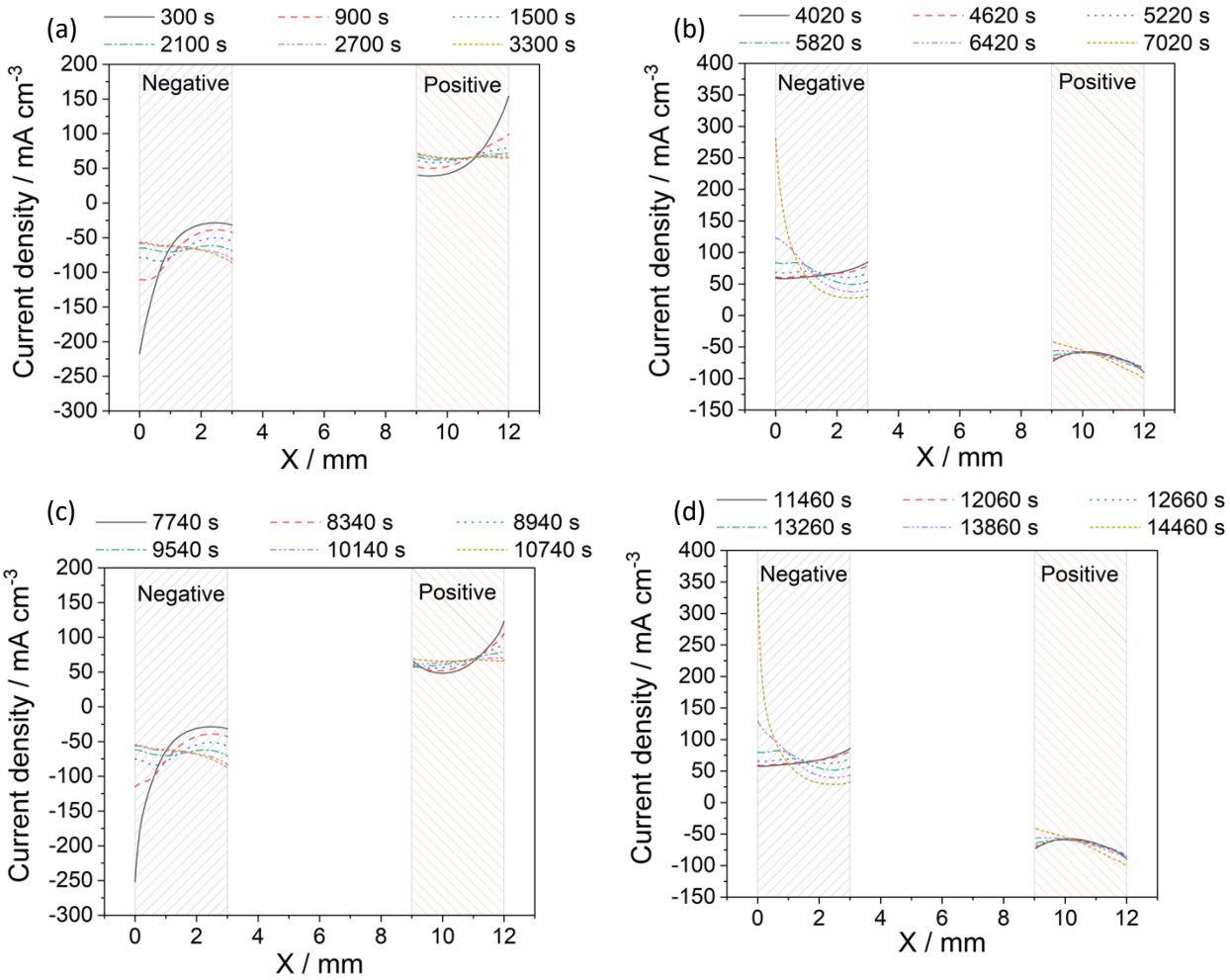

Figure 6: Current distribution in the x-direction at the mid-height of the electrodes for the undivided configuration of the 10 ppi electrodes with an applied current density of 20 mA cm^{-2} for the first charge (a), the first discharge (b), the second charge (c) and the second discharge (d).

required to calculate the period of rapid potential change. For brevity, general trends from the simulation results are discussed using the 10 ppi case as a representative example. Other grades of RVC are included where relevant comparisons are made.

Figure 5 shows the velocity profile across the cell, where 0-3 mm corresponds to the negative electrode domain, 3-9 mm corresponds to the electrolyte domain and 8-12 mm corresponds to the positive electrode domain. The three velocity profiles shown correspond to just after the start of the first charge (t = 50 s), the end of the first charge period (t = 3600 s) and the end of the first discharge period (t = 7320 s). In this configuration, as seen in Figure 5, the electrolyte velocity is considerably lower in the porous electrodes than in the free electrolyte, even at initial conditions and for the RVC grade with the largest pore size (10 ppi). It can be seen that by the end of the first charge period, the velocity within both positive and negative electrode domain decreases, corresponding to the increase in tortuosity caused by the build-up of deposits. By the end of the first discharge period, the velocity profile in the negative electrode is broadly similar to that of the starting state. In contrast, the velocity in the positive electrode remains lower than the starting state, indicating a build-up of insoluble leady oxides. Figure 5 shows that after the first charge, when the velocity distribution changes by a similar magnitude, the velocity in the positive electrode stays very low during the remaining cycles, irrespective of SoC. However, the velocity in the negative electrode returns to near its initial value at the end of discharge. This is due to the side reaction at the positive electrode meaning solid PbO remains even after discharge. Therefore, the positive electrode permeability remains lower than that of the negative electrode. The peak velocity in the middle of the electrolyte domain increases as deposits are built up within the electrodes. More electrolyte is forced through the lower resistance, free electrolyte domain.

The current density in the porous electrodes varied spatially in both *x* and *y* directions. Figure 6 shows the current distribution

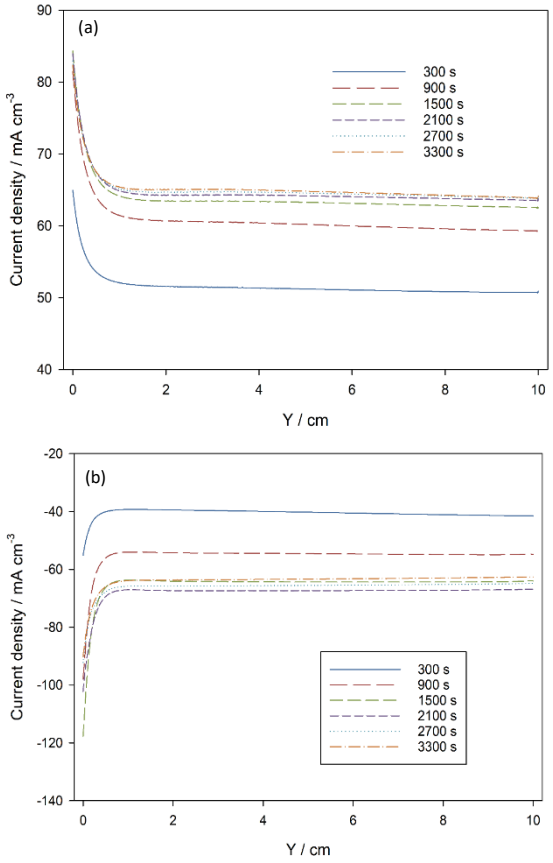

Figure 7: Current distribution in the y-direction taken as a slice at the midpoint of the electrode domains for the 10 ppi electrodes. y=0 is at the inlet at the bottom of the cell. The distribution is shown in the positive electrode (a) and the negative electrode (b). There is a significantly increased current density in both electrodes in the first 1 cm of the domain. Current density varies with time as the current is not even in the *x*-direction.

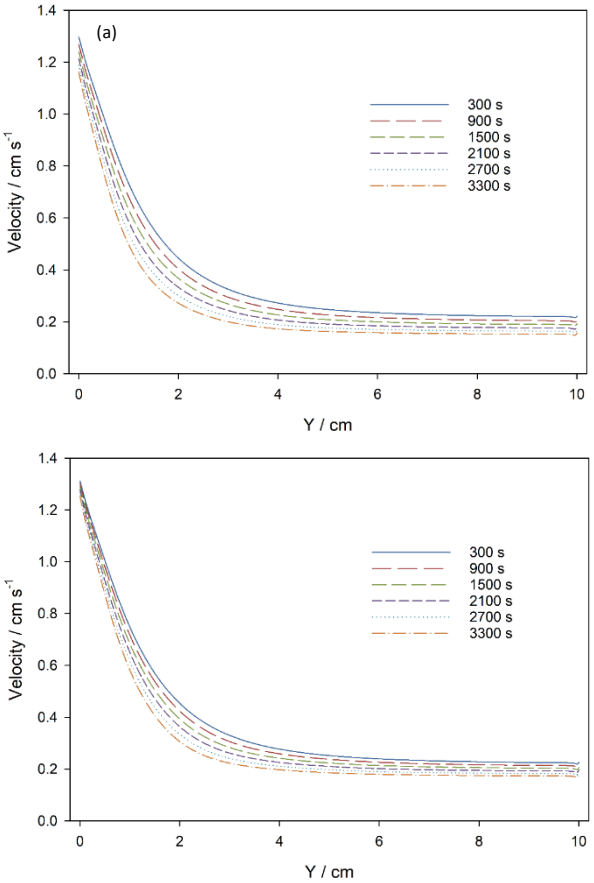

Figure 8: Velocity distribution in the y-direction at the midpoint of the 10 ppi positive electrode (a) and negative electrode (b). The velocity begins at over 1 cm s^{-1} near the inlet in both electrodes but rapidly reduces with increased distance from the inlet. The change in velocity levels off after approximately 4 cm and remains relatively constant between 1.5 and 3 mm s^{-1} in both electrodes.

in the *x*-direction at regular intervals during each charge and discharge. The first charge is from 0-3600 s, the first discharge from 3720-7320 s, the second charge from 7440-10740 s and the second discharge from 11160-14760 s. For each grade of RVC and at all applied current densities, the current was initially highest near the current collectors. As the cell charged, the current density became more evenly distributed in the *x*-direction.

The current density was highest near the inlet throughout charge and discharge in both electrodes in this configuration. Figure 7 shows the current distribution in the *y*-direction at the midpoint of both porous electrodes. There was a substantial increase in current density in both electrodes in the closest 1 cm to the inlet.

As such, as charging continued, the higher deposition rate reduced the porosity near the inlet. The electrolyte flow was, therefore, further diverted around the electrodes. As shown in Figure 8, which shows the electrolyte velocity distribution in the

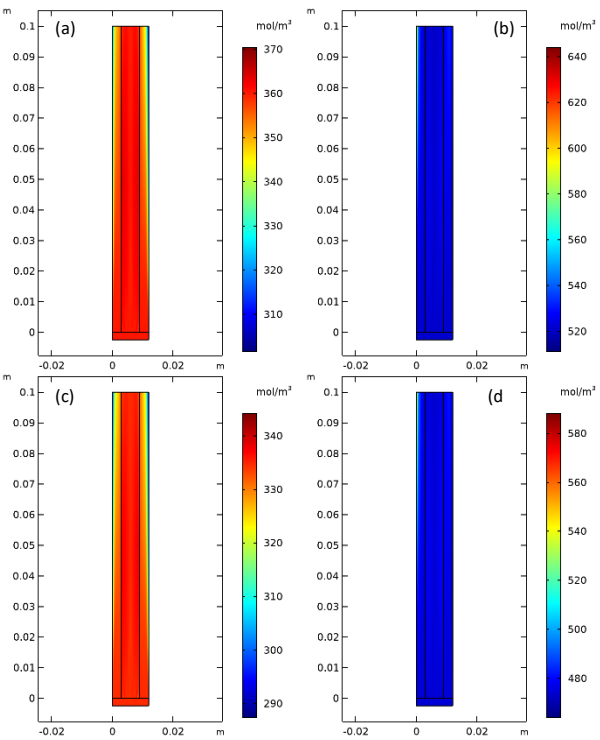

Figure 9: Pb^{2+} concentration distribution near the end of the first charge for the 50 mA cm^{-2} cell using 10 ppi electrodes during charge 1 (a), discharge 1 (b), charge 2 (c) and discharge 2 (d).

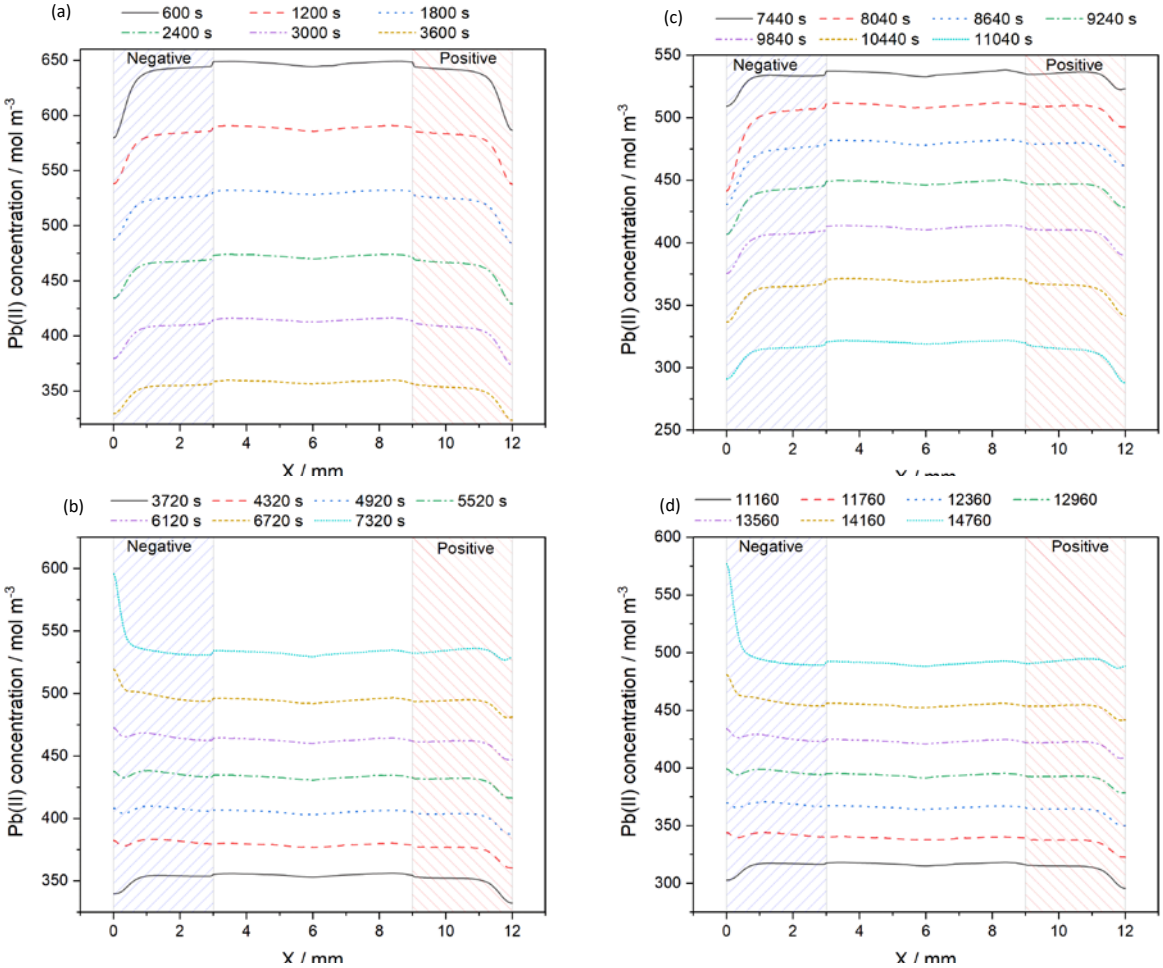

Figure 10: Distribution of Pb^{2+} concentration in the x-direction at the mid height of the electrodes for the undivided configuration of the 10 ppi electrodes with an applied current density of 20 mA cm^{-2}.

y-direction with the midpoints of both electrodes, the electrolyte velocity distribution is uneven in the *y*-direction as the charge cycle continues. Throughout cycling, the electrolyte velocity decreases sharply in the first few cm of the electrodes. By the end of the first charge, the flow in the top 6 cm of both electrodes drops below 2 mm s^{-1}, less than 10% of the bulk velocity. Figure 9 shows the concentration distribution after 3550 s, shortly before the end of the first charge. Here it is seen that with the reduced electrolyte flow, the Pb^{2+} concentration within the electrodes was not readily replenished. Near the outlet, the Pb^{2+} concentration in both electrodes drops to below 0.1 mol dm^{-3}.

Figure 10 shows the concentration distribution across the cell at the midpoint of the electrodes at varying times and current densities for each RVC grade. At higher rates of charge and grades of RVC with a larger number of pores, the concentration gradients are larger and for all cells at 50 mA cm^{-2} near the end of charge, the Pb^{2+} concentration drops to below 0.1 mol dm^{-3} compared to a bulk concentration of 0.22 mol dm^{-3}, see Figure 9. This indicates that the electrolyte flow and diffusion of Pb^{2+} are inadequate to maintain a high current within the electrodes near the current collector when lead utilisation in the bulk electrolyte is high. The reduced Pb^{2+} concentration leads to a higher overpotential required to maintain a current density, and hence in areas with a lower Pb^{2+} concentration, the current density is decreased. A higher current density is therefore seen close to the boundary with the bulk electrolyte. In real cells, this may lead to Pb being deposited at the interface between the porous electrode domain and the electrolyte domain, as is described by Iacovangelo and Will during zinc deposition on porous carbon electrodes [43], negating the advantage of a lower local current density from a porous electrode.

5.3 Divided cell

The free electrolyte domain was removed to encourage a higher flow within the electrodes and overcome this reduction in Pb^{2+} concentration. Clearly, the electrodes cannot be touching, and in a real cell, dendrites are common and can grow between the electrodes [10]. Hence, a non-conducting microporous separator domain was placed between the electrodes to

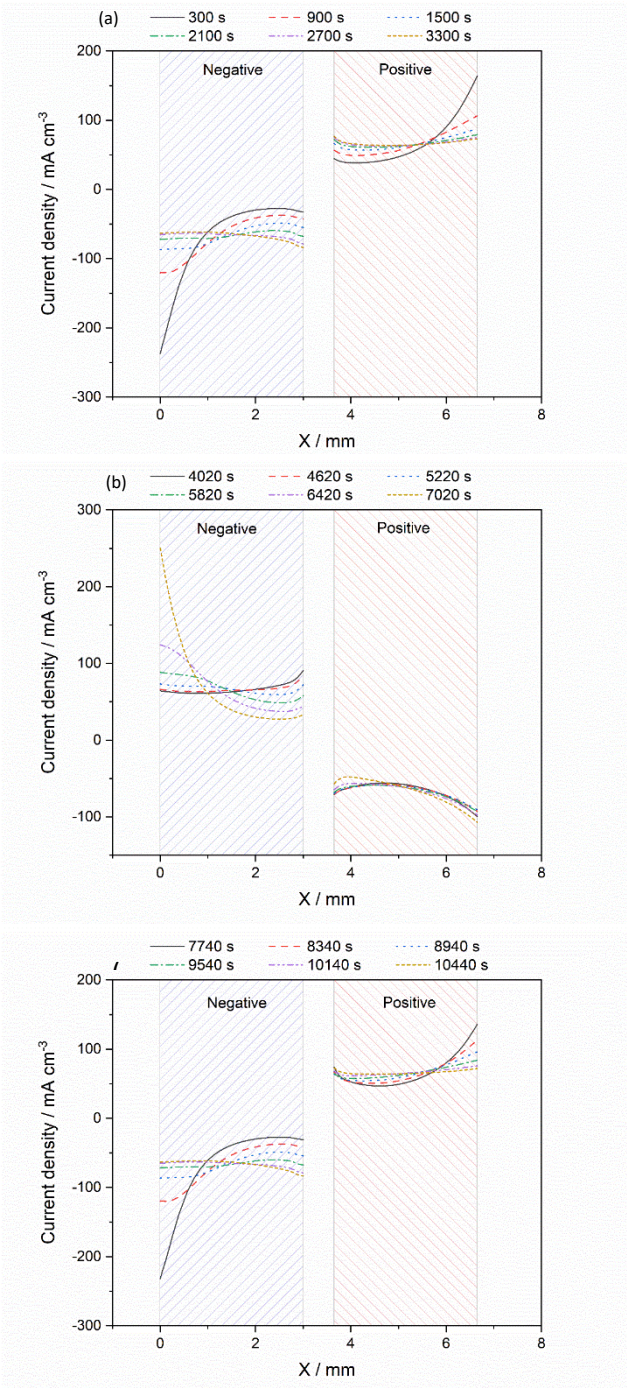

Figure 11: Current distribution in the x-direction at the mid-height of the electrodes for the divided configuration of the 10 ppi electrodes with an applied current density of 20 mA cm^{-2} during charge 1 (a), discharge 1 (b) and charge 2 (c).

prevent short-circuiting but to allow the transfer of ions. A typical example is microporous polyethylene, which is commonly used in Zn-Br RFBs [44].

The same 1 hour charge cycle was applied to this divided arrangement, with 20, 30 and 50 mA cm^{-2} applied to each grade of RVC. Figure 11 shows the current distribution in the *x*-direction for the divided arrangement. The distribution of current within the electrodes is very similar to that in the undivided configuration.

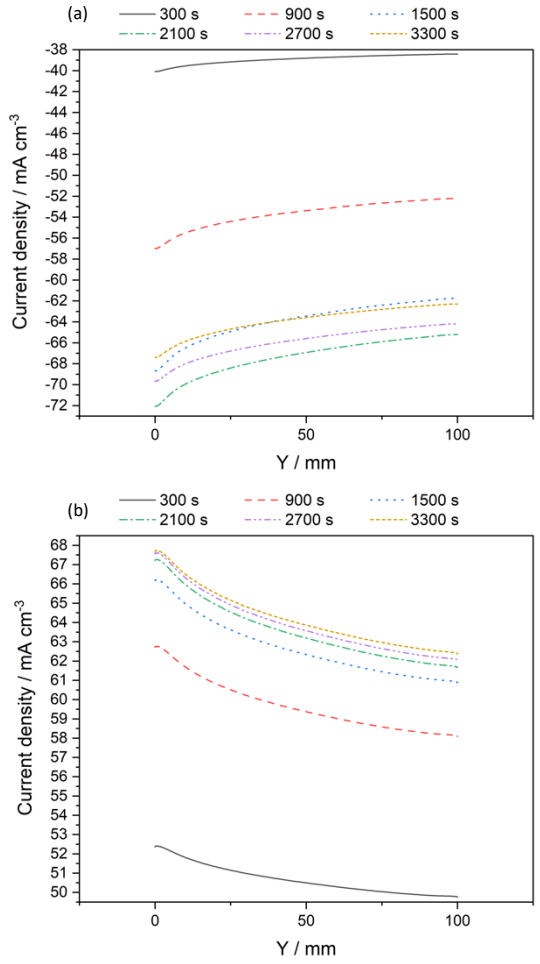

Figure 12: Current density distribution in the y-direction at the midpoint of the 10 ppi negative (a) electrode and the positive (b) electrode of the divided cell.

The current density starts off highest closest to the current collector at the start of charge. By the end of the 1 hour charge, while there is a slight increase in current at the outer edge of both electrodes, the current distribution is far more even. The current density near the inlet is also substantially less pronounced. The current density averaged across the inlet is approximately 71 mA cm^{-3} at the positive electrode and 69 mA cm^{-3} in the negative electrode, compared to the average in the electrode of 67 mA cm^{-3}. Figure 12 shows that while there is some variation in current density vs *y*, which is to be expected due to the increased concentration overpotential with increased distance from the inlet, there is not the sharp increase near the inlet as seen with the undivided configuration.

As the electrolyte is forced through the electrodes, the concentration of soluble species remains far more constant. There is also a virtually flat concentration profile in the *x*-direction other than close to the separator boundary. These effects complement work by Masliy et al., who describe the

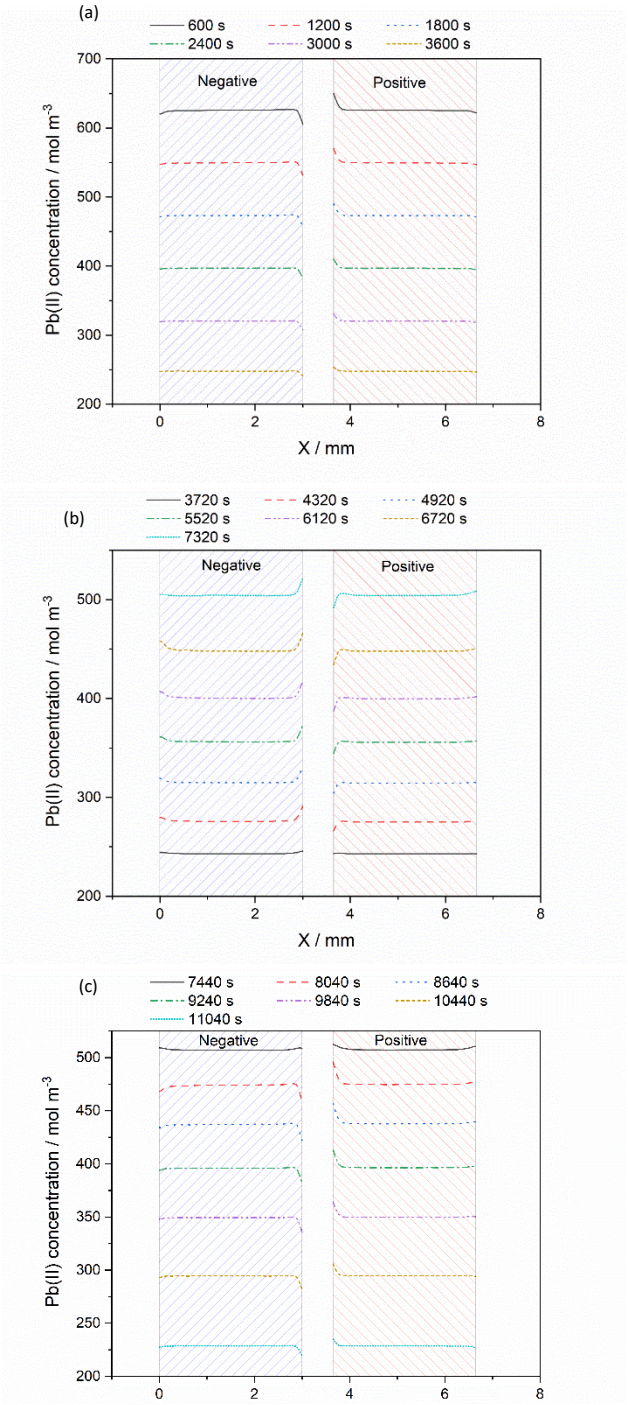

Figure 13: Pb^{2+} concentration distribution in the x-direction at the mid height of the electrodes for the divided configuration of the 10 ppi electrodes with an applied current density of 20 mA cm^{-2} during charge 1 (a), discharge 1 (b) and charge 2 (c).

expected current density distribution for a generalised redox reaction in porous electrodes [45]. In the negative electrode, both Pb^{2+} and H^{+} concentration decrease as the separator boundary is approached during charge, while in the positive electrode, the concentration of both species increases. The opposite is true during discharge.

Comparing different grades of RVC, there is little difference in the current distribution of the divided cells. However, in

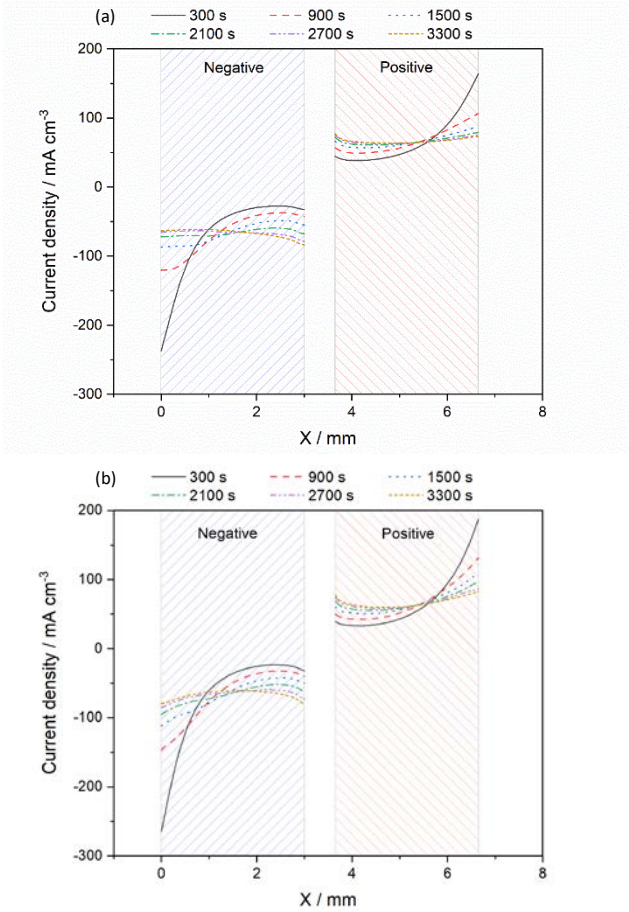

Figure 14: Current distribution in the x-direction at the mid height of the electrodes for the divided configuration of the 10 ppi (a) and 100 ppi (b) grades of RVC with an applied current density of 20 mA cm^{-2}.

general, the grades of RVC with a larger pore size gave a more even current distribution in the *x*-direction. As the cell is charged, the current distribution initially changes rapidly. However, with further charging, the current distribution stabilises. At 20 mA cm^{-2}, this occurs after approximately 2700 s, at 30 mA cm^{-2} by 2100 s, and at 50 mA cm^{-2} by 1500 s. At 50 mA cm^{-2}, this stable current distribution varies from circa 0.16 A cm^{-3} at the current collector to 0.13 A cm^{-3} at its lowest near the centre and 0.34 A cm^{-3} near the membrane in the 100 ppi negative electrode. In the 10 ppi negative electrode, it varies from 0.14 A cm^{-3} to 0.15 A cm^{-3} to 0.30 A cm^{-3}, see Figure 14. A similar trend is seen in the positive electrodes.

The most striking difference between different grades of RVC is the overpotential. This is to be expected, as while the starting porosity is roughly equivalent across the different grades, the surface area varies significantly. A higher surface area leads to a lower local current density, and by inspecting the Butler-Volmer equations (eq(3.10) and eq(3.11)), it can be determined that this leads to a lower overpotential. Accordingly, the 100 ppi

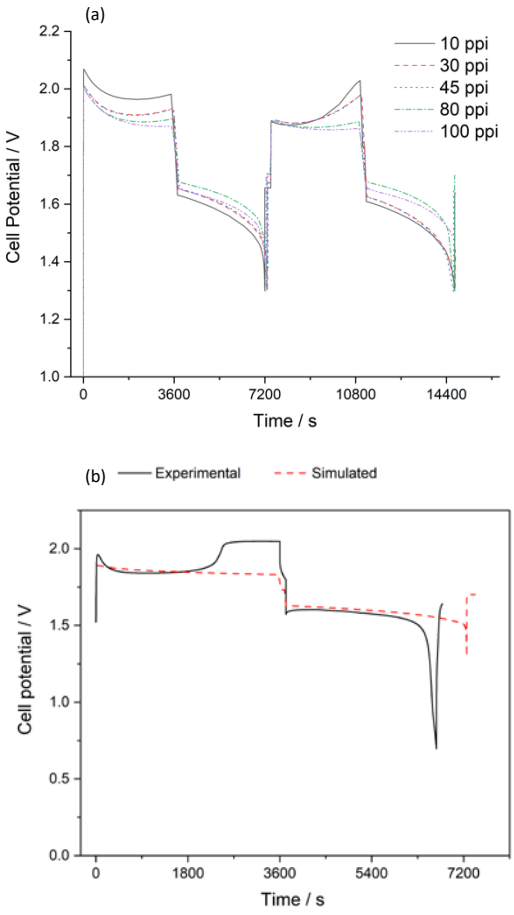

Figure 15: Cell potential vs time for (a) different grades of RVC with an applied current density of 20 mA cm^{-3} and (b) experimental and simulated results for 80ppi RVC electrodes with an applied current density of 20mA $cm^{-2,}$ the first cycle is omitted.

electrodes, which have smaller pores and hence a larger surface area, have a greatly reduced overpotential during both charge and discharge than the lower ppi electrodes. When compared to the 10 ppi electrodes, the overpotential is reduced by approximately 100 mV, see Figure 15 (a).

Figure 15 (b) shows a comparison between experimental and simulated cell potential of a cell cycled at 20 mA cm^{-2} using 80 ppi RVC electrodes. The model setup was modified to match the dimensions of the experimental cell. The first cycle is omitted. The simulated potential closely matches the experimental at the start of both the charge and discharge steps. At the end of the charge, the experimental cell potential rises to approximately 2.05 V. However, the simulated voltage remains at approximately 1.85 V. This suggests that the kinetics of the reactions at the positive electrode could be improved. The side reaction in this model is simplified. Further work is required to fully understand this reaction. During discharge, while the coulombic efficiency of the experimental cell is lower, the cell potential of the simulated cell is closely matched to that of the experimental cell. In both cells, a voltage efficiency of over 80 % is achieved.

Applied current density appears to have a much greater impact on variation in current distribution. While the general trend of decreasing current near the current collectors and increasing near the membrane boundary is true for all the simulated applied current densities, once it has settled, the current remains approximately even throughout the electrode at 20 mA cm^{-2} in the 10 ppi electrodes. However, as the current density increases, the current near the separator boundary increases more than in the remainder of the electrodes. This is true for both the positive and the negative electrodes.

One method to decrease the variability in current density within the electrodes would be to combine grades of RVC to form a graduated electrode. A similar method is used with lithium-ion batteries [46]. While it appears that there would be little benefit in this method at lower current densities, at higher currents, the region close to the separator boundary would benefit from a relative reduction in current density. This could be achieved by using a larger pore size close to the centre of the cell than for the bulk electrode. Only a small region would require this increased pore size, allowing the remainder of the electrode to take advantage of the lower overpotential and hence increased efficiency gained from using RVC with smaller pores.

Conclusions

A novel numerical model for investigating three-dimensional electrodes in the soluble lead flow battery, which has been validated against experimental results, has been developed. The model highlights the benefits of using reticulated vitreous carbon as an electrode material at both electrodes. The model emphasises the issues with using thin layers of RVC divided by a region of free electrolyte, as has been used in previous experimental studies of RVC in the SLFB. Even with the high permeability of RVC, there is a significant reduction in electrolyte velocity within the electrodes. A high current density is predicted near the inlet, which causes a build-up of deposit in this area, further diverting the electrolyte out of the electrode domains. Forcing the electrolyte through the RVC electrodes by

replacing the free electrolyte domain with a microporous separator significantly improved the current distribution in the *y*-direction. In the divided configuration, the concentration is substantially less varied in both *x* and *y* directions.

The higher surface area of RVC with smaller pores leads to a reduction in overpotential. Comparing 100 ppi with 10 ppi RVC, there is a reduction in overpotential of over 100 mV when cycled with an applied current density of 50 mA cm^{-2}. At 20 mA cm^{-2}, a voltage efficiency of over 80 % is achieved experimentally. While using a single grade of RVC for each electrode still gives an uneven current distribution, in future, by taking advantage of their different overpotentials, it may be possible to combine different grades of RVC to provide an optimal current distribution for a specific application.

Conflicts of interest

There are no conflicts to declare.

Acknowledgements

The authors acknowledge the use of the IRIDIS High Performance Computing Facility at the University of Southampton during the completion of this work. The authors also acknowledge the financial support received from the Engineering and Physical Sciences Research Council (EPSRC) through the Centre for Doctoral Training in Energy Storage and its Applications grant EP/L016818/1 and from UK aid from the UK Government through the Faraday Institution and the Transforming Energy Access Programme (Grant number FIEE-002 – Reclaimed Electrolyte, Low Cost Flow Battery RELCo-Bat); however, the views expressed do not necessarily reflect the UK government's official policies.

References

[1] M.S. Ziegler, J.M. Mueller, G.D. Pereira, J. Song, M. Ferrara, Y.-M. Chiang*, et al.* (2019) Storage requirements and costs of shaping renewable energy toward grid decarbonization, *Joule,* **3** (9), pp. 2134-2153,

[2] S. Homan, N. Mac Dowell and S. Brown (2021) Grid frequency volatility in future low inertia scenarios: Challenges and mitigation options, *Applied Energy,* **290**, p. 116723,

[3] US Department of Energy (2020), DOE Global Energy Storage Database. Available: https://www.sandia.gov/ess-ssl/global-energy-storage-database/ [Accessed:10/01/2021].

[4] L. da Silva Lima, M. Quartier, A. Buchmayr, D. Sanjuan-Delmás, H. Laget, D. Corbisier*, et al.* (2021) Life cycle assessment of lithium-ion batteries and vanadium redox flow batteries-based renewable energy storage systems, *Sustainable Energy Technologies and Assessments,* **46**, p. 101286,

[5] S. Ha and K.G. Gallagher (2015) Estimating the system price of redox flow batteries for grid storage, *Journal of Power Sources,* **296**, pp. 122-132,

[6] E. Sánchez-Díez, E. Ventosa, M. Guarnieri, A. Trovò, C. Flox, R. Marcilla*, et al.* (2021) Redox flow batteries: Status and perspective towards sustainable stationary energy storage, *Journal of Power Sources,* **481**, p. 228804,

[7] K. Orapeleng, R.G. Wills and A. Cruden (2018) Performance of recovered and reagent grade electrolyte in a soluble lead redox cell, *Journal of Energy Storage,* **20**, pp. 49-56,

[8] K. Orapeleng, R.G. Wills and A. Cruden (2017) Developing electrolyte for a soluble lead redox flow battery by reprocessing spent lead acid battery electrodes, *Batteries,* **3** (2), p. 15,

[9] D. Pletcher and R. Wills (2004) A novel flow battery: A lead acid battery based on an electrolyte with soluble lead (II) Part II. Flow cell studies, *Physical Chemistry Chemical Physics,* **6** (8), pp. 1779-1785,

[10] M. Krishna, E.J. Fraser, R.G.A. Wills and F.C. Walsh (2018) Developments in soluble lead flow batteries and remaining challenges: An illustrated review, *Journal of Energy Storage,* **15**, pp. 69-90, 10.1016/j.est.2017.10.020

[11] M.G. Verde, K.J. Carroll, Z. Wang, A. Sathrum and Y.S. Meng (2013) Achieving high efficiency and cyclability in inexpensive soluble lead flow batteries, *Energy & Environmental Science,* **6** (5), pp. 1573-1581, 10.1039/C3EE40631H

[12] M. Lanfranconi and H.-J. Lilienhof (2019) All-lead-flow-batteries as promising candidates for energy storage solutions, *Journal of Sustainable Development of Energy, Water and Environment Systems,* **7** (2), pp. 343-354,

[13] D. Pletcher and R. Wills (2005) A novel flow battery: A lead acid battery based on an electrolyte with soluble lead(II) Part III. The influence of conditions on battery performance, *Journal of Power Sources,* **149** (0), pp. 96-102, http://dx.doi.org/10.1016/j.jpowsour.2005.01.048

[14] A.A. Shah, X. Li, R.G. Wills and F.C. Walsh (2010) A mathematical model for the soluble lead-acid flow battery, *Journal of The Electrochemical Society,* **157** (5), pp. A589-A599, 10.1149/1.3328520

[15] M.N. Nandanwar, K.S. Kumar, S. Srinivas and D. Dinesh (2020) Pump-less, free-convection-driven redox flow batteries: Modelling, simulation, and experimental demonstration for the soluble lead redox flow battery, *Journal of Power Sources,* **454**, p. 227918,

[16] M. Nandanwar and S. Kumar (2019) A modelling and simulation study of soluble lead redox flow battery: Effect of presence of free convection on the battery characteristics, *Journal of Power Sources,* **412**, pp. 536-544, 10.1016/j.jpowsour.2018.11.070

[17] M. Nandanwar and S. Kumar (2016) Charge coup de fouet phenomenon in soluble lead redox flow battery, *Chemical Engineering Science,* **154**, pp. 61-71, 10.1016/j.ces.2016.07.001

[18] M.N. Nandanwar and S. Kumar (2014) Modelling of Effect of Non-Uniform Current Density on the Performance of Soluble Lead Redox Flow Batteries, *Journal of The Electrochemical Society,* **161** (10), pp. A1602-A1610, 10.1149/2.0281410jes

[19] A. Bates, S. Mukerjee, S.C. Lee, D.-H. Lee and S. Park (2014) An analytical study of a lead-acid flow battery as an energy storage system, *Journal of Power Sources,* **249**, pp. 207-218, 10.1016/j.jpowsour.2013.10.090

[20] A. Oury, A. Kirchev and Y. Bultel (2014) A numerical model for a soluble lead-acid flow battery comprising a three-dimensional honeycomb-shaped positive electrode, *Journal of Power Sources,* **246**, pp. 703-718, 10.1016/j.jpowsour.2013.07.101

[21] L. Arenas, C.P. de León and F. Walsh (2020) Critical review—The versatile plane parallel electrode geometry: An illustrated review, *Journal of The Electrochemical Society,* **167** (2), p. 023504,
[22] A. Banerjee, D. Saha, T.N.G. Row and A.K. Shukla (2013) A soluble-lead redox flow battery with corrugated graphite sheet and reticulated vitreous carbon as positive and negative current collectors, *Bulletin of Materials Science,* **36** (1), pp. 163-170, 10.1007/s12034-013-0426-7
[23] A. Czerwiński and M. Żelazowska (1997) Electrochemical behavior of lead dioxide deposited on reticulated vitreous carbon (RVC), *Journal of Power Sources,* **64** (1–2), pp. 29-34, http://dx.doi.org/10.1016/S0378-7753(96)02496-2
[24] A. Czerwiński and M. Żelazowska (1996) Electrochemical behavior of lead deposited on reticulated vitreous carbon, *Journal of Electroanalytical Chemistry,* **410** (1), pp. 55-60,
[25] R.G.A. Wills, J. Collins, D. Stratton-Campbell, C.T.J. Low, D. Pletcher and F. Walsh (2010) Developments in the soluble lead-acid flow battery, *Journal of Applied Electrochemistry,* **40** (5), pp. 955-965, 10.1007/s10800-009-9815-4
[26] A. Hazza, D. Pletcher and R. Wills (2005) A novel flow battery: A lead acid battery based on an electrolyte with soluble lead(II) Part IV. The influence of additives, *Journal of Power Sources,* **149** (0), pp. 103-111, http://dx.doi.org/10.1016/j.jpowsour.2005.01.049
[27] F. Walsh, L. Arenas, C. Ponce de León, G. Reade, I. Whyte and B. Mellor (2016) The continued development of reticulated vitreous carbon as a versatile electrode material: Structure, properties and applications, *Electrochimica Acta,* **215**, pp. 566-591,
[28] E.J. Fraser, K.K.J. Ranga Dinesh and R.G.A. Wills (2020) Development of a two-dimensional, moving mesh treatment for modelling the reaction chamber of the soluble lead flow battery as a function of state of charge for Pb and PbO2 deposition and dissolution, *Journal of Energy Storage,* **31**, p. 101484,
[29] SGL (2019), SIGRACELL Bipolar Plate datasheet. Available: https://www.sglcarbon.com/en/markets-solutions/material/sigracell-bipolar-plates-and-end-plates/ [Accessed:17/03/2019].
[30] M. Krishna, L. Wallis, R. Wills, D. Hall and A. Shah (2017) Measurement of key electrolyte properties for improved performance of the soluble lead flow battery, *International Journal of Hydrogen Energy,* **42** (29), pp. 18491-18498, 10.1016/j.ijhydene.2017.05.004
[31] D.A. Nield and A. Bejan, *Convection in porous media* vol. 3: Springer, 2006.
[32] E.J. Fraser, K.R. Dinesh and R. Wills (2021) A two dimensional numerical model of the membrane-divided soluble lead flow battery, *Energy Reports,* **7**, pp. 49-55,
[33] R.H.P.D.W. Green, R.H. Perry, D.W. Green and Knovel, *Perry's Chemical Engineers' Handbook, Eighth Edition*: McGraw-Hill Education, 2008.
[34] J. Cook, M. Laubitz and M. Van der Meer (1974) Thermal conductivity, electrical resistivity, and thermoelectric power of Pb from 260 to 550 K, *Journal of Applied Physics,* **45** (2), pp. 510-513,
[35] W. Mindt (1969) Electrical Properties of Electrodeposited PbO2 Films, *Journal of The Electrochemical Society,* **116** (8), pp. 1076-1080, 10.1149/1.2412217
[36] L.F. Arenas, R.P. Boardman, C.P. de León and F.C. Walsh (2018) X-ray computed micro-tomography of reticulated vitreous carbon, *Carbon,* **135**, pp. 85-94,
[37] J. Le Houx and D. Kramer (2021) X-ray tomography for lithium ion battery electrode characterisation—A review, *Energy Reports,* **7**, pp. 9-14,
[38] C.A. Schneider, W.S. Rasband and K.W. Eliceiri (2012) NIH Image to ImageJ: 25 years of image analysis, *Nature methods,* **9** (7), pp. 671-675,
[39] J. Le Houx and D. Kramer (2021) OpenImpala: OPEN source IMage based PArallisable Linear Algebra solver, *SoftwareX,* **15**, p. 100729,
[40] J. Le Houx, M. Osenberg, M. Neumann, J.R. Binder, V. Schmidt, I. Manke*, et al.* (2020) Effect of Tomography Resolution on Calculation of Microstructural Properties for Lithium Ion Porous Electrodes, *ECS Transactions,* **97** (7), p. 255,
[41] The Iridis Compute Cluster. Available: https://www.southampton.ac.uk/isolutions/staff/iridis.page [Accessed:07/07/2021].
[42] M. Doube, M.M. Kłosowski, I. Arganda-Carreras, F.P. Cordelières, R.P. Dougherty, J.S. Jackson*, et al.* (2010) BoneJ: free and extensible bone image analysis in ImageJ, *Bone,* **47** (6), pp. 1076-1079,
[43] C.D. Iacovangelo and F.G. Will (1985) Parametric study of zinc deposition on porous carbon in a flowing electrolyte cell, *Journal of The Electrochemical Society,* **132** (4), pp. 851-857,
[44] G. Tomazic and M. Skyllas-Kazacos, "Chapter 17 - Redox Flow Batteries," in *Electrochemical Energy Storage for Renewable Sources and Grid Balancing*, P. T. Moseley and J. Garche, Eds., ed Amsterdam: Elsevier, 2015, pp. 309-336.
[45] A. Masliy, N. Poddubny, A.Z. Medvedev and V. Lukyanov (2015) Analysis of the distribution of geometrical current density along the direction of solution flow inside flow-by porous electrodes, *Journal of Electroanalytical Chemistry,* **757**, pp. 128-136,
[46] Y. Qi, T. Jang, V. Ramadesigan, D.T. Schwartz and V.R. Subramanian (2017) Is there a benefit in employing graded electrodes for lithium-ion batteries?, *Journal of The Electrochemical Society,* **164** (13), p. A3196,